Complexes polynucléaires d'Uranium : structure réactivité et propriétés

Victor Mougel

UNIVERSITÉ DE GRENOBLE

THESIS

For obtaining the degree of

DOCTOR OF PHILOSOPHY OF UNIVERSITÉ DE GRENOBLE

Specialty **Inorganic and Bio-Inorganic Chemistry**

Arrêté ministériel : 7 août 2006

Presented by

Victor MOUGEL

Thesis directed by **Marinella MAZZANTI**

Thesis prepared in the **Laboratoire de Reconnaissance Ionique et Chimie de Coordination** du **Service de Chimie Inorganique et Biologique, INAC, CEA-Grenoble**
In the **Ecole Doctorale Chimie Sciences Du Vivant**

Polynuclear compounds of uranium: structure, reactivity and properties

Thesis scheduled the **28 september 2012**,
in presence of:

Dr. Stéphane MENAGE
Directeur de recherche au CEA-Grenoble (Président)
Pr. Karsten MEYER
Professor at FAU Erlangen-Nuremberg (Rapporteur)
Dr. Stephen LIDDLE
Associate Professor at the University of Nottingham, (Rapporteur)
Dr. Anne DOLBECQ
Directrice de recherche à l'Université de Versailles-St-Quentin (Examinatrice)
Pr. Christophe DEN AUWER
Professeur à l'Université de Nice Sophia-Antipolis (Examinateur)
Dr. Marinella MAZZANTI
Directrice de recherche au CEA-Grenoble (Directrice de thèse)

Université Joseph Fourier / Université Pierre Mendès France / Université Stendhal / Université de Savoie / Grenoble INP

UNIVERSITÉ DE GRENOBLE

THÈSE

Pour obtenir le grade de

DOCTEUR DE L'UNIVERSITÉ DE GRENOBLE

Spécialité : **Chimie Inorganique et Bio-inorganique**

Arrêté ministériel : 7 août 2006

Présentée par

Victor MOUGEL

Thèse dirigée par **Marinella MAZZANTI**

préparée au sein du **Laboratoire de Reconnaissance Ionique et Chimie de Coordination** du **Service de Chimie Inorganique et Biologique, INAC, CEA-Grenoble**
dans **l'École Doctorale Chimie Sciences du Vivant**

Complexes polynucléaires d'uranium : structure, réactivité et propriétés

Soutenance prévue le **28 septembre 2012**,
devant le jury composé de :

Dr. Stéphane MENAGE
Directeur de recherche au CEA-Grenoble (Président)

Pr. Karsten MEYER
Professeur à l'Université FAU Erlangen-Nuremberg (Rapporteur)

Dr. Stephen LIDDLE
Professeur associé à l'Université de Nottingham, (Rapporteur)

Dr. Anne DOLBECQ
Directrice de recherche à l'Université de Versailles-St-Quentin (Examinatrice)

Pr. Christophe DEN AUWER
Professeur à l'Université de Nice Sophia-Antipolis (Examinateur)

Dr. Marinella MAZZANTI
Directrice de recherche au CEA-Grenoble (Directrice de thèse)

Université Joseph Fourier / Université Pierre Mendès France / Université Stendhal / Université de Savoie / Grenoble INP

RÉSUMÉ

L'étude et la compréhension de la chimie fondamentale des actinides constitue un axe de recherche privilégié notamment dans le cadre de la technologie nucléaire tant en amont pour le développement de nouveaux combustibles qu'en aval pour l'étude du retraitement des déchets nucléaires. Une des problématiques principales au cours de ces études réside dans la capacité que possèdent les actinides à subir des réactions rédox et à former des assemblages polynucléaires. Néanmoins, très peu d'assemblages polynucléaires peuvent être synthétisés de manière reproductible, la plupart des complexes polynucléaires d'actinides décrits dans la littérature sont formés de façon fortuite plutôt que par conception rationnelle. En outre, les assemblages polynucléaires s'uranium ont été identifiés comme particulièrement prometteurs pour l'élaboration de matériaux magnétiques et pour leur réactivité. L'objectif de ce travail réside dans la synthèse d'assemblages polymétalliques à base d'uranium en mettant à profit quelques aspects de sa réactivité redox et de sa chimie de coordination. De nouvelles voies de synthèse de composés polynucléaires d'uranium ont été développées, et l'étude des propriétés physico-chimique des composés a été réalisée. La première approche utilisée repose sur la synthèse d'assemblages d'uranyle pentavalent. L'uranyle pentavalent est connu pour sa facilité d'agrégation via des interactions entre groupement uranyles appelées interaction cation-cation, mais l'isolation de ce type de composé a été très largement limitée par l'instabilité de l'uranyle(V) vis-à-vis de la dismutation. L'utilisation de ligands base de Schiff de type salen a permis dans ces travaux l'isolation du premier assemblage polynucléaire d'uranyle(V). Sur la base de ce résultat, la variation des ligands et des contre-ions utilisés a permis l'isolation d'une large famille d'assemblages polynucléaires d'uranyle(V) et l'étude fine des paramètres régissant leur stabilité. Par ailleurs, l'étude des propriétés magnétiques de ces assemblages a mis en valeur de rares exemples couplages antiferromagnétiques. En outre, cette voie de synthèse a été exploitée pour synthétiser le premier cluster 5f/3d présentant des propriétés de molécule aimant. Le deuxième axe d'approche suivi dans ce travail repose sur l'isolation de clusters oxo/hydroxo d'uranium. La réactivité d'hydrolyse de complexes d'uranium trivalent en présence de ligand à pertinence environnementale à permis la synthèse d'assemblages d'uranium dont la taille à pu être variée en fonction des conditions de synthèse employées. Enfin, de nouveaux assemblages présentant des topologies originales ont été isolés en exploitant la réactivité de dismutation de précurseurs d'uranium pentavalent.

Mots-clés
uranium, uranyle(V), interaction cation-cation, CCI, salen, cluster, magnétisme, molécule aimant, SMM, acide benzoïque

Discipline
Chimie Inorganique

Laboratoire
Laboratoire de Reconnaissance Ionique et Chimie de Coordination
Service de Chimie Inorganique et Biologique, UMR-E3 CEA-UJF
Institut Nanosciences et Cryogénie, CEA Grenoble
17 Rue des Martyrs, 38054 Grenoble Cedex, France

ABSTRACT

The study and comprehension of actinide's fundamental chemistry has important implications both for the development of new nuclear fuel and for the nuclear fuel reprocessing. One of the major issues in these processes is the ease of uranium to undergo redox reactions and to form polynuclear assemblies, which largely perturb these processes. However, despite their relevance, few synthetic routes towards polynuclear uranium assemblies are described in the literature, and most of the polynuclear complexes reported are formed by serendipity rather than by rational design. Moreover, polynuclear uranium compounds are highly promising for the design of magnetic materials with improved properties and for reactivity studies. The aim of this work is the synthesis of polynuclear uranium complexes and the study of their reactivity and coordination properties. New synthetic routes to uranium polynuclear assemblies were developed and the study of their physico-chemical properties was carried out. The first approach investigated was based on pentavalent uranyl chemistry. Uranyl(V) is known to form aggregates via an interaction between uranyl moieties often named cation-cation interaction, but the isolation of uranyl(V) complexes had been largely limited by its ease of disproportionation. We isolated the first stable uranyl(V) polynuclear assembly using salen-type Schiff base ligand. Based on this result, a fine tuning of the ligand and counterion properties resulted in the isolation of a large family of uranyl(V) polynuclear assemblies and in a better understanding of the parameters ruling their stability. Moreover, rare examples of clear antiferromagnetic couplings were observed with these complexes. In addition, this synthetic path was used to build the first 5f-3d cluster presenting single molecule magnet properties. The second approach used in this thesis consisted in the synthesis of oxo/hydroxo uranium clusters. The controlled hydrolysis of trivalent uranium in presence of an environmentally relevant ligand lead to the synthesis of clusters, which size could be varied in function of the reaction conditions employed. Finally, new uranium clusters with original topologies were synthesised through the induced disproportionation of pentavalent uranyl precursors.

Keywords
uranium, uranyl(V), cation-cation interaction, CCI, salen, cluster, magnetism, single molecule magnet, SMM, benzoic acid

Specialty
Inorganic Chemistry

Laboratory
Laboratoire de Reconnaissance Ionique et Chimie de Coordination
Service de Chimie Inorganique et Biologique, UMR-E3 CEA-UJF
Institut Nanosciences et Cryogénie, CEA Grenoble
17 Rue des Martyrs, 38054 Grenoble Cedex, France

ACKNOWLEDGEMENTS / REMERCIEMENTS

First of all I would like to thank all the members of my committee for accepting to review this thesis work.

I would like to acknowledge my advisor, Dr. Marinella Mazzanti, not simply because it is standard issue to do so, but because she truly is the single most important factor to which I can attribute any success I was able to achieve during my PhD studies. From her I have learned a great deal about coordination chemistry and, by her example, much about scientific curiosity and discipline. I am grateful both for her excellent guidance as well as her willingness to let me take the project in the directions I found most interesting.

Je souhaiterais souligner la profonde influence de Bernard Seguin, mon professeur de Physique/Chimie de collège, dans mon choix de poursuivre une carrière scientifique. Je tiens également à remercier Yann Bretonnière à l'ENS de Lyon, qui fut mon premier contact avec le monde de la recherche, et m'a permis d'y prendre gout.

At Durham University, David Parker's enthusiasm for lanthanides chemistry got me interested in f-elements and his encouragements and advices contributed to the choice of this PhD subject.

This work would not have been possible without the teammates of the "uranium room", Biplab, Roy, Johannes and especially Pawel and Greg who introduced me to uranium chemistry. Un grand merci à Lucile également, qui a travers son très bon stage de master 2 a contribué scientifiquement et humainement a cette thèse.

Ce travail n'aurait été possible sans l'aide de Jacques Pécaut pour son expertise cristallographique, alliée à un sens de l'humour et de la pédagogie hors pair! Je tiens également à remercier Lionel Dubois et Jean Francois Jacquot pour leur aide pour les mesures magnétiques, Colette Lebrun pour la spectrométrie de masse et Pierre-Alain Bayle pour les études RMN.

I am also very thankful to Prof. Roberto Caciuffo and his group for the a.c. magnetic measurement and their interpretation, and for welcoming me in Karlsruhe for the measurement and synthesis campaigns.

Merci également à Pascale Maldivi pour m'avoir accueilli au sein de son laboratoire, à Zohra Termache, secrétaire hors pair, et à tous les membres du labo qui ont contribué à mon envie quotidienne de venir au labo.

My special thanks are for my friends and colleagues: Gaylord, Gülay, Marco, Pawel, Eugen, Roy, Greg, Lydia, Yves, Nicolas, Biplap, Lucile, Johannes, Graeme, Anais, Laetitia, Céline, Julie and Valentin. Thursday evening pub sessions with them were the carrot-on-a-stick that got me through some long weeks! Un immense merci aux ENS-potes, Benji, Julien, Martin, Florian, Maryam et Naoko, pour les breaks détente passés ensemble et les discussions chimiques passionnées et passionnantes!

Un scientifique tatillon ferait remarquer l'oubli d'une personne dans ces remerciements: le cas de Clément est à part car il rentre dans un trop grand nombre de catégories, étant à la fois ami, collègue, confident... Clément possède l'incroyable qualité de réaliser tout ce qu'il entreprend, y compris en chimie, avec plus d'enthousiasme et de cœur que quiconque.

Un immense merci à mes sœurs Mathilde et Eléonore, et à mes parents, pour leur soutien sans faille et leur indéfectible affection, et pour ne pas m'avoir renié en dépit de mon peu de disponibilité depuis trois ans!

Un merci particulier à toi Fanny pour ta compréhension, ton amour et pour m'avoir supporté ces derniers mois (dans tous les sens du terme).

Table of contents

Introduction

CHAPTER I. Introduction

I.1 Introduction to uranium and the actinides

In 1789, while French citizens were busy at writing the *Declaration of the Rights of Man and of the Citizen*, another revolution took place on the other side of the Rhine, with the discovery of uranium by the German chemist Martin Heinrich Klaproth from Sankt Joachimsthal Pitchblende. He named it after the planet Uranus discovered eight years earlier. Although at the time Klaproth thought that he had discovered uranium metal [1], its actual isolation was not achieved until 1841, when the French chemist Eugène Melchior Péligot reduced the anhydrous uranium tetrachloride with potassium[2]. Uranium is the 51st element in the order of abundance on earth crust, and also the highest-numbered element to be naturally found in significant quantities on earth. It has been widely used in the colouring of glass before its formal identification, but one of its most interesting properties has only been discovered in 1896 by the French physicist Henry Becquerel, who noticed that photographic plates were "fogged" after standing close to a uranium sample. He determined that a form of invisible light or ray emitted by uranium had exposed the plate, and introduced the concept of uranic ray [3], later generalized by Marie Curie under the concept of radioactivity.

Subsequent researches of Otto Hahn proved that the 235 isotope of uranium can undergo nuclear fission, a property exploited by Enrico Fermi to initiate the first self-sustained nuclear chain reaction during the Manhattan Project. This discovery quickly leads to the development of the first nuclear bombs, and later to the civil nuclear reactors.

Elements beyond uranium are all man-made, and were discovered consequently to the Manhattan project and the work of Glenn Seaborg along the 20th century, to complete the actinide family.

I.2 Characteristics of the actinides

As depicted in Table I-1, the accessible oxidation states of the actinides strongly vary along the actinide series. For the early actinides (Th-Np), the highest oxidation state (not necessarily the most stable) reflects the total number of electrons that can be released from the outer shell. This resemblance to the transition metals was noted for uranium in the early studies of the uranium tetrachloride by Péligot [2] and initially made chemists think that the actinides were another block of transition metals. The late actinides (from Bk), similarly to lanthanides tend to exhibit only the +3 oxidation state.

Table I-1 Electron configuration of the actinides for neutral atom and accessible oxidation state. Most stable oxidation states are printed in red (+ VII oxidation states of Np, Pu and Am are not represented, due to their rarity). Adapted from [4]

Actinide	Neutral Atom Electron Configuration	Ground state electronic configuration				
		II (M^{2+})	III (M^{3+})	IV (M^{4+})	V (MO_2^{+})	VI (MO_2^{2+})
Ac	$[Rn]7s^2 6d^1$		[Rn]			
Th	$[Rn]7s^2 6d^2$			[Rn]		
Pa	$[Rn]7s^2 6d^1 5f^2$			$[Rn]\ 5f^1$	[Rn]	
U	$[Rn]7s^2 6d^1 5f^3$		$[Rn]\ 5f^3$	$[Rn]\ 5f^2$	$[Rn]\ 5f^1$	[Rn]
Np	$[Rn]7s^2 6d^1 5f^4$		$[Rn]\ 5f^4$	$[Rn]\ 5f^3$	$[Rn]\ 5f^2$	$[Rn]\ 5f^1$
Pu	$[Rn]7s^2 5f^6$		$[Rn]\ 5f^5$	$[Rn]\ 5f^4$	$[Rn]\ 5f^3$	$[Rn]\ 5f^2$
Am	$[Rn]7s^2 5f^7$		$[Rn]\ 5f^6$	$[Rn]\ 5f^5$	$[Rn]\ 5f^4$	$[Rn]\ 5f^3$
Cm	$[Rn]7s^2 6d^1 5f^7$		$[Rn]\ 5f^7$	$[Rn]\ 5f^6$		
Bk	$[Rn]7s^2 5f^9$		$[Rn]\ 5f^8$	$[Rn]\ 5f^7$		
Cf	$[Rn]7s^2 5f^{10}$		$[Rn]\ 5f^9$	$[Rn]\ 5f^8$		
Es	$[Rn]7s^2 5f^{11}$		$[Rn]\ 5f^{10}$			
Fm	$[Rn]7s^2 5f^{12}$	$[Rn]\ 5f^{12}$	$[Rn]\ 5f^{11}$			
Md	$[Rn]7s^2 5f^{13}$	$[Rn]\ 5f^{13}$	$[Rn]\ 5f^{12}$			
No	$[Rn]7s^2 5f^{14}$	$[Rn]\ 5f^{14}$	$[Rn]\ 5f^{13}$			
Lr	$[Rn]7s^2 6d^1 5f^{14}$		$[Rn]\ 5f^{14}$			

The 5f subshell has 7 f-orbitals, for which angular electronic distribution is given Figure I-1. Early in the actinide series, 6d orbitals are at lower energy than the 5f orbitals, as highlighted by the ground state configuration of the atoms given in Table I-1, which show that the 6d

orbitals are filled before the 5f ones. In addition, the energy difference between the $5f^n7s^2$ and $5f^{n-1}6d^17s^2$ is usually small, which means that more outer shell electrons are potentially available, explaining the range of oxidation states observed.

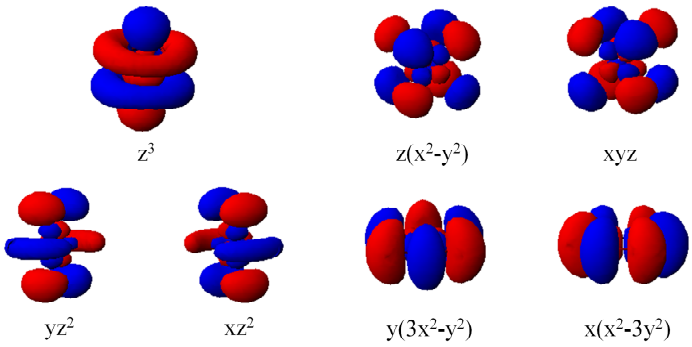

Figure I-1 Angular electronic distribution of 5f orbitals.

The radial extension of the 5f orbitals is larger than for the 4f orbitals, as highlighted in Figure I-2 comparing the radial electronic distribution of Sm^{3+} and Pu^{3+}, and the 5f orbitals are not shielded by the filled 6s and 6p subshell as much as the 4f orbitals of the lanthanides are (by the 5s and 5p respectively). It should also be noticed that due to the larger size, the relativistic effects are also larger for actinides than for lanthanides, these effects also contribute to the larger radial extension of the 5f orbitals. This observation has two direct consequences on complexes formation. The actinide-ligand interaction will be mainly ionic, resulting in a weak stereochemical preference and a labile coordination sphere, leading to variable coordination numbers (from 3 to 12) and geometries [5] but, unlike the lanthanides, the lower shielding results in more covalent metal-ligand interactions than with the lanthanide ions, these stronger interactions resulting in a larger sensitivity of the spectroscopic and magnetic properties to the coordination environment. Actinides and lanthanides are Pearson hard acids, preferring to bind to hard acids like oxygen and fluorine donors than to soft donors, but the increased covalency of actinides with respect to lanthanides results in a slightly higher affinity for soft electron donors, such as aromatic amines. This increased affinity for soft donors has been used to develop selective extractant for the separation of minor actinides (such as Am^{3+}) from lanthanides in spent nuclear fuel retreatment.[6, 7]

Finally, as the 5f electrons do not shield each other from the nucleus effectively due to the large extension of the 5f orbitals, the ionic radius of the actinides decrease with increasing atomic number.

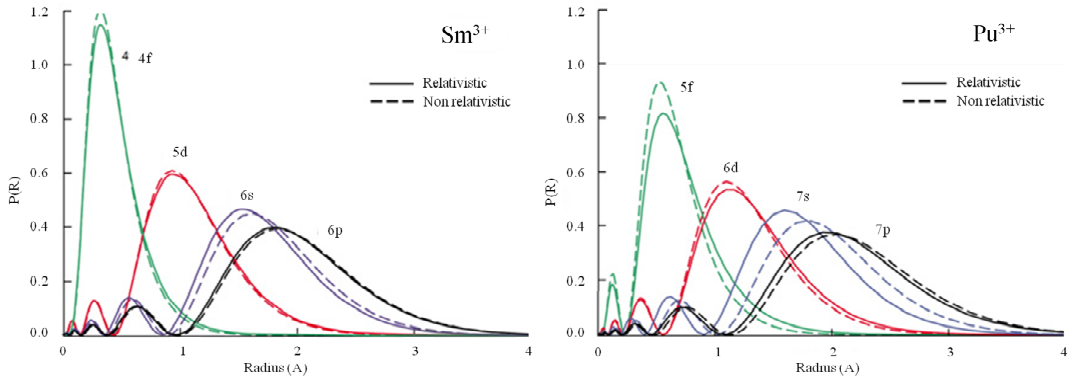

Figure I-2 Comparison of the radial distributions of the electronic orbitals for Sm^{3+} and Pu^{3+}. [8]

I.3 Polynuclear complexes of uranium

I.3.1 Introduction

The hard acid character of actinides is at the origin of the oxophilicity of actinide ions, resulting in the formation of very stable complexes with oxo or hydroxo ligands. These two ligands are well known to bridge metal centres, resulting in a strong tendency of actinides to form polynuclear complexes observed both in the environment and in the nuclear energy production related processes. The aggregation behaviour of the actinides strongly depends on their oxidation state, their multiple accessible oxidation numbers being at the origin of a large family of chemically distinct species. Given the large difference in the properties of actinide compounds in different oxidation state, it is convenient to discuss some general feature of the most abundant actinides (U, Np, Pu) to draw up a comprehensive analysis of their chemical behaviour. The known oxidation states of the actinides are summarized in Table I-1. We can observe that U, Pu and Np can exist in four oxidation states from +III to + VI (and in rare examples +VII for Np and Pu). Within these four accessible states, two different moieties exist, the ionic forms An^{n+} (An^{3+} and An^{4+} being the most common oxidation states observed) strongly differing from the bis-oxo moieties called actinyls AnO_2^{+} and AnO_2^{2+}. The latter cations are contained within linear moieties in which the actinide centre is bound to two oxygen atoms, resulting in an ion with an overall charge of +I or +II. The presence of two oxygens on the opposite sides of the metal centre implies that the coordination of additional ligands occurs in the equatorial plane of the actinyl ion, coordination number of four to six in this equatorial plane being usual. In contrast, the actinides in the +III and +IV oxidations

states are only found in the An^{n+} form, and thus have very small geometric preferences and can present a large array of coordination number (from 3 to 12).

The specificities of the different oxidation states in complexes formation are strongly related to the effective charge of the ion. While the An^{3+} and An^{4+} ions have a straightforward +3 and +4 effective charge, the partially covalent binding between the actinide and the two oxygen atoms in actinyl ions enhances the effective charge of the central actinide ion to +2.3 for AnO_2^{+} and +3.3 for AnO_2^{2+} (Scheme I-1) [9]

Scheme I-1

	An^{4+}	> AnO_2^{2+}	> An^{3+}	> AnO_2^{+}
Effective charge	4	3.3	3	2.2

Due to the highest effective charge of An(IV) ions, they form the most stable complexes in solution, and also form the most stable precipitates, with the lowest solubility. Conversely, the actinyl(V) moieties usually form very soluble species and are likely to form more labile species. However, depending on the solvent, pH or redox conditions found during the environmental migration or nuclear fuel reprocessing, very different behaviours and stabilities can be observed.

I.3.1.1 +IV oxidation state

The high charge allows the An^{4+} ions to easily hydrolyze and to form polynuclear oxo/hydroxo complexes through olation and oxolation reactions, as highlighted in Scheme I-2[10].

Scheme I-2 Hydrolysis, olation and oxolation reactions of tetravalent actinides

Hydrolysis of Actinide(IV) ions $An^{4+} + n\,H_2O \rightleftharpoons [An(OH)_n]^{(4-n)+} + n\,H^+$

Olation reaction $[An(OH)_n]^{(4-n)+} + [An(OH_2)_n]^{4+} \rightleftharpoons$ "An-OH-An" $+ H_2O$

Oxolation reaction $2\,[An(OH)_n]^{(4-n)+} \rightleftharpoons$ "An-O-An" $+ H_2O$

While the +IV oxidation state in the most stable for plutonium, uranium and neptunium(IV) compounds are common, but present a higher sensitivity to oxidation reactions. Plutonium(IV) is well known to hydrolyze even in dilute acidic solutions and, at concentrations greater than 10^{-6} M, will undergo oligomerization and polymerization to form

very stable colloids [11]. Once formed, these colloids are very stable in near-neutral solution, and the generation of Pu(IV) colloids has been shown to be one of the main processes that complicates the determination of thermodynamic constants and the accurate prediction of plutonium concentrations in solution. Depending on their size, their stability and their structural features, these polynuclear complexes can exhibit a wide range of solubilities, from insoluble polymers to very mobile colloids. These polynuclear complexes, usually regrouped under the term of plutonium hydrous polymers, have been at the origin of numerous studies during the past sixty years because of their interference in nuclear fuel ion exchange and extraction schemes.

I.3.1.2 +V oxidation state

As stated before, the chemistry of the actinides in the +V oxidation state is dominated by actinyl-type complexes, built around the AnO_2^+ moiety. Typically, only neptunium favours the +V oxidation state, but uranium and plutonium complexes in the pentavalent oxidation state can be observed transiently. Due to the low effective charge located on the metal centre, actinyl(V) are usually described as very soluble species due to the weak electrostatic interactions between the metal centre and external ligands. However, the strong Lewis basicity of the oxygen atoms of the actinyl moieties leads to the formation of complexes through the coordination of other metal ions to the actinyl oxygen. The direct linkage of two actinyl ions through the bonding of an oxo ion from one AnO_2^+ moiety as the equatorial ligand on an adjacent AnO_2^+ion has been designated as a cation-cation interaction (CCI) leading to the formation of polynuclear complexes of actinides with different geometries, described in Scheme I-3.

Scheme I-3 Type of cation-cation interactions encountered with actinyl(V) ions. M represent another metal cation.

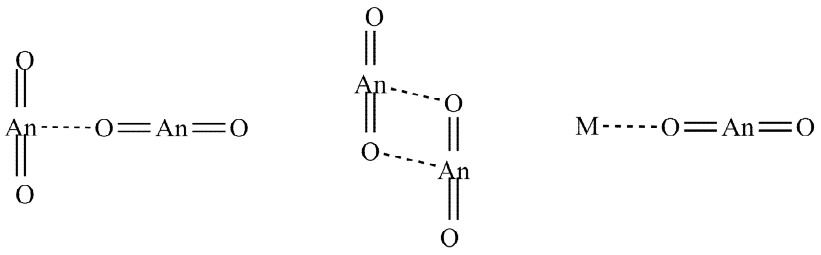

T-Shape Diamond Shape Linear

The stability of actinide cation-cation (CC) complexes is relatively low, but increases substantially with an increase in the ionic strength of the media or in organic solutions. The stability of An(V) CC complexes have been shown to decrease in the series $UO_2^+ > NpO_2^+ > PuO_2^+$ [12, 13]. Numerous studies have established that these CCI strongly affect the solubility and solution properties of actinyls in the +V oxidation state. However, the studies of these CC assemblies have been limited both by the radioactivity of plutonyl and neptunyl and by the instability of uranyl(V) towards disproportionation reaction. While neptunyl(V) and plutonyl(V) can also undergo disproportionation reaction under specific conditions, their stability domains are larger than for uranyl(V) for which disproportionation reaction occurs in most cases.

The study of this characteristic reactivity is critical in the understanding of the behaviour of pentavalent uranyl in solution.

I.3.1.2.1 *Uranyl(V) disproportionation*

I.3.1.2.1.a In aqueous solution

As highlighted by the Pourbaix diagram presented below Figure I-3, uranium is highly unstable as uranyl(V) because of the rapid disproportionation to UO_2^{2+} and U^{4+}, except in a very small pH region, between pH 2 and 5 in a very limited range of potential

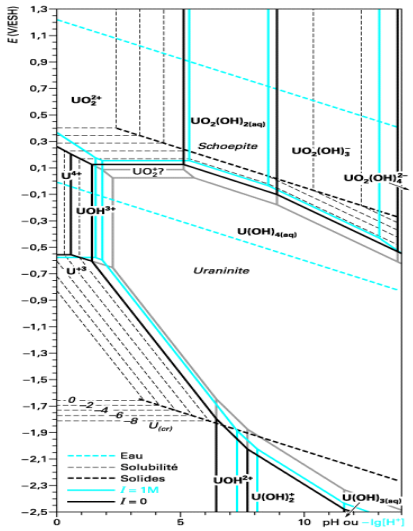

Figure I-3 Pourbaix diagram of uranium in aqueous solution [14]

However, a detailed study of the disproportionation reaction would be critical to the understanding of a very large range of reactions where a uranyl(V) intermediate is involved. This disproportionation reaction has thus been proved to be a key point in the isotopic

exchange of uranium in uranium(IV)/(VI) solutions [15], in the U(V) catalysed exchange of oxygen between U(VI) and water [16, 17], and in the more recently studied bioreduction of uranyl(VI) by bacteria [18]. Both early and recent studies agree that the disproportionation reaction can be described as Eq 1, in which the destabilizing effect of protons is evident.

$$2\ UO_2^+(aq) + 4\ H^+ \longrightarrow UO_2(aq)^{2+} + U^{4+}(aq) + 2\ H_2O \qquad (1)$$

In order to explain this H^+ dependence of the disproportionation mechanism, kinetic studies, based on polarographic and spectroscopic experiments were carried out [19-23]. The disproportionation rate had been found to be first order in H^+ concentration (Eq 5), suggesting the following mechanism, originally postulated by Orleman [21], that involves an initial protonation step to form a protonated uranyl(V) species which further reacts with another uranyl(V) in a rate limiting step (Eq 2-4).

$$UO_2^+ + H^+ \longrightarrow UO_2H^{2+} \qquad (2)$$

$$UO_2^+ + UO_2H^{2+} \rightleftharpoons UO_2^{2+} + UO_2H^+ \qquad (3)$$

$$2\ UO_2^+ + H^+ \longrightarrow UO_2^{2+} + UO_2H^+ \qquad (4)$$

This mechanism would explain the rate law observed for dilute uranyl(V) solutions in moderately acidic media described by Eq 5. These early studies also indicated that the disproportionation rate is also dependant on the total ionic strength and the nature of the anion present.

$$-\frac{d\,[UO_2^+]}{dt} = k.[H^+].[UO_2^+]^2 \qquad (5)$$

However, latter studies in deuterated solutions indicated that the rate of the reaction was not as significantly lowered as expected, which indicated that the proton transfer required in the first step of this mechanism was very improbable. Moreover Newton and Baker [23] obtained evidence for the formation of a binuclear complex through the association of uranyl(VI) with uranyl(V), the formation of this complex lowering the disproportionation rate of uranyl(V) as the uranyl(VI) concentration is raised. These observations lead to the proposition of an alternative mechanism by Ekström [24], involving the formation of a binuclear uranyl(V) CC dimeric intermediate, followed by the protonation steps. Recent mechanistic studies, based on DFT calculations tend to confirm this disproportionation mechanism through CCI [25-27]. The calculated mechanism implied three steps in aqueous solution, as described Figure I-4.

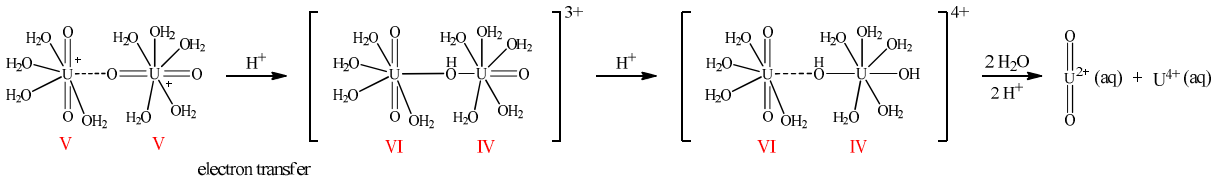

Figure I-4 Schematic mechanism of the uranyl(V) disproportion according to Steele and Taylor [25]

In this mechanism, the authors claim that the redox process occurs in the first step, the protonation of the bridging O_{yl} of the cation-cation (CC) complex being immediately followed by a single electron transfer from the unprotonated uranyl to the second one, resulting in a formal U(VI) and U(IV) centres. Following this step, the CC bond decreased of around 0.1 Å, due to the higher charge on the U(VI) centre, this effect being amplified by the second protonation of the O_{yl} of the U(IV) centre. The last step of the reaction pathway consists in the introduction of a water molecule in the coordination shell of the U(VI) centre, resulting in a breaking of the CCI to yield two monomeric uranium complexes.

At the molecular orbital level, calculation of the orbital occupancies of the CC intermediate gave clues about the electron transfer step; assuming that the electron transfer should occur via an orbital localised along the CC interaction, the model revealed that the highest occupied orbital located along the uranyl bond involved in CCI was the HOMO-2 (Figure I-8), and the author hypothesised that this orbital would facilitate the electron transfer mechanism.

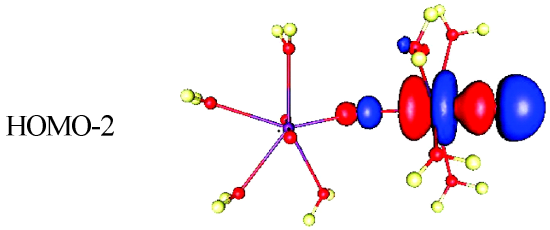

Figure I-5 HOMO-2 for the singly protonated dimer [25]

Moreover, this model seems to be very consistent with experimental facts, the rate law being verified with this mechanism, and this mechanism being coherent with the less favoured disproportionation observed in the presence of uranyl(VI)indicative of the primary formation of a cation-cation adduct before protonation.

I.3.1.2.1.b In organic media

However, while a large number of studies of the disproportionation of uranyl(V) in aqueous solution have been published, up to very recently the only cases of non aqueous studies of the disproportionation of uranyl(V) were a few studies in ionic liquids[28-30]. These few studies are very specific from molten salt chemistry, but a very interesting property observed in these non

aqueous media is that, depending on the reaction condition, the Eq (1) can be shifted in the direction of the disproportionation or in the direction of the comproportionation, if protons are added or removed from the media.

The critical role of cation-cation interactions in the disproportionation reaction of uranyl(V) largely limited the isolation of polynuclear complexes of uranyl(V). However, the rational design of polynuclear pentavalent assemblies would provide valuable information for the understanding of uranyl(V) behaviour in solution.

I.3.1.3 +VI oxidation state

Similarly to the pentavalent oxidation state, hexavalent actinides are mainly present under the form of the bis oxo actinyl(VI) moiety AnO_2^{2+}. Uranyl(VI) is the main species observed in the +VI oxidation state in the actinides series, since uranyl(VI) represents the most stable species of uranium. The effective charge of the actinide atom in actinyl(VI) moieties being higher than in the +V analogue, the Lewis basicity of the two oxo atoms is lowered with respect to its pentavalent analogue. This weakens the CC interactions, which are rarely observed in this oxidation state. However, the larger effective charge on the metal centre allows forming stable polynuclear complexes with strong Lewis bases, such as oxo, hydroxo or peroxo ligands coordinated in the equatorial plane of the actinyl moiety (Scheme I-4). The result of the linkage of actinyl moieties through their equatorial plane is the formation of extended and often highly complex structures [10, 31].

Scheme I-4 Formation of hydroxo, oxo and peroxo bridged actinyl(VI) dimer

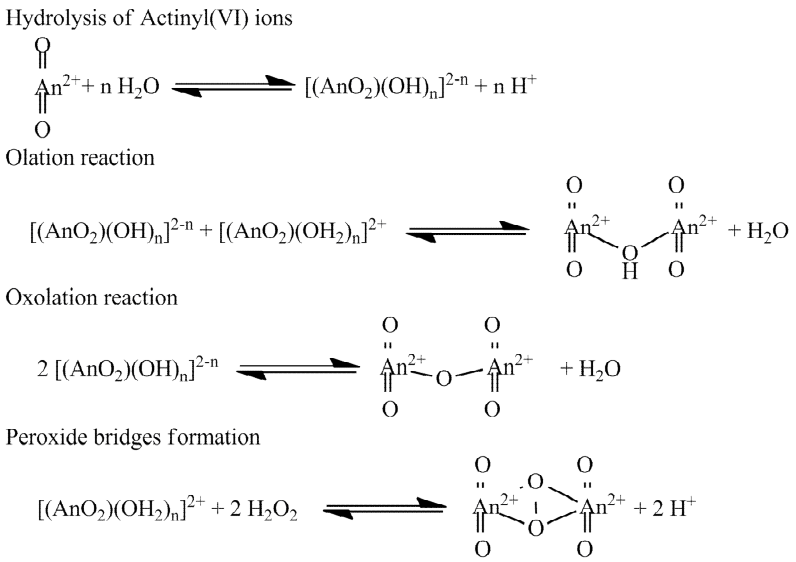

The hydrolysis of uranyl(VI) has been studied extensively and begins at about pH = 3. In solutions containing less than 10^{-4} M uranium, the first hydrolysis product is believed to be $UO_2(OH)^+$. At higher uranium concentrations, it is accepted that polymeric U(VI) species are predominant in solution, the formation of dimeric or trimeric uranyl hydroxo complexes being observed at uranium concentrations above 10^{-4} M[10].

I.3.2 Relevance of actinide clusters in the environment

The nuclear weapons and nuclear energy generation programmes of the second half of the last century have created a legacy of waste and contamination worldwide. Moreover, the storage of spent nuclear fuel raises important questions for future generations concerning the mobility of actinides in the environment during the long term geological storage. Three of the most problematic radioactive contaminants are the ones cited above: uranium, neptunium and plutonium. All three pose long term environmental risks, due to their high chemical and radiological toxicities. The chemical behaviour of these actinides is complex since, as stated in part I.3.1, they are likely to undergo redox reactions even under mild conditions, and often display two or more oxidation states simultaneously in solution. Thus, to predict how an actinide might spread through the environment and how fast transport occurs, all the parameters of the media should be well characterised. Indeed, the fate of the actinides in the environment strongly depends on the pH conditions, redox potentials and ligands present in the media.

The dispersion is thus strongly linked to the nature of the soil polluted by the radionuclides, strongly influencing their mobility through the formation of soluble or insoluble species. Each local environment being unique, the site-specific conditions determine which actinide species predominate as well as each species overall transport and migration characteristics. Actinides migrate in the environment under three main forms: as soluble molecular complexes, as small complexes adsorbed onto mobile particulates or under colloidal form [32]. The interaction of a dissolved species with mineral and rock surfaces and/or colloids determines if and how it will migrate through the environment.

Most of the mobility studies carried out so far have been realized in aqueous media, since water is the dominant transport medium for most elements in the environment. The typical conditions observed in the environment for aqueous solutions are a nearly neutral pH (from 5 to 9), with a wide range of redox potentials (from 0 to +1 volt) and various ionic strength, the most extreme case being envisaged for the German underground storage test site in a former salt mine. The water conditions will determine which actinide oxidation states predominate

and which actinide species are stable. Because of intrinsic differences in redox potentials, each actinide will exhibit a different set of oxidation states for a given set of solution conditions. The Pourbaix diagrams for U, Np and Pu given in Figure I-6 highlight that the normal range of natural waters outlined in the figure overlaps with the stability fields of uranium in the +VI and +IV oxidation states, Np in the +V and +IV oxidation states and plutonium in the III, IV, and V oxidation states.

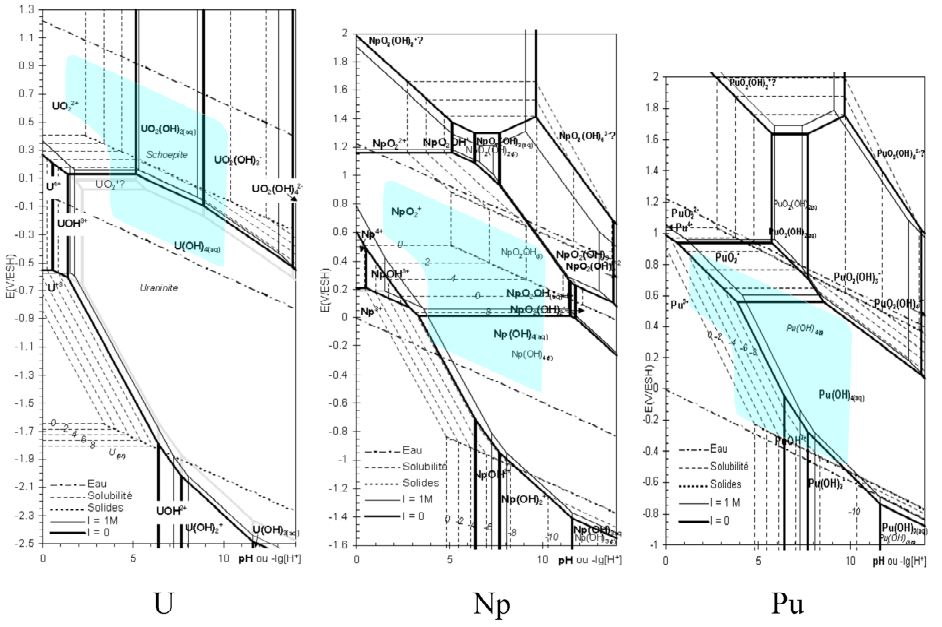

Figure I-6 Pourbaix diagrams of U, Np and Pu [14] and E-pH values encountered in natural water (light blue zone) [33]

One of the main contributions to the formation of actinide polynuclear compounds in the environment arises from the well described uranyl(VI) hydrolysis[34, 35] (Scheme I-4), leading to complexes ranging from monomers to hexamers as well as infinite chains and sheets. [36-40] The hydrolysis equation suggests that at higher pH oligomerization of the uranyl cation is expected to occur more easily, which has been experimentally observed above pH 4.5 [41]. However, despite numerous examples of isolated complexes, the understanding of the factors that favours one building block over another remains one of the obstacles to predict the structure of the complexes. Additional chemical processes occurring in solution are likely to influence the actinide oligomerization. Another example of the formation of assemblies of uranyl(VI) in solution results from the radiolytic formation of oxidizing species, especially peroxides. Uranyl(VI) possesses the original property to form stable polymeric peroxide complexes, the minerals studtite and metastudtite ($[(UO_2)O_2(H_2O)_4]_n$ and $[(UO_2)O_2(H_2O)_2]_n$, Figure I-7) being the only known peroxide bearing minerals. Natural radioactivity in a

uranium deposit or the radioactivity of nuclear waste has been proven to create sufficient amounts of H_2O_2 by alpha hydrolysis for in situ studtite formation [42].

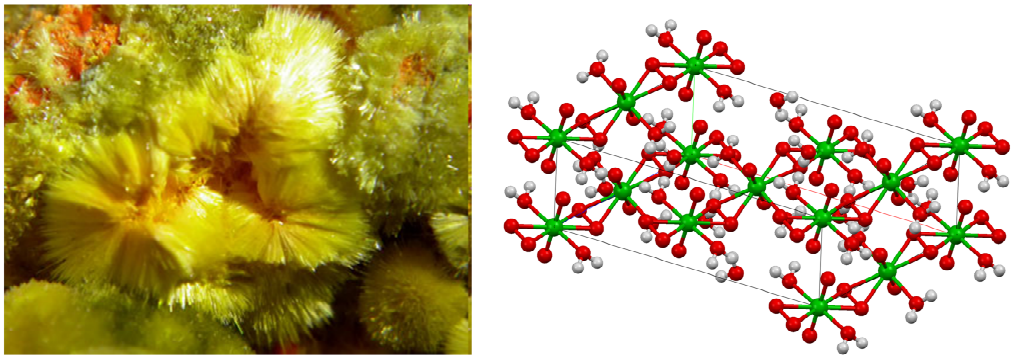

Figure I-7 Photograph (left) and crystal structure (right) of Studtite [43]

Similar reaction conditions have been proven to possibly lead to discrete actinyl peroxide nanospheres, which could have a profound impact on the mobility of actinides in the environment given their persistence in solution [44, 45]

The +V oxidation state chemistry is dominated by the very soluble neptunyl(V) moiety, that is usually described as forming monomeric complexes in solution, except for a few extended carbonate complexes observed in concentrated carbonate solutions.[10] However, the strong tendency of neptunyl(V) to interact with other actinyls through cation-cation interactions has a strong indirect influence on the mobility of actinides in the environment: if the intrinsic stability of these assemblies in aqueous media is relatively low, it strongly affects the rates of various redox reaction, and thus can lead to the formation of otherwise unstable species [46, 47].

Finally, tetravalent actinides tend to yield soluble hydroxide or oxide complexes through hydrolysis, as well as insoluble hydroxides and oxides (Scheme I-2). Due to the high charge-to-radius ratio of actinides(IV) ions, hydrolysis reactions are significant at almost any pH values found in natural waters, forming hydrolysis products even in acidic solutions. [4, 10]

If the solution is oversaturated, and in the absence of strong dissociating ligands, the polynuclear units aggregate to yield stable colloids [48-50] Such colloids may be highly mobile under environmental conditions, as it has been demonstrated for Pu(IV) and U(IV).[11, 33, 51]

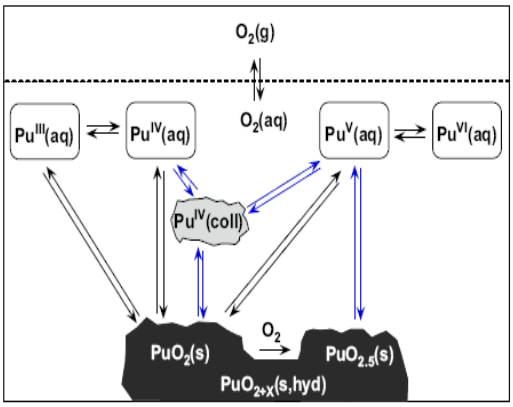

Figure I-8 Solubility and redox equilibriums of plutonium in aqueous solution[52]

Due to the large insolubility of tetravalent actinides, the reduction of An(VI) to An(IV), especially relevant for uranium, greatly decreases the actinide mobility through precipitation of sparingly soluble An(IV) minerals and has therefore been extensively studied using biotic and abiotic processes. Abiotic reductants investigated include green rust [53] clay in the presence of organic materials [54] or Fe(II) adsorbed species.[55]

Moreover, one of the main contributions in the actinide redox migration results from the action of microorganisms. Thus, it has been observed that the radioactivity does not eradicate the microbial populations in storage sites[56], but effects a selection, assuring the survival of several species among the multitude of microorganisms initially present [57]. These microbes will affect the actinide mobility directly by changing the oxidation state or indirectly by producing reducing compounds (H_2S, Fe(II)...) thus deeply affecting their solubility. These processes of bioreduction of actinides have been the subject of numerous studies in the past twenty years, due to their high potential for contaminated site remediation, these organisms transforming the highly soluble actinyl(VI) species onto insoluble materials [58, 59]. Thus, under anaerobic conditions, several microorganisms can respire by the reduction of alternative electron acceptors, such as high valent actinides. To date, several microorganisms have been observed to use uranyl(VI) as an electron acceptor, and under anaerobic conditions, acetate or hydrogen is oxidized with the concomitant reduction of uranyl(VI) to insoluble uraninite, secreted outside the bacteria cell, as highlighted Figure I-9 [18]. The reduction of UO_2^{2+} by anaerobic microorganisms is thought to proceed via the reduction of uranyl(VI) by cytochrome C3 to yield an unstable uranyl(V) species which then rapidly undergoes acid mediated disproportionation to yield UO_2^{2+} and U(IV) products (Scheme I-5)[60]. However, the detailed study of the generated particles indicated that the uranium(IV) compound was generated under the form of nanoparticles with strong mobility in the environment [11, 18].

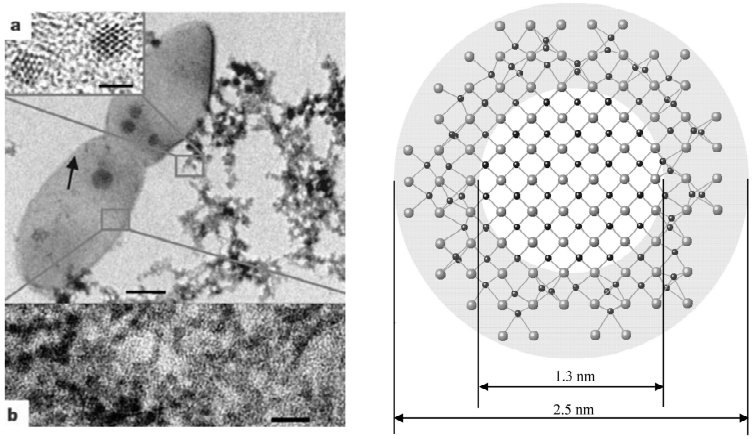

Figure I-9 Characterisation of bioreduced uraninite (UO_2) nanoparticles by TEM[18] (left) and EXAFS structural determination of biogenic uraninite nanoparticles[61] (right, U atoms were represented in grey, O atoms in black).

Scheme I-5 Schematic reaction chain of the bioreduction occurring in the bacteria cells. Hgse: Hydrogenase ; Cyt c_3: cytochrome c_3 ; ECP: Electron Carrier Protein ; Hmc: High molecular weight cytochrome ; ADP: Adenosine diphosphate ; ATP: Adenosine triphosphate ; Pi: inorganic pyrophosphate.

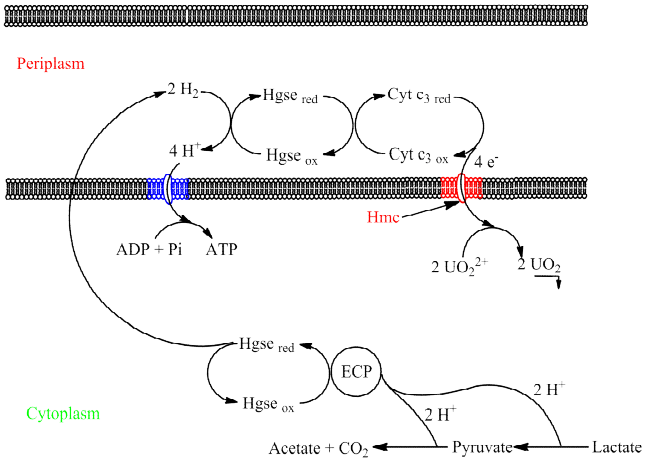

Finally, this bioreduction has been proven to be largely dependent on the media parameters; organic acids have thus been found to enhance the bioreduction of U(VI) yielding insoluble forms of U(IV) such as colloidal nanoparticles and molecular-scale clusters [4, 18, 62-64] while high concentrations of bicarbonate, sulfate or nitrate ions appear to impact negatively the bacterial removal of uranium[65].

In conclusion, the migration of actinides in the environment is a complex process dominated by many variables, including redox reactions in solution or in solid phase. The understanding of actinide bioreduction could lead to the development of new approaches for the remediation of uranium contaminated sites based on U(VI) reduction via the engineered addition of appropriate reductants. In view of the similarities between different actinides in the same oxidation state, the use of uranium to model the behaviour of more radioactive actinides in the

environment can be envisaged. However, the full understanding of this complex set of interacting processes requires the individual analysis of the elemental processes occurring during these transformations. Notably simple molecular models are needed to understand the separate parameters influencing polynuclear assembly formation.

I.3.3 Relevance of actinide clusters in nuclear fuel industry

Nuclear reprocessing technologies were developed to chemically separate and recover the different elements from spent nuclear fuel. While originally reprocessing was solely used to extract plutonium for producing nuclear weapons, the reprocessing today is mostly focused on reducing the volume of high-level waste, but also on a smaller scale the reprocessed plutonium is recycled back into Mixed OXide (MOX, containing a mixture of uranium and plutonium) nuclear fuel for thermal reactors. The reprocessed uranium, which constitutes the bulk of the spent fuel material, can in principle also be re-used as fuel, but this is only economic when uranium prices are high. The understanding of the actinide behaviour in solution during this process is critical, and the formation of polymeric or colloidal assemblies of actinide, and especially plutonium has been found to be one of the biggest challenges in the separation processes.

Most of the industrial fuel reprocessing facilities, including the Areva reprocessing facility in La Hague, use the PUREX (Plutonium Uranium Refining by EXtraction) process. This process is based on a liquid-liquid extraction of the uranium and plutonium in an organic phase while the other fission products remain in the aqueous phase (Scheme I-6). After a first step of solubilisation of the spent nuclear fuel in concentrated nitric acid, the solution is filtered to remove insoluble colloids altering the extraction processes, and the filtrate is mixed with a Kerosene solution of terbutylphosphate (TBP), $OP(OC_4H_9)_3$. The extraction relies on the selectivity of TBP towards U(VI) and Pu(IV), forming stable complexes only with uranium and plutonium. Due to the high solubility of TBP in organic solvent, the TBP complexes of Pu(IV), $[Pu(NO_3)_4(TBP)_2]$, and uranyl(VI), $[UO_2(NO_3)_2(TBP)_2]$ are extracted in the organic phase while the other elements remain in the concentrated nitric acid aqueous solution. This selectivity is due to the strong negative polarisation of the terminal oxo of the phosphate molecule. In order to further separate the co-extracted uranium and plutonium complexes, the plutonium(IV) complex is reduced to the trivalent state by the use of Fe(II), while no reduction of the uranyl(VI) complex is observed. Due to a reduced effective charge, Pu(III) is not efficiently complexed by the TBP ligand, and the plutonium is extracted in a nitric acid solution through a second liquid-liquid extraction. However, a consistent separation

of neptunium during the PUREX process is not straightforward, dissolution of spent reactor fuel in nitric acid yielding a solution containing a mixture of Np(V) and Np(VI). While Np(VI) is extracted in the organic phase by TBP and can be recovered from the U/Pu mixture in an additional partition step, Np(V) stays in the aqueous solution containing the other fission products. However, control of neptunium partitioning can be accomplished through the use of a mild oxidant, to selectively oxidize Np(V) to Np(VI). The resulting Np(VI) can be extracted in the organic phase and be further separated from U and Pu[4].

Scheme I-6 Schematic representation of PUREX process

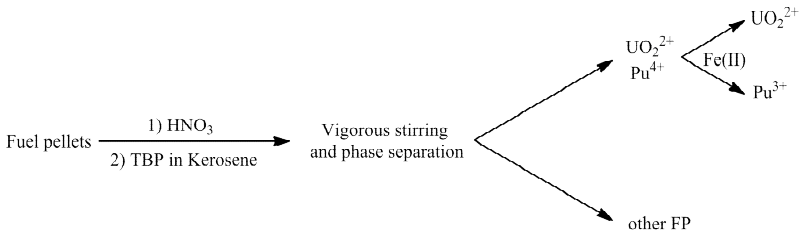

Other extraction steps have been developed in order to further separate Lanthanides, Am, Cm and other fission products. While these processes are not used in industrial scale yet, a pilot plant exists in the CEA site of Marcoule, France, where the fission products and lanthanides are further separated using similar liquid-liquid extractions in presence of more selective extractants. These extractants are based on a diamide ligand which selectively complex lanthanides and Am/Cm in the DIAMEX process (DIAMide EXtraction) and on a bistriazinylpyridine ligand which can finally separate Lanthanides from Am and Cm (Figure I-10) in the SANEX process (Selective ActiNide EXtraction).

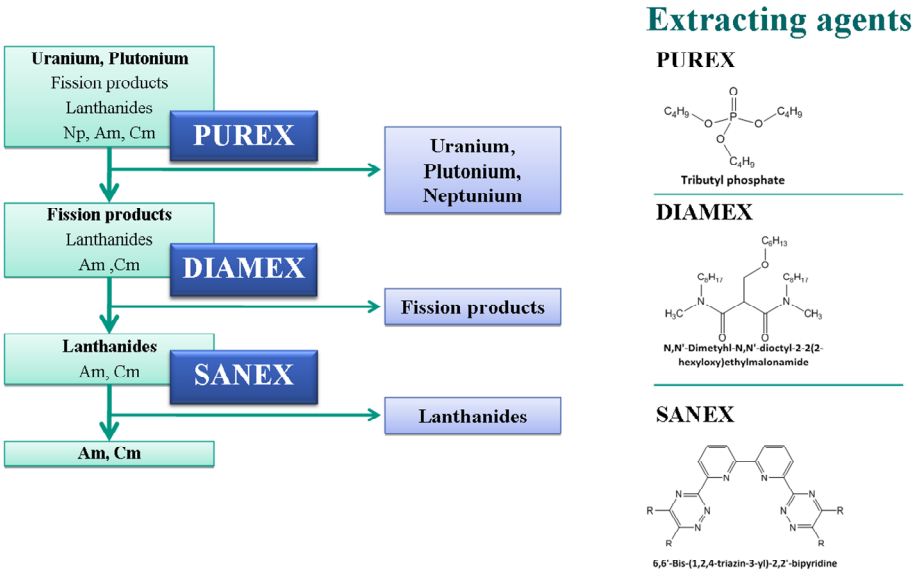

Figure I-10 PUREX, DIAMEX and SANEX extractions processes.

Within the fuel reprocessing processes, polynuclear assemblies of uranium are encountered at different stages, and often represent problematic steps in the extraction processes. Three main phenomena can be distinguished: (a) The formation of polymeric or colloidal polynuclear assemblies of actinides, particularly observed with plutonium(IV) in the present case, can vitiate the extraction process by the persistence of multinuclear metal oligomers that cannot be efficiently extracted [66, 67], and can also be at the origin of the formation of emulsions during the mixing of organic and aqueous phases (usually called the third phase phenomenon). [68] (b) The formation of bimetallic complexes that are extracted by the ligand in the organic phase and can thus pollute the extracted phase with unwanted co-extracted metals, often observed with Re and Tc. [69] (c) The formation of cation-cation complexes observed with actinyl moieties can influence redox reactions during the extraction process and thus significantly affects the separation of the elements. This behaviour is mainly observed with neptunium(V), for which disproportionation rates are strongly dependant from cation-cation interactions in solution [70].

The formation of Pu(IV) colloids has been first identified after observing unexplained ineffectiveness of ion-exchange and solvent extraction separation methods with plutonium [71]. This phenomenon, well studied because of its impact on plutonium solution chemistry, occurs even at low pH values and low concentrations, and has been proven to be a major concern in the large scale chemistry associated with nuclear fuel reprocessing. [72] A large number of attempts to separate Pu colloids have been carried out, but usual solvent extraction methods were proven to be inefficient with Pu colloids. [73, 74]

These plutonium species, initially thought to be polymeric, have been recently identified as nanocrystalline PuO_2, forming assemblies with size varying from few nanometres to hundred nanometres, these species presenting well defined optical, XANES and powder X-ray spectra [75]The formation of these colloids involves the condensation of plutonium hydroxides through an olation/oxolation reaction of the hydrolysed plutonium species to yield oxo-hydroxo bridge species (Scheme I-2). [76]

Recently, two $Pu_{38}O_{54}$ clusters have been isolated by crystallisation from plutonium colloid solutions, and the single crystal X-ray diffraction resolution revealed the presence of pseudocubic clusters presented Figure I-11[72] [67]. The isolation of these well defined cluster led to new approaches for their separation, and resulted in the development of a new efficient liquid-liquid extraction method using trichloroacetic acid as an extractant (Figure I-11)[67].

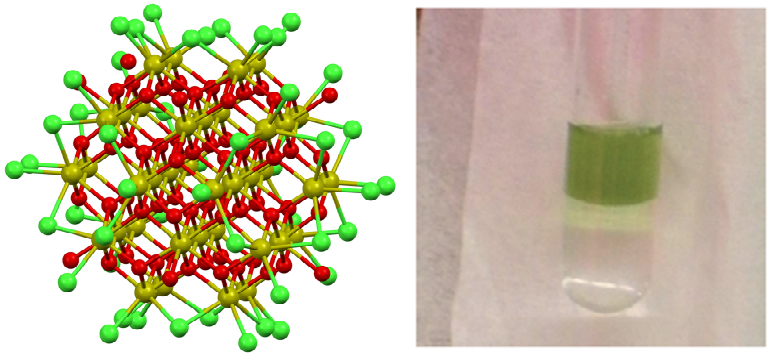

Figure I-11 Mercury view of the $Pu_{38}O_{54}Cl_{42}$ cluster (left) [72] and its extraction in organic phase using trichloroacetic acid as extractant (right) [67].

^{99}Tc is a fission product of ^{235}U, and is thus formed quantitatively in used nuclear fuel rods, and thus in solution after dissolution of the fuel rods in nitric acid. However, unlike most of the other fission products Tc is not found in its cationic form but as the anionic pertechtenate TcO_4^- form. Since the extraction process is mainly designed to extract cationic species, most of the technetium compounds are not extracted and stay in the aqueous solution during the PUREX process. Moreover, it has been observed that the pertechtenate anion co-extract with a wide range of metal cations in different oxidation states, contaminating the extracted metals and sometimes catalysing unwanted side reactions.[77] The origin of this co-extraction has been attributed to the formation of bimetallic complexes containing Tc, the pertechtenate oxos acting as ligands for the cationic metals centres. Complexes containing both TcO_4^- (or its non radioactive analogue ReO_4^-) have been isolated with UO_2^{2+}, [77-79] NpO_2^+,[80] U^{4+} and Th^{4+} [79, 81] (Figure I-12). The complexes isolated in these works are also decorated with TBP or TBP analogues, and provides a good molecular model of the co-extraction process.

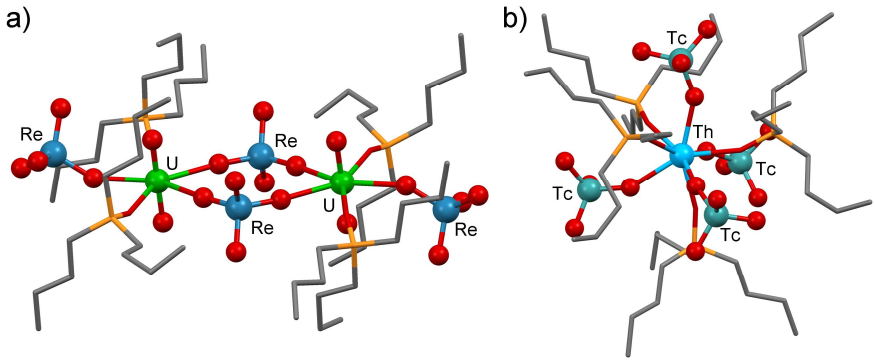

Figure I-12 Mercury plot of $[UO_2(\mu_2\text{-}ReO_4)(ReO_4)(TBP)_2]$ (a) and $[Th(TcO_4)_4(TBP)_4]$ (b) taken from refs[77, 78] (TBP ligands were represented in wireframe for clarity).

One of the main reasons of the poor efficiency of neptunium separation arises from the difficulty to maintain Np in a single oxidation state. Under ambient conditions, the most stable oxidation state of neptunium is Np(V); however, Np(V) can disproportionate to Np(IV) and Np(VI). This disproportionation reaction is slow in aqueous solution, but the rate of disproportionation has been proven to be more than 500 times faster in the PUREX extraction condition (30% TBP in kerosene solution), resulting in a very complicate behaviour during the extraction process[70]. Sarsfield et al. observed that the disproportionation rate was strongly enhanced by the formation of CC assemblies, more easily formed in organic solutions. Whilst they found evidence of the formation of Np(V)-Np(V) and Np(V)-Np(VI) assemblies in solution, the equilibrium constant of their formations was more than an order of magnitude lower than for Np(V)-Np(IV). This mixed valent Np(V)-Np(IV) assembly was found to significantly enhance the disproportionation reaction, the disproportionation of Np(V) in solution being thus ruled by the coexistence of the two reactions described in Scheme I-7, one between two Np(V) centre and one between Np(V) and a mixed valent Np(V)-Np(IV) species.

Scheme I-7 Np(V) disproportion reactions in organic media[70]

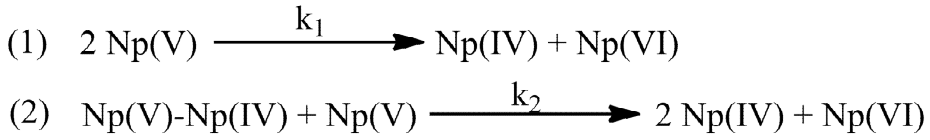

I.3.4 Applications of f-element clusters

In addition to their implications in nuclear fuel reprocessing and in the understanding of the migration of the actinides in the environment, actinide clusters, and more generally f element clusters have received a growing attention in the recent years for the design of new compounds with enhanced reactivity and magnetic properties. Actinide clusters thus combine the polymetallic assembly properties with the unique f-elements characteristics. This chapter will be mainly focused on uranium assemblies, the larger radioactivity of the other actinides limiting their potential applications in catalysis or magnetism.

I.3.4.1 Reactivity of uranium complexes

The recent decades have provided a large number of well defined uranium complexes exhibiting unique reactivity towards small molecule activations. The large range of accessible oxidation states and the original coordination properties of uranium highlight the promising properties of uranium for the design of catalysts able to promote original reactions [82]. These properties had been early observed by Fritz Haber, who noticed that uranium could be a very efficient catalyst for the later called Haber-Bosch process, and was able to produce nearly half a litre of ammonia per hour with this catalyst.

In the recent years, uranium complexes have been proven to promote a large number of original reactions with small molecules such as N_2, CO_2 and CO.

The first uranium dinitrogen complex was reported only a decade ago by Scott and co-workers who explored uranium chemistry with polydentate amino/amide coordination environments [83, 84] (Scheme I-8, a)). They observed the reversible bonding of N_2 to a trivalent uranium complex, forming a side-on bridging μ_2-η^2:η^2 dinitrogen sandwiched complex in which the N_2 unit was essentially unperturbed as the N-N bond length (1,109(7) Å) was not much different from that found in dinitrogen gas (1,097 Å). Following this work, other sides on dinitrogen complexes have been isolated, showing different degree of activation of N_2 (Scheme I-8, b))[85]. Complexes of uranium have also been shown to bind N_2 in a terminal end-on manner,[86] or bridging heterobimetallic U/Mo complexes[87](Scheme I-8, c)) . Moreover dinitrogen cleavage was achieved with a calixarene uranium(III) complex in presence of one equivalent of potassium naphthalenide [88], which demonstrated that uranium(III) complexes are able to reduce dinitrogen when combined to an external reducing agent(Scheme I-8, d)).

Scheme I-8 Dinitrogen coordination and reduction by U(III) complexes

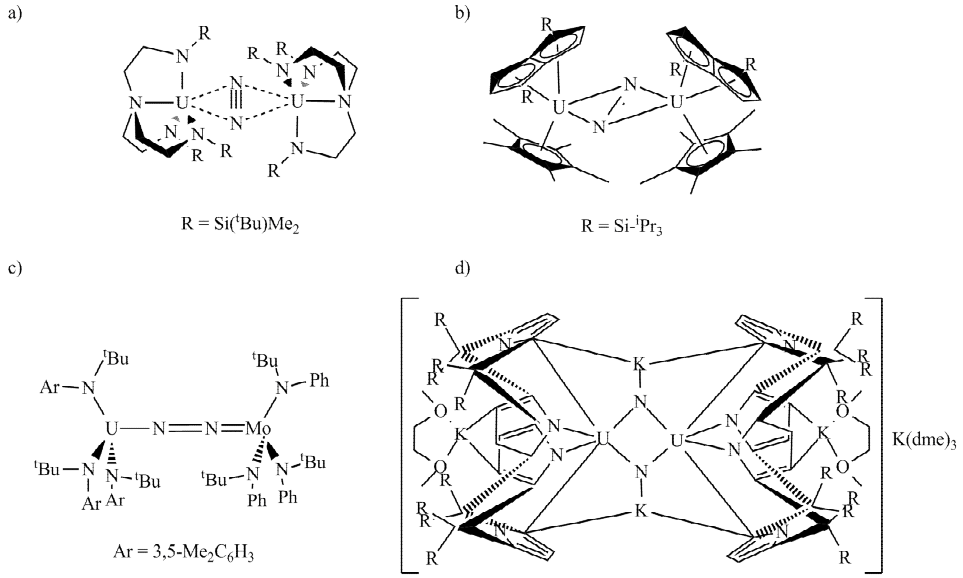

Low valent uranium complexes have also allowed unprecedented activation of carbon monoxide, leading to the isolation of deltate ($C_3O_3^{2-}$)[89], squarate ($C_4O_4^{2-}$)[90] or ynediolate ($C_2O_2^{2-}$)[91-93] complexes of uranium(Scheme I-9). Recently, the treatment of a reductively coupled CO complex with organosilyl halides, led to the quantitative conversion to furanones [94].

Scheme I-9 Reductive coupling of CO forming deltate ($C_3O_3^{2-}$)[89], squarate ($C_4O_4^{2-}$)[90] or ynediolate ($C_2O_2^{2-}$) [92] anions

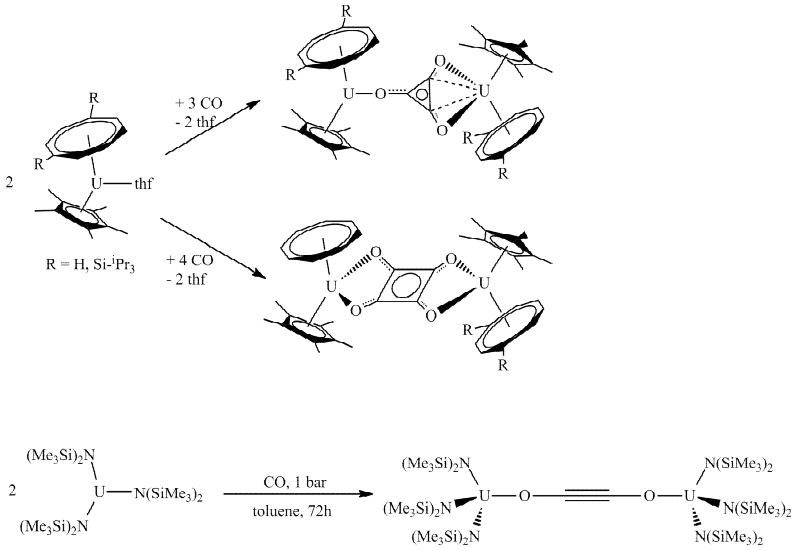

Moreover, a few uranium complexes have recently allowed unprecedented activation and functionalization of CO_2. Notably, in addition of the oxide[95] and carbonate[90, 96] bridged complexes obtained by reduction of CO_2, a previously unseen end-on $CO_2^{\cdot-}$ radical anion complex was isolated by using a very sterically hindered complex[97]. The Meyer group

rationalised the role of the ligand on the mechanism and the reaction products during CO_2 reduction by trivalent uranium complexes and proposed that the steric bulk of the ligand determine the final product (Scheme I-10).[96, 98-100]. Recently, the feasibility of a close synthetic cycle with similar U(III) complexes was demonstrated, the carbonate being realeased by addition of stoichiometric amounts of KC_8, resulting in an uranium mediated reductive conversion of CO_2 to carbon monoxide and potassium carbonate [101].

Scheme I-10 Comparison of the reactivity of tris(aryloxide) U(III) complexes towards CO_2 affording oxide, carbonate or radical anion complexes depending of the steric bulk of the ligand[100]

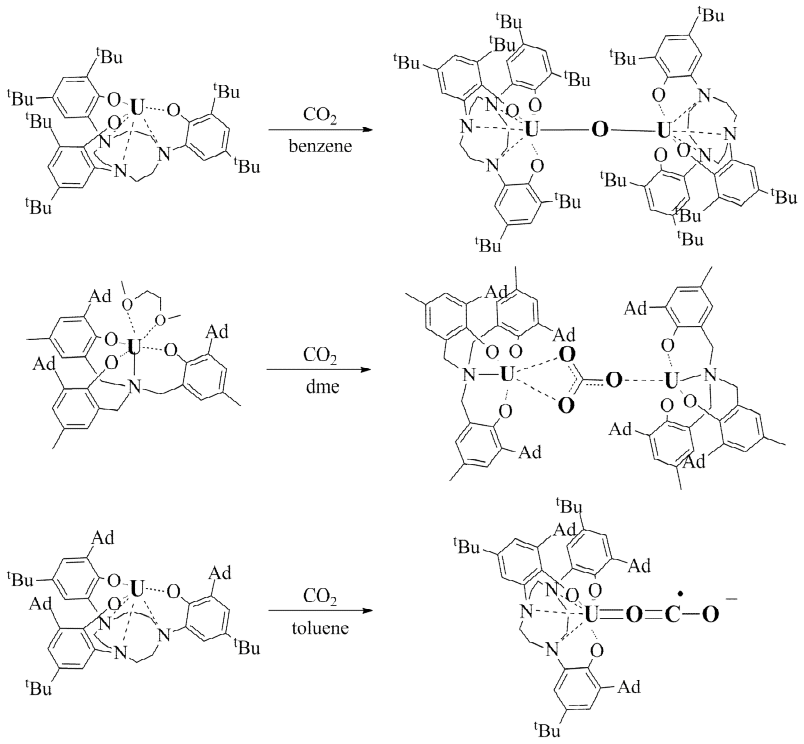

However, despite the very promising capacity of uranium complexes to activate small molecules, polymetallic uranium assemblies that are able to transfer a large number of electrons to a substrate have been rarely isolated [102, 103]. The combination of a large number of electrons available through a polynuclear core with the redox and coordination properties of metal centres, has proven to be efficient with transition metal systems for small molecule activation or electrocatalysis.[104-107] Thus, uranium polynuclear complexes are highly promising for small molecules activation.

I.3.4.2 Single Molecule Magnets

The discovery, almost twenty years ago, that magnetic bistability can be observed for assemblies as small as molecules, lead to the growth of a whole new field at the border between physics and chemistry, for the design of new molecules capable of storing magnetic information, thus named single molecule magnets (SMMs). The first SMM behaviour was reported in a Mn_{12} transition-metal cluster, and was followed by several studies on discrete clusters of a small number of paramagnetic transition metals linked together by simple bridges such as O^{2-}, OH^-, OCH_3^-, CN^-... [108, 109]. These studies identified the two parameters required for the observation of SMM properties: the molecule should possess a high spin ground state to provide a sizeable magnetic signal and a high zero field splitting to be able to store the magnetic information over a long period of time. The research of SMM with improved properties focused on the design of molecules containing several metal ions to achieve the first requirement while the magnetic anisotropy was given through ligand field splitting of the electronic energy states of the metal atoms.

Recent approaches have turned to Ln(III) ions because of their large spin-orbit coupling, responsible for the magnetoanisotropy. Two general strategies have been identified: a lanthanide-only approach in polymetallic clusters, and another so-called 3d–4f approach, where first-row transition-metal ions are coupled with lanthanide ions. While a detailed reviews of these assemblies is beyond of the scope of this introduction, these two strategies can be illustrated by two significant examples; A heterobimetallic cluster containing iron(III) and dysprosium(III) ions in an unusual $\{Fe_4Dy_4\}$ ring structure was reported by Powell et al., the combination of the strong paramagnetism of iron(III) ions with strongly anisotropic dysprosium(III) ions resulted in a SMM with improved properties[110]. The second strategy, using dimeric lanthanide only clusters was developed first in Long's group, who obtained record blocking temperature by bridging Dy or Tb ions with magnetically active radicals such as N_2^{2-}. [111, 112]

An established way to achieve high spin ground states is by the creation of paramagnetic complexes with strong exchange coupling between paramagnetic centres. Achieving this in homo- or hetero-metallic lanthanide complexes is difficult due to the poor overlap between f-f or d-f magnetic orbitals that results in a weak exchange coupling. The actinides, with the peculiar nature of their 5f orbitals that show higher degrees of covalency in bonding than their

lanthanides counterparts, hold the promise of larger magnetic exchange. Moreover, the increased spin orbit coupling observed with actinide results in a larger spin anisotropy, and could represent another path toward enhanced magnetization relaxation barriers [113].

This latter property was exploited by Long and Rinehart, who reported the first actinide-based SMM with a simple trigonal prismatic uranium(III) complex containing three diphenylbis(pyrazolylborate) Ph_2BPz_2 ligands.[114] The isolated complex presents a single uranium centre, and the slow relaxation is thus of pure magnetic anisotropy origin. This behaviour, named by extension Single Ion Magnet, has been observed in two other U(III) complexes [115] [116] and one Np(IV) complex [117], all of them presenting the same $5f^3$ electronic configuration. The odd number of electrons in this configuration inevitably leads to a magnetic ground state after Kramer's degeneracy is lifted by the magnetic field. However, the larger ligand field typical of 5f elements in these complexes did not lead to significant improvements of the energy barrier, due to the absence of exchange coupling between metallic centres. Two examples of polynuclear actinide assemblies have been shown to exhibit SMM properties. Caciuffo's group related the slow magnetic relaxation of a trimeric neptunyl(V)/neptunyl(VI) complex (see part I.5 for its structure description) presenting superexchange coupling through the neptunyl oxos [118], and the second example was observed in a toluene uranium(III) sandwich compound [119].

The efficiency of single molecule magnet is evaluated through two parameters: the anisotropy barrier, U_{eff}, and the blocking temperature T_B. The first is defined by considering an Arrhenius-type relationship for the magnetic relaxation time of the molecule $\tau = \tau_0 \exp(U_{eff}/k_BT)$. This value is obtained from the fit of the dynamic relaxation studies carried out in an oscillating magnetic field (a.c. SQUID measurements), and describes the high-temperature dynamics of SMM. However, the low temperature of SMM often differs from this Arrhenius behaviour as alternate relaxation processes can shortcut the classical relaxation phenomenon. In this low temperature regime, the value commonly used to evaluate the properties of the SMM is the blocking temperature, defined by the maximum temperature at which a magnetic hysteresis can be observed for the compound. However, one of the main problems of using this value to compare SMM properties is that the T_B values are largely depending on the sweep rates, and values of sweep rates ranging from 0.004 Oe/s to 0.46 Oe/s have been used in the literature, resulting in very different values of T_B observed. Thus, since sweep rates are not normalised yet, T_B is not a very good parameters to compare the efficiency of the SMMs. Table I-2 displays the T_B and U_{eff} values for the strongest f-elements

and transition metal SMM. In view of the large anisotropy barriers observed for actinides complexes with respect to the transition metal ones, the rational design of new actinide complexes should lead to new architectures presenting improved blocking temperatures and anisotropy barriers.

Table I-2 Relaxation barrier and blocking temperature for selected single-molecule magnets

Molecule	U_{eff} (K)	T_B (K)
$\{Mn_6O_2(sao)_6(O_2CPh_2).EtOH\}$ [120]	86.3	4.5
$[Fe_4Dy_4(teaH)_8(N_3)_8(H_2O)]$[110]	30.5	6.8
$[\{[(Me_3Si)_2N]_2(thf)Dy\}_2N_2]^-$ [111]	177	8.3
$[\{[(Me_3Si)_2N]_2(thf)Tb\}_2N_2]^-$ [112]	326.6	14
$U(Ph_2BPz_2)_3$[114]	28.8	/
$U(H_2BPz_2)_3$ [115]	11.5	/
$[U(TpMe_2)_2(bipy)]I$[116]	26.2	/
$[\{Np^{VI}O_2Cl_2\}\{Np^{V}O_2Cl(thf)_3\}_2]$[117]	140	/
$[(U(BIPM^{TMS}H)(I))_2(\mu\text{-}\eta_6\text{:}\eta_6\text{-}C_6H_5CH_3)]$[119]	/	1.8

I.3.5 Outlook

Polymetallic actinide complexes are involved at multiple stages of the fuel reprocessing techniques and have a strong contribution on the migrations processes of actinides in the environment. Nevertheless the absence of molecular models in most of the cases raises difficulties with the understanding of self assembly processes and therefore their control. The controlled preparation of polymetallic actinide complexes is still a great challenge due to their relatively unpredictable chemical properties of actinide ions, with various oxidation states and geometries. Actinide cluster chemistry is still in its infancy, especially when compared to that of transition metals or lanthanides. [121, 122]. The potential applications of actinide clusters due to their unique catalytic and magnetic properties should lead to a more intense development in close future.

In the next section the state of the art of the few existing strategies for the synthesis of polymetallic actinide edifices will be presented.

I.4 Molecular and Supramolecular Polynuclear Actinide Complexes

Compared to the large number of studies on mononuclear actinide complexes, there are very few examples of polynuclear actinide complexes, despite their high relevance for the study of actinide environmental migration and for magnetic and catalytic applications. This scarcity of polynuclear complexes contrasts with the large number of polynuclear transition metal complexes synthesised in the last decades, through well understood synthetic routes. [123] As described in part I.3, the nature of the polynuclear assembly is strongly affected by the actinide oxidation states. While low valent cations, in +III and +IV oxidations states behave similarly to lanthanide ions, with small geometrical preferences, the higher valent +V and +VI oxidation states are usually found in the linear actinyl $AnO_2^{+/2+}$ moiety, leading to very different kinds of interactions and assemblies. The clusters presented in this part will thus be sorted according to the metal oxidation state, and within these categories, we will focus on the diverse synthetic routes to access polynuclear uranium assemblies

I.4.1 Actinyl clusters

I.4.1.1 Hexavalent oxidation state

Due to the high stability of the uranyl(VI) cation, most studies concerning actinyl(VI) have been carried out on uranyl(VI) precursors, in aqueous solution. The fact that these studies were mainly carried out in aqueous media explains the limited number of crystallographically characterised complexes. The complex speciation in aqueous solution renders the isolation of crystalline material considerably more challenging in aqueous media.

The number of polynuclear uranyl(VI) complexes containing more than two metal ions described in the literature before 2005 is relatively small, with only a few trinuclear[124-128] and tetranuclear[129-135] clusters bridged by hydroxo or oxo groups described.

The main contribution to uranyl(VI) cluster chemistry originates from Burns' group, who has developed, from 2005, a large family of polynuclear peroxide-bridged uranyl assemblies. They demonstrated that the synthesis of actinyl peroxide compounds in aqueous media under ambient conditions can lead to the isolation of uranyl(VI) clusters with cluster core constituted from 16 to 120 uranium atoms[31, 43, 44, 136-144] The size of the clusters obtained can

be modulated by using different alkaline counterions to balance the charge of the clusters, or by varying the pH of the solution.

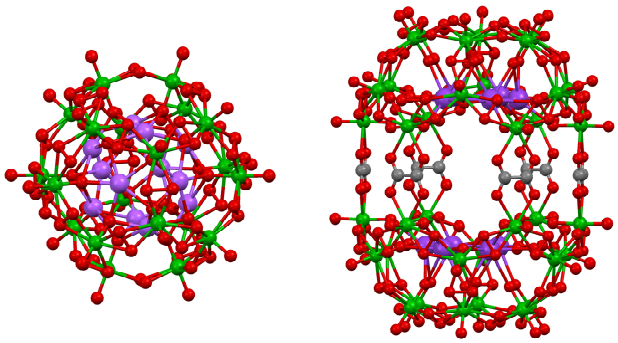

Figure I-13 Mercury views of U_{20} and U_{36} uranyl(VI) peroxide nanospheres [31] (K are represented in purple, C in grey, O in red and U in green)

While CCI are exceedingly rare in actinyl(VI) chemistry, due to the low Lewis basicity of uranyl(VI) oxo, four examples of uranyl (VI) CC complexes can be found in the literature.

A uranyl(VI) trimer assembled through T-shape cation-cation interactions was synthesised and crystallised in the early work of Taylor, and consists in the uranyl(VI) bis hexafluoroactetylacetonate trimer $[UO_2(hfac)_2]_3$, represented Figure I-14 (left). [145]

Similarly, the salt metathesis reaction between uranyl(VI) chloride and a potassium alkoxide salt in organic media afforded the tetrameric cation-cation complex of uranyl(VI) $[UO_2(OCH(^iPr)_2)_2]_4$ (Figure I-14, right). [146]

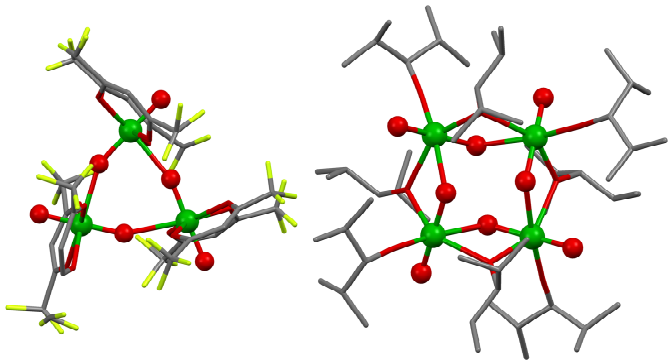

Figure I-14 Mercury views of the trimeric and tetrameric uranyl(VI) CC complexes $[UO_2(hfac)_2]_3$ (left) and $[UO_2(OCH(^iPr)_2)_2]_4$ (right) (Ligands are represented with pipes for clarity, C are represented in grey, O in red, F in light green and U in green)

The two last examples of uranyl(VI) complexes presenting CCI have been obtained using large calixarenes. The calixarenes cavities allow the coordination of two uranium centres within the calixarene core, and the proximity of the uranium atoms probably plays a significant role in the stabilisation of the otherwise less stable UO_2^{2+}-UO_2^{2+} interactions. A trinuclear cluster with two uranyl(VI) moieties coordinated to a third one through CCI has

been isolated using a calix[8]arene (Figure I-15, left).[125] The use of a calix[7]arene lead to the isolation of an hexanuclear uranyl complex constituted by two dimeric CC complexes coordinated in the calixarene pocket and connected by two uranyl bridged through μ_3-oxo(Figure I-15, right).[39]

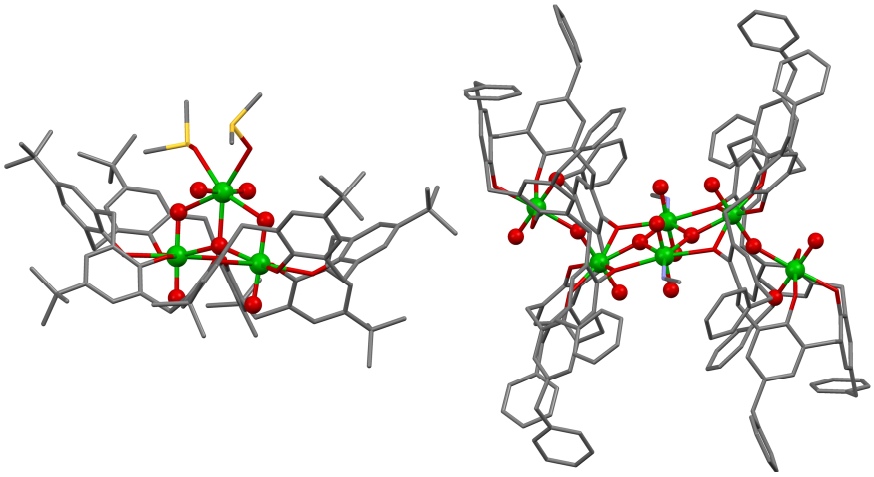

Figure I-15 Mercury views of the trinuclear (left) and hexanuclear (right) uranyl(VI) calixarene complexes presenting CCI (Ligands are represented with pipes for clarity, C are represented in grey, O in red, S in yellow and U in green)

As described in the few examples presented here, the uranyl(VI) moiety, which imposes the coordination of ligands in its equatorial plane has lead to the isolation of a large family of clusters. For these systems with a well defined coordination sphere, a rational design of the final assembly is possible by using appropriate ligands and reaction conditions. However, the $5f^0$ configuration of uranyl(VI) prevents its use for magnetism or reduction reactivity, due to the absence of electrons in its outer shell.

I.4.1.2 Pentavalent actinyl complexes

The main difference between actinyl(V) and actinyl(VI) moieties arises from the more pronounced Lewis basicity of the AnO_2^+ oxygen atoms with respect to its hexavalent analogue, and explain the increased ability of actinyl(V) to form cation-cation complexes.
Hence, cation-cation assemblies have mainly been observed with NpO_2^+, which is the only actinyl(V) stable under ambient conditions, and more than 25 neptunyl(V) compounds presenting CCI were crystallographically characterised.[46] Most of these crystal structures present extended networks, and only a few crystal structures correspond to finite polynuclear actinide cores, constituted from two to four actinide centres.

I.4.1.2.1 ***Neptunyl(V)***

The first structure was described by Choppin et al. in 1984, and consists of a neptunyl dimer, connected through a diamond shape cation-cation interaction (Figure I-16). This complex was isolated by reacting the sodium salt of mellitic acid (Benzene-1,2,3,4,5,6-hexacarboxylic acid) with neptunyl(V) in aqueous solution to yield crystals of the $Na_4[(NpO_2)_2(C_6(COO)_6)]$ complex. [147] In this complex, the two neptunyl moieties are connected by CCI and are bridged by two bidentate carboxylate groups from mellitic acid. The coordination sphere of each neptunyl is completed by two carboxylate functions of the same mellitate ligand coordinated in a monodentate fashion. Each mellitate ligand is coordinated to two dinuclear cores. The charge of the assembly is balanced by the presence of four sodium counterions per dimer. The most striking structural feature of this complex is the short distance between neighbouring Np atoms (3.48 Å), among the smallest described in the literature.

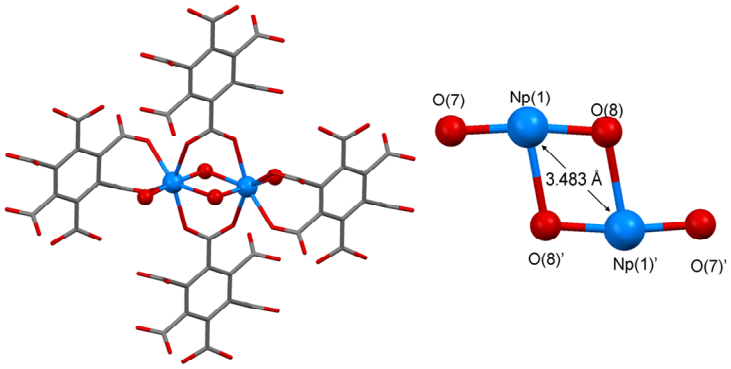

Figure I-16 Mercury view of $Na_4[(NpO_2)_2(C_6(COO)_6)]$ and core detailed (Ligands are represented with pipes for clarity, C are represented in grey, O in red, and Np in Blue)

More recently, three other dimeric complexes were isolated: $[(NpO_2)_2(C_6H_4F(COO))_2(bipy)_2]$ [148], $[(NpO_2)_2(C_6H_5(COO))_2(bipy)_2]$ and $[(PuO_2)_2(C_6H_5(COO))_2(bipy)_2]$ [149]. These three complexes present a similar core, with actinyl(V) ions connected through CCI and bridged by bidentate benzoate ligands, and very similar metrical parameters within the dimeric core for the neptunium dimers with an average Np-Np distance of 3.43(1) Å, and an average lengthening of the Np-O bond involved in the cation-cation interaction of 0.6 Å with respect to the unbound Np-O. The Np-Np distance in these two neptunyl complexes is 0.5 Å smaller than the same distance in the mellitate dimer, which could be explained by the higher steric bulk of the mellitate ligand preventing the approach of the two neptunyl centres. In the isostructural Pu complex, the Pu-Pu distance of 3.4088(2) Å, was observed to be 0.3 Å smaller than for Np, as a result of the smaller size of Pu centres due to the actinide contraction. The coordination sphere of the actinyl moieties is completed by a bipyridine

molecule in their equatorial plane. It should be noticed that the plutonyl(V) dimer $[(PuO_2)_2(C_6H_5(COO))_2(bipy)_2]$ is the only example of CC complex of plutonium isolated to date.

Two trimeric assemblies of neptunyl were crystallographically characterised, in aqueous and organic media respectively. The trimeric oxalate complex $\{Cs[NpO_2(C_2O_4)]\}_3$ reveals a cluster core constituted by three neptunyl centres placed at the edge of a triangle connected through T-shaped CCI[150]. The coordination sphere of the neptunyl atoms is completed by two bidentate oxalate ligands per neptunyl. The overall charge of the assembly is balanced by the presence of three caesium ions coordinated to the neptunyl oxo and the oxalate ligands (Figure I-17). The exact analogue with plutonyl(V) had been synthesised too, with similar metric parameters, but with ammonium cations in place of the caesium ones[151]. The mixed valent neptunyl(V)/neptunyl(VI) trimeric complex $[\{Np^{VI}O_2Cl_2\}\{Np^{V}O_2Cl(thf)_3\}_2]$, (which shows SMM properties, see section I.3) was obtained by reduction of the hexavalent neptunyl precursor $[NpO_2Cl_2(thf)_2]$ in thf solution[152]. This complex consists of a trinuclear core with neptunyl atoms placed at the edge of a triangle. The two neptunyl(V) moieties are linked through two bridging chlorides, with their coordination sphere completed by three thf molecules. One neptunyl oxygen from each of the two neptunyl(V) moieties coordinates to the equatorial plane of a neptunyl(VI) centre, for which the coordination sphere is completed by two thf molecules (Figure I-17). This trimeric complex was the first neptunyl cluster isolated in organic solution, and suggested that organic solutions could provide a very convenient media for the isolation of polynuclear assemblies.

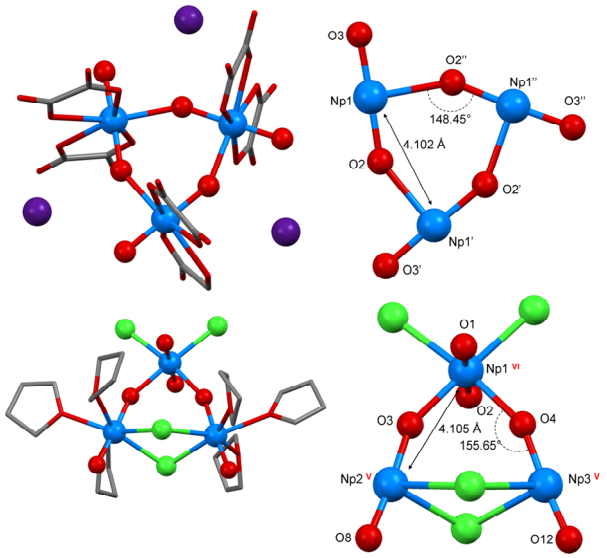

Figure I-17 Mercury view of the trimeric neptunyl assemblies $\{Cs[NpO_2(C_2O_4)]\}_3$ (top) and $[\{Np^{VI}O_2Cl_2\}\{Np^{V}O_2Cl(thf)_3\}_2]$ with their core detailed (Ligands are represented with pipes for clarity, C are represented in grey, O in red, Cl in green, Cs in purple and Np in blue)

The largest neptunium finite assembly has been isolated in 2010, in Moisy's group, and consists in a tetranuclear mixed valent Np(IV)-Np-(V) assembly, $[BuMeIm]_5[(NpO_2)_3Np(H_2O)_6Cl_{12}]$ [153]. This complex, isolated from an ionic liquid is constituted of three neptunyl (V) molecules connected through their oxygen atoms to a Np(IV) centre in a pseudo D_{3h} symmetry (Figure I-18). In this study, the authors demonstrated by DFT calculations that this assembly is stabilized through significant charge transfer from the neptunyl(V) species towards the vacant Np(IV) orbitals. This shows the strong interaction between An(IV) and actinyl(V) ions, which is critical in the redox reactions involving Np(V) during the Purex process, as described in part I.3.

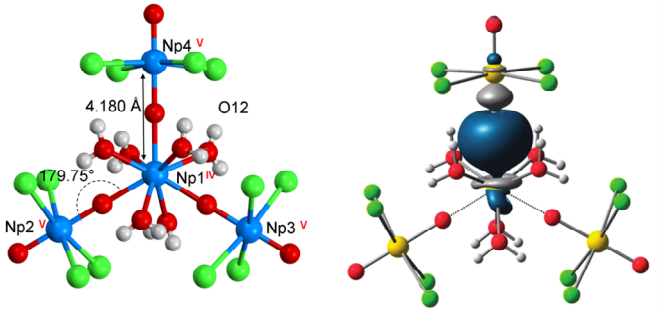

Figure I-18 Mercury view of $[(NpO_2)_3Np(H_2O)_6Cl_{12}]^{5-}$ (left) and schematic representation of the molecular orbital corresponding to one of the Np(IV)-O σ bond [153] (right) (Cl are represented in green, O in red, and Np in Blue(left scheme) or yellow (right scheme))

I.4.1.2.2 *Uranyl(V)*

The highest stability constant for cation-cation interaction is obtained with uranyl(V) ions.[46], and one should expect the occurrence of cation-cation bond in a large number of uranyl(V) complexes. The design of CC clusters of uranyl(V) is particularly attractive for the study of magnetic communication. Notably, by its $5f^1$ electronic configuration, the uranyl(V) moiety does not present interelectronic repulsion in its valence shell, and simplifies the modelisation of magnetic exchange coupling, often exceedingly complicated with actinides. In addition, the radioactivity of uranium is negligible with respect to Np or Pu, and the study of uranyl(V) analogues of these two radioactive neighbours would allow a very convenient access to actinyl(V) polynuclear assemblies.

However, despite the early observation of CCI in uranyl(V) aqueous solution, [154] preparation of compounds with mutual coordination of UO_2^+ was not observed until 2007, due to the easy disproportionation of uranyl(V). Indeed, NpO_2^+ is stable in a wide range of conditions, but pentavalent uranyl can only be stabilized in concentrated carbonate media,[10, 155, 156] or in

reducing environments at mineral surfaces[157]while it readily disproportionates in water to U(IV) and uranyl(VI) species [4], as detailed in part I.3.1.2.1.

Both early experimental studies [24, 158] and recent theoretical studies of the mechanism of disproportionation [25, 26] suggested that the key step in the disproportionation reaction of uranyl(V) in water was the formation of a T-shaped CCI, followed by electron transfer. This reaction was found to be quantitatively accelerated by the presence of protons in the reaction media. It had thus been suggested that these cation-cation complexes formed by uranyl(V) would be too reactive to be isolated.

However, a significant synthetic effort in the last decade in uranyl(V) chemistry in organic solutions has lead to the isolation of the first uranyl(V) complexes, and to the definition of the conditions required for the synthesis of pentavalent uranyl compounds. Notably, the exclusion of protons by using non-aqueous solvents and the use of bulky ligands to prevent cation-cation interaction are essential steps for the preparation of stable pentavalent uranyl complexes.

The directing idea of the earlier attempts to prepare stable uranyl(V) complexes was to electrochemically reduce a uranyl(VI) compound containing suitable organic or inorganic ligands. Notably Ikeda and co-workers have provided spectroscopic evidence that uranyl(V) compounds can be electrochemically produced from the reduction of uranyl(VI) in the presence of ligands of various denticity (mono, bi- tetra- or pentadentate) such as β-diketonates and Schiff bases using the aprotic solvent dmso (Scheme I-11).[159-167] Uranyl(VI) complexes of these ligands were reversibly reduced in dmso and dmf in a large window of potential, varying from -0.52 V to -1.67 v (vs. Fc^+/Fc couple). Some of these complexes were proven to be stable over time in dmso solution, and allowed the physical characterisation of the uranyl(V) moiety through IR and UV-Vis studies. Most likely in these systems, dmso or dmf act as a ligand competing with the uranyl oxygen for the coordination of the uranium centre and therefore prevents cation-cation interaction.[168] These electrochemical studies suggested that the choice of an appropriate ligand set could stabilize UO_2^+ in solution. However, dmso and dmf are not very suitable solvents for reactivity studies and prevented the isolation of the complexes on crystalline form.

Scheme I-11 Representation of uranyl(V) complexes generated electrochemically.

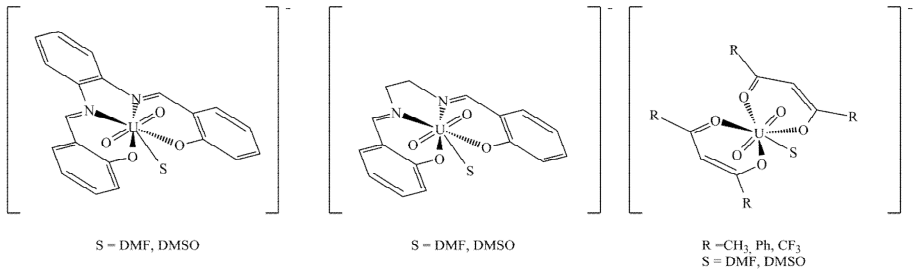

The first pentavalent uranyl complex characterised by single crystal X-ray diffraction studies was obtained from the serendipitous isolation of few crystals of $[UO_2(OPPh_3)_4](OTf)$. [169]. However, attempts to synthesise this complex by reduction of the hexavalent analogue through chemical or photochemical methods failed. The isolation of this uranyl(V) complex encouraged the pursuit of the synthesis of other stable uranyl(V) complexes.

The first reproducible synthesis of a uranyl(V) complex was developed in our group, using a different approach: instead of reducing a uranyl(VI) compound, a two electron oxidation of U(III) was performed to give a UO_2^+ complex. The pentavalent uranyl coordination polymer $\{[UO_2py_5][KI_2py_2]\}_n$, **1** was reproducibly synthesised by oxidation of $UI_3(thf)_4$ with a mixture of pyridine N-Oxide and water.[170] Nevertheless, because the reaction conditions were complicated to control, an easier synthetic path was found, using a mixture of pyridine N-oxide and water, to give the desired compound. The molecular structure of the coordination polymer was determined by X-ray diffraction, as presented in Figure I-19, which showed the presence of a 1-D coordination polymer structure arising from a cation-cation interaction between UO_2^+ and K^+. A second route for synthesising this compound was later reported by Berthet et al., which consisted in the reduction of $UO_2I_2(thf)_3$ with sodium cyclopentadienide followed by the addition of KI.[171]

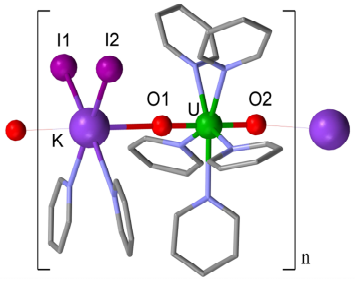

Figure I-19 Mercury view of $\{[UO_2py_5][KI_2py_2]\}_n$ (H were omitted; ligands are represented with pipes for clarity, C are represented in grey, O in red, K in purple, N in blue and U in green) Selected bond length (Å) and angles: U-O1 = 1.8361(17), U-O2 = 1.8343(17), O1-K = 2.8340(18), O2-K = 2.8472(18) and O1-U-O2 = 178.88(7).

The synthesis of this UO_2^+ polymer, which provides a very convenient starting material, opened a new field of exploration for the development of the coordination chemistry of

uranyl(V). This precursor allowed the direct synthesis of the first cation-cation complex of pentavalent uranyl. With the aim of isolating the dbm (Hdbm = dibenzoylmethane) complexes of uranyl(V), $\{[UO_2py_5][KI_2py_2]\}_n$ was reacted with two equivalents of Kdbm in pyridine. Blue crystals of the tetrameric pentavalent uranyl complex $\{[UO_2(dbm)_2]_4[K_6py_{10}]\}I_2py_2$ were isolated[172] (Scheme I-12).

Scheme I-12 Synthesis of $\{[UO_2(dbm)_2]_4[K_6py_{10}]\}I_2py_2$

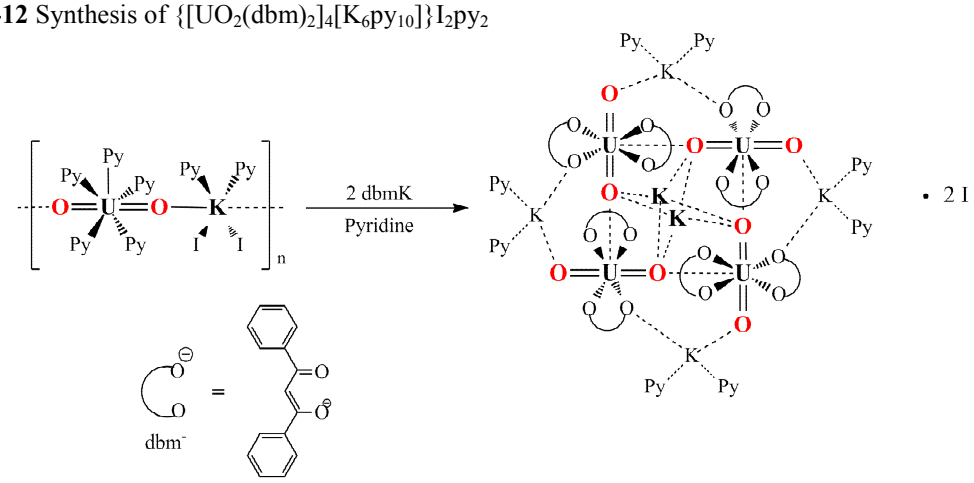

This structure is constituted of four $[UO_2(dbm)_2]$ complexes assembled by cation-cation interaction (CCI) between the UO_2^+ moieties, as shown Figure I-20. The crystallographic study of this structure shows the desymmetrisation of the uranyl cation, the U=O bond involved in the cation-cation interaction being 0.11 Å longer than the terminal ones, for which the distance was very similar to that found in the two previously synthesised uranyl(V) complexes described above.

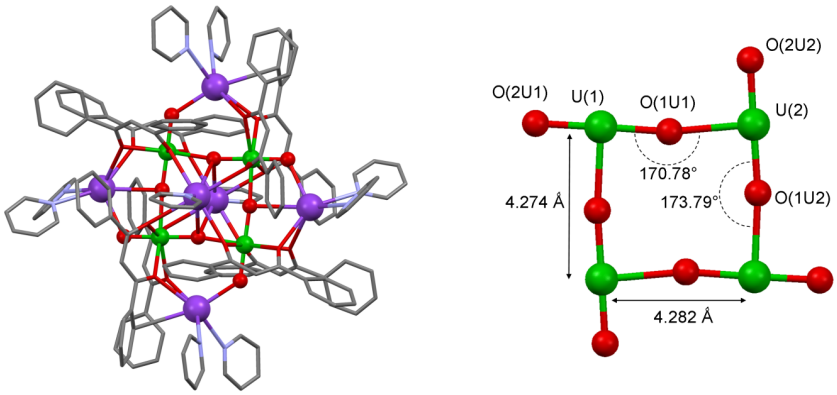

Figure I-20 Mercury view and core detailed of $\{[UO_2(dbm)_2]_4[K_6py_{10}]\}^{2-}$ with associated distances and angles. (H, I^- anions and co-crystallised pyridine molecules were omitted; ligands are represented with pipes for clarity, C are represented in grey, O in red, K in purple, N in blue and U in green).

The synthesis of this first cation-cation uranyl complex was followed by an in depth study of the nature of this interaction, with the objective of better understanding the link between CCI and stability. By letting stand the previously synthesised complex in acetonitrile, crystals of

the acetonitrile solvate $\{[UO_2(dbm)_2]_2[\mu\text{-}K(MeCN)_2][\mu_8\text{-}K]\}_2$ were obtained.[168] Both pyridine and acetonitrile solvates presented the same environment for the uranyl cation, each one being coordinated by the four oxygens of two bidentate dbm ligands, resulting in the presence of four seven-coordinate uranium ions with a pentagonal bipyramidal geometry. The main difference between these two structures is the number of potassium ions involved in an additional CCI with the uranyl oxygen, six potassium ions being involved in the pyridine solvate, instead of four for the acetonitrile one (Scheme I-13). The first consequence of this structural difference is the charge of the complexes: the acetonitrile solvate is neutral while the pyridine one is positively charged, and needs two iodine anions to balance the charge due to the additional potassium ions.

Scheme I-13 Schematic representations of the structures of $\{[UO_2(dbm)_2]_4[K_6py_{10}]\}I_2py_2$ (left) and $\{[UO_2(dbm)_2]_2[\mu\text{-}K(MeCN)_2][\mu_8\text{-}K]\}_2$ (right)

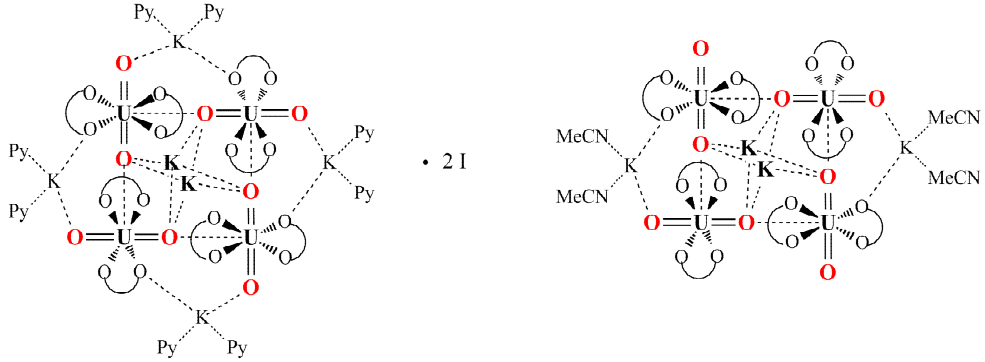

Another significant consequence is the lengthening of the distance between the uranyl oxygens and the uranium centre of the interacting UO_2^+ groups for the acetonitrile solvate compared to the pyridine one (Figure I-21), which suggests the presence of a weaker cation-cation interaction, and give some insights into the role of coordinating cations in the stabilization of such structures.

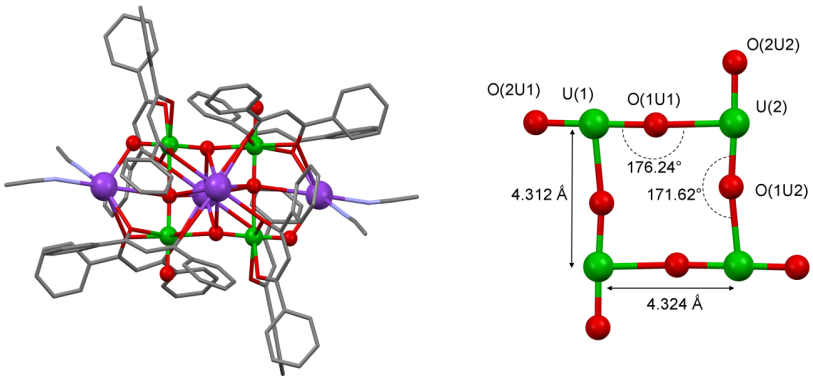

Figure I-21 Mercury view and core detailed of $\{[UO_2(dbm)_2]_2[\mu\text{-}K(MeCN)_2][\mu_8\text{-}K]\}_2$ with associated distances and angles. (H and co-crystallised acetonitrile molecules were omitted; ligands are represented with pipes for clarity, C atoms are represented in grey, O in red, K in purple, N in blue and U in green).

A further study of the role of the coordinated potassium counterions was realized, to assess the influence on the stability of uranyl(V) towards disproportionation. In order to evaluate their electronic and structural role, the reaction of the pyridine solvate $\{[UO_2(dbm)_2]_4[K_6py_{10}]\}I_2py_2$ with 18-crown-6 ether (18C6) was investigated. The crown ether was chosen, knowing its affinity for potassium, to remove potassium from the structure, or at least to weaken the Lewis acidity of the potassium cations. The reaction yielded a centrosymmetric dimer of $[UO_2(dbm)_2]^-$, $[UO_2(dbm)_2K(18C6)]_2$, in which both units are assembled through a diamond shaped cation-cation interaction (Scheme I-14).

Scheme I-14 Synthesis of $[UO_2(dbm)_2K(18C6)]_2$

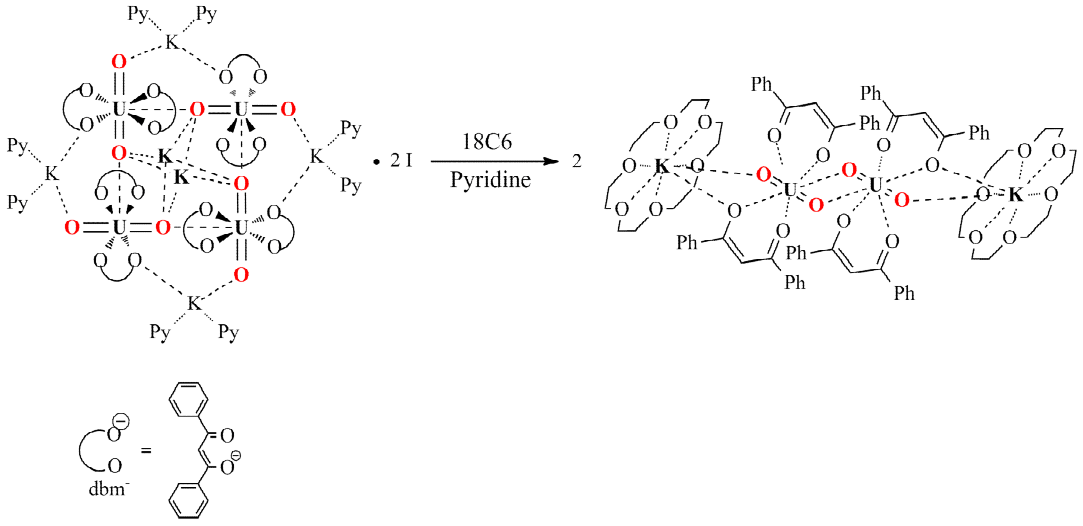

The structure presented in Figure I-22 shows that UO_2^+ units are mutually coordinated, and presents a cation-cation interaction between a potassium ion coordinated by a crown ether moiety and the uranyl oxygen not involved in the UO_2^+-UO_2^+ interaction. Moreover, in this complex, the U=O-K distance is longer than in the tetramers, which shows that the interaction of the (18C6)-bound potassium ion is significantly weaker than the one of the potassium alone. As a result, the desymmetrisation of the U=O bonds is also smaller than the one observed in the tetrameric structures, suggesting a weaker cation-cation interaction between uranyl moieties in the dimeric structure.

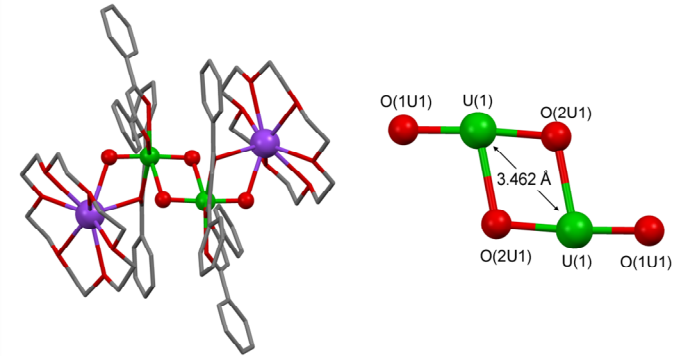

Figure I-22 Mercury view and core detailed of $[UO_2(dbm)_2K(18C6)]_2$ with associated distances and angles. (H atoms were omitted; ligands are represented with pipes for clarity, C atoms are represented in grey, O in red, K in purple, N in blue and U in green).

The preparation of the first oxo-bridged polymetallic complexes of U(V) provided suitable compounds for the exploration of their magnetic properties. The measured temperature-dependent magnetic susceptibility highlights the presence of an unambiguous antiferromagnetic coupling between the two uranium centres of the $[UO_2(dbm)_2K(18C6)]_2$ dimer, with appearance of a maximum in χ vs. T at 5 K (Figure I-23). The coupling probably occurs via a super-exchange pathway through the bridging oxygen atoms involved in the diamond shaped CCI. The different behaviour of the tetrameric complex, which probably involves a magnetic coupling occurring at lower temperature, can be ascribed to the different geometric arrangement of the interacting uranyl(V) groups (T-shaped in the tetramer versus diamond-shaped in the dimer). These results provided the first example of magnetic coupling between uranium ions via uranyl(V) oxo bridges and opened broad perspectives for the use of cation-cation complexes as a new class of polymetallic uranium compounds for the study of magnetic interactions and intermetallic communication in actinides (Figure I-23).

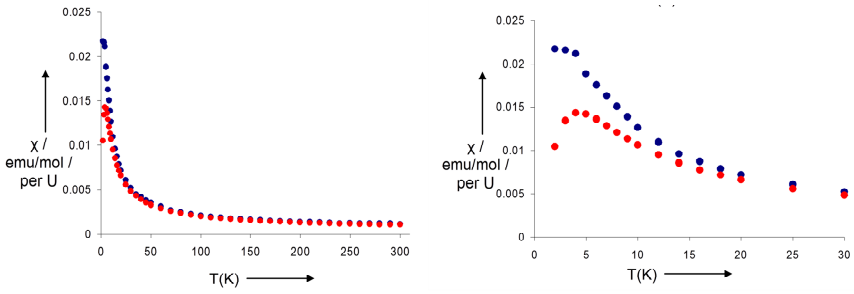

Figure I-23 Temperature dependant magnetic susceptibility data for $\{[UO_2(dbm)_2]_4[K_6py_{10}]\}I_2py_2$ (blue circles)and $[UO_2(dbm)_2K(18C6)]_2$ (red circles) in the range of 2-30 K. .[168]

In order to better understand the role of such cation-cation interaction in uranyl(V) disproportionation, stability studies in solution were carried out. While both tetrameric species disproportionate slowly in pyridine solutions with ligand loss, their dissolution in dmso

yielded the monomeric complex $[UO_2(dbm)_2(dmso)_x]K$, which proved to be fully stable. The high stability of this monomeric uranyl(V) complex could be explained by the strong coordination of dmso to the uranyl centre, preventing the T-shaped interaction between two uranyl moieties by competing with the uranyl oxygen for the available binding site in the equatorial plane of the uranyl moiety. These studies provided the first unambiguous experimental evidence of cation-cation interaction in uranyl(V) complexes, and demonstrated that the preparation of uranyl(V) complexes in organic media is a suitable route for the design of polynuclear uranium(V) assemblies. Moreover, these initial results seemed to validate the general assumption that the formation of cation-cation complexes would inevitably result in the disproportionation of the pentavalent uranyl species.

In view of these results, and in order to prevent the formation of polynuclear intermediates leading to disproportionation, the groups of Hayton and Arnold and ours have designed bulky polydentate ligands or macrocyclic ligands which have resulted in the preparation of monomeric complexes of pentavalent uranyl, stabilized by the prevention of cation-cation interaction.[173-177]

During the period of my PhD work, Arnold et al. reported the reduction of the uranyl(VI) complex of a flexible macrocyclic ligand with the divalent lanthanide complex $[Sm(N(Si(Me)_3)_2)_2]$, affording the simultaneous reduction and functionalization of the hexavalent uranyl (Scheme I-15).[178] The macrocycle ligand in the presence of uranyl adopts a folded structure, called "Pac-Man-like", where one coordination pocket of the ligand is occupied by the uranyl moiety, and the second one coordinates the samarium centre. The uranyl(V) moiety is coordinated to a second uranyl(V) group from a second complex through a diamond shape interaction similar to the one observed in $[UO_2(dbm)_2K(18C6)]_2$, to form the uranyl-samarium complex $[UO_2Sm(py)_2(Pcm)]_2$, where Pcm refers to the macrocyclic Pac-man ligand. The crystal structure of this complex is presented Figure I-24. A similar reduction of uranyl(VI) in the "Pac-man" was observed while using the redox inactive yttrium silylamide complex $[Y(N(Si(Me)_3)_2)_3]$ yielding an analogous dimeric uranyl(V) complex. This reduction might occur through a sterically induced reduction, based on the Y-N bond homolysis induced by the large steric bulk of the silylamide moieties.

Scheme I-15 Synthesis of $[UO_2M(py)_2(Pcm)]_2$, with M = Sm, Y.

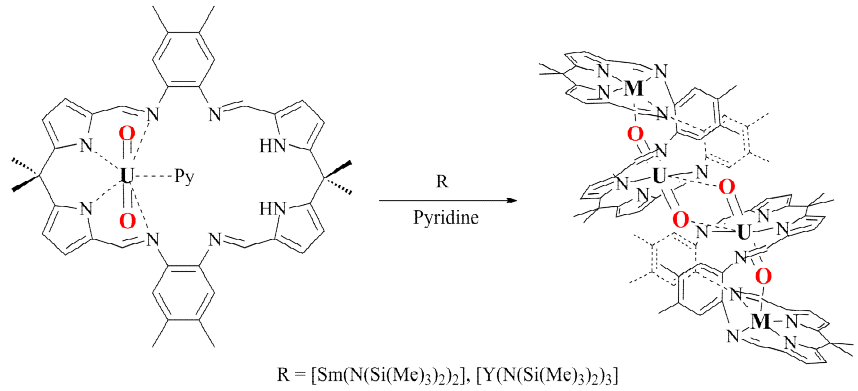

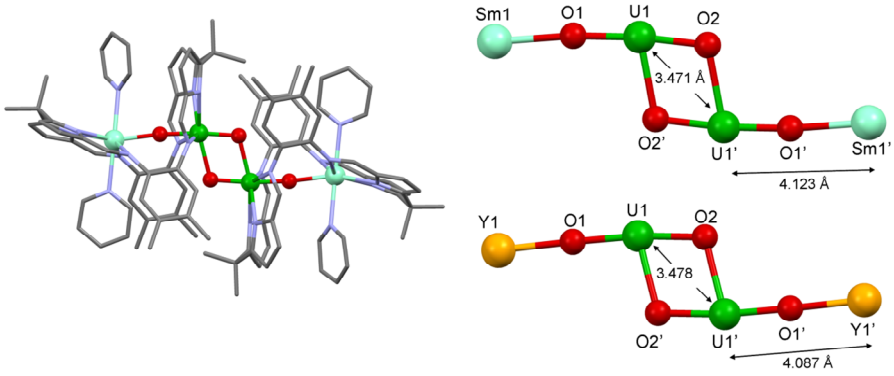

Figure I-24 Mercury view of $[UO_2Sm(py)_2(Pcm)]_2$ (left) and core detailed of $[UO_2Sm(py)_2(Pcm)]_2$ (right, top) and $[UO_2Y(py)_2(Pcm)]_2$ (right bottom) with associated distances. (H and co-crystallised pyridine molecules were omitted; ligands are represented with pipes for clarity, C atoms are represented in grey, O in red, N in blue, Sm in turquoise, Y in yellow and U in green).

Magnetic coupling within these systems were investigated. The comparison of the magnetic properties of the $4f^5$ samarium complex with the properties of its diamagnetic $4f^0$ yttrium analogue shows the influence of the lanthanide ion on the magnetic properties. The two compounds were shown to present very different behaviours. While the samarium-uranyl complex presents an antiferromagnetic coupling with a maximum in the magnetic susceptibility observed at around 10 K, the yttrium analogue did not present any significant interaction (Figure I-25). The author assumed that the antiferromagnetic coupling arises from the coupling of the Sm ion with the uranyl group, and that no significant interactions were present within the uranyl cation-cation complex.

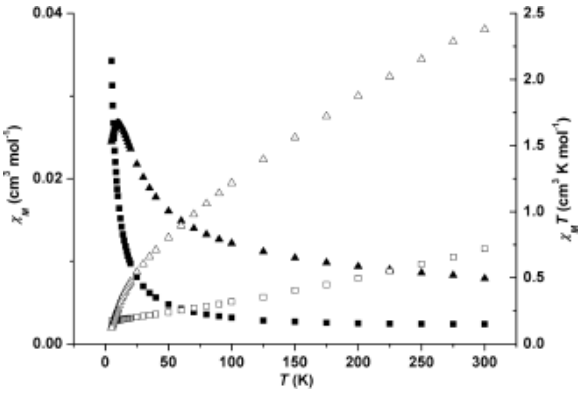

Figure I-25 Variable-temperature magnetic data for $[UO_2Sm(py)_2(L)]_2$ (χ, ▲; χT, △) and $[UO_2Y(py)_2(L)]_2$ (χ, ■; χT, □).[178]

Very recently, Liddle et al. isolated a dinuclear mixed valent methanide uranyl(V)/uranyl(VI) cation-cation complex while attempting to deprotonate a uranyl(VI) methanide. The addition of benzyl sodium to the uranyl(VI) methanide $[UO_2(BIPMH)Cl(thf)]$, did not afford the expected carbene but resulted instead in the reduction of uranyl(VI) to its uranyl(V) analogue, affording the mixed valent CC dimer $[\{UO_2(BIPMH)\}_2(\mu_2\text{-}Cl)]$ in 80 % yield (Scheme I-16).[179] A small amount of the trinuclear mixed valent complex $[\{UO_2(BIPMH)\}_3(\mu_3\text{-}Cl)]$ was also isolated during the course of the synthesis.

Scheme I-16 Isolation of the dinuclear and trinuclear mixed valent CC carbene complexes $[\{UO_2(BIPMH)\}_2(\mu_2\text{-}Cl)]$ and $[\{UO_2(BIPMH)\}_3(\mu_3\text{-}Cl)]$

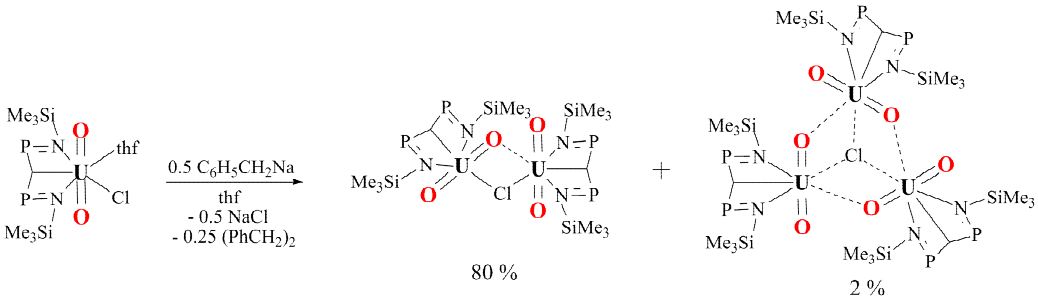

Besides the few crystal structures described here and in part 0, no other polynuclear structures of uranyl(V) have been isolated. However, the $5f^1$ configuration of the uranyl(V) cation is of first interest for the investigation of the magnetic properties of the polynuclear compound formed, the absence of interelectronic repulsion simplifying the analysis of the magnetic behaviour. Moreover, the lower radioactivity of uranium with respect to its actinide neighbour Np and Pu highlights that uranyl(V) could provide a very convenient model for the investigation of the more radioactive actinyl assemblies. This fact incited us to pursue the quest for synthetic routes to stable uranyl(V) polynuclear assemblies.

I.4.2 Non-actinyl assemblies

The coordination flexibility of the non actinyl actinide ions in the oxidation state +III to +V has lead to a wide variety of different topologies for polynuclear actinide complexes. Although this chemistry is poorly developed, few examples have been isolated and will be described according to the bridging groups leading the cluster formation (O^{2-}, N^{3-}…).

I.4.2.1 Oxo/hydroxo actinide clusters

As previously mentioned, the ability of low valent actinides to hydrolyse in aqueous media is the origin of phenomena of aggregation. The study and the understanding of this phenomenon is critical, since the aggregates or colloids formed through hydrolysis of low valent actinides significantly impact the reprocessing and storage of nuclear waste. However, few controlled synthetic routes leading to the formation of polynuclear oxo/hydroxo assemblies are known. Such synthetic strategies are important for the design of new functional actinide materials.

I.4.2.1.1 *Aqueous solution*

Due to the easy hydrolysis of tetravalent actinide, oxolation and olation reactions easily take place in aqueous solution, resulting in the formation of polynuclear oxo/hydroxo assemblies. However, these reactions often lead to complicate mixtures of compounds, and only a few clusters have been structurally characterised from aqueous solution.

The first structurally characterised uranium clusters was the result of the very early work of Lundgreen in 1952, who isolated and crystallographically characterised an hexanuclear uranium(IV) oxo-hydroxo cluster, decorated with sulphate ions. This cluster was obtained during the course of a hydrothermal reaction of uranium(IV) sulphate in 0.5 M sulphuric acid, yielding light green crystals of $[U_6O_4(OH)_4(SO_4)_6]$. In this structure, presented in Figure I-26 the six uranium atoms are assembled at the corners of an octahedron, with each one of the triangular faces capped by triply bridging oxygen, resulting in a U_6O_8 core. The presence of four protons per clusters was revealed by elemental analysis, confirming the $U_6O_4(OH)_4$ core. Each uranium ion is coordinated to four sulphate oxygens, two oxo and two hydroxo groups. Each sulphate moiety is coordinated to two separate clusters, resulting in an extended network of U_6O_8 clusters bridged by sulphate ligands. This cluster is particularly interesting because most of the later structurally characterised clusters present the same hexanuclear core.

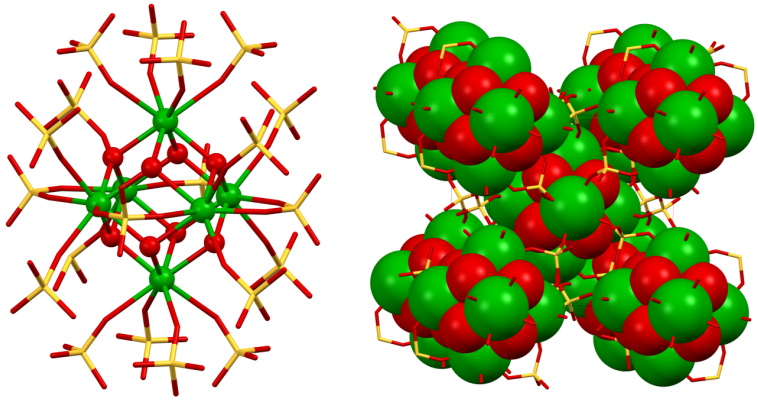

Figure I-26 Mercury view of $[U_6O_4(OH)_4(SO_4)_6]$ (left) and representation of its crystal network with spacefill representation of the cluster core (right) (H were not determined in the crystal structure. Sulphate ligands are represented with pipes for clarity, S atoms are represented in yellow, O in red and U in green).

Surprisingly, this very early report of the formation of a polynuclear assembly of uranium in aqueous solution was not followed by the isolation of other uranium(IV) cluster in aqueous solution until 2009.

Takao et al. carried out accurate studies on the formation of polynuclear actinide complexes in aqueous solution in the presence of carboxylic groups [50]. The formation of hexanuclear U(IV) and Th(IV) complexes from formate aqueous solutions were proven to occur even in acidic media, and the hexanuclear uranium complex was shown by EXAFS and UV-Vis experiments to be the main species present in aqueous solution from pH = 1.5 at least up to pH = 3.25 (Figure I-27, right). The actinide(IV) hexanuclear $[An_6O_4(OH)_4(HCOO)_{12}(H_2O)_6]$ complexes were prepared from aqueous solutions of An^{4+} in presence of formic acid at low pH. The structure of the uranium complex is presented Figure I-27, and presents the same $U_6O_4(OH)_4$ cluster core as observed in the sulphate cluster isolated by Lundgreen. As shown in Figure I-27, the octahedron defined by the six U centres is distorted, due to the presence of two different kinds of μ_3-bridging oxygen atoms (as O^{2-} and OH^-) which have different deviation from the plane defined by the three U atoms capped by the oxygen atom. This feature is common to all the $U_6O_4(OH)_4$ cluster that will be presented in this section. The authors suggest that the $HCOO^-$ moiety acts as a bridging ligand, which prevents the formation of polynuclear hydrolysis species like U(IV) hydrous oxide colloids. Very recently, the same authors identified that similar clusters were forming at low pH in similar condition with Np(IV) cations [48].

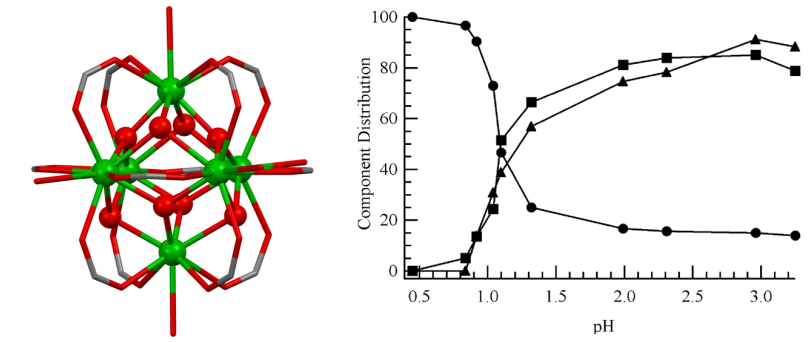

Figure I-27 Mercury view of $[U_6O_4(OH)_4(HCOO)_{12}(H_2O)_6]$ (left; H were not determined in the crystal structure. Formate ligands and water molecules are represented with pipes for clarity, C are represented in grey, O in red and U in green) and species distribution in U(IV)/HCOOH aqueous solution in function of pH (right; Circles and triangles: UV-Vis titration of mononuclear U(IV) and hexanuclear cluster in solution respectively; Squares: EXAFS titration of $[U_6O_4(OH)_4(HCOO)_{12}(H_2O)_6]$) [50]

At higher pH values, tetravalent actinides, and especially plutonium(IV), due to its stability under ambient condition, undergo olation and oxolation reaction to yield oxide colloids, or polymers. Soderholm et al. isolated in 2008 a finite plutonium cluster from a solution containing plutonium colloids. The Pu_{38} cluster $Li_{12}[Pu_{38}O_{56}Cl_{42}(H_2O)_8](H_2O)_x$ presented in part I.3 was first isolated from an aqueous solution through an empirical synthetic method involving several steps of treatment of the aqueous solution with hydroxides, peroxides followed by treatments with nitric and hydrochloric acids[72]. Recently, a more convenient method was reported, which involves the neutralisation of a Pu(IV) solution in concentrated HCl with LiOH while the solution is boiling[67]. However, if this second synthetic method is reproducible, no quantitative synthesis of this plutonium cluster has been described yet. The crystal structures of $Li_{12}[Pu_{38}O_{56}Cl_{42}(H_2O)_8](H_2O)_x$ and $Li_2[Pu_{38}O_{56}Cl_{42}(H_2O)_{20}](H_2O)_{15}$ obtained by recrystallisation of the first cluster in HCl/LiCl aqueous solution, consists of plutonium clusters with the same $[Pu_{38}O_{56}]^{40+}$ core, decorated with various number of chloride anions(Figure I-11). Within the $[Pu_{38}O_{56}]^{40+}$ core three crystallographically distinct types of plutonium centres can be found. The central cluster, constituted of 6 Pu ions each coordinated by eight oxygen atoms, has the same fluorite-type topology than bulk PuO_2. Eight plutonium cations are bound to these eight oxygen atoms, at the vertices of a cube containing 14 plutonium atoms. These 8 plutonium atoms are coordinated to seven oxo groups and one water molecule. The remaining 24 plutonium ions complete the faces of the pseudo cube thus defined, each being bound to four oxo groups and chloride anions (Figure I-28). It should be noticed that bond valence calculations on the cluster indicated that all plutonium atoms are present at the +IV oxidation state and that the oxo group are not protonated. This compound is

the largest actinide(IV) cluster ever isolated, and gives strong information concerning the structure of actinide colloids in solution, demonstrating that they are built of molecular complexes, rather than amorphous oxide/hydroxides.

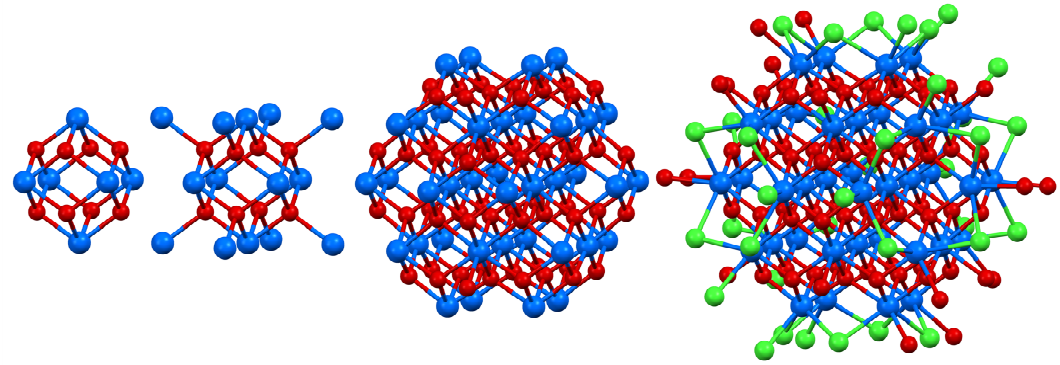

Figure I-28 Mercury views, from left to right, of the hexahedral Pu_6O_8 core, of the pseudocubic Pu_{14} shell, of the $Pu_{38}O_{56}$ cluster core and of the total cluster $Li_{12}[Pu_{38}O_{56}Cl_{54}(H_2O)_8](H_2O)_x$] (H and Li atoms were not determined in the crystal structure. Cl are represented in green, O in red and Pu in blue)

I.4.2.1.2 *Organic media*

Despite its environmental relevance, the isolation of polynuclear assemblies in aqueous solution is very difficult due to the complexity of hydrolysis/redox chemistry in aqueous media. In order to develop rational synthetic routes towards polynuclear assemblies, organic solvents have been used to better control the reaction parameters involved in the cluster synthesis.

I.4.2.1.2.a Serendipitous hydrolysis/oxidations

The propensity of low valent actinide to hydrolyze is important in aprotic organic media, and most of the actinide oxo complexes isolated to date in anaerobic organic media resulted from hydrolysis with adventitious traces of water in the reaction mixture. Nevertheless, serendipitous hydrolysis/oxidation of low valent uranium complexes led to the characterisation of a large number of clusters with various nuclearities and original topologies which usually cannot be reproduced by the controlled addition of water in the media. Three trimeric uranium complexes have been isolated serendipitously with different ligands decorating the uranium cluster. [180, 181] Two of these trimeric complexes possess similar cluster cores, with three uranium atoms placed at the vertices of an μ_3-oxo centred triangle and bridged by a compartmental Schiff base ligand L' = N,N'-bis(3-hydroxysalicylidene)-2-methyl-1,2-propanediamine (Figure I-29, left) or by a calix[3]arene ligand (Figure I-29, centre)). The third trimer is constituted by three uranium(IV) centres bridged in a linear

fashion through μ_2-oxo and coordinated in their equatorial plane by terpyridine (terpy) ligands[182] (Figure I-29, right).

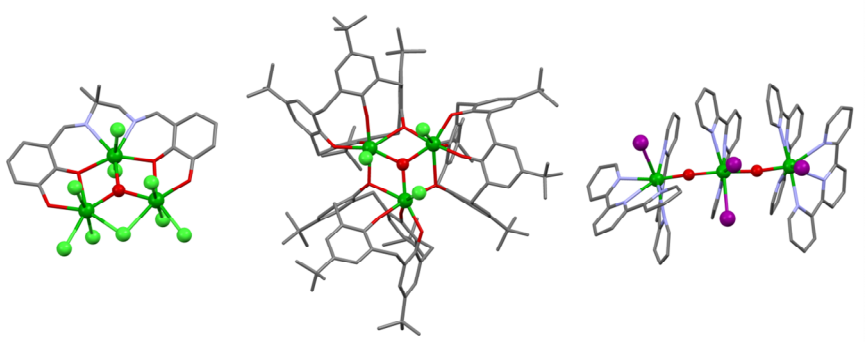

Figure I-29 Mercury views of the uranium trimers isolated in organic media after reaction of low valent precursors with adventitious water: $[U_3L'Cl_9(\mu_3\text{-}O)]^{3-}$ [181] (left), $[\{UCl(^t\text{Bu-calix}[_4]\text{arene})\}_3(\mu_3\text{-}O)]$ [180] (centre) and $[\{UI(terpy)_2(\mu\text{-}O)\}_2\{UI_2(terpy)\}]^{4+}$ (right) [182] (Non coordinated counterions, co-crystallised solvent and H atoms were omitted for clarity. Ligands are represented with pipes, C are represented in grey, O in red, N in blue, Cl in light green, I in purple and U in green.)

In these structures, the coordination geometry of the μ-oxo groups is critical for the final assembly shape. Adventitious water entry in a solution of uranium(IV) complex of the compartmental Schiff base ligand L" = N,N'-bis(3-hydroxysalicylidene)-2,2-dimethyl-1,3-propanediamine leads to the isolation of a tetranuclear cluster with a unique U_4 tetrahedral core, held by a central μ_4-oxo (Figure I-30, left) [181]. Charpin et al. isolated the very different tetranuclear cluster $[U_4(CF_3COO)_{16}(\mu_3\text{-}O)_2]K_4$ through the hydrolysis of a uranium(IV) pyridine solution in presence of potassium trifluoroacetate[183]. This cluster possess a U_4 core built around two fused U_3 triangles with central μ_3-oxo, resulting in a planar tetramer, each uranium(IV) centre being bridged by bidentate trifluoroacetate ligands (Figure I-30, centre). As observed for the linear trimer presented Figure I-29, terpyridine ligands favours linear assemblies, and a linear tetranuclear cluster $[\{U(terpy)_2(\mu_2\text{-}O)\}_2(\mu_2\text{-}O)(OTf)_6\}]K_4$ has been isolated by Berthet et al. (Figure I-30, right).[182]

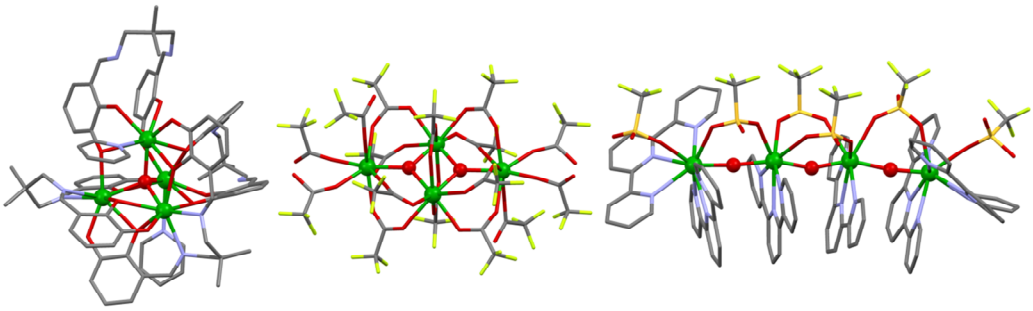

Figure I-30 Mercury views of the uranium tetramers isolated in organic media after reaction of low valent precursors with adventitious water: $[U_4(L")_2(HL)_2(py)_2(\mu_3\text{-}O)_2]^{2+}$ [181] (left), $[U_4(CF_3COO)_{16}(\mu_3\text{-}O)_2]^{4-}$ [183] (centre) and $[\{U(terpy)_2(\mu_2\text{-}O)\}_2(\mu_2\text{-}O)(OTf)_6\}]^{4+}$ (right) [182] (Non coordinated counterions, co-crystallised

solvent and H atoms were omitted for clarity. Ligands are represented with pipes, C are represented in grey, O in red, N in blue, F in light green, S in yellow and U in green.)

Finally, two original octanuclear uranium clusters were isolated in organic media after reaction of low valent precursors with adventitious traces of water. These two clusters present very distinct shapes. The core of the cluster $[U_8L'''_4Cl_{10}(\mu_4\text{-}O)_4]^{2-}$, obtained in presence of the compartmental Schiff base ligand L''' = N,N'-bis(3-hydroxysalicylidene)-1,2-phenylenediamine, consists of four distorted uranium tetrahedron, each of them sharing a common edge with its three neighbours and containing a μ_4-oxo at its centre[184]. The cluster $[U_8Cl_{24}(\mu_4\text{-}O)_2(\mu_3\text{-}O)_2(Cp^*py)]^{2-}$ is constituted from two fused μ_4-oxo uranium tetrahedral, each one sharing an edge with a μ_3-oxo centred uranium triangle[185]. This uranium core is decorated with 24 chloride anions and two (Cp*py) at the extremities of the cluster.

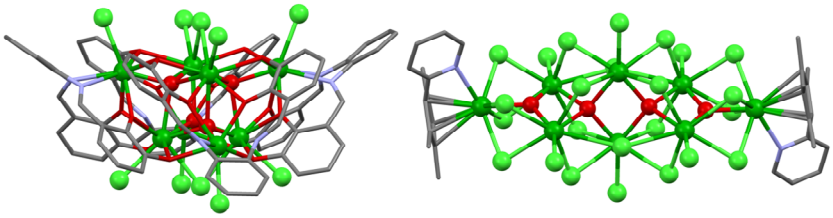

Figure I-31 Mercury views of the uranium octamers isolated in organic media after reaction of low valent precursors with adventitious water: $[U_8L'''_4Cl_{10}(\mu_4\text{-}O)_4]^{2-}$ [184]. (left) and $[U_8Cl_{24}(\mu_4\text{-}O)_2(\mu_3\text{-}O)_2(Cp^*py)]^{2-}$ (right) [185] (Non-coordinated counterions, co-crystallised solvent and H atoms were omitted for clarity. Ligands are represented with pipes, C are represented in grey, O in red, N in blue, Cl in light green and U in green.)

The complexes described above highlight the possibility of isolating uranium oxo clusters of different topologies from the hydrolysis of low valent precursors in organic media. However, all the complexes presented in this section were isolated serendipitously, and no reproducible synthetic method was reported.

I.4.2.1.2.b Controlled reaction with H_2O

In view of the significant number of clusters obtained serendipitously by hydrolysis in organic solutions, synthetic routes have been developed to reproducibly synthesise polynuclear oxo/hydroxo clusters through the reaction of low valent precursors with stoichiometric amounts of water or oxo donors, in presence of organic ligands to direct the cluster shape and nuclearity.

Andersen et al. demonstrated that the stoichiometric addition of water to a trivalent uranium hydride precursor could lead to the isolation of hydroxo and oxo bridged polynuclear clusters. The authors noted that the reaction of two equivalents of water on the trivalent uranium

hydride dimer $[Cp''_2U(\mu_2\text{-}H)]_2$ in hexane lead to a trivalent uranium hydroxide dimer $[Cp''_2U(\mu_2\text{-}OH)]_2$, which can be converted quantitatively to its oxide analogue upon heating at 100°C (Scheme I-17). [186] The crystal structure of the hydroxo dimer is given in Figure I-32.

Scheme I-17 Hydrolysis of $[Cp''_2U(\mu_2\text{-}H)]_2$and oxidative elimination of the hydrolysis product

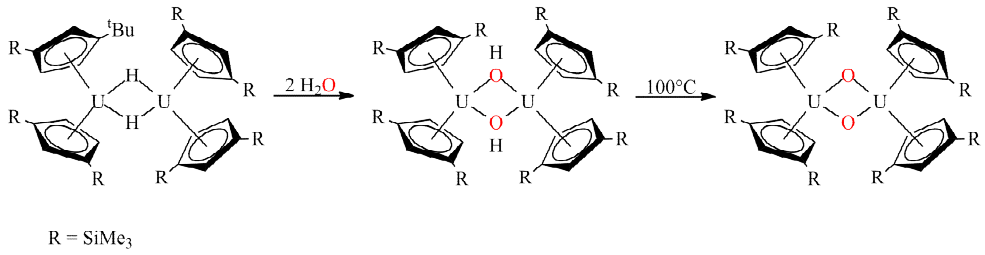

R = $SiMe_3$

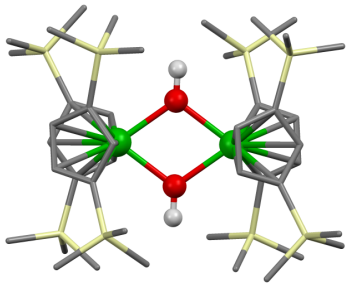

Figure I-32 Mercury view of $[Cp''_2U(\mu_2\text{-}OH)]_2$ (The H atoms of the hydroxo groups were not present in the original crystal structure, and are positioned in calculated positions. Ligands are represented with pipes, C are represented in grey, O in red, Si in light yellow and U in green.)

It should be noticed that the final bis-oxo complex had also been isolated previously by the acid-base reaction of water on the tetravalent uranium precursor $[Cp''_2U(NMe_2)_2]$ [187].

More recently, Mazzanti et al. demonstrated that the reaction of the trivalent tpa complex $[U(tpa)_2]I_3$ with stoichiometric amounts of water lead to the isolation of a uranium(IV) trimer with uranium atoms placed at the vertices of a triangle [188]. These uranium atoms are connected by three μ_2-O placed along the edges of the triangle and one μ_3-iodine atom placed above the plane defined by the three uranium centres. Each uranium atom is coordinated by a tetradentate tpa ligand, which suggests that the tpa ligand probably prevents the formation of larger assemblies (Figure I-33). The two deprotonations of water occur here in one step, presumably through the formation of an unstable hydroxo uranium(IV)complex by reductive elimination of H_2 followed by an oxolation reaction.

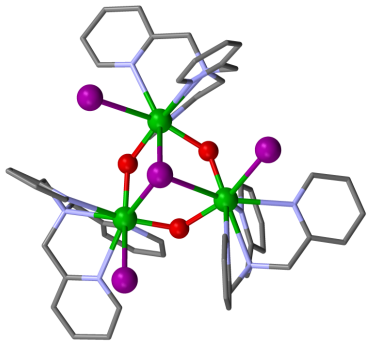

Figure I-33 Mercury view of $\{[U(tpa)(\mu_2\text{-}O)I]_3(\mu_3\text{-}I)\}^{2-}$ (H atoms, co crystallised solvent molecules and non coordinated iodine counterions were omitted for clarity. Ligands are represented with pipes, C are represented in grey, O in red, N in blue, I in purple and U in green.)

Based on these observations, our group carried out the controlled hydrolysis of trivalent uranium precursors with less bulky ligands in order to increase the nuclearity of the assemblies. The addition of two equivalents of water to an acetonitrile solution of the trivalent precursor $[U(OTf)_3(CH_3CN)_3]$ in presence of two equivalents of potassium triflate lead to a mixture of several clusters, all presenting the same fluorite-like U_6O_8 cores but with different structural characteristics [189]. Three different types of clusters have been crystallographically characterised from this reaction mixture. All the clusters are constituted from six uranium atoms situated at the vertices of an octahedral with the six triangular faces of the octahedral bridges by μ_3-oxo groups. Eight bidentate triflate moieties bridge uranium atoms in a μ_2 fashion along the edge of the octahedron. The main difference between these different structures arises from the presence or the absence of potassium counterions, as a consequence of different numbers of triflate ligands per cluster. These potassium ions are involved in the formation of extended networks, and resulted in three species with different structures, namely the 3D $\{[U_6(\mu_3\text{-}O)_8(\mu_2\text{-}OTf)_{12}(H_2O)_{3.5}]\ [K_4(\mu_2\text{-}H_2O)_2(H_2O)_4]\cdot 4.5H_2O\}_n$, the 2D $[U_6(\mu_3\text{-}O)_8(\mu_2\text{-}\ OTf)_8(\eta_2\text{-}OTf)_4]K_2$ extended networks, and the discrete cluster $[U_6(\mu_3\text{-}O)_8(\mu_2\text{-}OTf)_{12}(H_2O)_3]\cdot 23H_2O$ (Figure I-34). It should be noticed that the 3D cluster forms a framework with an original zeolite-like topology with large rhombihexahedral cavities about 2.5 nm wide. The oxidation state of the uranium centres within the cluster cores were determined through bond valence sum analysis; while the cluster implicated in the 3D network is constituted of six U(IV) ions, the two other clusters are formed by four U(IV) and two U(V) ions delocalized on the cluster core.

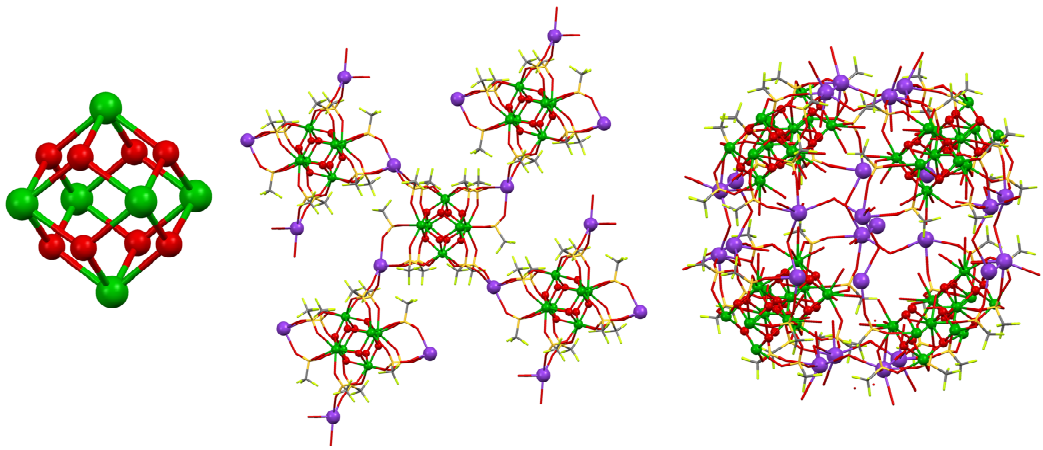

Figure I-34 Mercury views of the U_6O_8 core found in the clusters $\{[U_6(\mu_3\text{-}O)_8(\mu_2\text{-}OTf)_{12}(H_2O)_{3.5}]\ [K_4(\mu_2\text{-}H_2O)_2(H_2O)_4]\cdot 4.5H_2O\}_n$, $[U_6(\mu_3\text{-}O)_8(\mu_2\text{-}\ OTf)_8(\eta_2\text{-}OTf)_4]K_2$ and $[U_6(\mu_3\text{-}O)_8(\mu_2\text{-}OTf)_{12}(H_2O)_3]\cdot 23H_2O$ (left), of the 2D network in $[U_6(\mu_3\text{-}O)_8(\mu_2\text{-}\ OTf)_8(\eta_2\text{-}OTf)_4]K_2$ (centre) and the 3D network in $\{[U_6(\mu_3\text{-}O)_8(\mu_2\text{-}OTf)_{12}(H_2O)_{3.5}]\ [K_4(\mu_2\text{-}H_2O)_2(H_2O)_4]\cdot 4.5H_2O\}$ (right) (Co-crystallised solvent and H atoms were omitted for clarity. Ligands are represented with pipes, C are represented in grey, O in red, N in blue, F in light green, S in yellow, K in purple and U in green.)

When a similar reaction is carried out with the uranium(III) iodine precursor $[UI_3(thf)_4]$ instead of the uranium(III) triflate starting material, the dodecanuclear uranium cluster $[U_{12}(\mu_3\text{-}OH)_8(\mu_3\text{-}O)_{12}I_2(\mu_2\text{-}OTf)_{16}(CH_3CN)_8]$ is isolated in a pure form.[189] The X-ray crystal structure analysis of this complex revealed the presence of a discrete dodecanuclear oxo/hydroxo complex, which can be described as a double-decker square-antiprism, in which two stacked distorted square antiprisms share the square plane formed by the four symmetry-related uranium ions (Figure I-35).

This cluster core can be also described as the assembly of two entities similar to the cluster core described above for the cluster $[U_8L_4Cl_{10}(\mu_4\text{-}O)_4]^{2-}$, obtained in presence of a compartmental Schiff base ligand [184] each U_8 unit being orthogonal and sharing their four uranium square base. Bond valence sum analysis and magnetic measurement revealed the presence of ten U(IV) centres and two U(V) ions, with a charge delocalized on the cluster core.

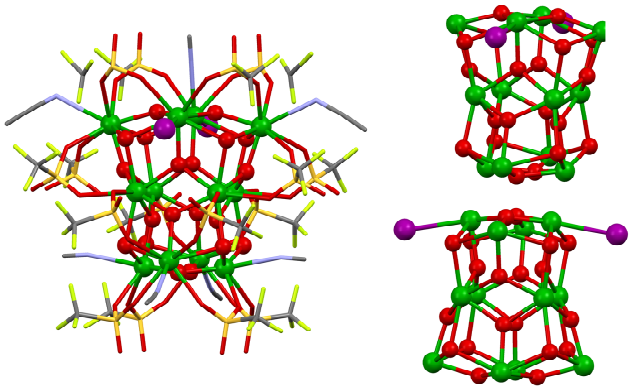

Figure I-35 Mercury view of $[U_{12}(\mu_3\text{-}OH)_8(\mu_3\text{-}O)_{12}I_2(\mu_2\text{-}OTf)_{16}(CH_3CN)_8]$ (left) and details of the cluster core (right) (Co-crystallised solvent and H atoms were omitted for clarity. Ligands are represented with pipes, C are represented in grey, O in red, N in blue, F in light green, S in yellow, I in purple and U in green.)

Recently, Nocton demonstrated that the triflate ions decorating the surface of the various clusters cited above could be replaced by dibenzoylmethanate (dbm) ligands. This ligand substitution had dramatic effect on the cluster size: the unique cluster observed with dbm was a $U_6O_4(OH)_4$ cluster decorated with bridging dbm ligands, $[U_6O_4(OH)_4(\eta\text{-}dbm)_{12}]$ (Figure I-36), even when the $U_{12}O_{20}$ cluster was used as a starting material. This cluster is obtained analytically pure in good yield, and its high solubility in solution allowed an easy characterisation of the cluster in solution by NMR studies. However, the dbm cluster decomposes in solution to afford after 72h $U(dbm)_4$ as unique product(Scheme I-18).

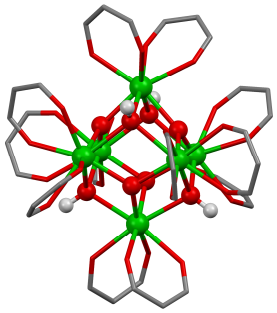

Figure I-36 Mercury view of $[U_6O_4(OH)_4(\eta\text{-}dbm)_{12}]$ (H atoms phenyl groups and co crystallised solvent molecules were omitted for clarity. Ligands are represented with pipes, C are represented in grey, O in red and U in green.)

Scheme I-18 U_{12} cluster dissociation by dbm ligand

$$\underset{\text{in situ}}{[U_{12}(\mu_3\text{-}OH)_8(\mu_3\text{-}O)_{12}I_2(\mu_2\text{-}OTf)_{16}(CH_3CN)_8]} \xrightarrow[MeCN]{24\ \text{K dbm}} [U_6O_4(OH)_4(dbm)_{12}] \xrightarrow[MeCN]{72\ \text{h}} [U(dbm)_4]$$

The example of controlled hydrolysis of low valent complexes presented above proves that quantitative and reproducible synthesis can be accessed by this method. Moreover, the fact that the triflate and iodide ligands coordinated on the cluster edges can be exchanged and

change the cluster nuclearity, as highlighted by the last example, pave the way for easy new cluster synthesis by ligand exchange.

I.4.2.1.2.c Reactions with O_2/O-atom transfer agents

Reaction with O_2 or more generally with oxo group donors such as amine or phosphine oxides, N_2O, etc has been widely investigated with tri and tetravalent uranium complexes.

A relatively large number of uranium(IV) oxo polynuclear complexes have been reported in the literature, and have been reviewed recently [190-192]. Most of the oxo complexes isolated by reaction with O^{2-} donors presented a dimeric structure with uranium(IV) atoms bridged by a linear μ_2-oxo. A large number of reactions with uranium(III) derivatives have lead to the isolation of μ_2-oxo dimers. Oxo coupled dimers have been obtained from tris(cyclopentadienyl) uranium(III) precursors by oxidation with O_2 [193]or N_2O [194], from homoleptic tris aryloxide complexes by reaction with N_2O, NO, Me_3NO,and pyNO[195].

More recently, Meyer et al. isolated several μ_2-oxo uranium(IV) complexes with bulky polydentate ligands constituted from three aryloxide arms anchored on triazacyclononane, amine or mesityl ligands. Such dimers where synthesised by reaction of the trivalent complexes [(($^{t\text{-}Bu}$ArO)$_3$mes)U] and [((^{Ad}ArO)$_3$N)U] with excess N_2O[96] or by the reduction of CO_2 on [((^{tBu}ArO)$_3$tacn)U] [95]. This last example presented a rare antiferromagnetic coupling between the uranium(IV) centres, with a maximum in the magnetic susceptibility observed at 20K. A dimer with the same connectivity was produced by treating with 0.5 equivalent of Me_3NO the uranium(III) complex obtained with the polydentate amide/amine ligand $[N(EtN(SiMe_2{}^tBu)_3]^{3-}$.[196]

Interestingly, a very different reactivity when different oxo donors where used on the U(III) complex bearing a tripodal tris(aryloxide) ligand with a single nitrogen anchor [((^{Ad}ArO)$_3$N)U]; while its reactivity with N_2O in excess lead to the previously described linear μ-oxo uranium(IV) dimer [{((^{Ad}ArO)$_3$N)U}$_2$(μ_2-O)], the addition of 1.5 equivalents of pyridine N-oxide lead to the isolation of the pentavalent uranium bis-μ-oxide complex [{((^{Ad}ArO)$_3$N)U}$_2$(μ_2-O)$_2$] (Scheme I-19). [197] This observation highlights the fact that subtle change in the choice of the oxygen atom transfer agent can have strong influence on the final compound assembly. This complex present a short U-U distance of 3.4346 Å, and present an unusual magnetic behaviour with a magnetic moment at 2K lower than what expected, potentially due to antiferromagnetic interactions within the complex.

Scheme I-19 Synthesis of [{((^Ad ArO)$_3$N)U}$_2$(μ_2-O)] and [{((^Ad ArO)$_3$N)U}$_2$(μ_2-O)$_2$]

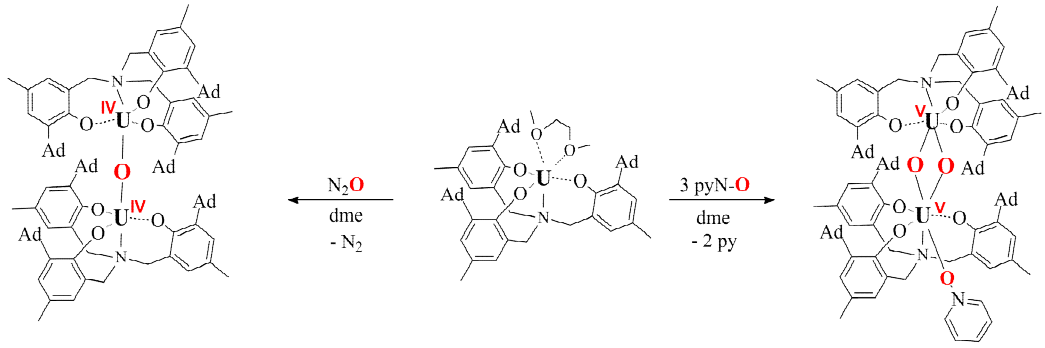

The influence of the oxygen atom source on the final compound isolated by oxidation of a uranium(III) precursor has been elegantly exemplified by Hayton et al., who demonstrated that the U(III) tris(hexamethyldisilylamide) [U(HMDS)$_3$] complex form a uranium(IV) μ_2-oxo dimer when treated with 0.5 equivalents of Me_3NO and a uranium(V) terminal oxo when treated with one equivalent of TEMPO. [198] This different reactivity was postulated to arise from the slower kinetic of the oxo transfer with Me_3NO, resulting in the presence of unreacted U(III) complex in the media and leading to the dimeric compound (Scheme I-20).

Scheme I-20 Oxo atom transfer on U(HMDS)$_3$

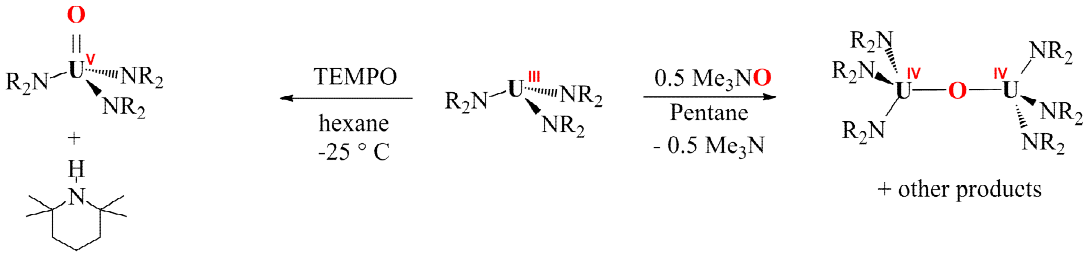

Very reactive trivalent uranium complexes have been proven to occasionally present unexpected reactivity with the solvent molecules, especially observed with compounds likely to form stable oxides such as polynuclear complexes. For example, in an attempt to prepare a trivalent uranium complex from a tetracyclohexyl substituted calixtetrapyrrole potassium salt with $UI_3(thf)_4$ in thf, a μ_2-oxo uranium(IV) dimer was isolated, in which the oxygen is believed to originate from thf. [199]

Recently, Cloke et al. observed the activation and reduction of diethyl ether during the reaction of UI_3 and $KCp^{RR'}$ ($Cp^{RR'}$ = pentamethylcyclopentadienyl, trimethylsilylcyclopentadienyl or tetramethylcyclopentadienyl) in diethyl ether. In these reactions a two-electron reduction of the solvent was described, forming the trimetallic, mixed valence uranium(III/IV) [(U($Cp^{RR'}$)(μ_2-I)$_2$]$_3$(μ_3-O) clusters (Scheme I-21).[200] The clusters possess a trinuclear uranium core with two uranium(IV) and one uranium(III) centres,

disposed along the vertices of a μ_3-oxo centred triangle (Figure I-37). The charge was not localised on the uranium centres from the crystal structure analysis.

Scheme I-21 Two electron reduction of Et_2O affording trinuclear $[(U(Cp^{RR'})(\mu_2\text{-}I)_2]_3(\mu_3\text{-}O)$ clusters

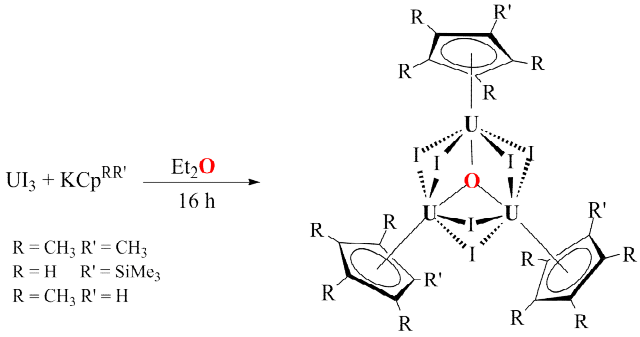

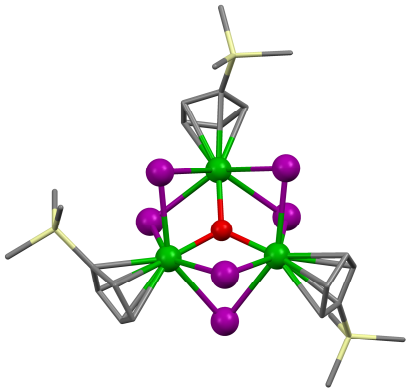

Figure I-37 Mercury view of $[(U(C_5H_4SiMe_3)(\mu_2\text{-}I)_2]_3(\mu_3\text{-}O)$ (H atoms phenyl groups and co crystallised solvent molecules were omitted for clarity. Ligands are represented with pipes, C are represented in grey, O in red, Si in light yellow, I in purple and U in green.)

In an attempt to synthesise an organometallic uranyl(VI) complex with a bulky cyclopentadienyl ligand, Andersen et al. observed the unexpected formation of a U_6O_{13} cluster[201]. Reduction of $[Cp'''_2UCl_2]$ with two equivalents of KC_8, followed by an addition of two equivalents of pyridine N-Oxide lead to the isolation of the cluster compound $[U_6O_{13}(Cp''')_4(bipy)_2]$ in which the six U(V) ions define a slightly distorted octahedron with an interstitial μ_6-oxo group in the centre of the isopolyoxometalate core (Scheme I-22 and Figure I-38). This U_6O_{13} core mimics the isopolyoxometalate Lindqvist structure usually found in molybdenum and tungsten chemistry. However, in the Lindqvist structure, a terminal oxo ligand on each metal centre would normally complete the coordination sphere, whereas here these terminal sites are occupied instead by Cp''' ligands. This synthesis surprisingly combined the two electron oxidation of the uranium centres to "uranyl(V)-like" moieties with the coupling of the pyridyl radicals generated during the reaction. This complex was the first large uranium oxo cluster synthesised in organic solution.

Scheme I-22 Synthesis of $[U_6O_{13}(Cp''')_4(bipy)_2]$

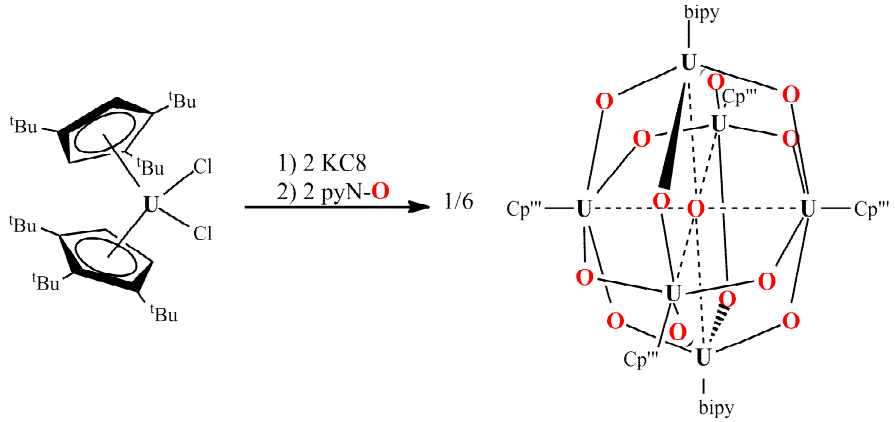

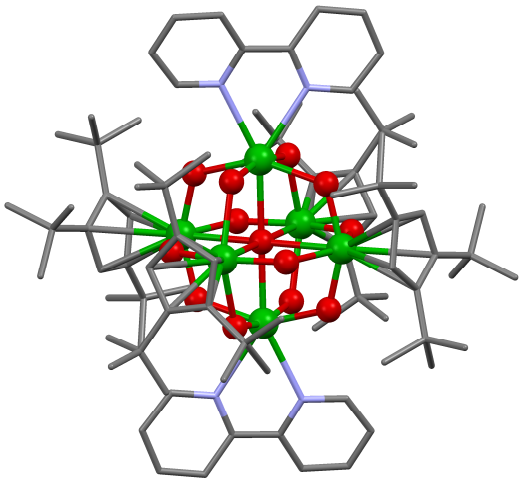

Figure I-38 Mercury view of the cluster $[U_6O_{13}(Cp''')_4(bipy)_2]$ (H atoms were omitted for clarity, ligands are represented with pipes, C are represented in grey, O in red, N in blue and U in green.)

I.4.2.1.2.d Reactions with CO_2

A few polynuclear complexes have been isolated after treatment of low valent uranium precursors with carbon dioxide. The first example described in the literature by Calderazzo et al. consists in a tetranuclear uranium cluster obtained by the reaction in strictly anhydrous conditions of UCl_4 in a CO_2 saturated solution of Et_2NH in heptane (Scheme I-23). The structure, presented Figure I-39, consists in the same U_4 core than obtained for $[U_4(CF_3COO)_{16}(\mu_3\text{-}O)_2]^{4-}$ [183] (see section I.4.2.1.2.a), with diethylcarbamate ligands bridging the uranium centres instead of the trifluoroacetate groups. The author suggested that uranium catalyses the carbamate formation from CO_2 and amine to form a transient $[U(Et_2NCOO)_4]$ species that further reacts to give $[U_4(Et_2NCOO)_{12}(\mu_3\text{-}O)_2]$ and isocyanoethane.

Scheme I-23 Synthesis of $[U_4(Et_2NCOO)_{12}(\mu_3\text{-}O)_2]$

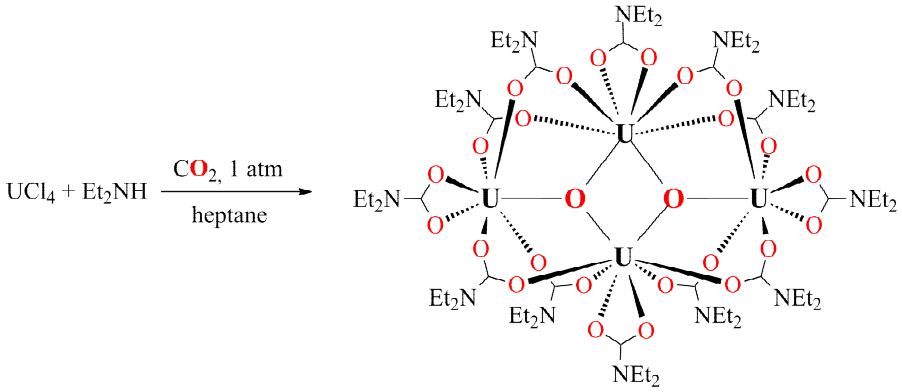

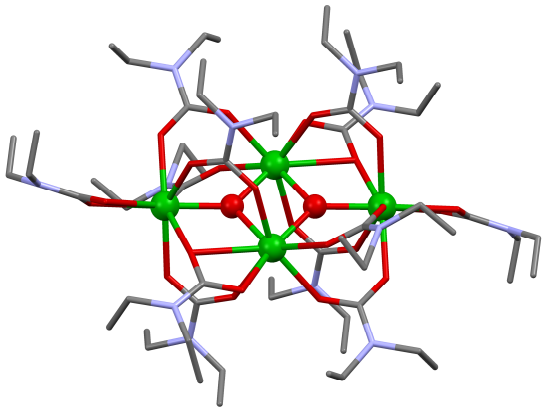

Figure I-39 Mercury view of the cluster $[U_4(Et_2NCOO)_{12}(\mu_3\text{-}O)_2]$ (H atoms were omitted for clarity, ligands are represented with pipes, C are represented in grey, O in red, N in blue and U in green.)

Several μ_2-oxo bridged uranium(IV) dimers were isolated from the reduction of CO_2 and the subsequent CO release[95, 194]. This reactivity can be associated to CO_2 insertion in the U-ligand bond, as observed by Arnold et al. with the tris-aryloxide uranium(IV) dinitrogen dimer $\{[U(OTtbp)_3]_2(N_2)\}$. [93]

Finally, the reaction of carbon dioxide on low valent uranium precursors has lead to the recent isolation of two uranium(IV) dimers connected by carbonate ligands previously described in section I.3.4.1. [90, 96]

I.4.2.1.2.e Reduction of actinyl moieties

In alternative to the oxidation of low valent precursors with oxygen atoms donors, synthetic route have been developed using the uranyl moiety as a convenient oxide precursor for the synthesis of polynuclear uranium oxo/hydroxo assemblies. In 1996, Carrano et al. observed that the reduction of uranyl(VI) acetate with a vanadium(III) hydridotris(pyrazolyl)borate (Tp) precursor in aqueous acetonitrile in presence of diphenylphosphate ligands afford the synthesis of a U_6 cluster decorated with phosphate ligands (Scheme I-24). Each uranium

centres is coordinated to four bridging bidentate phosphate ligands to afford the cluster [$U_6(OH)_8(Ph_2PO_2)_{12}$] (Figure I-40). [202] While the authors describe the cluster with a $U_6(OH)_8$ core, thus containing four U(III) and two U(IV) centres, both the experimental conditions (in presence of water) and the structural parameters of the cluster core suggest that the cluster may actually contain the more common $U_6O_4(OH)_4$ core described above.

Scheme I-24 Synthesis of [$U_6(OH)_8(Ph_2PO_2)_{12}$]

$$UO_2(ac)_2 + 2\ TpVCl_2 + 6\ Ph_2POONa \xrightarrow[R.T.\ 12h]{MeCN/H_2O} [U_6O_4(OH)_4(Ph_2POO)_{12}]$$

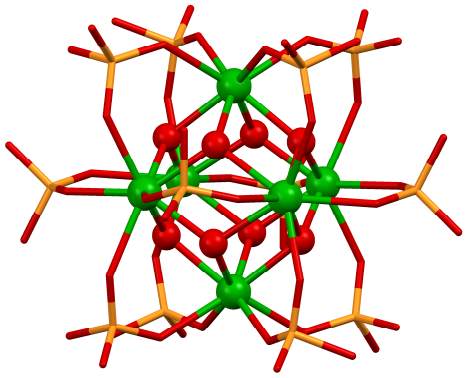

Figure I-40 Mercury view of the cluster [$U_6(OH)_8(Ph_2PO_2)_{12}$] (H atoms and phenyl groups were omitted for clarity, ligands are represented with pipes, P are represented in orange, O in red and U in green.).

However, the reaction described above had been carried out in aqueous acetonitrile and could result from the functionalization of the uranyl oxo but also from classical hydrolysis of low valent uranium species formed from the reduction of the uranyl(VI) complex.

Strict functionalization of uranyl oxo was achieved by the comproportionation reaction between the uranyl(VI) triflate precursor $UO_2(OTf)_2$ and the trivalent triflate uranium complex $U(OTf)_3$ in anhydrous conditions to afford the hexanuclear tetravalent uranium cluster [$U_6O_8(OTf)_8(py)_8$] (Figure I-41) [203]. The authors confirmed that the reaction occurs through the comproportionation reaction described Scheme I-25, since their attempts to synthesised [$U_6O_8(OTf)_8(py)_8$] through the reduction of $UO_2(OTf)_2$ with classical reductants failed and that $U(OTf)_4$ was released in the reaction solution.

Scheme I-25 Comproportionation reaction affording the hexanuclear cluster [$U_6O_8(OTf)_8(py)_8$]

$$8\ U(OTf)_3 + 4\ UO_2(OTf)_2 \xrightarrow{pyridine} [U_6O_8(OTf)_8(py)_8] + 6\ U(OTf)_4$$

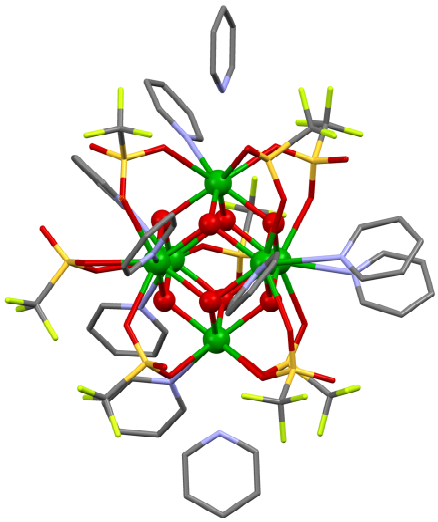

Figure I-41 Mercury view of the cluster $[U_6O_8(OTf)_8(py)_8]$ (H atoms were omitted for clarity. Ligands are represented with pipes, C are represented in grey, O in red, N in blue, F in light green, S in yellow and U in green.)

Similarly, the reaction of the reputedly very robust uranium(IV) bis-cyclooctatetraene (cot) complex with hexavalent precursors such as $UO_2(OTf)_2$ or $UO_2I_2(thf)_3$ affords the synthesis of U_6O_8 clusters decorated with triflate, cot and iodide ligands, depending on the reaction conditions described Scheme I-26. In these reactions, the reactivity is driven by the unique redox behaviour of the cot^{2-} ligand, that can deliver four electrons. These results provide a new synthetic route to the previously described $[U_6O_8(OTf)_8(py)_8]$ cluster and allowed the isolation of the cluster $[U_6O_8I_8(py)_{10}]$ only decorated with iodine ions (Figure I-42). Moreover, the reaction of $UO_2(OTf)_2$ with an excess of $U(cot)_2$ afforded the isolation of a cot decorated cluster $[U_6O_8(OTf)_6(cot)(py)_8]$ (Figure I-42).

Scheme I-26 Synthesis of $[U_6O_8I_8(py)_{10}]$ and $[U_6O_8(OTf)_8(py)_8]$

$$2\ U(cot)_2 + 4\ UO_2(OTf)_2 \xrightarrow{\text{pyridine}} [U_6O_8(OTf)_8(py)_8] + 4\ cot$$

$$2\ U(cot)_2 + 4\ UO_2I_2(thf)_3 \xrightarrow[-\ 12\ thf]{\text{pyridine}} [U_6O_8I_8(py)_{10}] + 4\ cot$$

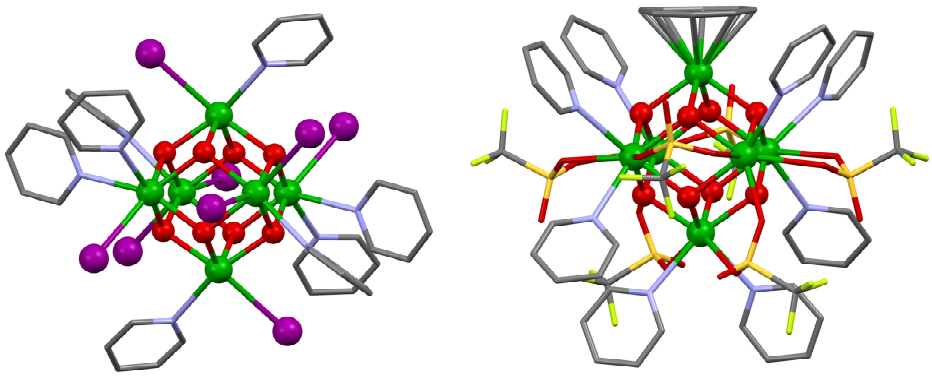

Figure I-42 Mercury views of the uranium clusters $[U_6O_8I_8(py)_{10}]$ (left) and $[U_6O_8(OTf)_6(cot)(py)_8]$ (right) (Co-crystallised solvent and H atoms were omitted for clarity. Ligands are represented with pipes, C are represented in grey, O in red, N in blue, F in light green, S in yellow, I in purple and U in green.)

Recently, Arnold et al. described a reaction combining the reduction and the oxo-silylation of a uranyl(VI) pacman complex. The reaction of the uranyl(VI) pacman complex with the uranyl(VI) silylamide salt $UO_2(N(SiMe_3)_2)_2$ resulted in the reduction of the uranyl(VI) moieties to uranium(V) ions and the silylation of the uranyl oxygens to afford a binuclear uranium(V) complex with a similar bis-μ-oxide core than observed for the pentavalent uranium complex $[\{((^{Ad}ArO)_3N)U\}_2(\mu_2\text{-}O)_2]$ previously described (Scheme I-27) [204]. The main difference between these two complexes results from the coordination of the silyloxide ligand in trans position of the same bridging oxo, affording the original butterfly shape complex $[\{(Me_3SiO)U(\mu_2\text{-}O)\}_2(Pcm)]$.

Scheme I-27 Synthesis of $[\{(Me_3SiO)U(\mu_2\text{-}O)\}_2(Pcm)]$

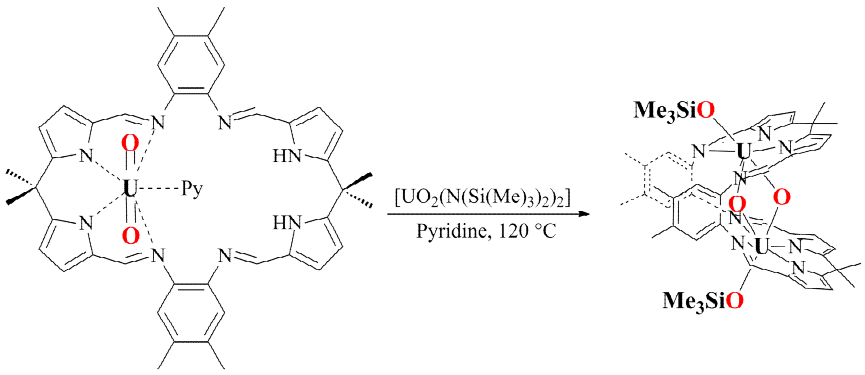

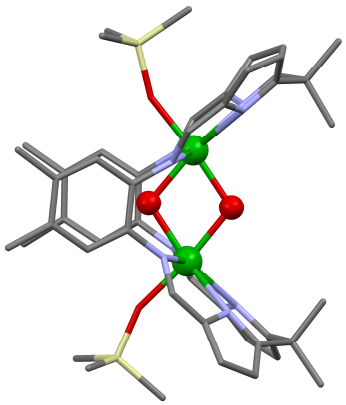

Figure I-43 Mercury view of the butterfly-shaped dimer [{$(Me_3SiO)U(\mu_2\text{-}O)\}_2$(Pcm)] (H atoms were omitted for clarity. Ligands are represented with pipes, C are represented in grey, O in red, N in blue, Si in light yellow and U in green.)

This complex presented an interesting magnetic behaviour, with a clear signature of antiferromagnetic coupling between the uranium centres, as observed with a maximum in the magnetic susceptibility curve peaking at a Néel temperature of 17 K. The magnetic susceptibility was fitted using calculated g parameters and afforded a large exchange interaction of -33 cm^{-1} (Figure I-44)

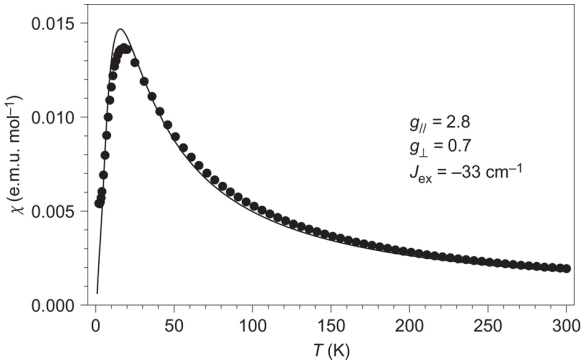

Figure I-44 Solid-state magnetic behaviour of [{$(Me_3SiO)U(\mu_2\text{-}O)\}_2$(Pcm)] between 2 and 300 K (Black circles are the experimentally measured temperature dependence of the magnetic susceptibility and the line shows the calculated fit to the data) [204]

I.4.2.2 Nitrogen bridged uranium cluster

In addition to the dinitrogen complexes cited and described in part I.3.4.1, a small number of polynuclear complexes assembled through nitrogen containing bridges have been isolated.

These complexes can be isolated through redox or non redox processes, and will be distinguished in this chapter by the type of bridging group between the uranium centres.

I.4.2.2.1 *Alkylamido/imino ligands*

Amines can be deprotonated by redox active uranium centres or by external reductants such as alkali metals or magnesium to give the anions R_2N^- or RNH^-, and these species can act as ligands to link uranium centres and form polymetallic assemblies.

Polynuclear uranium amino complexes have been first investigated by Edelstein et al. with the synthesis of the uranium(IV) diethylamino complex $[U(NEt_2)_4]_2$, presenting two bridging diethylamino ligands.[205] This complex allowed the synthesis of the tri and a tetranuclear uranium complexes $[U_3(CH_3NCH_2CH_2NCH_3)_6]$ (Figure I-45, left) and $[U_4(CH_3NCH_2CH_2NCH_3)_8]$ (Figure I-45, right) as the main and the minor products of the reaction of tetrakis(diethylamido)uranium(IV) with dimethylethylenediamine in pentane[206, 207]

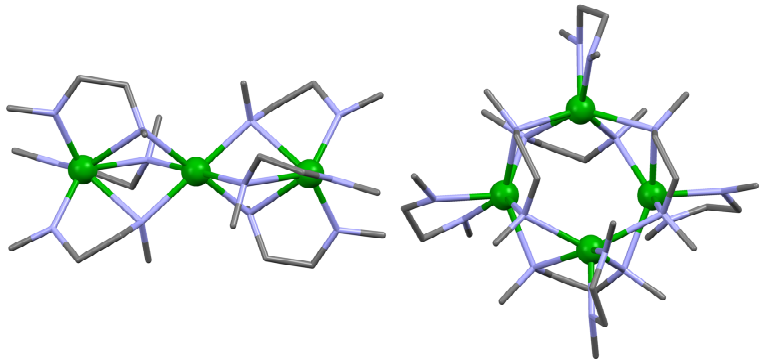

Figure I-45 Mercury views of the uranium trimer $[U_3(CH_3NCH_2CH_2NCH_3)_6]$ (left) and tetramer $[U_4(CH_3NCH_2CH_2NCH_3)_8]$ (right).(H atoms were omitted for clarity. Ligands are represented with pipes, C are represented in grey, N in blue and U in green.)

Three other dinuclear uranium amino complexes are referenced in the literature, with mesitylamine [208] or macrocyclic ligands such as calixpyrrole[209] or cyclam.[210]

Two interesting examples of trinuclear uranium clusters assembled by imino ligands possessing two distinct coordination sites separated by aromatic linkers have been isolated by Kiplinger et al. Aiming to isolate dinuclear assemblies from the reaction of tetracyanobenzene with the uranium(IV) alkyl complexes $[Cp^*_2UMe_2]$, the authors observed the cyclisation of one side of the tetracyanobenzene and the formation of a trinuclear triangular shaped uranium(IV) complex, as described in Scheme I-28. [211] The triangular complex $\{(Cp^*)_2UL''''\}_3$, presented in Figure I-46 (left), did not exhibit any significant metal-metal coupling. Conversely, the trimeric complex $[Cp^*_2U\{N{=}C(Bz))(tpy\text{-}UCp''''_2)\}]$, with three uranium centres connected by two asymmetric ligands with two distinct coordination sites, was isolated in the same group and shows evidence (electrochemistry) of electronic

communication within the assembly. This complex, the structure of which is presented in Figure I-46 (right), is constituted of a uranium(IV) centre connected to two ligands bearing terpyridine moieties, each of them containing a trivalent uranium centre. [212]

Scheme I-28 Uranium mediated cyclisation of tetracyanobenzene affording a self assembled uranium trimer

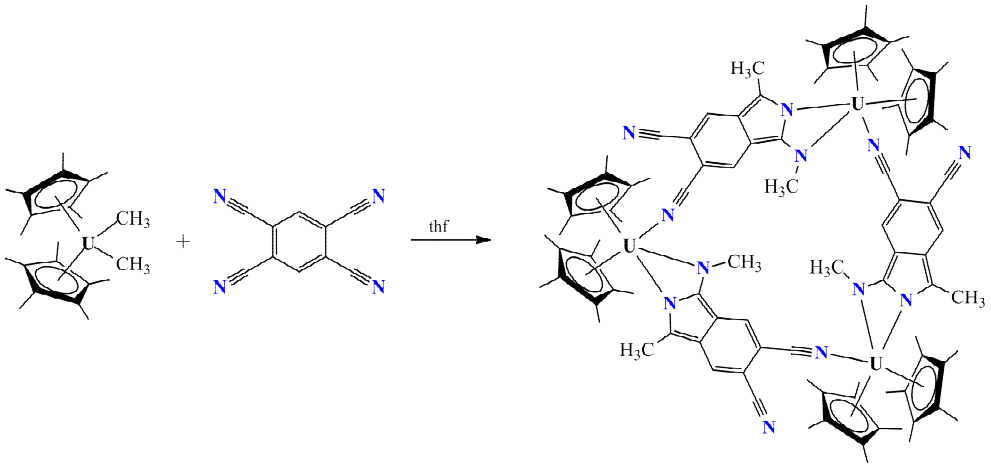

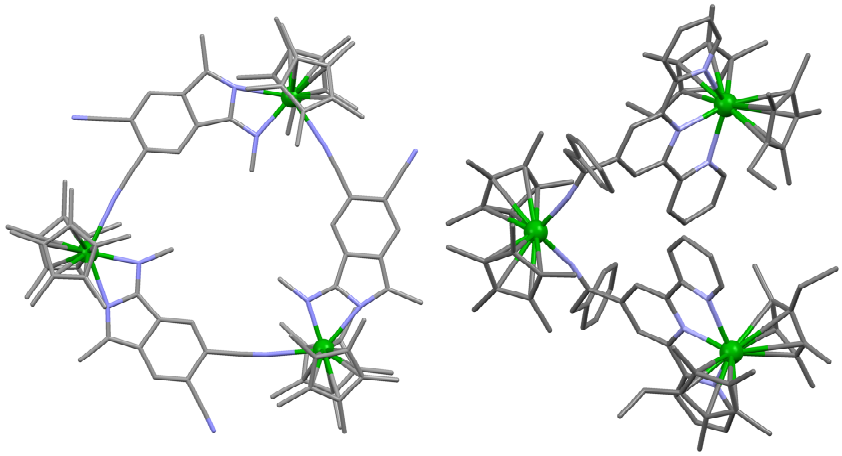

Figure I-46 Mercury views of the uranium trimers {(Cp*)$_2$UL””}$_3$ (left) and [Cp*$_2$U{N=C(Bz)}(tpy-UCp””$_2$)}], (right).(H atoms were omitted for clarity. Ligands are represented with pipes, C are represented in grey, N in blue and U in green.)

Recently, Diaconescu et al. isolated a tetranuclear square shaped uranium(IV) cluster from the reaction of an inverted μ-toluene sandwich diuranium complex with quinoxaline. This reaction affords the tetranuclear square shaped uranium(IV) complex with ferrocene diamide uranium(IV) vertices and reduced quinoxaline edges presented in Figure I-47. [213]

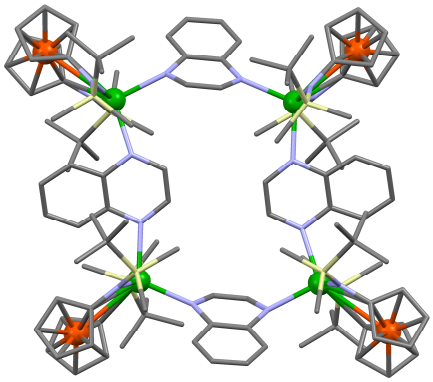

Figure I-47 Mercury view of the uranium(IV) tetramer isolated by Diaconescu et al. (H atoms were omitted for clarity. Ligands are represented with pipes, C are represented in grey, Fe in orange, N in blue, Si in light yellow and U in green.)

I.4.2.2.2 *Pyrazolate complexes*

Two polynuclear uranium complexes have been obtained using the 3,5-dimethylpyrazolate ligands. The reaction of potassium dimethylpyrazolate with UCl_4 afforded the synthesis of the binuclear complex $[U(Me_2Pz)_4]_2$ (Me_2Pz- = 3,5-dimethylpyrazolate). The structure of the dimer consists of two U(IV) centres, each coordinated in a pseudo trigonal bipyramidal geometry, connected through two bridging Me_2Pz^- ligands(Figure I-48, left). [214] When a similar reaction is carried out with uranium(III) in place of uranium(IV), uranium(III) reductively cleave Me_2Pz^-, leading to a series of three similar tetranuclear uranium(IV) clusters incorporating the ketimidopent-2-ene-2-imido ($kipi^{3-}$) ligands (Scheme I-29 and Figure I-48, right) [215]

Scheme I-29 Reduction of 3,5-dimethylpyrazolate

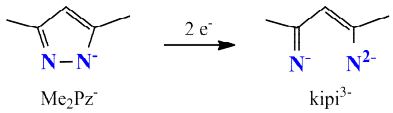

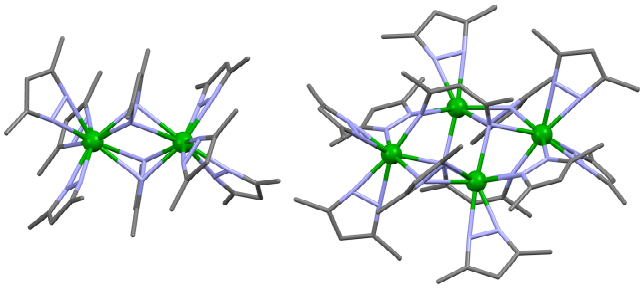

Figure I-48 Mercury views of the uranium assemblies $[U(Me_2Pz)_4]_2$ (left) and $[(Me_2Pz)_{10}U_4(kipi)_2]$ (right).(H atoms were omitted for clarity. Ligands are represented with pipes, C are represented in grey, N in blue and U in green.)

The authors used the dimeric $[U(Me_2Pz)_4]_2$ complex as a starting material for the synthesis of 3d-5f clusters via the insertion of (cyclam)MCl_2 complexes into the uranium(IV) 3,5-dimethylpyrazolate dimer to give linear, chloride-bridged heterotrimetallic clusters. Notably, a weak ferromagnetic coupling was observed within a linear U(IV)-Cl-Ni(II)-Cl-U(IV) linear cluster.[214]

I.4.2.2.3 *Azide ligands*

Azide ligands are well established in transition metal chemistry to bridge metal centres in end-to-end or end-on manner. However, only a few examples have been described with uranium centres. Two binuclear, one trinuclear and three similar octanuclear uranium clusters present end-to-end bridging azides[216], while only one hexanuclear cluster possess end-on bridging azides[217]. The last two examples also present nitride centres, and will be described in detail in the corresponding section.

The uranium(IV) binuclear end-to-end azide complexes have been isolated with the sterically hindered complexes $[(C_5H_4(SiMe_3)U]$ [218] and $[(({}^{tBu}ArO)_3tacn)U]$ [95] (Figure I-49). Evans and co-workers described the synthesis of an original trinuclear uranium(IV) complex with azides bridging the uranium centres along the edge of a triangle in a end-to-end fashion to afford the $[(C_5Me_5)_2UN_3(\mu_2\text{-}N_3)]_3$ complex (Figure I-49). [219]

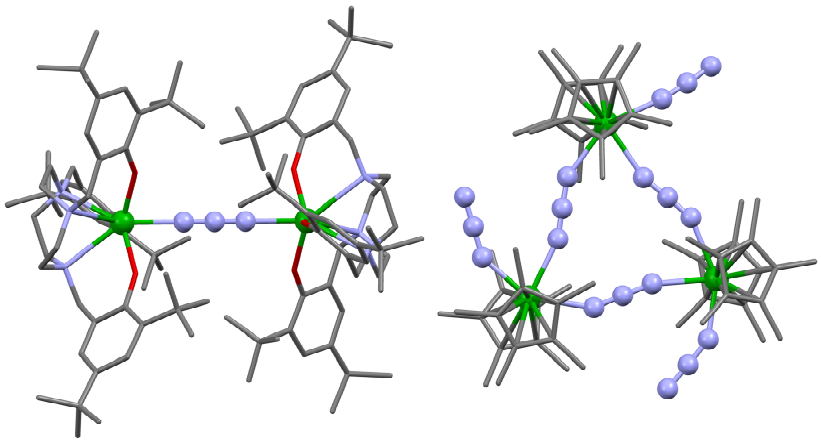

Figure I-49 Mercury views of the uranium assemblies $\{(\mu_2\text{-}N_3)[(({}^{tBu}ArO)_3tacn)U]_2\}$ (left) and $[(C_5Me_5)_2UN_3(\mu_2\text{-}N_3)]_3$ (right).(H atoms were omitted for clarity. Ligands are represented with pipes, C are represented in grey, N in blue and U in green.)

I.4.2.2.4 *Alkylimido ligands*

Double deprotonations of amine, reductive elimination of N_2 from organic azides, or reductive breaking of diazene compounds, afford anions of general formula RN^{2-}. Several polynuclear imido uranium complexes have been isolated, most of them being binuclear. Five

uranium(IV) complexes presenting the same $U_2(\mu_2\text{-NR})_2$ core have been isolated, through the valence comproportionation reaction of $[(MeC_5H_5)_3U(thf)]$ with $[(MeC_5H_5)_2UNR]$ [220], during the course of the four electrons reduction of azobenzene by the symmetrical toluene adduct $(\mu\text{-}C_7H_8)[U(N((CCH_3)(3,5\text{-}C_6H_3Me_2)))_3]_2$ [102] or during the reaction of RNH_2 with organoalkyl uranium(IV) complexes [221].

Larger assemblies, organised around μ_3 and μ_2 PhN^{2-} ligands, have been described by Ephritikhine et al., who isolated tetra and heptanuclear uranium(IV) clusters by reaction of UCl_4 with $\{PhNMg(thf)\}_6$ (Scheme I-30) [222, 223]. The crystal structures of the tetranuclear $[U_4(\mu_3\text{-NPh})_2(\mu_2\text{-NPh})_4Cl_4(py)_6]$ and the heptanuclear $[Mg(thf)_5][U_7(\mu_3\text{-NPh})_6(\mu_2\text{-NPh})_6Cl_6(thf)_6]$ clusters are presented in Figure I-50.

Scheme I-30 Synthesis of $[U_4(\mu_3\text{-NPh})_2(\mu_2\text{-NPh})_4Cl_4(py)_6]$ and $[Mg(thf)_5][U_7(\mu_3\text{-NPh})_6(\mu_2\text{-NPh})_6Cl_6(thf)_6]$

$$4\ UCl_4 + [\{PhNMg(thf)_3\}_6] \xrightarrow[100°C]{py} [U_4(\mu_3\text{-NPh})_2(\mu_2\text{-NPh})_4Cl_4(py)_6] + 8\ MgCl_2$$

$$7\ UCl_4 + 2\ [\{PhNMg(thf)_3\}_6] \xrightarrow[100°C]{py} [Mg(thf)_5][U_7(\mu_3\text{-NPh})_6(\mu_2\text{-NPh})_6Cl_6(thf)_6] + 11\ MgCl_2$$

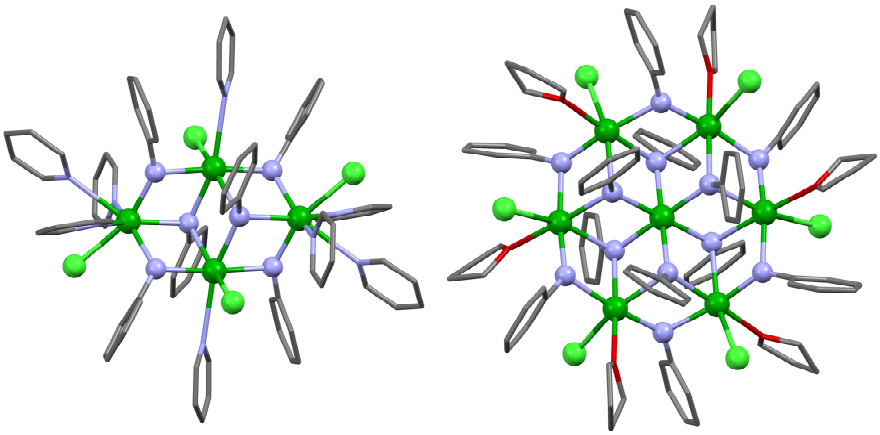

Figure I-50 Mercury views of the uranium assemblies $[U_4(\mu_3\text{-NPh})_2(\mu_2\text{-NPh})_4Cl_4(py)_6]$ (left) and $[U_7(\mu_3\text{-NPh})_6(\mu_2\text{-NPh})_6Cl_6(thf)_6]^{2-}$ (right).(H atoms were omitted for clarity. Ligands are represented with pipes, C are represented in grey, N in blue, O in red and U in green.)

Andersen et al. exploited the reactivity of trivalent uranium with organoazide to isolate uranium(V) organoimides through the oxidative elimination of N_2 first described by the same authors. [224] In order to obtain polynuclear complexes, the authors used diazidobenzene derivatives, thus affording the binuclear complexes of uranium $[Cp'_3U]_2[\mu\text{-}1,4\text{-}N_2C_6H_4]$ and $[Cp'_3U]_2[\mu\text{-}1,3\text{-}N_2C_6H_4]$ (Scheme I-31).[225]

Scheme I-31 Synthesis of bimetallic uranium imido dimers

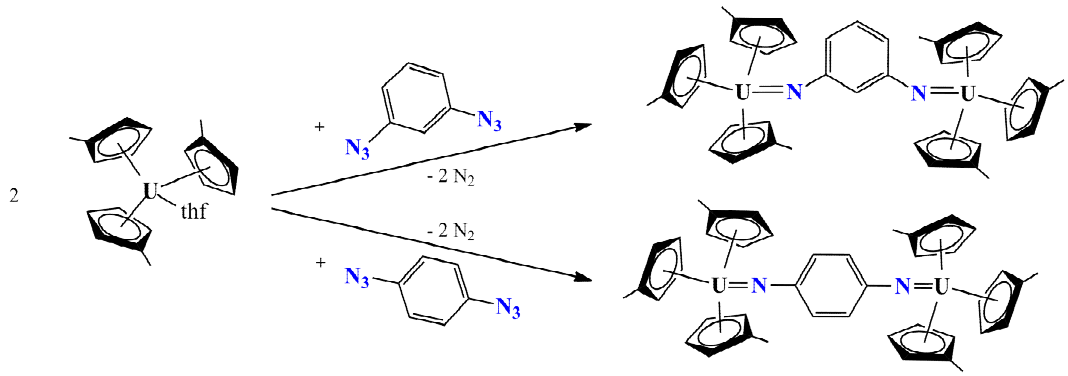

The magnetic properties of these two complexes were measured up to 5 K, and the authors observed that substitution position of the benzene spacer had a strong influence on the magnetic coupling properties. The two complexes present very similar magnetic susceptibility in the region 300K-40K, but below 40 K an antiferromagnetic coupling between the two U(V) ions with a maximum at 20 K was observed for the [μ-1,4-$N_2C_6H_4$] coupled complex while the [μ-1,3-$N_2C_6H_4$] coupled uranium(IV) ions behave as two independent paramagnets (Figure I-51).[225] The exchange constant J was estimated around -19 cm^{-1} by fitting the observed susceptibility considering that the bimetallic molecule could be considered as two monomeric U(V) complexes connected by the diimide moiety through which the exchange take place. The author proposed a superexchange pathway through the diimine ligand to rationalize this behaviour, as represented in Figure I-51.

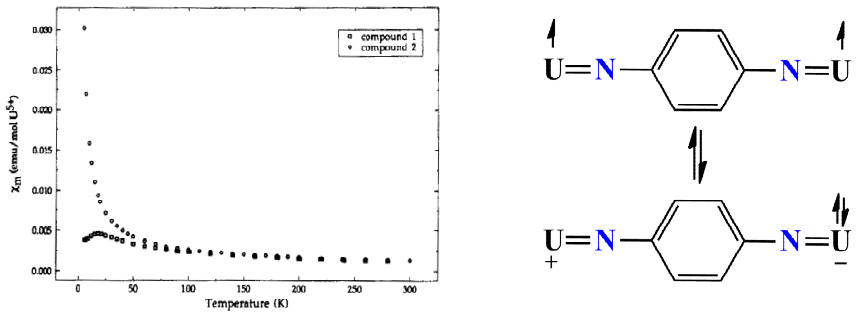

Figure I-51 Experimental magnetic susceptibility data of [Cp'$_3$U]$_2$[μ-1,4-$N_2C_6H_4$] (compound 1) and [Cp'$_3$U]$_2$[μ-1,3-$N_2C_6H_4$] (compound 2) as a function of temperature (left) and resonances structures illustrating the potential superexchange mechanism.

The reduction of the bis(imido) uranium(VI) ion, $[U(N^tBu)_2]^{2+}$ with the cyclopentadienyl anion afforded the uranyl(V) analogue $[U(N^tBu)_2]^+$ (Scheme I-32). This pentavalent uranium moiety self assemble into the bis(imido) uranium(V) dimeric complex [{U(N^{t}Bu)$_2$I(^{t}Bu$_2$bipy)}$_2$], which structure is presented in Figure I-52. [226] This dimer presents a binuclear diamond-shaped core analogous to the core of the dinuclear uranyl(V) complex

$[UO_2(dbm)_2K(18C6)]_2$ presented above, and also present a clear antiferromagnetic coupling between the uranium centres, with a maximum of the susceptibility measured at 13K.

Scheme I-32 Synthesis of $[\{U(N^tBu)_2I(^tBu_2bipy)\}_2]$

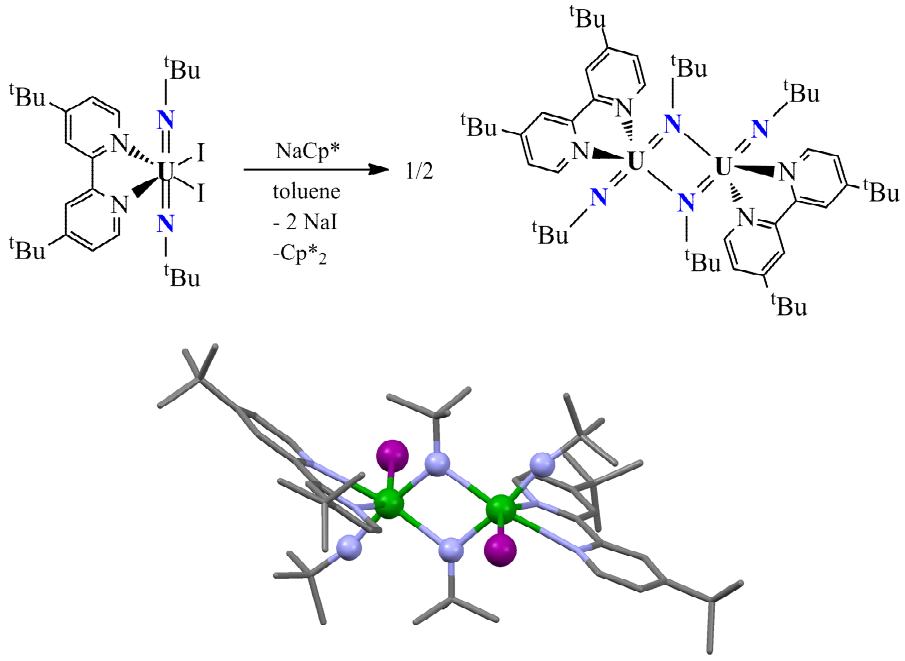

Figure I-52 Mercury view of the uranium dimer $[\{U(N^tBu)_2I(^tBu_2bipy)\}_2]$.(H atoms were omitted for clarity. Ligands are represented with pipes, C are represented in grey, N in blue, I in purple and U in green.)

Recently, the reduction of the uranium(IV) complex $[U(Ts^{Xy})(Cl)(thf)]$ (Ts^{Xy}=HC-$(SiMe_2NAr)_3$; Ar=3,5-$Me_2C_6H_3$) with KC_8 resulted in a reductive C-N bond activation of the ligand to afford a imido-bridged dimer presenting a rare example of ferromagnetic coupling between the two uranium centres[227] (Scheme I-33).

Scheme I-33 Synthesis of $[U\{HC(SiMe_2Ar)_2(SiMe_2\text{-}\mu\text{-}N)\}(m\text{-}\eta_1{:}\eta_1\text{-}Ar)U\text{-}(Ts^{Xy})]$

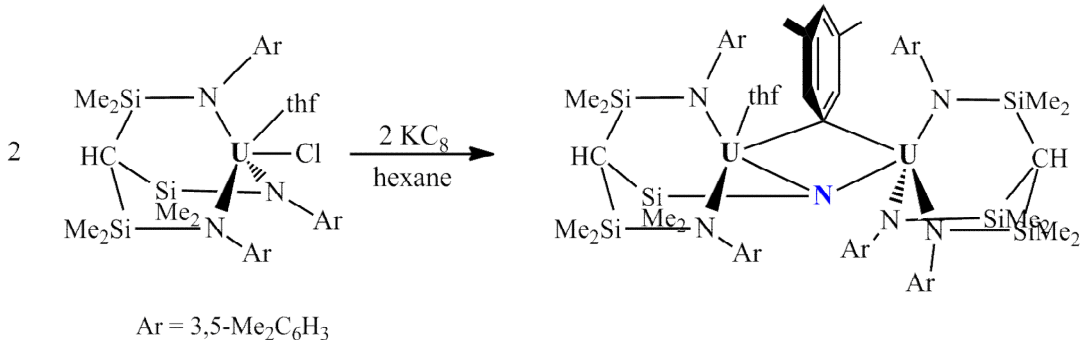

I.4.2.2.5 *Nitrido clusters*

The nitride ion, N^{3-}, is one of the strongest of π donors and affords strongly coupled polynuclear complexes. Moreover, the quest of soft synthesis of uranium nitrides, potentially used in future nuclear fuel, has initiated the synthesis of several polynuclear uranium complexes in the recent years. Nitride ions are known to bridge metal complexes in μ_2, μ_3 or μ_4 coordination modes, and uranium complexes illustrate these four types of bonding. With the exception of one example from dinitrogen reduction[88], all the syntheses of nitride uranium clusters used the reduction of azide precursors.

The reaction of the trivalent uranium complex $[U(N((CCH_3)(3,5\text{-}C_6H_3Me_2)))_3(thf)]$ with sodium or terbutylammonium azide yielded the μ_2-nitride bridged bimetallic uranium(IV) complex $\{(\mu_2\text{-}N)[U(N((CCH_3)(3,5\text{-}C_6H_3Me_2)))_3]_2\}^-$ (Scheme I-34). [228] This dimer can be quantitatively oxidized to form the analogous U(V)/U(IV) and U(V)/U(V) dimers. The structure of the mixed valent U(IV)/U(V) complex is represented in Figure I-53. In these dimers, the uranium centres are bridged in a linear fashion, while the analogous reaction of sodium azide on the trivalent uranium complex $[U(N(Si(Me)_3)_2)_3]$ afford a bent UNU moiety, represented in Figure I-53. [198] This uranium(IV) dimer can be oxidized with 1 equiv of Me_3NO to afford a *trans* oxo-nitrido $[O{=}U{=}N]^+$ moiety.

Scheme I-34 Synthesis and controlled oxidations of $\{(\mu_2\text{-}N)[U(N((CCH_3)(3,5\text{-}C_6H_3Me_2)))_3]_2Na\}$

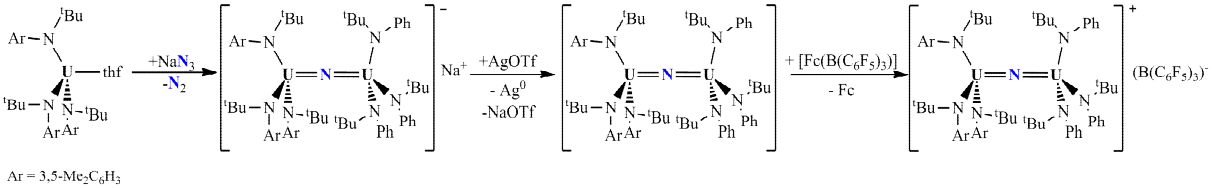

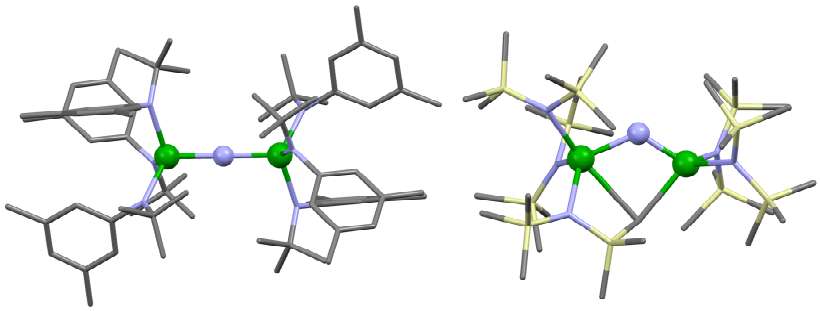

Figure I-53 Mercury views of the uranium nitride dimers $\{(\mu_2\text{-}N)[U(N((CCH_3)(3,5\text{-}C_6H_3Me_2)))_3]_2\}^-$ (left) and $[(N(Si(Me)_3)_2)_2U(\mu\text{-}N)(CH_2SiMe_2N(Si(Me)_3))U(N(Si(Me)_3)_2)_2]^-$ (right).(H atoms were omitted for clarity. Ligands are represented with pipes, C are represented in grey, N in blue, Si in light yellow and U in green.)

Linear μ_2-nitrides have also been observed in the large octanuclear clusters synthesised by Evans et al.[216] Three analogous clusters, with 24-membered uranium-nitrogen rings constituted of uranium(IV) centres alternatively bridged by linear μ_2-nitride and end-to-end azides were isolated by reaction of sodium azide with the uranium(III) organometallic complex $[Cp^*_2U][(\mu\text{-}Ph)_2BPh_2]$ (Scheme I-35 and Figure I-54)

Scheme I-35 Synthesis of $[Cp^*_2U(\mu_2\text{-}N)U(\mu_2\text{-}N_3)Cp^*_2]_4$

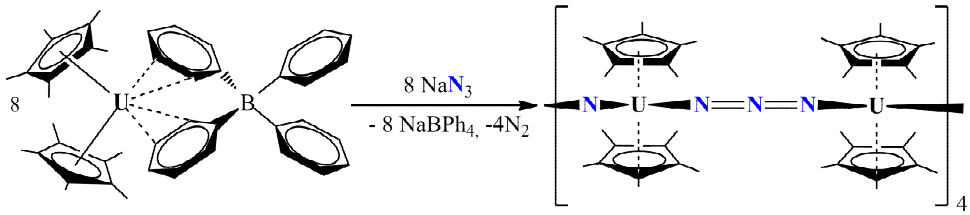

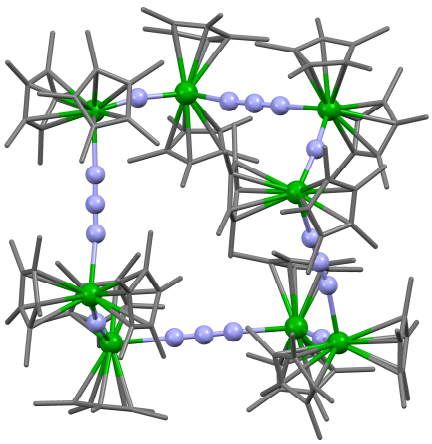

Figure I-54 Mercury view of the uranium octamer $[Cp^*_2U(\mu_2\text{-}N)U(\mu_2\text{-}N_3)Cp^*_2]_4$.(H atoms were omitted for clarity. Ligands are represented with pipes, C are represented in grey, N in blue and U in green.)

A μ_3-nitride uranium complex has been isolated by the reaction of the trivalent uranium complex $[Cp^*UI_2(thf)_3]$ with sodium azide (Scheme I-36). [219]The isolated trinuclear uranium cluster is isostructural to the μ_3-oxo uranium trimer $[(U(Cp^*)(\mu_2\text{-}I)_2]_3(\mu_3\text{-}O)$ isolated by Cloke et al.[200] and presented in section I.4.2.1.2.c. The identity of the nitride complex was confirmed by mass spectroscopy and labelling experiments. The second example of polynuclear uranium complex bearing two μ_3-nitride moieties[88], synthesised by Gambarotta et al., has been already described in section I.3.4.1.

Scheme I-36 Isolation of $[(U(Cp^*)(\mu_2\text{-}I)_2]_3(\mu_3\text{-}N)$

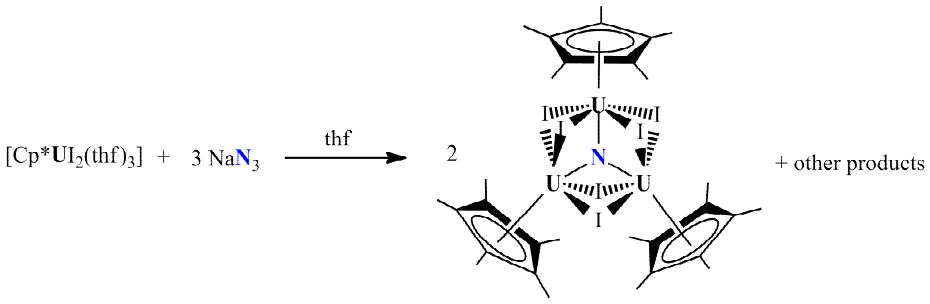

The unique polynuclear uranium μ_4-nitride complex has been isolated in our group through the use of a tetravalent uranium azide as nitrido nitrogen source which provided a very convenient route for the self-assembly of the tetranuclear azido/nitrido U(IV) cluster ($[U_4(\mu_4\text{-}N)(\mu\text{-}1,1\text{-}N_3)_8(CH_3CN)_8I_6][(Cs(CH_3CN)_3])_n$ (Scheme I-37). [217] In this cluster the μ_4-nitride group bridges four uranium centres placed at the edge of a tetrahedron. Eight end-on azide moiety bridge the uranium centres along the vertices of the tetrahedron defined by the four uranium centres, as highlighted in Figure I-1.

Scheme I-37 Synthesis of $([U_4(\mu_4\text{-}N)(\mu\text{-}1,1\text{-}N_3)_8(CH_3CN)_8I_6][(Cs(CH_3CN)_3])_n$

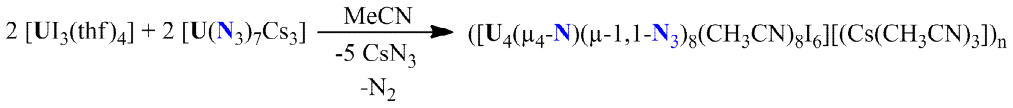

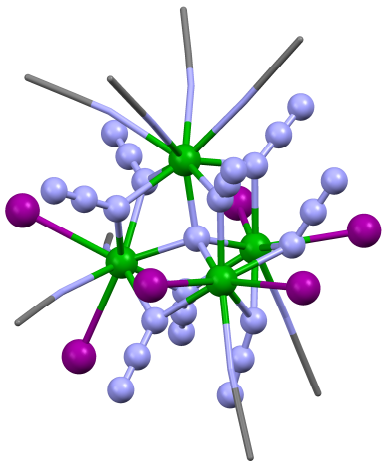

Figure I-55 Mercury view of the uranium μ_4-nitride cluster $[U_4(\mu_4\text{-}N)(\mu\text{-}1,1\text{-}N_3)_8(CH_3CN)_8I_6]^-$ (H atoms were omitted for clarity. Ligands are represented with pipes, C are represented in grey, N in blue, I in purple and U in green.)

It should be finally noticed that a terminal uranium nitride has been very recently isolated by Liddle et al. [229], achieving the quest of an isolated UN moiety.

I.4.2.3 Miscellaneous bridging units

In addition to the oxygen and nitrogen bridged polynuclear compounds presented above, several polynuclear complexes have been described in the literature with various bridging units. A vast majority of these polynuclear assemblies possess dimeric structures, with the exception of a few larger assemblies. These structures will not be described in detail in this work, but highlights the possible assemblies observed with uranium complexes.

Halogen bridged complexes have been widely observed in the literature, with more than 140 dimeric uranium complexes bridged by halogens structurally characterised[230-236] and one larger assembly constituted from a trinuclear complex organised around a μ_3-chloride[237].

Four uranium dimers have been structurally characterised with hydrides bridging moieties [238-241] and often present very interesting reactivities.

The structural diversity of chalcogenides bridged uranium complexes is larger, with, in addition to the sulphur[102, 195, 197, 242, 243] and selenide or telluride dimers[197, 244, 245], a few tri-[246-248] and tetranuclear tetrameric complexes[249, 250]. An original heptameric sulphur complex has also been isolated.[251]

Recently, several arene bridged uranium dimeric complexes presenting “inverted sandwich” cores have been isolated, some of them presenting interesting reactivity or magnetic properties.[102, 119, 213, 252-257]

I.5 Purpose and objectives of the project

Polynuclear actinide assemblies have strong implications in the understanding of actinide migration in the environment. Moreover, the study of the magnetic and reactivity properties of actinide complexes in the recent years has casted a glow on the unique properties of actinides for the design of magnetic materials or new reagents able to promote original reactivities.

Consequently, there is considerable interest in understanding the properties of these assemblies, especially because there are a less well understood class of actinide compounds that may have applications that extend beyond nuclear technologies. Thus, the detailed study of polynuclear actinide complexes necessitates the synthesis of well defined model complexes.

The coordination chemistry of actinides has historically been dominated by aqueous synthesis, which limited the isolation of well defined complexes. Albeit non aqueous chemistry of actinides has grown steadily in the last 30 years, only few controlled synthetic strategies have been developed in order to prepare polynuclear actinide complexes. The strong radioactivity of most of the actinides has also been a limiting factor for their broad study.

The objectives of this thesis work are the development of new synthetic strategies to prepare discrete high nuclearity polymetallic uranium clusters. These syntheses target the formation of polynuclear uranium complexes with potential magnetic properties, and necessitate the presence of f electrons, which implies using uranium in an oxidation state lower than +VI.

This goal will be pursued following two different but related methods, the synthesis of stable pentavalent uranyl clusters assembled by CCI and the development of controlled synthetic paths towards uranium oxo/hydroxo complexes.

As shown in the introduction, the chemistry of the labile uranyl(V) moiety in organic media, has significantly developed in the recent years. Notably, in our laboratory the first uranyl(V) starting material, $[(UO_2py_5)(KI_2py_2)]$ has been isolated. In addition, two polynuclear uranyl(V) assemblies connected via CCI have been obtained in our laboratory using this pentavalent uranium precursor, but these assemblies show limited stability and disproportionate over time. Therefore, the first goal of this work is the understanding of the factors ruling the formation and the stability of uranyl(V) CC assemblies. This target will be reached via a synthetic coordination chemistry approach. New uranyl(V) complexes will be synthesised using the pentavalent uranyl precursor with suitable organic ligands. Reactivity

studies, coupled with a detailed study of their physical properties will also be performed to identify the parameters controlling the stability of these assemblies. In particular, we will try to control the uranyl(V) clusters structure and properties through a fine tuning of the ligand and of the synthetic conditions. Our studies will be focused on simple tetradentate ligands leaving some coordinating vacancies in the equatorial plane of the uranyl ion to promote the CC assembly of large uranyl clusters. Finally, with the aim of designing polynuclear uranyl(V) assemblies with improved magnetic properties, the formation of heteronuclear complexes containing both uranyl(V) and transition metals will be explored.

The second objective of this thesis work, intended to extend the understanding of the formation of uranium(IV) oxo/hydroxo clusters, will be built on the foundations that were set in the team for the synthesis of uranium clusters. These synthetic routes exploit the controlled hydrolysis of trivalent uranium precursors in organic media, and have provided polynuclear uranium oxo/hydroxo clusters containing up to 12 uranium centres. However, the parameters ruling the clusters formations have been proven difficult to control.

Therefore, with the objective of a better understanding of the parameters directing the assembly formation, we will exploit the previously described trivalent uranium hydrolysis to isolate new uranium clusters, with a focus on the influence of the media characteristics (solvent, acidity, etc) on the cluster formation and topology. In particular, these controlled hydrolysis reactions will be carried out in presence of environmentally relevant ligands, in order to investigate their role in the formation of environmentally encountered nanoparticles.

Finally, new synthetic methods for the isolation of uranium oxo clusters will be investigated. These synthesis will be intended to explore the peculiar properties of uranyl(V) to build new polynuclear oxo architectures. As stated in the previous section, the bacterial induced formation of uranium oxo particles occur via a mechanism that involves uranyl(V) disproportionation. In an attempt to synthetically reproduce this behaviour, we will investigate the disproportionation reaction of uranyl(V) in presence of biologically relevant ligands.

The possibility of using uranyl(V) as an oxo donor group in the course of reactions with low valent uranium precursors will be investigated, in order to build a new synthetic path to uranium oxo clusters with original topologies. The magnetic properties of the new polynuclear uranium clusters isolated through these routes will be then investigated.

Polynuclear assemblies based on cation-cation interaction

CHAPTER II. Polynuclear assemblies based on cation-cation interaction

II.1 Objectives

The bibliographical overview given in the previous section highlighted the interest of uranyl(V) chemistry, and showed that the chemistry of uranyl(V) remains a highly challenging task.

The aim of our approach is to provide synthetic routes to the synthesis of polynuclear uranyl(V) CC complexes. During these syntheses, a special attention will be given on the parameters ruling the stability of such assemblies towards the disproportionation reaction. In particular, the access to stable polynuclear uranyl(V) clusters should allow a more detailed understanding of the parameters involved in the disproportionation of uranyl(V). Finally, the study of the magnetic properties of these complexes could provide insights on their electronic properties, and lead to the design of uranyl(V)-based single molecule magnets.

II.2 Synthesis of stable CC assemblies

II.2.1.1 Choice of the ligands

As seen in part I.4.1.2.2, partial ligand loss was observed during the course of the disproportionation of the CC assemblies formed in presence of the β-diketonate dibenzoylmethanate (dbm) ligand. In order to avoid decoordination of the ligand, we decided to focus our studies on polydentate ligands. Given the usual pentacoordination of uranyl in its equatorial plane, tetradentate ligands seem especially tailored for the design of uranyl(V) CC complexes. Indeed, such ligands would provide a sufficient chelate effect to avoid decoordination and would leave a coordination site available for the assembly of uranyl complexes through CCI. Schiff-base ligands seemed appropriate for this purpose, due to their well known ability to stabilize metal centres in various oxidation states. Moreover, this family of ligands is well suited for the stabilisation of pentavalent uranyl, as highlighted by the electrochemical studies from Ikeda [161, 162, 164, 258, 259] and the recent uranyl(V) mononuclear complexes isolated in our laboratory [175, 176].

II.2.1.2 Tetramers based on Schiff base ligand

II.2.1.2.1 *Synthesis of $[UO_2(salen)]_4[\mu_8\text{-}K]_2\}(K(18C6)py)_2$*

The reaction of the uranyl(V) polymer $[(UO_2py_5)(KI_2py_2)]_n$, **1**,[170] with $salenK_2$ in pyridine leads to the formation of the complex of pentavalent uranyl **2** as a violet powder which is insoluble in pyridine. However, dissolution of this powder in dmso indicates the formation of a uranyl(V) complex, as revealed by the presence of a characteristic absorption feature, very similar to the one observed by Ikeda for uranyl(V) salophen electrochemically generated in dmso [161]. The elemental analysis of **2** indicates the presence of a complex of general formula $[(UO_2)(salen)K(py)]\cdot 1.4KI$, which has most likely a solid state polymeric structure. While no crystal structure can be obtained from dmso solutions of **2,** the insoluble violet powder can be dissolved in pyridine by the addition of 18-crown-6 ether (18C6). The addition of *n*-hexane to the resulting pyridine solution afforded blue crystals of the tetrameric pentavalent uranyl complex $[UO_2(salen)]_4[\mu_8\text{-}K]_2\}(K(18C6)py)_2$, **3**, in which four uranyl(V) units are assembled by a T-shaped cation-cation interaction with two linear UO_2^+ groups arranged perpendicular to each other (Scheme II-1). Complex **3** can be reproducibly obtained in an overall 69% yield.

Scheme II-1. Synthesis of **3**

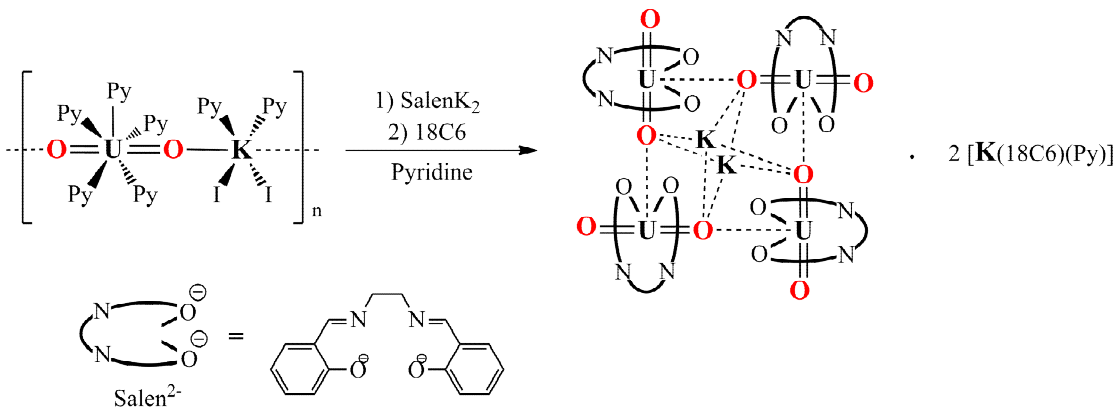

The crystal structure of **3** was determined by single crystal X-ray diffraction. A Mercury diagram of **3** is presented in Figure II-1. The structure of the complex consists of a centrosymmetric tetramer of UO_2^+ coordinated to each other in a monodentate fashion to form a square plane with two crystallographically inequivalent uranyl complexes. Two potassium ions located respectively above and below the plane of the UO_2^+ tetramer (at 2.14 Å) bind four different uranyl oxygens and four different salen oxygens. Two isolated 18C6 bound potassium cations are also found in the unit cell. The two crystallographically independent U

atoms in **3** are seven-coordinated with a slightly distorted pentagonal bipyramidal geometry by two trans oxo groups, two nitrogens and two oxygens from the salen^{2-} ligand and one bridging oxygen from the adjacent uranyl complex. Similarly to the dbm tetramer**,** the UO_2^+-UO_2^+ interaction results in a significant lengthening of the involved U=O bonds (average inner U=O bound = 1.933(5) Å) with respect to the unbound oxygens with a similar mean difference between the two U=O bonds of 0.1 Å. The overall metric parameters of the square core are also very similar in the complexes $[UO_2(dbm)_2]_2[\mu\text{-}K(py)_2]_2[\mu_8\text{-}K(py)]_2I_2{\cdot}py_2$.[168, 172] and **3** (mean U-U distance = 4.315(5) Å in the dbm tetramer and 4.31(3) in **3** ; mean U-O-U angle = 172.2(7)° in the dbm tetramer and 168.3(7) in **3**).

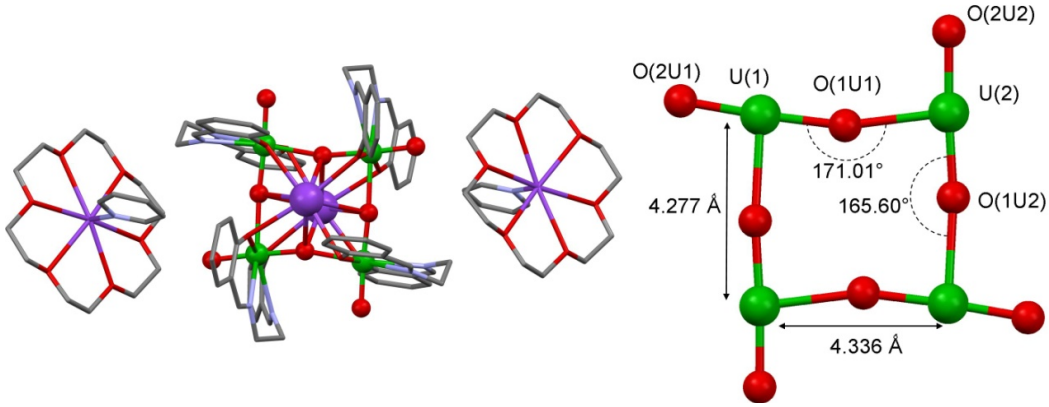

Figure II-1 Mercury view and core detailed of complex 3 with associated distances and angles. Hydrogen atoms, counterions and solvent molecules were omitted for clarity. Selected bonds lengths (Å) and angles (°): U(1)–O(1U1).1.841(5), U(1)–O(2U1) 1.936(5), U(1)–O(1U2) 2.421(5), U(2)–O(1U2) 1.929(5), U(2)–O(2U2) 1.840(5), U(2)–O(2U1) 2.374(5), O(1U1)–U(1)–O(2U1) 176.9(2), O(1U2)–U(2)–O(2U2) 176.2(2).

The ^{1}H NMR of pyridine solutions of **3** (Figure II-2) shows 7 signals in agreement with the presence of a tetrameric D_{4h} symmetric solution species.

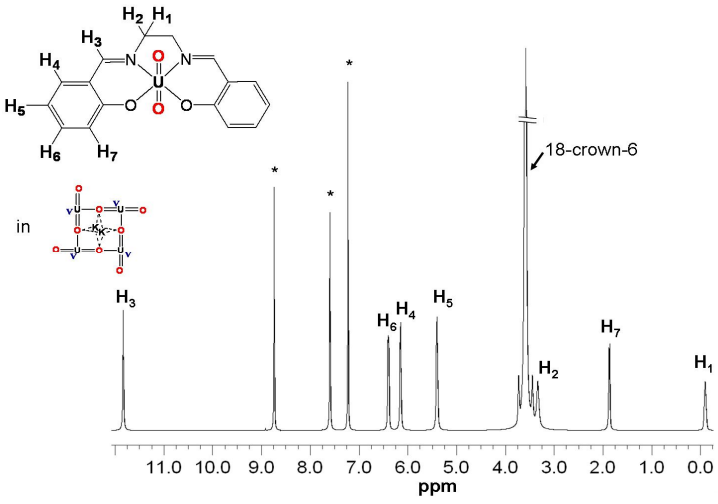

Figure II-2 ^{1}H NMR spectra of **3** in pyridine-d_5 (1.7mM) (Bruker Advance 500MHz, * : solvent residual peaks)

Pulsed-Field Gradient STimulated Echo (PFGSTE) diffusion NMR[260] was used to measure the diffusion coefficient (D) of **3** in 1 mM pyridine solutions using the U(VI) complex $[UO_2(salen)(py)]$ as an external reference. The D value measured for **3** ($D = 2.98(2)\ 10^{-10}\ m^2.s^{-1}$ in pyridine) suggests the presence of a tetrameric species in pyridine solution. The D value measured in dmso also confirmed that the polymetallic structure is also retained in dmso solution, contrary to what was observed for the dbm complex $[UO_2(dbm)_2]_2[\mu\text{-}K(py)_2]_2[\mu_8\text{-}K(py)]_2I_2{\cdot}py_2$.[168, 172] which is immediately disrupted in dmso to form a stable monomeric complex. This suggests that in complex **3** the mutual coordination of the uranyl groups is stronger than in the dbm tetramer and that dmso cannot effectively compete for the coordination of the UO_2^+ ion.

Table II-1 Diffusion coefficient values of **3** and **4,** and estimated spherical radii.

Solvent	Compound	D [$m^2.s^{-1}$]	r_{sph} [Å]$_{exp}$	r_{sph} [Å] (evaluated from crystal structure)
dmso η=1.987 mPa.s (298K)	**3**	$1.00(7)\ 10^{-10}$	10.8	7.9 for $\{[UO_2(salen)]_2[\mu_8\text{-}K]\}_2^{2-}$
Pyridine η=0.879 mPa.s (298K)	**4**	$5.68(8)\ 10^{-10}$	4.3	4.6 for $[UO_2(salen)(py)]$
	3	$2.98(2)\ 10^{-10}$	8.3	7.9 for $\{[UO_2(salen)]_2[\mu_8\text{-}K]\}_2^{2-}$

ESI/MS experiments (m/z = 1111.4, corresponding to the $[UO_2(salen)]_2[\mu_8\text{-}K]_2^{2-}$, Figure II-3) indicate that complex **3** retains its tetrameric form also in gas phase, highlighting the strength of the interaction within the tetrameric core.

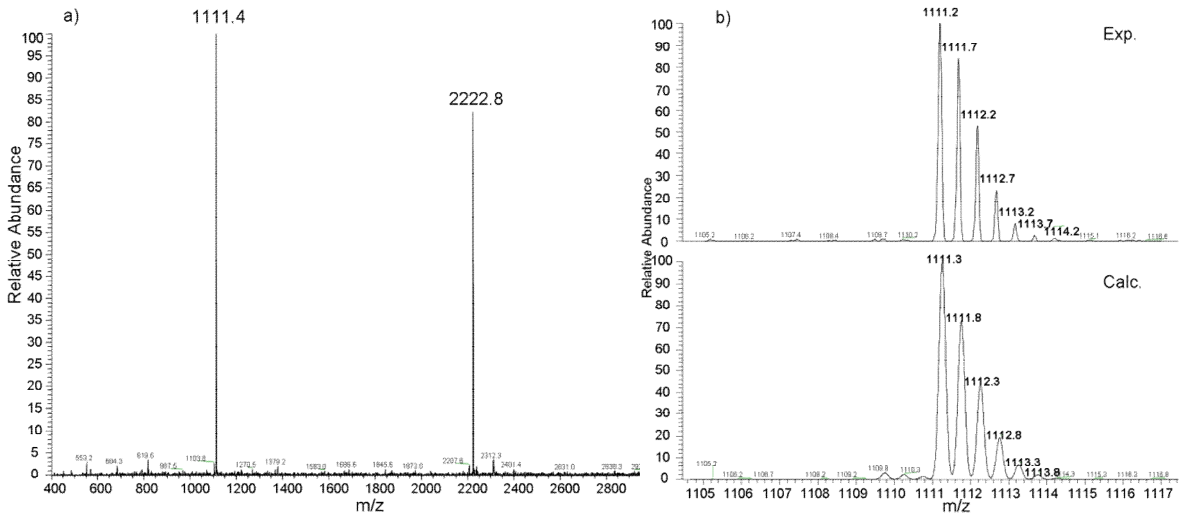

Figure II-3 ESI/MS spectra of **3** in pyridine/acetonitrile 1:3 (a), and (b) zoom on the molecular peak compared with the theoretical isotopic profile calculated for $\{[UO_2(salen)]_2[\mu_8\text{-}K]\}_2^{2-}$. The peak at 1111.4 corresponds to the double charged tetramer $\{[UO_2(salen)]_2\ [\mu_8\text{-}K]\}_2^{2-}$. The one at 2222.8 is attributed to the single charge tetramer resulting of the oxidation of one uranyl moiety in the apparatus and corresponds to the mixed valent $\{[UO_2(salen)]_2\ [\mu_8\text{-}K]\}_2^{-}$.

As indicated previously, the reaction of $[(UO_2py_5)(KI_2py_2)]_n$ with two equivalents of dbmK results in the disproportionation of the resulting pentavalent cation-cation intermediate.[261] In contrast, the salen ligand yields a cation-cation complex of pentavalent uranyl that shows a remarkable stability in organic solvents with respect to the disproportionation reaction. This highlights that small electronic/steric effects can play an important role on the stability of pentavalent uranyl cation-cation species. Moreover complex **3** shows a remarkable stability also in the presence of controlled amounts of added water (5-25 equivalents), while water addition accelerates significantly the rate of decomposition of the dbm tetramer.

Cyclic voltammetry studies of complex **3** were performed in pyridine (Figure II-4). Two consecutive redox processes could be identified. Firstly complex **3** undergoes a reversible (Figure II-4, insert) one-electron oxidation at $E_{1/2}$ = -1.51 V (*vs.* Fc^+/Fc couple) which does not involve a rearrangement of the tetrameric structure. At higher potential the irreversible three electron oxidation of the mono-oxidized tetramer occurs to produce the monomeric uranyl(VI) complex **4** which can be reversibly reduced to the monomeric pentavalent form ($E_{1/2}$ = -1.68 V *vs.* Fc^+/Fc, Wave d). These results encouraged us to find synthetic methods to selectively produce the corresponding mixed-valent complex.

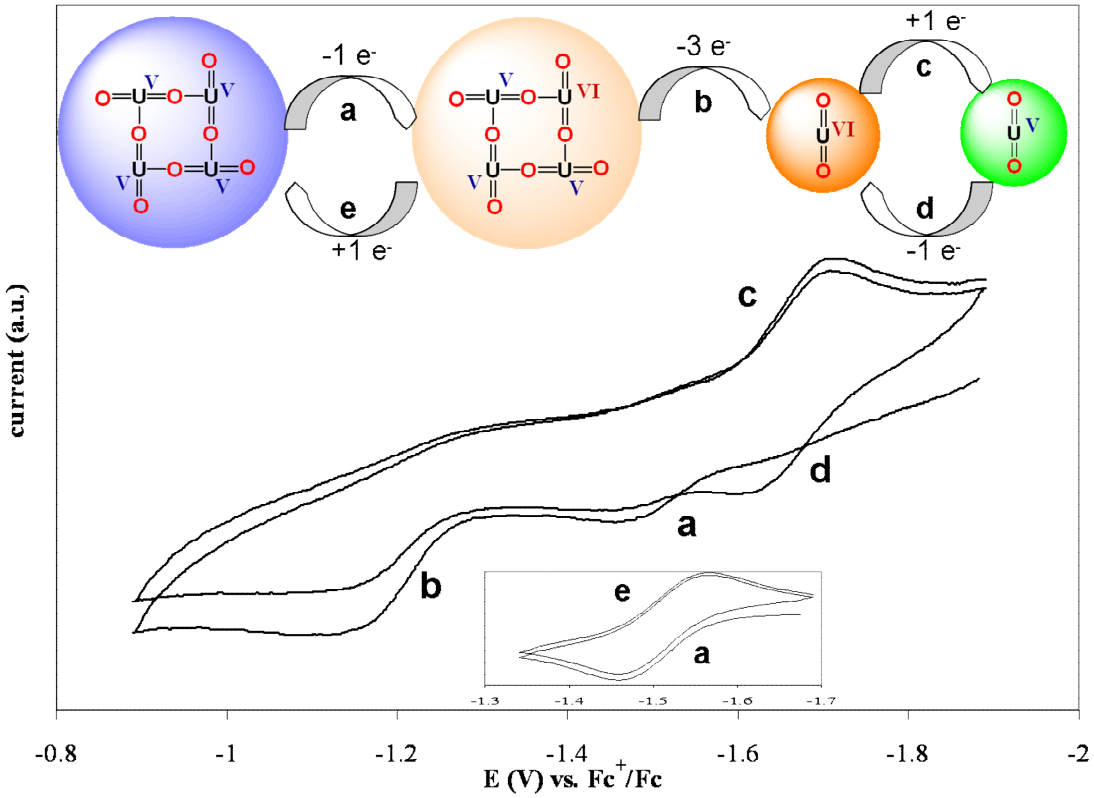

Figure II-4 Room temperature cyclic voltamogramm at 100mV/s for **3** in pyridine (0.1 M $[NBu_4][PF_6]$ as supporting electrolyte). (Insert: cyclic voltamogramm at 100mV/s centred at -1.51 V *vs.* Fc^+/Fc)

II.2.1.2.2 *Synthesis of {[UO₂(salen)μ-K(18C6)][UO₂(salen)]₃}[μ₈-K]₂*

Accordingly the reaction of 0.75 equivalent of **3** with 1 equivalent of $[U^{VI}O_2(salen)(py)]$ **4** allows the selective synthesis of the first uranyl(VI)/uranyl(V) mixed-valent cation-cation complex, $\{[UO_2(salen)\mu\text{-}K(18C6)][UO_2(salen)]_3\}[\mu_8\text{-}K]_2$, **5**. The crystal structure of **5** was determined by single crystal X-ray diffraction. A Mercury view of **5** is presented in Figure II-5. Similarly to the structure of **3,** the crystal structure of **5** presents a tetrameric unit consisting of uranyl moieties coordinated to each other to form a square plane capped by two bridging potassium ions. However in this case the four uranyl complexes are crystallographically non-equivalent as a result of the presence of a K(18C6) cation bound to the uranyl oxygen of one of the four uranyl complexes. Moreover, as clearly shown in Figure II-5, the smaller values of the U=O distances (1.804(12) and 1.862(14) Å) found for U1 with respect to the other uranyl groups distances (1.833(12)-2.022(11) Å, 1.797(14)-1.941(12) Å and 1.863(13)-1.964(12) Å for U4,U2 and U3 respectively) suggest that the valence is localised, with U1 identified as a U(VI). Very similar values of the U^{VI}=O distances were found in extended frameworks presenting UO_2^{2+}…UO_2^{2+} cation-cation interactions.[262, 263]

The replacement of one UO_2^+ by a UO_2^{2+} results in significant differences in the metric parameters of the tetranuclear core which is less distorted in **5** than in **3.** The bond valence sum analysis, performed using the empirical expression and constants proposed by Brown,[264] are in agreement with the presence of three pentavalent uranium and one localised hexavalent uranium in **5**.

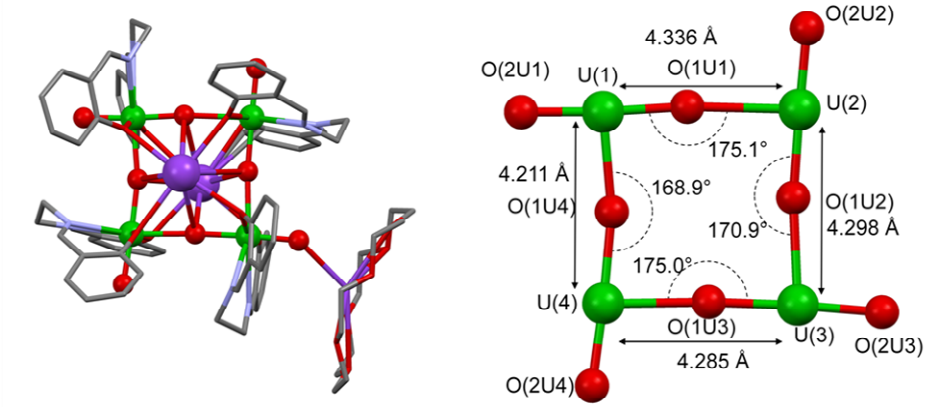

Figure II-5 Mercury view and core detailed of complex **5** with associated distances and angles. Hydrogen atoms, counterions and solvent molecules were omitted for clarity. Selected bonds lengths (Å) and angles (°): U(1)–O(1U1) 1.862(14), U(1)–O(2U1) 1.804(12), U(1)–O(1U4) 2.208(11), U(2)–O(1U2) 1.941(12), U(2)–O(2U2) 1.797(14), U(2)–O(1U1) 2.474(14), U(3)–O(1U3) 1.964(12), U(3)–O(2U3) 1.863(13), U(3)–O(1U2) 2.369(12), U(4)–O(1U4) 2.022(11), U(4)–O(2U4) 1.833(11), U(4)–O(1U3) 2.324(12).

The complex **5** is selectively obtained as a pure crystalline solid. However, when this solid is dissolved in pyridine, it quickly undergoes a rearrangement to yield a mixture of complexes **5**, **4** and **3**. The mixed-valent tetrameric compound **5** can also be obtained by chemical oxidation of **3** with CuI. In turn, the reduction of **5** with one equivalent of Cp^*_2Co yields **3**, therefore indicating that the oxidation process is reversible. Complex **5** is the only mixed-valent complex isolated or identified in the electrochemical or chemical oxidation processes. Similarly, **5** is the only mixed-valent species obtained from the reaction of **3** with **4** independently of the stoichiometric ratio used, confirming that three U(V) species and 1 U(VI) species self-assemble selectively. The presence of mixed-valent U(V)/U(VI) systems has been reported in few naturally occurring oxide minerals[265] and in rare examples of oxide compounds obtained under hydrothermal conditions.[266-268] However none of these systems contains pentavalent uranyl, while the first example of mixed-valent Np(V)/Np(VI) cation-cation complex has been only very recently isolated.[152] Moreover, this selective synthesis of the first mixed-valent $UO_2^+ \ldots UO_2^{2+}$ molecular complex provides a rare example of functionalization of the U^{VI}=O group.[177, 269]

This observation of a stable cation-cation complex of pentavalent uranyl suggests that such polymetallic species can be stabilized by an appropriate choice of conditions and ligands. These results highlighted that cation-cation interaction is a convenient route for the expansion of uranium supramolecular chemistry. With the aim of gaining some insight on the parameters leading to stable cation-cation complexes *versus* disproportionation products, we decided to investigate the reaction of pentavalent uranyl with different Schiff base ligands possessing different geometric and electronic properties.

II.2.1.2.3 ***Synthesis of {[UO_2(acacen)]$_4$(μ_8-K)$_2$][K(18C6)]$_2$} 2py***

The former example provides evidence that fully stable polymetallic assemblies of pentavalent uranyl can be prepared in the presence of tetradentate Schiff base ligands. In order to understand the molecular parameters controlling the stability and reactivity of complexes of pentavalent uranyl, the reaction of UO_2^+ with Schiff base ligands presenting different geometric and electronic characteristics was investigated, through the reaction with the more flexible acacen ligand (H_2acacen = *N*,*N*′-ethylene-bis-(acetylacetoneimine)) and the more aromatic salophen (H_2salophen = *N*,*N*′-phenylene-bis-(salicylideneimine)) and dophen (H_2dophen = 2,9-bis(2-hydroxyphenyl)-1,10-phenanthroline)) ligands.

Proton NMR studies in deuterated pyridine show that the reaction of **1** with the Schiff base salt acacenK_2 yields a uranyl(V) compound which is stable for more than 30 days under argon atmosphere. However, due to its high solubility in pyridine, isolation of this compound in a pure form proved difficult. Nevertheless, the tetrameric pentavalent uranyl complexes {[UO_2(acacen)]$_4$[μ_8-K]$_2$[K(18C6)(py)]$_2$}, **6** and {[UO_2(acacen)]$_4$[μ_8-K] } ·2[K(222)(py)], **7**, can be prepared analytically pure in 34% and 53% yield from the reaction of **1** with acacenK_2 in pyridine followed by addition of 18C6 or of [2,2,2] cryptand ([222]) respectively (Scheme 1). It should be noted that higher yield can be obtained when the diffusion time of the counter solvent is increased, which however results in contamination of the final product with co-crystallized potassium salts.

Scheme II-2 Reaction of **1** with K_2acacen to yield **6** and **7**.

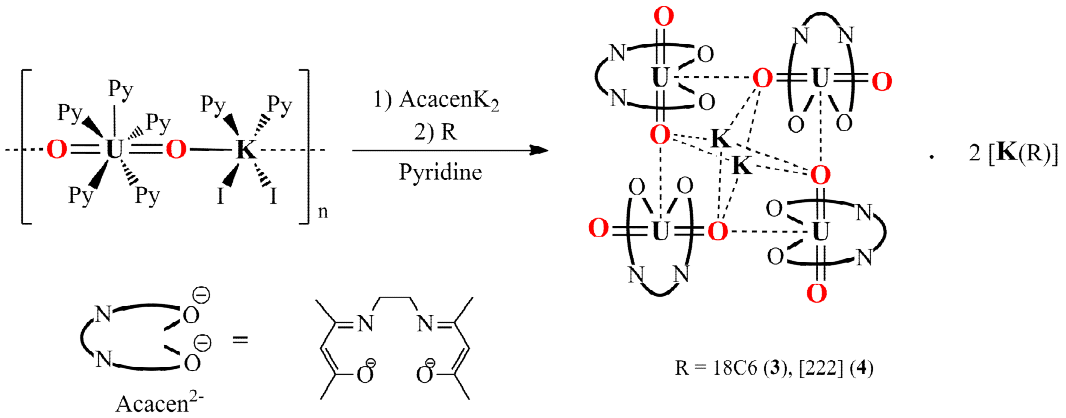

X-Ray quality crystals of **6** and **7** were obtained by slow diffusion of iPr$_2$O into the resulting pyridine solution. Mercury diagram of the complexes **6** and **7** are presented Figure II-6. The structure of the tetrameric cores are similar to the one previously observed in the reaction of uranyl(V) polymer with salen ligand, **3**, consisting in a centrosymmetric tetramer of UO_2^+ coordinated to each other in a monodentate fashion to form a square plane with two crystallographically non-equivalent uranyl complexes with two symmetry related potassium ions found respectively above and below the plane of the UO_2^+ tetrameric core (at 2.08 Å in **6** 2.13 Å in **7**, close to the 2.14 Å distance observed for **3**). The charge of this tetrameric core is balanced by the presence of two additional potassium ions found as $((18C6)K)^+$ and $([222]K)^+$ adducts in the unit cells, the main difference arising from the fact that in **6** the bulky $((18C6)K)^+$ ions are involved in a cation-cation interaction with two different uranyl oxygens located at the opposite sides of the tetramer while in **7** the two $([222]K)^+$ are found isolated in the cell. This implies that the square core defined by the four uranyl moieties appear more symmetric in **7** than in **6 .** The U-U distances (4.307(1) and 4.336(1) Å for **6** , and 4.303(1) and 4.310(1) Å for **7**) are very similar to those found in the $[UO_2(salen)]_4[\mu_8\text{-}K]_2^{2-}$ (4.3359(4) and 4.2766(4) Å) anion. The mean values of the K-O_{yl} (2.93(8) Å for **6** and 2.99(11) Å for **7**) and of the K-O_{acacen} distances (2.70(2) Å for **6** and 2. 71(3) Å for **7**) are close for the two complexes and are also very similar to the respective K-O_{yl} and K-O_{salen} distances (2.99(18) Å and 2.70(4) Å) observed in **3**. The two crystallographically independent U atoms in **6** and **7** are seven-coordinated, with slightly distorted pentagonal bipyramidal geometry, by two *trans* oxo groups, two nitrogens and two oxygens from the acacen ligand and one bridging oxygen from the adjacent uranyl complex. As observed for the previously salen tetramer **3** the $UO_2^{+\cdots}UO_2^+$ interaction results in a significant lengthening of the U=O bond distance for the uranyl oxygens involved in this interaction with a similar mean difference between the two

U=O bonds of about 0.1 Å in **6** and **7**. It should be noted that while the salen coordination in the tetramer **3** is almost planar, the acacen ligands adopt a so-called "boat" conformation [270, 271] in both **6** and **7**.

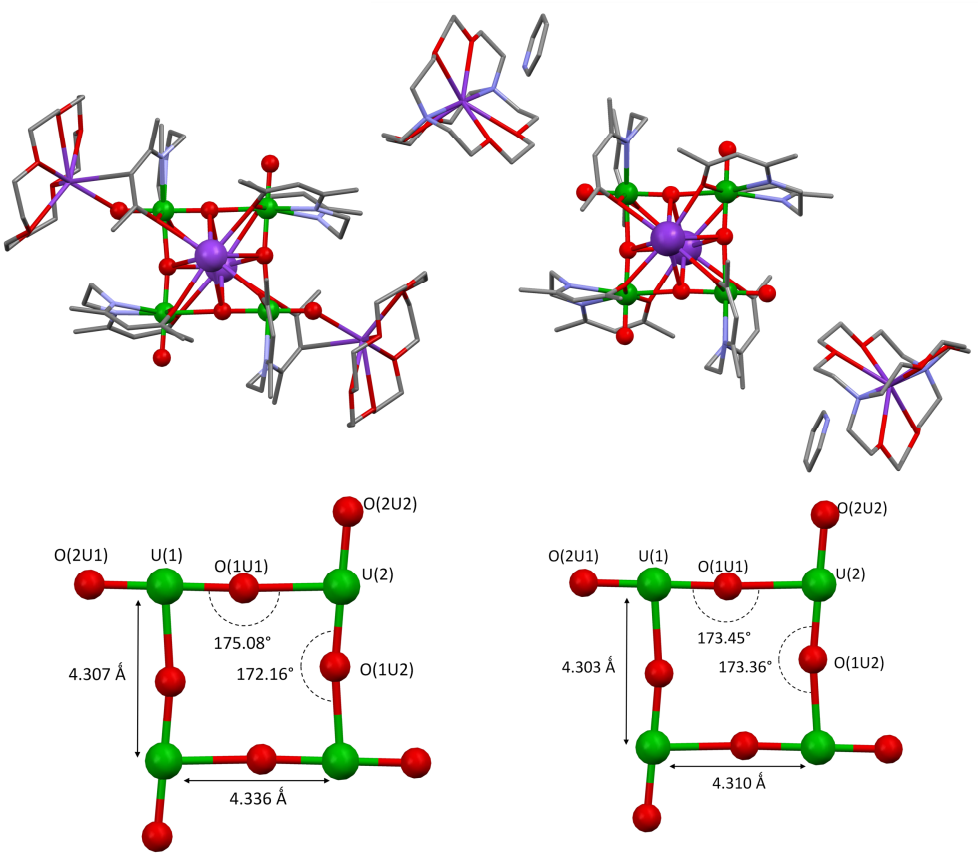

Figure II-6 Mercury diagrams of the complexes **6** and **7** (top, left and right) and metric comparison between the tetrameric core of complexes **6** and **7** (bottom, left and right), showing the interacting UO_2^+/UO_2^+ with associated distances and angles. The structures are represented along the axis formed by the two potassium ions and perpendicular to the plane of the uranium atoms (H were omitted for clarity, C are represented in grey, O in red, K in purple, N in blue and U in green)

Proton NMR studies in pyridine show that **6** and **7** are stable with respect to the disproportionation reaction over 30 days. PFGSTE diffusion NMR (D= 2.94(6) 10^{-10} $m^2.s^{-1}$ in pyridine, to be compared to the monomeric uranyl(VI) complex [(UO_2)(salen) (py)] **4** used as external reference, Table II-2) suggests the presence of a tetrameric species in pyridine solution similarly to what already found for **3** and for the dibenzoylmethanate tetramer.

Table II-2 Diffusion coefficient values of **3, 7** and **4** and estimated spherical radii.

Solvent	Compound	D [m².s^{-1}]	r_{sph} [Å]$_{exp}$	r_{sph} [Å] (evaluated from crystal structure)
Pyridine η=0.879 mPa.s (298K)	**3**	2.98(2) 10^{-10}	8.4	7.9 for $\{[UO_2(salen)]_4[\mu_8\text{-}K]_2\}^{2-}$
	7	2.94(6) 10^{-10}	8.4	7.2 for $\{[UO_2(acacen)]_4[\mu_8\text{-}K]_2\}^{2-}$
	4	5.40(1) 10^{-10}	4.6	4.8 for $[UO_2(salen)(py)]$

ESI/MS studies also point to the presence of a tetramer in pyridine solution (m/z = 1023.2, corresponding to the $[UO_2(acacen)]_2[\mu_8\text{-}K]_2^{2-}$ moiety, Figure II-7). These results show that the coordination properties of the acacen^{2-} ligand are very similar to those of the salen^{2-} in the reaction with the pentavalent uranyl iodide polymer **1.** Moreover the final tetrameric complexes are stable with respect to the disproportionation reaction similarly to what found for the salen tetramer.

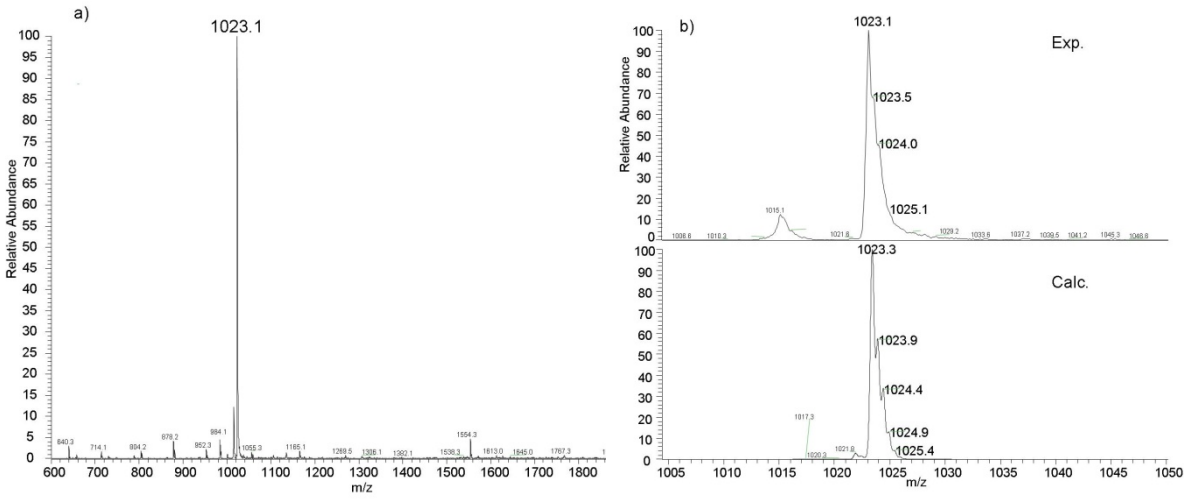

Figure II-7 ESI/MS spectra of complex **7** pyridine/acetonitrile 1:3 (a), and (b) zoom on the molecular peak compared with the theoretical isotopic profile calculated for $\{[UO_2(acacen)]_2[\mu_8\text{-}K]\}_2^{2-}$.

II.2.1.2.4 *Synthesis of {[UO_2(salophen)]$_4$[μ_8-K]$_2$[μ_5-KI]$_2$[(K(18C6)]} 2[K(18C6)(thf)$_2$]·2I*

In contrast, the reaction of the fully aromatic analogue of the salen^{2-} ligand, salophen^{2-} with the uranyl(V) polymer **1** in pyridine has a very different outcome. Proton NMR studies show that this reaction leads rapidly to the formation of a complicated mixture of disproportionation products (Figure II-8). We were able to identify the presence of the NMR signals arising from the previously reported U(VI) and U(IV) complexes [UO_2(salophen)(py)] [162] and [U(salophen)$_2$] which were independently prepared. Several other decomposition products remain unidentified.

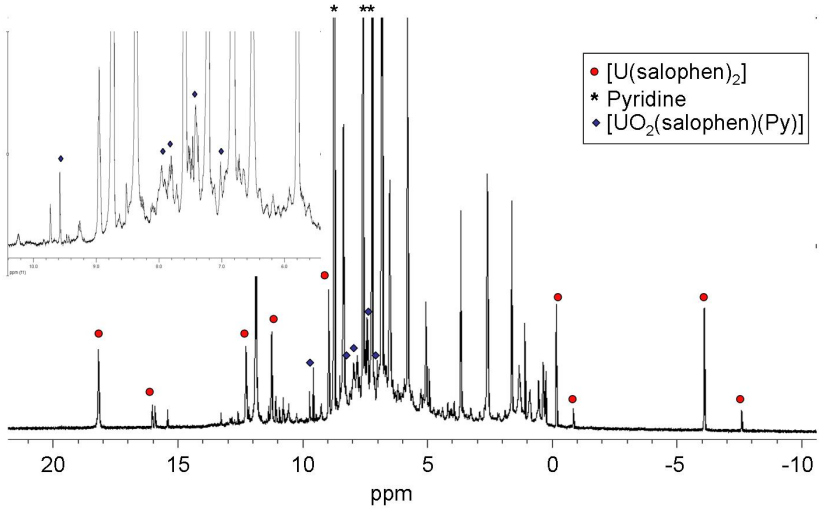

Figure II-8 ^{1}H NMR spectrum of reaction mixture ([(UO_2py_5)(KI_2py_2)]$_n$ + salophenK_2) after 3 hours

The observed difference in reactivity with respect to the disproportionation reaction between the salophen system and the salen tetramer is quite surprising considering the similarity of these two ligands. Indeed, previous DFT studies on mononuclear pentavalent uranyl complexes of salen and salophen ligands[272] had suggested the presence of a similar electronic structure and stability for the two monomeric systems, indicating that the main difference in the stability of the two compounds might lie in the stability of the cation-cation intermediate formed during the course of the reaction.

In order to understand the origin of the different stability observed for these similar ligand systems and to assess the role of potassium in the disproportionation mechanism, 18C6 was added to the salophenK_2 solution before reacting it with **1**, resulting in a very different behaviour, as highlighted by the proton NMR of the reaction mixture (Figure A-1).

The diffusion of *i*Pr_2O into the resulting green pyridine solution produces a powder that after recrystallisation from thf yields the tetrameric complex {[UO_2(salophen)]$_4$[μ_8-K]$_2$[μ_5-KI]$_2$[(K(18C6)]}·2[K(18C6)(thf)$_2$]·2I, **8** in a moderate yield as shown in Scheme II-3.

Scheme II-3 The reaction of **1** with Salophen K_2 in the presence or absence of 18C6 leads respectively to the stabilization of U(V) to yield **8** or to the disproportionation.

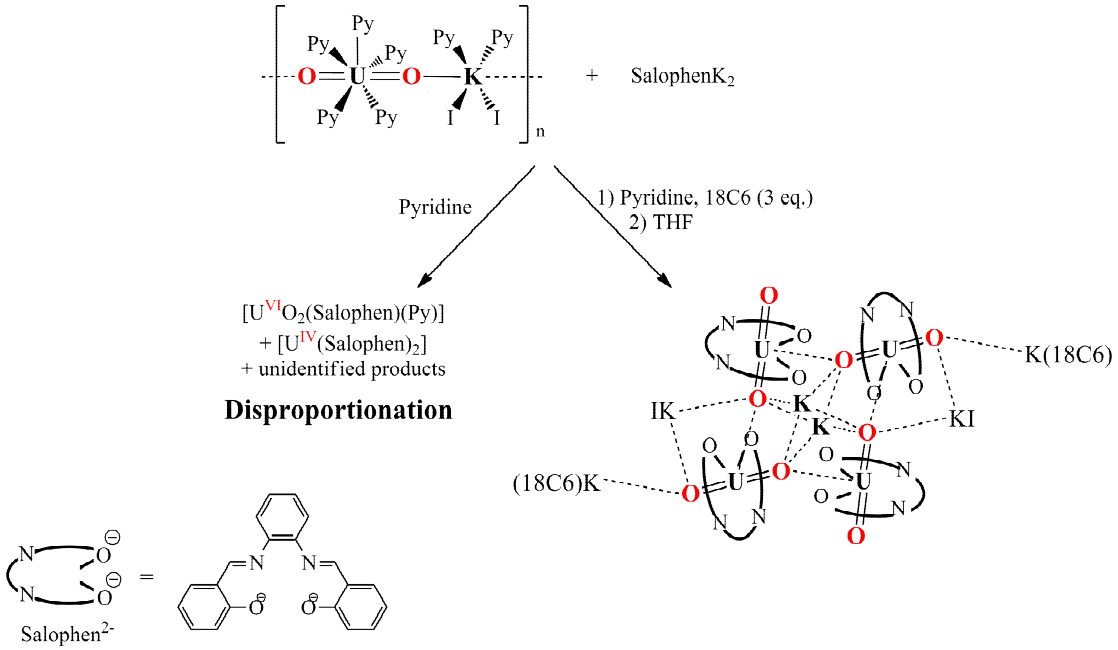

The crystal structures of complex **8** was determined by single crystal X-ray diffraction and is presented together with its tetrameric core in Figure II-9. This complex shows a structure similar to those found for the salen and acacen tetramers presenting four uranyl moieties linked with the same T-shaped cation-cation interaction to form a distorted square core with two crystallographically non-equivalent uranyl complexes. Similarly to the previously reported tetramers two symmetry related potassium ions are found respectively above and below the plane of the UO_2^+ tetrameric core (at 2.28 Å). Both potassium ions coordinate four different uranyl oxygens and four different ligand oxygens. The main difference with the previously described tetramers **3**, **6** and **7** is the presence of two additional potassium ions located in opposite sides of the tetranuclear complex, bridging uranyl oxygens from two different uranyl groups. The coordination sphere of these two symmetry potassium ions also presents an iodide. The coordination of six potassium to the uranyl oxygen had already been observed in the dbm tetramer $\{[UO_2(dbm)_2]_2[\mu\text{-}K(py)_2]_2[\mu_8\text{-}K(py)]\}_2I_2 \cdot py_2$.

The two crystallographically independent U atoms **8** are seven-coordinated, with slightly distorted pentagonal bipyramidal geometry, by two trans oxo groups, two nitrogens and two oxygens from the Schiff base ligand and one bridging oxygen from the adjacent uranyl complex. As noticed for the previously described tetramers **3**, **6** and **7,** the $UO_2^{+\cdots}UO_2^+$ interaction results in a significant lengthening of the U=O bond distance for the uranyl oxygens involved in this interaction (U=O bond range 1.942 - 1.954 Å) with respect to the

oxygens which do not participate to the $UO_2^{+\cdots}UO_2^+$ (U=O bond range = 1.818 - 1.874 Å) with a similar mean difference between the two U=O bonds of 0.1 Å.

Similarly to the acacen ligand in **6** and **7**, the salophen ligand adopt a "boat" conformation [270, 271] contrary to the almost planar coordination observed for the salen ligand in **3**. The mean U-N $_{\text{Schiff base}}$ and U-O$_{\text{Schiff base}}$ bond distances are very similar in the salen (mean U-N = 2.63(3) Å and mean U-O = 2.36(2) Å in **3**) and in the salophen (mean U-N = 2.64(3) Å and mean U-O = 2.34(3) Å in **8**) complexes. The mean U-salophen distances in complex **8** are also very close to those found in the mononuclear complex [U^VO_2(salophen-^{t}Bu$_2$)(thf)]K (mean U-N = 2.60(2) Å and mean U-O = 2.39(4) Å).[176]

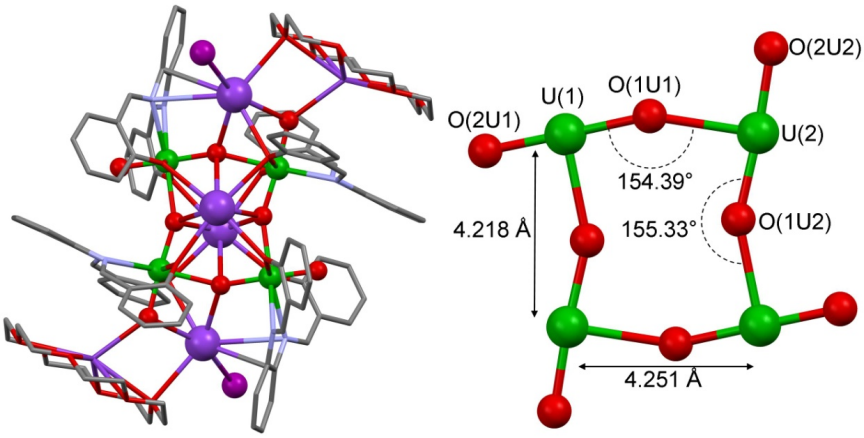

Figure II-9 Mercury view and core detailed of complex **8** with associated distances and angles. (H were omitted for clarity, C are represented in grey, O in red, K in purple, N in light blue and U in green. Selected distance (Å) and angles (°): U(1)–O(1U1) 1.871(4), U(1)–O(2U1) 1.942(3), U(1)–O(1U2) 2.404(3), U(2)–O(1U2) 1.818(3), U(2)–O(2U2) 1.954(3), U(2)–O(2U1) 2.374(3), O(1U1)–U(1)–O(2U1) 175.4(1), O(1U2)–U(2)–O(2U2) 174.7(1);

The major difference between the tetrameric complexes **3**, **6** ,**7** and **8** is found in the metric parameter of the square core. While the core geometry is very similar in the acacen and salen tetramers (mean value of the U-U distance = 4.31(3) Å in **3** and 4.30(6) Å in **6** ; mean value of the U-O-U angle = 172.2(7)° in **3** compared to 173.40(6)° in **6**), the metric parameters are significantly modified in **8**, with a shorter mean U-U distance (4.23(11) Å) and a smaller mean U-O-U angle (154.3(2)° (Figure II-9). The shorter U-U distance can be related to the presence of two additional potassium ions bridging the uranyl groups in **8** with respect to the other complexes. As a result of the potassium coordination the core geometry in **8** is significantly distorted from a square. The distortion of the core observed in **8** could play a role in the low stability of the pentavalent uranyl in such tetrameric cation-cation complex resulting in its rapid disproportionation. Moreover the presence of a different number of potassium ions coordinated to the uranyl oxygens in the salophen complex with respect to the

salen and acacen analogues probably mirrors a difference in the charge at the uranyl oxygens which is likely to play a role in the observed differences of stability.

Compound **8** shows limited solubility in thf and is not soluble in pyridine but can be dissolved in pyridine by addition of 2 equivalents of 18C6, affording the same ^{1}H NMR spectra than the crude reaction mixture presented Figure A-1. This solution also proved to be stable towards disproportionation up to 30 days in pyridine. It is interesting to notice that the addition of a catalytic excess of KI with respect to 18C6 (0.1 equivalents) in pyridine is sufficient to promote the complete disproportionation of **8** in 2 days.

We have performed PGFSTE diffusion NMR studies to investigate the nuclearity of complex **8** in pyridine. The measured hydrodynamic radius of **8** (D = 5.40(1) 10^{-10}**,** r_{sph} = 4.6 Å, Table II-3) suggests the presence of mononuclear species in pyridine (in presence of 2 equivalent of 18C6). This behaviour differs from what observed for the acacen and salen complexes **3**, **6** and **7** which retain their tetrameric structure in both pyridine and dmso. The stability of **8** in pyridine is probably associated to its monomeric form while, in the absence of crown ether, the presence of the potassium ion leads to the formation of a reactive tetrameric species (Scheme II-4).

Scheme II-4 Nuclearity of complex **8** in pyridine, in presence and absence of 18C6, and related stability

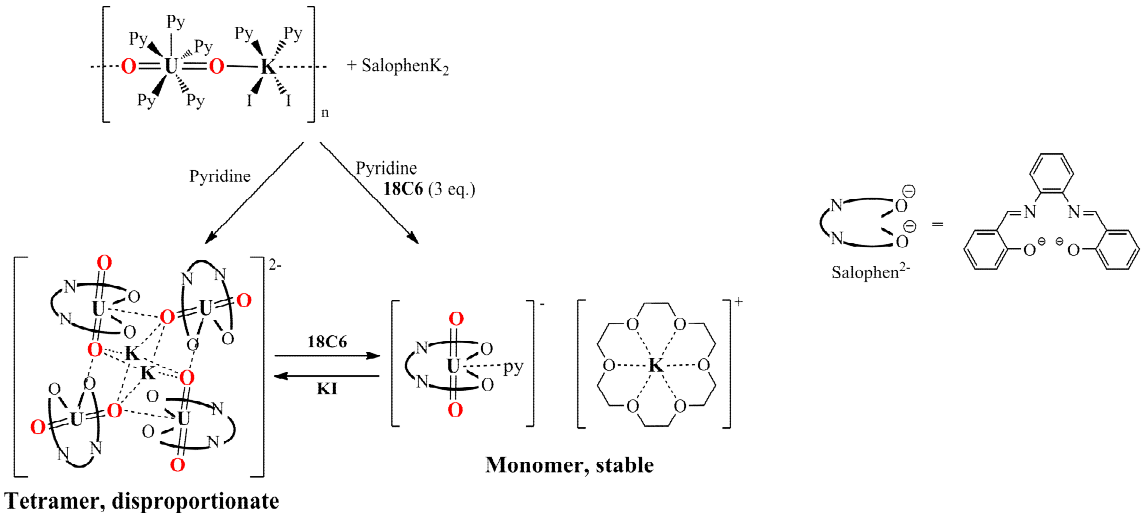

Table II-3 Diffusion coefficient values of **3, 7, 8** and **9** and estimated spherical radii.

Solvent	Compound	D [m².s^{-1}]	r_{sph} [Å]$_{exp}$	r_{sph} [Å] (evaluated from crystal structure)
pyridine η=0.879 mPa.s (298K)	**3**	2.98(2) 10^{-10}	8.4	7.9 for $\{[UO_2(salen)]_4[\mu_8\text{-}K]_2\}^{2-}$
	7	2.94(6) 10^{-10}	8.4	7.2 for $\{[UO_2(acacen)]_4[\mu_8\text{-}K]_2\}^{2-}$
	8	5.40(1) 10^{-10}	4.6	4.8 for $[UO_2(salophen)(py)]$
	9	4.57(7) 10^{-10}	5.5	4.8 for $[UO_2(salophen)(py)]$

Similarly to that previously reported for the UO_2^+ complex of the bulky salophen-^{t}Bu$_2$ ligand[176] proton NMR studies show that the reduction of the U(VI) complex $[UO_2(salophen)(py)]$ with Cp^*_2Co in pyridine affords the stable complex of pentavalent uranyl $[UO_2(salophen)(py)][Cp^*_2Co]$, **9** (Figure A—2)

Addition of KI to a pyridine solution of **9** results in rapid disproportionation, while the addition of K(18C6)I yields complex **8**, confirming the presence of a uranyl(V) complex. Moreover, PGFSTE experiments confirmed the monomeric structure of **9** in pyridine solution (Table II-3). However, the several crystallisation attempts of this complex in the solid state failed, due to its tendency to disproportionate in the presence of co-solvents such as *n*-hexane or in other solvent combinations. This effect could be explained by the decoordination of the pyridine molecule coordinated to the uranium centre due to the counter solvent addition. This observation thus indicates that in the absence of a strong coordinating cation, the pyridine provides a competitive ligand with respect to the uranyl oxygen of another pentavalent complex. A similar behaviour had been observed in the strongly coordinating solvent dmso for the $[U^VO_2(salophen)(dmso)]^-$ [161] due to the strong affinity of the dmso ligand for the uranium(V) centre that competes with cation-cation interaction. The coordination of a solvent molecule in the equatorial plane of the uranyl moiety thus provides a kinetic stability to the uranyl(V) centre by preventing the formation of cation-cation assemblies. In solvents less coordinating than dmso and in the presence of coordinating cations the complex of uranyl(V) with salophen forms a tetranuclear cation-cation complex, which leads eventually to disproportionation. This contrasts with the behaviour of the tetramers formed with salen and acacen which are fully stable towards disproportionation. However, a suitable choice of the reaction conditions renders possible to isolate a tetrameric cation-cation complex also for the salophen ligand.

II.2.1.2.5 *Synthesis of {[UO$_2$(dophen)]$_4$[μ$_8$-K(py)]$_2$[μ$_4$-K(py)$_2$]$_4$[μ$_2$-I]$_2$}*

While the acacen and salen uranyl(V) tetramers were fully stable towards the disproportionation reaction, the assembly formed with the more aromatic ligand salophen proved to be much more labile. In order to evaluate the contribution of the ligand aromaticity and geometry in the stability of the uranyl tetramer formed through CCI, the reaction of uranyl(V) the fully aromatic Schiff base ligand dophen was investigated. The reaction of one equivalent of the uranyl(V) polymer **1** with dophenK$_2$ in pyridine resulted in the formation of a dark green solution of the tetrameric uranyl(V) complex {[UO$_2$(dophen)]$_4$[μ$_8$-K(py)]$_2$[μ$_4$-K(py)$_2$]$_4$[μ$_2$-I]$_2$}, **10** stable for 30 days under argon (Scheme II-5).

Scheme II-5 The reaction of **1** with DophenK$_2$ to yield **10** .

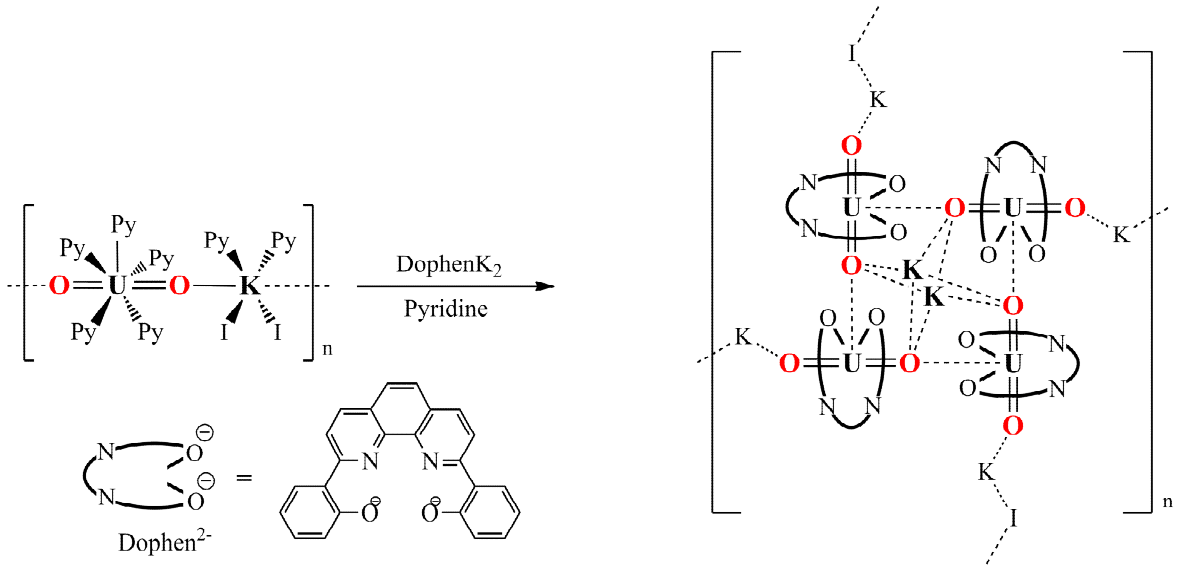

Slow diffusion of hexane into that pyridine solution resulted in the isolation of X-ray quality crystals of a 2D polymeric assembly of tetramers of uranyl(V), bound together through KI bridges in 77% yield. The crystal structure of **10** was determined by single crystal XRD, and is presented Figure II-10.

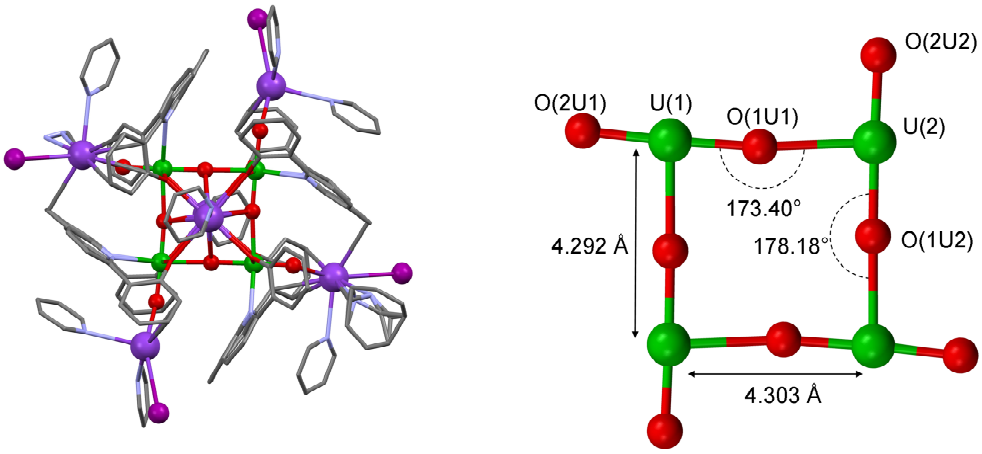

Figure II-10 Mercury diagrams of **10**. Hydrogen atoms, counterions and solvent molecules were omitted for clarity. Selected bonds lengths (Å) and angles (°) for 10: U(1)–O(1U1).1.893(18), U(1)–O(2U1) 1.848(17), U(1)–O(1U2) 2.321(18), U(2)–O(1U2) 1.972(18), U(2)–O(2U2) 1.827(16), U(2)–O(1U1) 2.417(18), O(1U1)–U(1)–O(2U1) 177.4(8), O(1U2)–U(2)–O(2U2) 177.6(7).

This complex shows a structure similar to those found for the salen, acacen and salophen tetramers presenting four uranyl moieties linked with the same T-shaped cation-cation interaction to form a distorted square core with two crystallographically non-equivalent uranyl complexes. The two crystallographically independent U atoms **8** are seven-coordinated, with a slightly distorted pentagonal bipyramidal geometry, by two trans oxo groups, two nitrogens and two oxygens from the Schiff base ligand and one bridging oxygen from the adjacent uranyl complex. The structure of the tetrameric core is analogous to the previously reported salen and acacen tetramers, with a square shaped planar core defined by four uranyl(V) connected by CCI (Figure II-10), with mean U-U distances of 4.30(2) Å, a similar mean difference between the two U=O bonds of 0.1 Å and two symmetry related potassium ions are found respectively above and below the plane of the UO_2^+ tetrameric core (at 2.13 Å). The coordination sphere of these two symmetry potassium ions also presents a pyridine molecule. Similarly to the acacen and salophen ligands in **6** , **7** and **8**, and despite the rigidity conferred by its aromaticity, the dophen ligand also adopt a "boat" conformation [270, 271] contrary to the almost planar coordination observed for the salen ligand in **3**. The mean U-$N_{Schiff\ base}$ and U-$O_{Schiff\ base}$ bond distances are very similar than in the salen and the salophen (mean U-N = 2.63(3) Å and mean U-O = 2.36(2) Å in **3**, and mean U-N = 2.64(3) Å and mean U-O = 2.34(3) Å in **8**) with a mean U-O distance of 2.31(7) Å and a mean U-N distance of 2.67(3) Å in **10**.

The main difference of the structure lies in the polymeric form of the assembly. The crystal structure of **10** thus consists in a 2D network of tetramers bound through KI bridges, as

represented Figure II-11. The complex **10** is more soluble than its salen analogue **2**, and can be obtained in a crystalline form without adding crown ether to solubilise it. In contrast the isolation of the salen analogue required the addition of 18C6 to solubilise the powder initially obtained. This structure shows that in absence of crown ether, the reaction of uranyl(V) on Schiff bases complexes affords polymeric structures. Moreover, the polymeric form of the complex **10** validates the assumption made in chapter II.2.1.2.1 that the powder isolated from the reaction of salen with uranyl(V), with a formula $[(UO_2)(salen)K(py)]\cdot 1.4KI$, **2**, was a polymeric assembly of tetramers. This observation highlights the critical role of the ionic strength of the media in the comprehension of these aggregation phenomena.

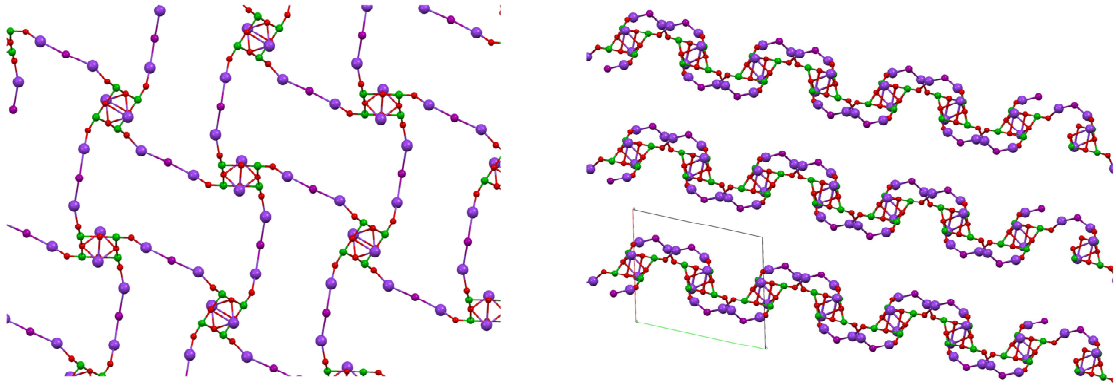

Figure II-11 Mercury view of the polymeric network in **10** presented along its a (left) and c (right) axis. Only uranyl groups, K and I atoms were presented for clarity.

Proton NMR revealed the presence of a single uranyl(V) species with 7 slightly paramagnetically shifted signal indicating pseudo D_{4h} symmetry in solution for the tetrameric species. PGFSTE experiments in pyridine lead to the measurement of a D coefficient of $2.72(3).10^{-10}$ $m^2.s^{-1}$ (Table II-4), indicating that the complex in solution is present under its tetrameric form and that no larger polymeric assemblies are maintained in pyridine solution.

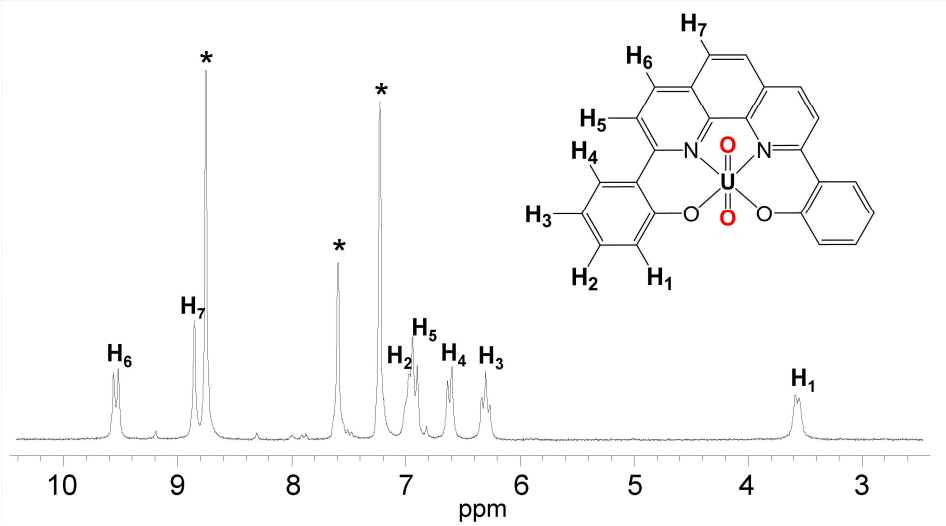

Figure II-12 ^{1}H NMR of **10** in pyridine-d_5.

Table II-4 Diffusion coefficient values of **3**, **7** and **10** and estimated spherical radii.

Solvent	Compound	D [$m^2.s^{-1}$]	r_{sph} [Å]$_{exp}$	r_{sph} [Å] (evaluated from crystal structure)
Pyridine η=0.879 mPa.s (298K)	**3**	2.98(2) 10^{-10}	8.4	7.9 for $\{[UO_2(salen)]_4[\mu_8\text{-}K]_2\}^{2-}$
	7	2.94(6) 10^{-10}	8.4	7.2 for $\{[UO_2(acacen)]_4[\mu_8\text{-}K]_2\}^{2-}$
	10	2.72(3) 10^{-10}	9.1	12.1 for $\{[UO_2(dophen)]_4[\mu_8\text{-}K(py)]_2\}^{2-}$

ESI/MS studies, similarly to what observed for the former tetrameric uranyl(V) complexes, point to the presence of a single tetramer in gas phase (m/z = 2686.2 corresponding to the $[UO_2(dophen)]_2[\mu_8\text{-}K]_2^{2-}$ adduct with H^+, Figure II-7). Three equally intense peaks can be observed in the ESI/MS spectra, at m/z = 2853.4, 2873.3 and 2907.9 which correspond to the KI, $KNaI^+$ and K_2I^+ adducts with the $[UO_2(dophen)]_2[\mu_8\text{-}K]_2^{2-}$ core which indicate that if the polymeric assembly through KI bridges can be disrupted in gas phase, the affinity of the cluster core for alkaline ions remains important, and leads to the formation of adducts within the mass spectrometer.

II.2.1.3 Effect of the counter ions - Alkaline cations

The potassium cations clearly play a role in the structure and stability of the tetramers presented in the previous section. This central role probably arise from two contributions: a structural role of potassium, leading to tetrameric assemblies through a template effect, and an electronic effect, the negative charge on the uranyl oxygen being decreased by the coordination of the alkaline ion, thus resulting in an increase of the oxidation potential, as highlighted by DFT and electrochemical studies.[176, 272] In order to get further insight on the effect of the counterions on both structure and stability, a systematic study was carried out on the very stable uranyl(V) salen complex.

II.2.1.3.1 *Synthesis of $[UO_2(salen)(py)][Cp^*_2Co]$*

The synthesis of uranyl(V) salen complexes with different counter ions requires a suitable uranyl(V) starting material. The previously used uranyl(V) starting material $[(UO_2py_5)(KI_2py_2)]$, **1**, is indeed not suitable for this use, this compound providing one molar equivalent of potassium ion per uranyl moiety, thus competing with other counter ions. In order to develop a "potassium free" synthetic route, the reduction of the uranyl(VI) salen complex $[(UO_2)(salen)\ (py)]$, **4**, was carried out. As highlighted in Figure A-4, in pyridine solution complex **4** can be reversibly reduced to its uranyl(V) analogue at a potential of -1.68 V versus the Fc/Fc^+ couple.

According to this observation, and similarly to the synthesis of the uranyl(V) salophen complex **9**, the reduction of uranyl(VI) salen was carried out with Cp^*_2Co, affording the highly soluble complex of uranyl(V) $[UO_2(salen)(py)][Cp^*_2Co]$, **11** (Scheme II-6).

Proton NMR revealed the presence of a single uranyl(V) species with 6 slightly paramagnetically shifted signal indicating a pseudo C_{2v} symmetry in solution (Figure A-5).

PGFSTE experiments in pyridine lead to the measurement of a D coefficient of 4.97(2) 10^{-10} $m^2.s^{-1}$(Table II-5), indicating that the size of the complex formed is slightly larger than the uranyl(VI) analogue **4** but smaller that the tetrameric assembly **3**, giving clues about the monomeric form of **11** in pyridine solution.

Table II-5 Diffusion coefficient values of **3**, **4** and **11** and estimated spherical radii.

Solvent	Compound	D [m².s^{-1}]	r_{sph} [Å]$_{exp}$	r_{sph} [Å] (evaluated from crystal structure)
Pyridine η=0.879 mPa.s (298K)	**3**	2.98(2) 10^{-10}	8.4	7.9 for $\{[UO_2(salen)]_4[\mu_8\text{-}K]_2\}^{2-}$
	4	5.40(1) 10^{-10}	4.6	4.8 for $[UO_2(salen)(py)]$
	11	4.97(2) 10^{-10}	5.0	4.8 for $[UO_2(salen)(py)]$
	12	3.96(2) 10^{-10}	6.3	6.5

However, similarly to the behaviour observed with **9**, the numerous attempts to isolate **11** in a crystalline form failed, slow diffusion of counter-solvents resulting in the fast disproportionation of the complex. The identity of complex **11** was here confirmed through an indirect characterisation of the complex, inspired by the early work of Ekström in water [24], who demonstrated by electrochemical kinetic studies that the disproportionation reaction of aqua pentavalent uranyl can be slowed down by the formation of dimeric U(V)/U(VI) cation-cation assemblies. In line with this observation, the reaction of $[U^{VI}O_2(salen)(py)]$, **4** with $[U^{V}O_2(salen)(py)][Cp^*_2Co]$ **11** in a 1:1 ratio was carried out, and yielded the dinuclear mixed valent complex $[UO_2(salen)(py)]_2[Cp^*_2Co]$, **12**, in 92 % yield as a dark green crystalline solid (Scheme II-6).

Scheme II-6 Synthesis of **11** and **12** from **4**

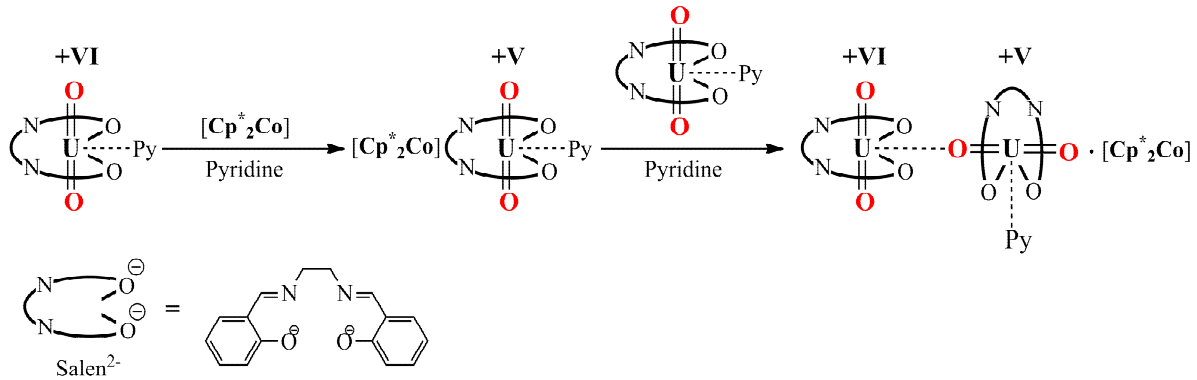

The paramagnetically shifted proton NMR spectrum of **12** (Figure II-13) differs from those of the starting materials, with 11 slightly paramagnetically shifted peaks corresponding to 10 peaks integrating for 2 protons each and 1 peak integrating for 4 protons.

Moreover, PGFSTE experiments, revealing a D value of 3.96(2) 10^{-10} $m^2.s^{-1}$, indicated that the dimeric assembly was retained in solution, and confirmed by comparison the probable

monomeric state of **11** in solution. The isolation for this dimeric complex in a crystalline form together with the fact that proton NMR studies proved that this dimeric complex is stable up to one month in pyridine solution confirmed that the formation of a mixed valent U(V)/U(VI) complex increase the stability towards disproportionation.

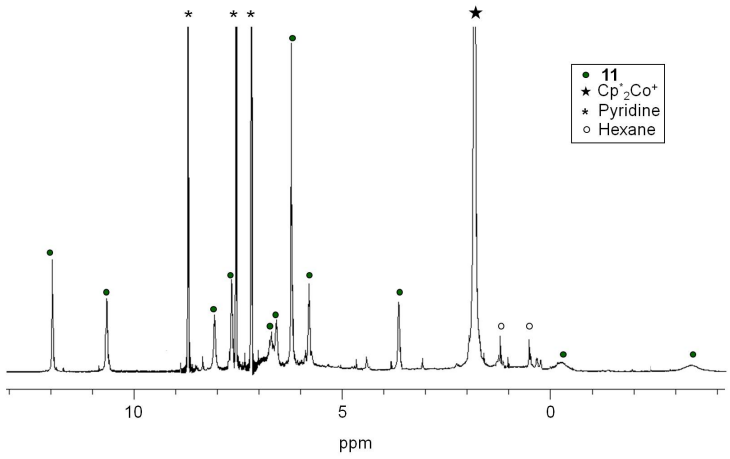

Figure II-13 ^{1}H NMR of **12** in pyridine-d_5

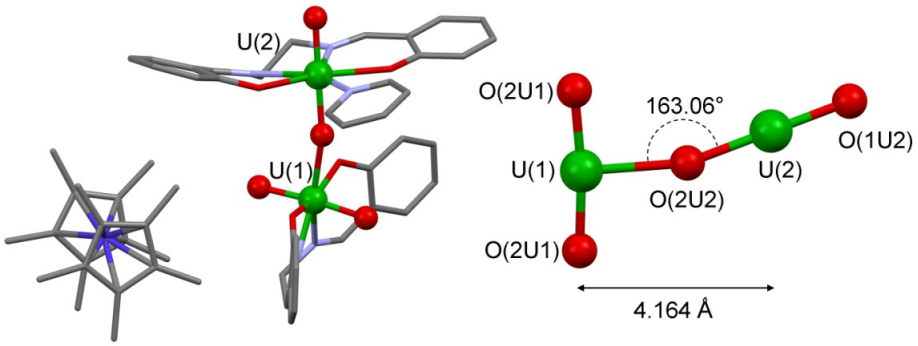

Figure II-14 Mercury diagram of complex 12 and a detail of the T-shaped UO_2^{2+}-UO_2^{+} interaction in **12** with associated distances and angles. (H were omitted for clarity, C are represented in grey, O in red, K in purple, N in light blue, Co in dark blue and U in green. Disorder on one of the pentamethylcyclopentadiene group has not been represented.) Selected distance (Å) and angles (°):U(1)-O(1U1) 1.792(12), U(1)-O(2U1) 1.801(12), U(1)-O(1) 2.268(13), U(1)-O(1U2) 2.277(10), U(1)-O(2) 2.283(11), U(1)-N(2) 2.581(15), U(1)-N(1) 2.627(15), U(2)-O(2U2) 1.820(13), U(2)-O(1U2) 1.933(10), U(2)-O(21) 2.318(12), U(2)-O(22) 2.317(13), U(2)-N(22) 2.596(13), U(2)-N(21) 2.620(14), U(2)-N(py) 2.666(13) and O(1U1)-U(1)-O(2U1) 173.6(5), O(2U2)-U(2)-O(1U2) 179.0(6), U(2)-O(1U2)-U(1) 163.0(6).

The crystal structure of the complex **12**, shown in Figure II-14, indicated that the charge is localised in the complex, with smaller values of the U=O distances (1.792(12) and 1.801(12) Å) found for U1, identified as a U(VI) with respect to the other uranyl group distances (1.820(13) - 1.933(10) Å for U2. Both uranium ions are heptacoordinated with a slightly

distorted pentagonal bipyramid geometry by the four donor atoms of the salen ligand located in the equatorial plane and the two uranyl oxygens in axial position; the seventh coordination position is occupied by a pyridine nitrogen in the U(V) complex and by a uranyl oxygen from the UO_2^+ group in the U(VI) complex.

This rare dimeric complex provides the only second example of an isolated molecular U(V)/U(VI) compound, following the mixed valent tetramer **5**. However, mixed-valent actinyl(V)/(VI) systems have been identified in a few naturally occurring oxide minerals[273], in some examples of oxide compounds obtained under hydrothermal conditions[266-268] but also in organic solution, as highlighted by the first example of mixed-valent Np(V)/Np(VI) cation-cation complex recently isolated.[152] These results show that interactions can occur between U(V) and uranyl(VI) produced from the disproportionation reaction, rendering more difficult the assignment of all disproportionation products. Interestingly, the decamethylcobaltocenium ion in **12** was proved to have no influence on the stability of complex **12**, and the tetramethylammonium salt of **12**, $[UO_2(salen)(py)]_2[Me_4N]$, **13** can be easily obtained by salt metathesis with tetramethylammonium iodide from **12**. The structure of single crystals of **13** obtained by slow diffusion of thf in a pyridine solution revealed a very similar structure presented Figure II-15, with essentially similar metric parameters but a slightly longer U-U bond distance of 4.189(2) Å with respect to 4.164(1) Å in **12**.

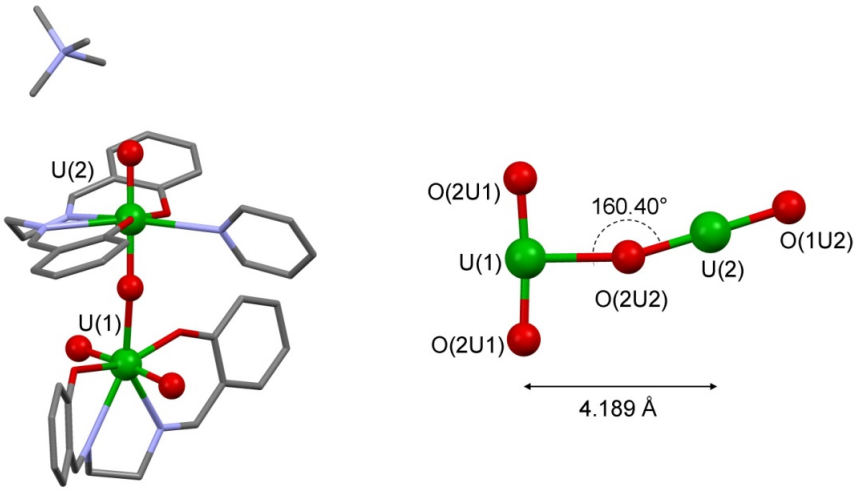

Figure II-15 Mercury diagram of complex **13** and a detail of the T-shaped UO_2^{2+}-UO_2^+ interaction in **13** with associated distances and angles. (H were omitted for clarity, C are represented in grey, O in red, K in purple, N in light blue and U in green. Co-crystallised solvent molecules have not been represented.) Selected distance (Å) and angles (°): U(1)-O(1U1) 1.787(6), U(1)-O(2U1) 1.807(6), U(1)-O(1U2) 2.321(6), U(2)-O(2U2) 1.855(6), U(2)-O(1U2) 1.930(6), U(2)-N(py) 2.651(8) and O(1U1)-U(1)-O(2U1) 174.8(3), O(2U2)-U(2)-O(1U2) 179.2(3), U(2)-O(1U2)-U(1) 160.5(3).

II.2.1.3.2 *Alternative synthetic path to $[UO_2(salen)]_4[\mu_8\text{-}K]_2[K(18C6)py]_2$*

The "potassium free" uranyl(V) complex **11** thus provides a suitable starting material for a systematic study of the influence of the counterion, and the addition of one equivalent of KI to **11** followed by the addition of 1 equivalent of 18C6 afford complex **3** in 85% yield, thus providing an alternative synthetic route to complex **3** (Scheme II-7).

Scheme II-7 Alternative synthesis of **3**

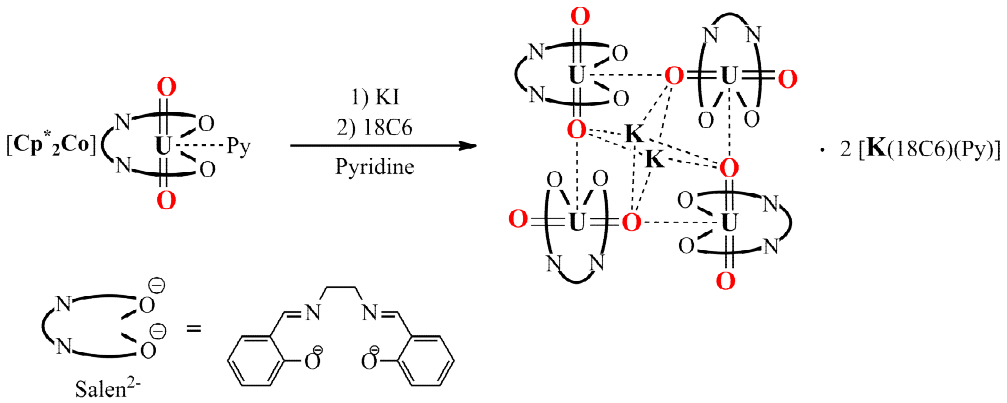

The complexation constant for potassium in the coordination pocket defined by the four uranyl(V) moieties in the tetramer was also highlighted by the reaction of **11** with K(18C6)I or K(222)I, which affords the tetrameric complex **3** in good yield. This fact underline the exceptional strength of coordination of potassium in the tetrameric pocket, its complexation constant being larger than the one of the very good potassium chelate 18C6 and [2,2,2] cryptand.

II.2.1.3.3 *Synthesis of $\{[UO_2(salen)_4][\mu 8\text{-}M]_2[M(18C6)]_2\}$, M=Na, Rb*

The potassium cation has two different roles in the complexes presented above. The structural role of potassium leading to tetramer formation has been clearly identified in the tetrameric assemblies described in part I.1.1.1. Potassium also has an electronic effect, notably it stabilizes the pentavalent uranyl species with respect to the oxidation reaction by decreasing the negative charge on the uranyl oxygen[176]. We have also observed that replacing K^+ with $K(18C6)^+$ is sufficient to stabilize the salophen tetramer against disproportionation. At the light of these observations, we decided to investigate the reaction of the monomeric complex $[UO_2(salen)(py)][Cp^*_2Co]$, **11**, with different alkali ions in order to evaluate the role of the counterion in both structural behaviour and stability of the uranium complexes. Similarly to the reaction described Scheme II-7, the reaction of $[U^VO_2(salen)(py)][Cp^*_2Co]$, **11** with NaI of RbI followed by the addition of 0.5 molar equivalent of 18C6 result in the formation of the

tetrameric complexes $[UO_2(salen)]_4[\mu_8\text{-}Na]_2[Na(18C6)(py)_2]_2$, **14** and $\{[UO_2(salen)]_4[\mu_8\text{-}Rb]_2[Rb(18C6)]_2\}$, **15** in 55% and 81% yield respectively (Scheme II-8).

Scheme II-8 Synthesis of **14** and **15** from **11**

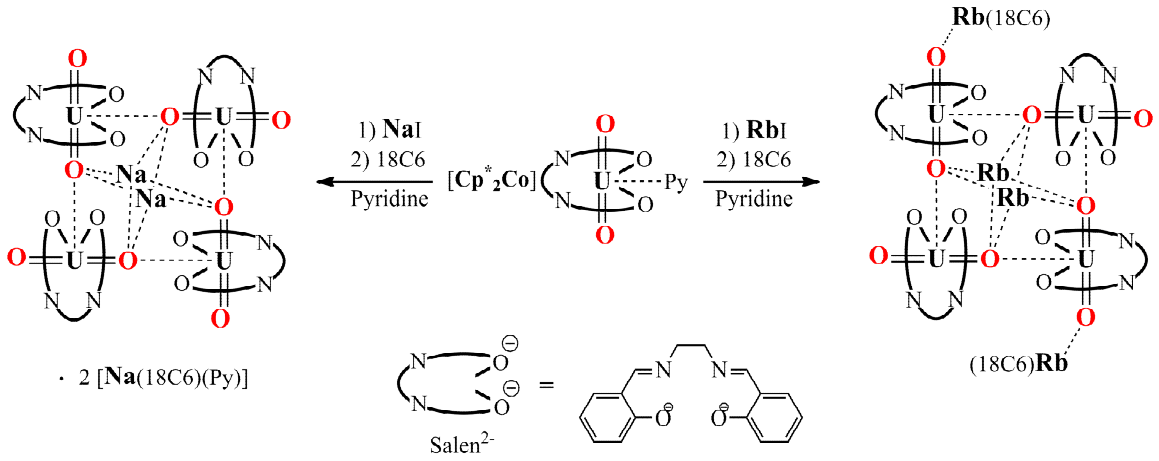

The two complexes show similar properties and are both stable towards the disproportionation reaction in pyridine solution. It should be noted however that the solubility in pyridine of the tetrameric complexes is inversely proportional to the size of the central ion. Slow diffusion of hexane on pyridine solution of **14** and **15** affords dark blue single crystals suitable for X-ray diffraction, and revealed a similar tetrameric structure. However some structural differences are observed in **14** and **15** with respect to **3,** as a result of the different size of the cations (Figure II-16). The major difference between the tetrameric complexes **3, 14** and **15** is found in the metric parameter of the square core, correlated to the sizes of the alkaline ion, with a mean U-U distance of 4.20(1) Å in **14**, of 4.30(4) Å in **3** and of 4.32(2) Å in **15**. The U-O distances within the uranyl(V) complexes are similar in the Na, K and Rb tetramers, with a mean U-O_{yl} involved in the cation-cation interaction (of 1.930(7) Å in **14**, of 1.933(5) Å in **3** and of 1.919(5) Å in **15**) 0.1 Å longer than the mean outer U-O_{yl} (of 1.827(3) Å in **14**, of 1.832(5) Å in **3** and of 1.859(4) Å in **15**). However, the main difference between these three tetramers lies in the U-O distance between two adjacent uranyl ions. This distance directly describe the strength of the cation-cation interaction, and a significant variation can be observed, this distance varying from 2.356(2) Å in **14** to 2.397(11) Å in **3** and 2.417(2) Å in **15**. This trend seems to indicate that the cation-cation interaction is stronger with the smaller alkaline cations. Moreover, it should be noticed that the shorter distance between uranyl groups is accompanied by smaller O-U-O angles and stronger distortion of the square geometry, with a mean O-U-O value of 158(6)° in **14** to 168(3)° in **3** and 171(1)° in **15**. The mean values of the Na-O_{yl} and of the Na-O_{salen} (2.82(30) Å and 2.52(7) Å) are shorter than the

respective K-O_{yl} and K-O_{salen} distances (2.99(18) Å and 2.70(4) Å), while the mean values of the Rb-O_{yl} and of the Rb-O_{salen} distances (3.17(16) Å and 2.83(4) Å) are respectively longer. This results in a shorter (respectively longer) distance between the oxygen atoms of adjacent salen ligands for **14** (**15** respectively) compared to **3,** as well as a shorter (respectively longer) distance between the sodium (rubidium respectively) cation and the mean plane defined by the four uranium centres (Na-mean plane distance = 1.93 Å in **14** K-mean plane distance = 2.14 Å in **3** and Rb-mean plane distance = 2.37 Å in **15**), leading to a slightly increased distortion from planarity of the salen ligand when increasing the central ions size.

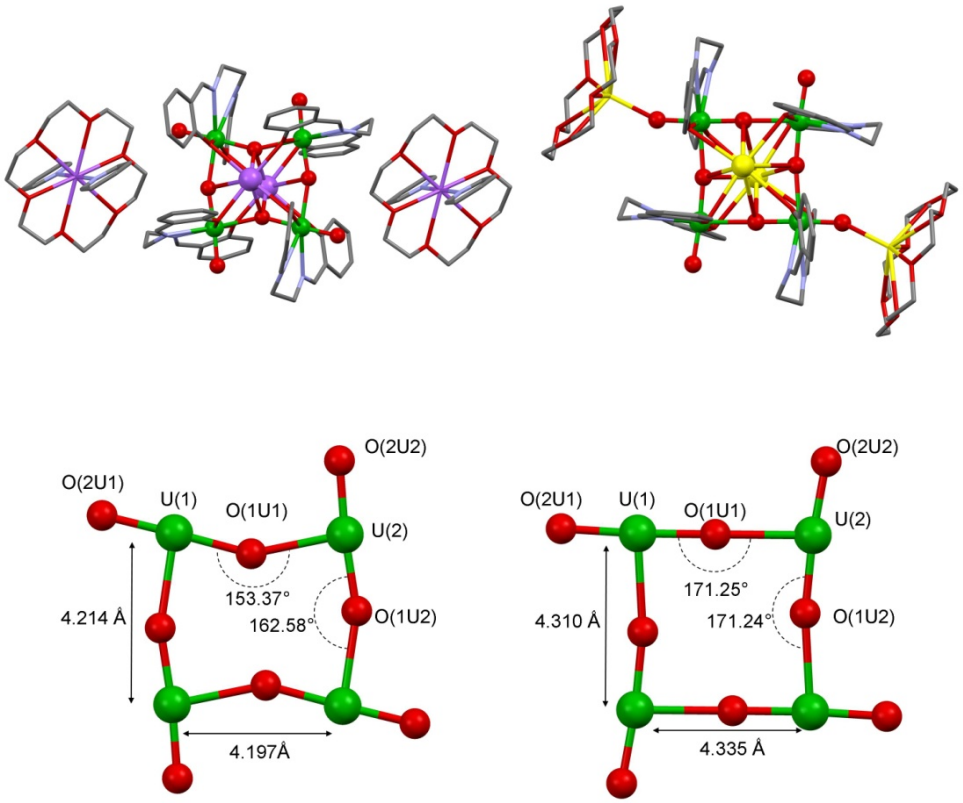

Figure II-16 Mercury view of the structure of **14** and **15** (top, left and right) and detail of their cores with associated distances and angles (bottom, left and right). The structures are represented along the axis formed by the two alkaline ions perpendicular to the uranium square plane (for clarity H and co-crystallised solvent molecules were omitted and only one of the two positions of the disordered Rb(18C6) group is shown, C are represented in grey, O in red, Na in pink, Rb in yellow, N in light blue and U in green.)

II.2.1.3.4 *Reaction with Li^+ ions*

In **3**, **14** and **15**, the presence of a different cation does not result in a different reactivity and the three tetramers are stable in pyridine with respect to the disproportionation reaction. In contrast, the reaction of $[UO_2(salen)(py)][Cp^*_2Co]$, **11** with the iodide salt of the smaller Li^+ ion results in the slow disproportionation of the resulting pentavalent complex yielding a mixture of decomposition products (Scheme II-9).

Scheme II-9 Disproportionation of **11** in presence of Li^+

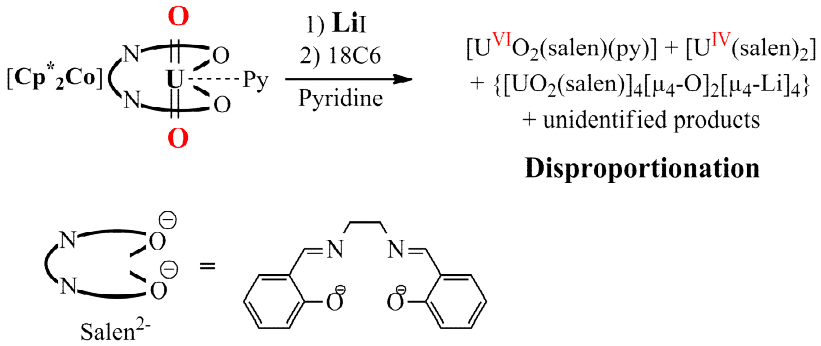

The ^1H NMR spectrum of the reaction mixture recorded after 30 days shows the presence of the $[U(salen)_2]$ complex and of a $[U^{VI}O_2(salen)(py)]$, **7**, species and additional unidentified species (Figure II-17). The lower stability of the UO_2^+ complex of salen in the presence of Li^+ is probably the result of both steric effects and electronic effects associated to the higher ratio charge/ionic radii of Li^+ compared to Na^+, K^+ and Rb^+. On one hand, the very small size of the Li^+ probably promotes the formation of cation-cation complexes with a lower stability due to geometry constrain in the core and to the short U-O distances between adjacent uranyl, as already observed in the sodium analogue. On the other hand, the stronger Lewis acidity of Lithium with respect to the other alkaline ions could result in a stronger Li-O_{yl} interaction, rendering the uranyl oxo more labile and thus destabilising the uranyl(V) moiety. These parameters will be discussed in detail in section II.2.1.6.

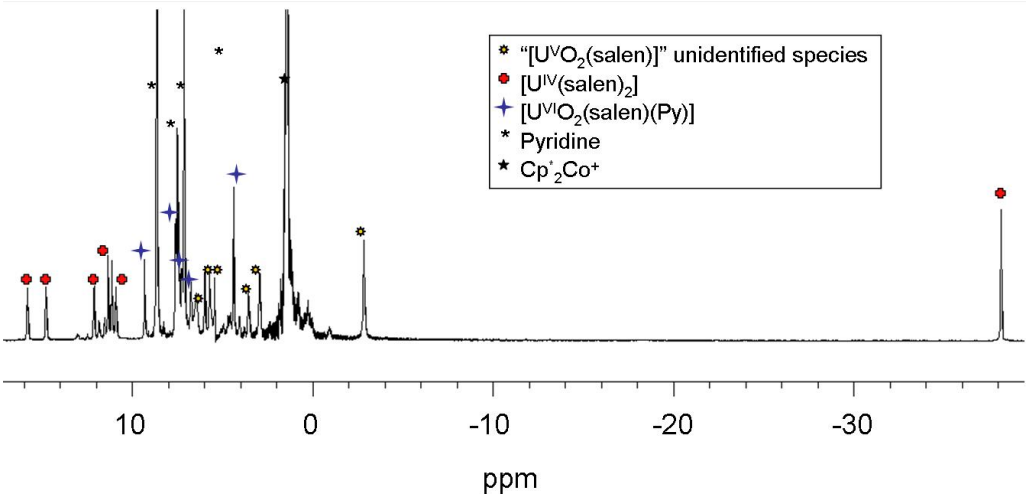

Figure II-17 ^{1}H NMR spectrum of the reaction of {[$U^{V}O_2$(salen)][Cp^{*}_2Co]},**11** with LiI in pyridine after one month storage at room temperature.

From the decomposition mixture, we were able to reproducibly isolate crystals of an interesting decomposition product. X-ray diffraction shows the presence of the oxo uranyl cluster {[UO_2(salen)]$_4$[μ_4-O]$_2$[μ_4-Li]$_4$}, **16**. A Mercury diagram of the structure of **16** is presented in Figure II-18. The quality of the structure is not sufficient for a discussion on the bond distances or for the localisation of the solvents molecules. It is therefore difficult to unambiguously assign the uranium ions oxidation state in the complex. However the connectivity of the structure is unambiguous. The structure consists of four uranyl groups arranged in a tetrahedral geometry, the uranyl groups being connected by two oxo groups bridging two adjacent U ions and by four Li^{+} ions yielding a [U_4Li_4] cubic cluster. Each Li ion is quadruply bridged to two salen oxygens, one uranyl oxygen and one bridging oxo-group. The presence of the μ-oxo groups in the structure accounts for the fate of the oxygen in the disproportionation reaction of pentavalent uranyl compounds in aprotic solvents. While the formation of U(IV) and U(VI) species had already been unambiguously identified by proton NMR studies of the decomposition process of UO_2^{+} dbm complexes, in the previous studies the fate of the oxygen remained unknown. The isolation of the decomposition product **16** demonstrates why it can be challenging to identify all the products of disproportionation of pentavalent uranyl in aprotic conditions.

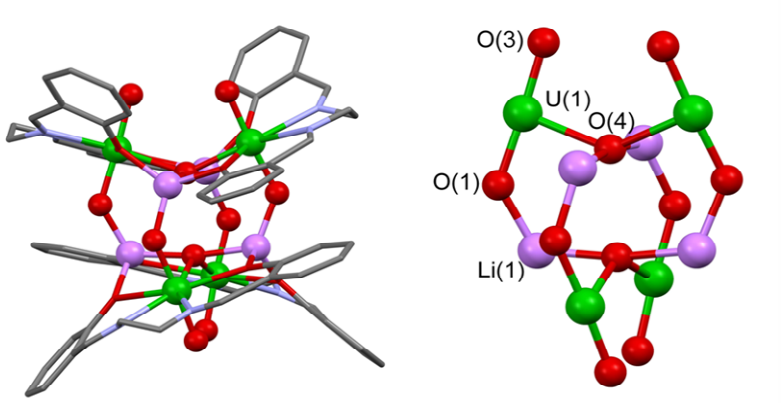

Figure II-18 Mercury view and core detailed of complex **16.** (H were omitted and ligands were represented in pipes for clarity, C are represented in grey, O in red, Li in pink, N in blue and U in green)

II.2.1.3.5 ***Reaction with protons***

The mechanism proposed from the DFT studies of the disproportionation of pentavalent uranyl presented in part I.3.1.2.1 in aqueous conditions involves the protonation of a cation-cation intermediates followed by electron transfer to yield the U(IV) and U(VI) aqua species and water.[25] The cation-cation complex **3** is stable in pyridine and thus provide an access to the transition state proposed in the mechanism of Steele and Taylor. It can therefore be used to investigate the second step of the mechanism, i.e. the protonation of the cation-cation intermediate.

Thus, the addition of two equivalents of pyridinium chloride (per uranium centre) to a solution of **3** resulted in the immediate disproportionation of the complex. The proton NMR spectrum of the decomposition products show a mixture of $[U^{VI}O_2(salen)(py)]$, **4** and of the uranium(IV) complexes $[U(salen)_2]$ and $[UCl_2(salen)]$, in ratio 6:2:3 (Scheme II-10). The formation of water in this reaction was also characterized by ^1H NMR (Figure II-19). This reactivity is in perfect agreement with the mechanism proposed for the disproportionation of pentavalent uranyl in water from theoretical studies.[25, 26]

Scheme II-10 Proton induced disproportionation of **3**

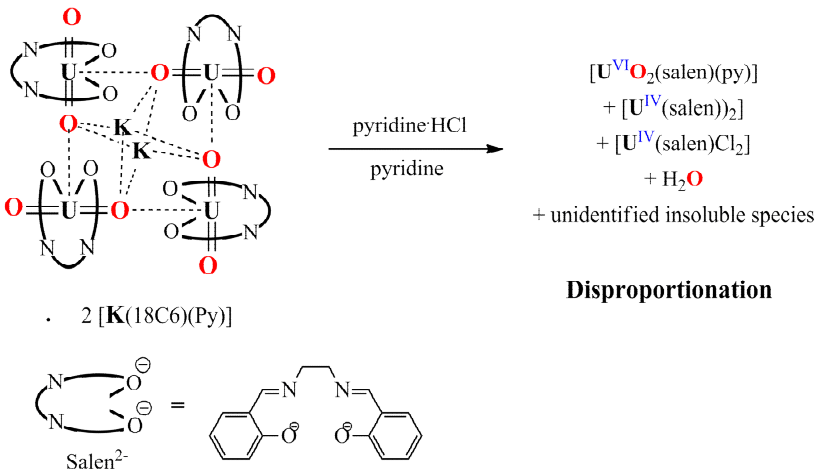

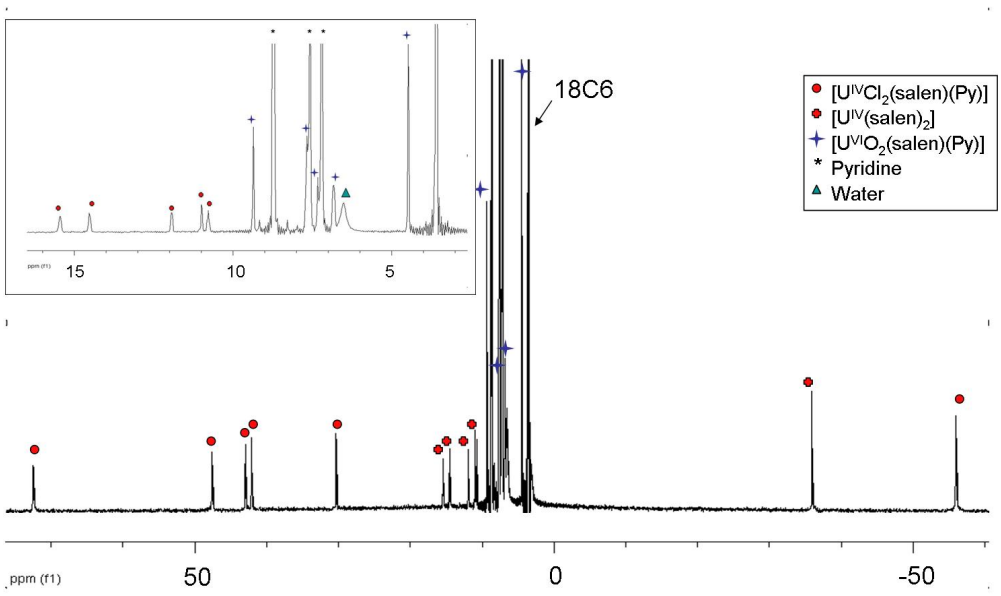

Figure II-19 ^{1}H NMR spectrum of **3** in pyridine after addition of py·HCl.

This reactivity highlights the important role played by the protons in the mechanism of disproportionation and confirms that the protonation of one oxygen atom to form a better leaving group is a key step in the disproportionation mechanism. Moreover, the formation of the very thermodynamically stable water molecules drives the disproportionation towards the formation of U(IV) and U(VI). In the absence of protons, stable cation-cation complexes can form depending on the ligand and reaction conditions. However for some ligand systems (such as salophen and dbm) the disproportionation occurs also in aprotic solvents but leads to the formation of more complex species and probably follows a different pathway.

II.2.1.4 Electrochemical behaviour in presence of cations

As observed in part II.2.1.2.1, electrochemistry provides an interesting tool to evaluate the stability of the tetrameric complexes in solution. Consequently, electrochemical measurements were carried out in presence of various alkaline metal counterions. The formation of the tetrameric assemblies can be followed by cyclic voltammetry studies.

Cyclic voltamogramms of uranyl(VI) salen **4** (2.5 mM) in pyridine containing 0.1 M $TBAPF_6$ in presence of 1 equivalent of RbI, KI, NaI, or LiI were acquired and are presented in Figure II-20.

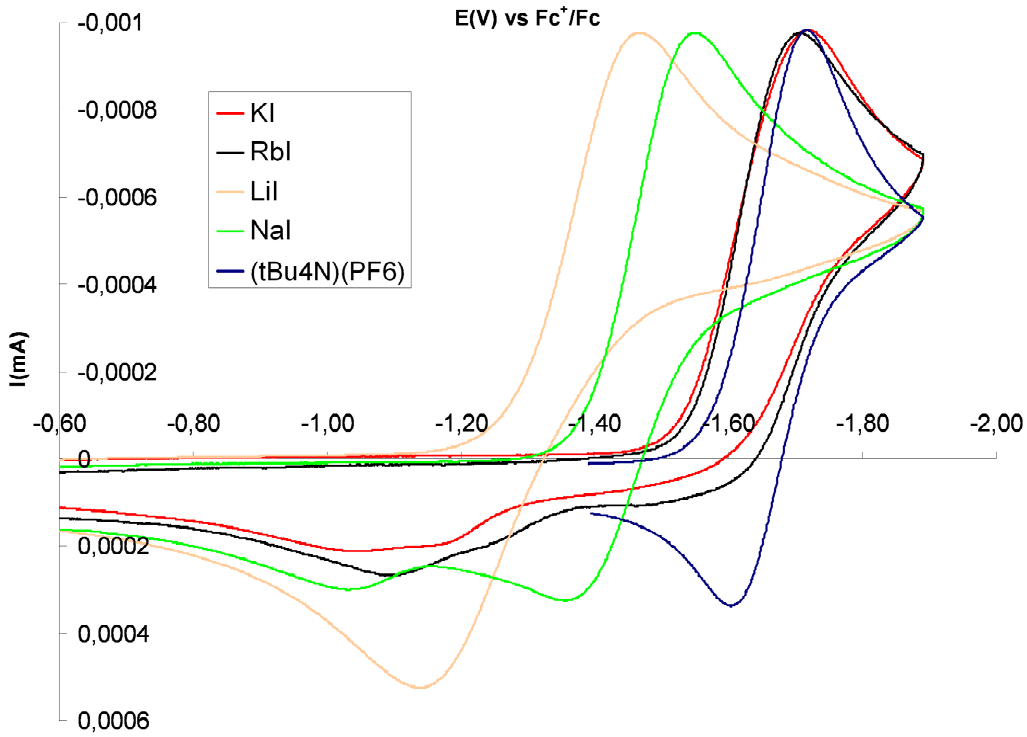

Figure II-20 Cyclic voltamogramms of uranyl(VI) salen **4** (2.5 mM) in pyridine (blue line) and in presence of 1 equivalent of RbI (black line), KI (red line), NaI (green line), or LiI (orange line) (0.1 M $TBAPF_6$ used as electrolyte)

While the cyclic voltamogramm of the uranyl(VI) complex in absence of additional counterion present the previously described quasi-reversible cycle centred at -1.68 V, we observed that the addition of 1 equivalent of KI per uranyl(VI) dramatically change the voltamogramm, with a shift of the anodic peak from -1.6 V to -1.1 V, rendering the system irreversible. This behaviour highlights the critical role of the potassium counterion in the stabilisation of uranyl(V), and indicates that even at low concentration in alkaline metal, the

irreversible reaction forming the tetrameric complex is quantitative. The formation of the tetramers follows an EC type mechanism described in Scheme II-11. This electrochemical behaviour clearly indicates that the uranyl(V) is largely stabilized towards oxidation through the formation of the tetrameric complex in presence of potassium, and this increased oxidation potential probably largely contribute to the stability of the tetrameric assemblies towards disproportionation.

Scheme II-11 EC mechanism of the electrochemical formation of the tetramers

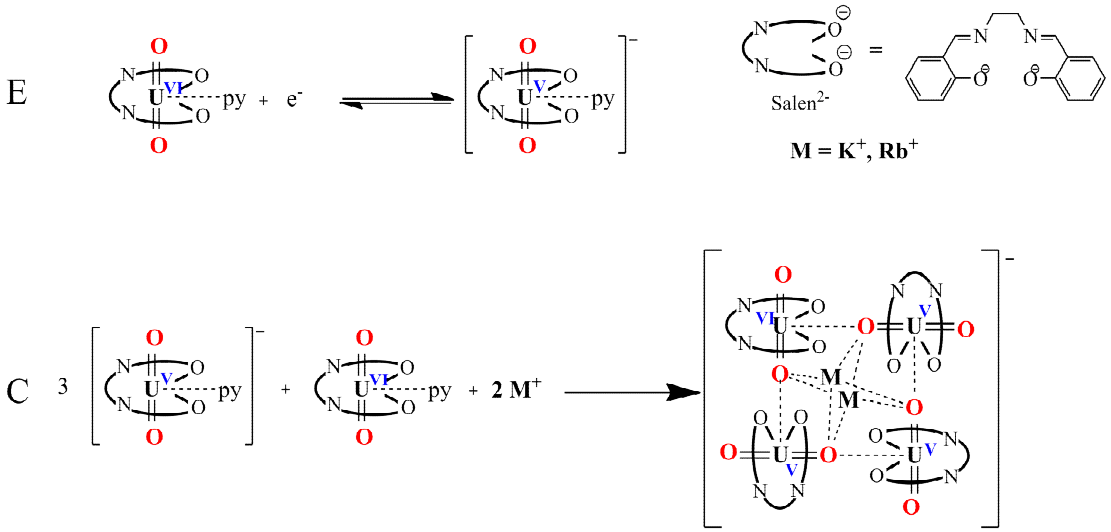

While addition of RbI afforded a very similar behaviour with a shift of the anodic peak from -1.6 V to -1.2 V, the addition of NaI and LiI resulted in a very different behaviour. As observed on the cyclic voltamogramms presented in Figure II-20, the addition of one equivalent of LiI or NaI to the solution resulted in the shift of both oxidation and reduction waves. The case of lithium is very different from the behaviour observed with potassium and rubidium: the cathodic peak is shifted from -1.7 V to -1.5 V, which indicates that the reduction of uranyl(V) (step E of Scheme II-11) is facilitated by the presence of lithium cations. This fact can be rationalised by the interaction of the acidic lithium cations with the uranyl oxos, weakening the U=O bonds, thus rendering the uranium centre easier to reduce. The large ΔE between the cathodic and the anodic peak indicates that the system probably still undergoes an EC-type process, but the different shape of the anodic peak suggests a different C step in the case of lithium.

The behaviour in presence of NaI appears to be intermediate between the behaviour in presence of KI or RbI and LiI, with two anodic peaks observed.

These preliminary electrochemical studies provide important information on the stability of the tetrameric assemblies, which form in situ through an EC process even in presence of a

stoichiometric amount of alkaline ions. Moreover, the very different behaviour in presence of lithium is in agreement with the instability observed for the uranyl(V) salen complex in presence of lithium described in part II.2.1.3.4. The use of electrochemistry in presence of various ions could provide quick information on the stability of the complex formed, and could provide quick preliminary information for the rational synthesis of uranyl(V) polynuclear assemblies.

II.2.1.5 Effect of the counter ions - divalent cations

Given the critical role of the counterion in the formation and stability of cation-cation complexes of uranyl(V), we also investigated further the role of the charge and the size of the cation on the stability of the assemblies. Moreover, the use of cations with favoured coordination geometry could lead to the synthesis of polynuclear assemblies with original topologies. Finally, the combination of the properties of uranyl(V) and of the counteraction could be used to build material combining magnetic properties of the two metals.

II.2.1.5.1 *Synthesis of {[UO_2(salen)]$_4Ca_2$}*

The strategy developed previously with alkaline ion was extended to prepare cation-cation clusters with earth alkaline divalent cations, in order to determine if the charge of the cation used had an influence on both the stability and the structure of the cluster formed. In order to evaluate specifically the role of the charge in the formation of the assembly without consideration of size parameters, the reaction with divalent Calcium was investigated, since Ca^{2+} possesses a very close ionic radius to the previously studied Na^+ ion (Ionic Radius Ca^{2+} = 1.12 Å and IR Na^+ = 1.18 Å).[274]

The reaction of two equivalents of the monomeric uranyl(V) complex [UO_2(salen)(py)][Cp^*_2Co] with one equivalent of $CaCl_2$(DME) in pyridine results in the formation of the tetrameric complex {[UO_2(salen)]$_4Ca_2$}, **17,** in 70% yield (scheme 1).

Scheme II-12 Reaction of the complex $[UO_2(salen)(py)][Cp^*_2Co]$, **11** with $CaCl_2(DME)$

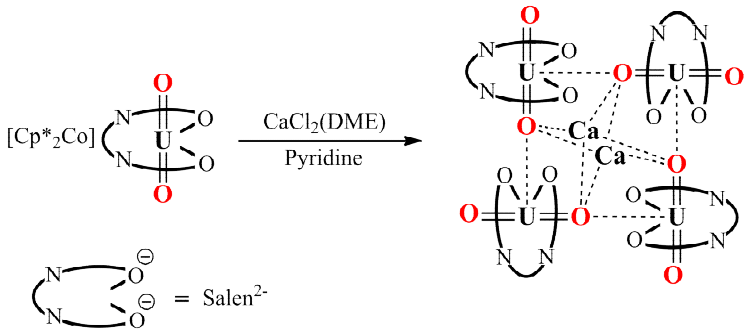

The X-ray diffraction study carried out on single crystals of **17** grown from a dichloromethane solution shows the presence of a square shaped tetranuclear structure similar to that found for the previously reported tetranuclear uranyl(V) salen complexes $\{[UO_2(salen)]_4[\mu_8\text{-}K]_2\}\cdot 2[K(18C6)(py)]$, **3**, $\{[UO_2(salen)]_4[\mu_8\text{-}Na]_2\}\cdot 2[Na(18C6)(py)_2]$, **14**, and $\{[UO_2(salen)_4][\mu_8\text{-}Rb]_2[Rb(18C6)]_2$, **15**. However some structural differences are observed as a result of the small size and of the double positive charge of the Ca^{2+} cation (Figure II-21).

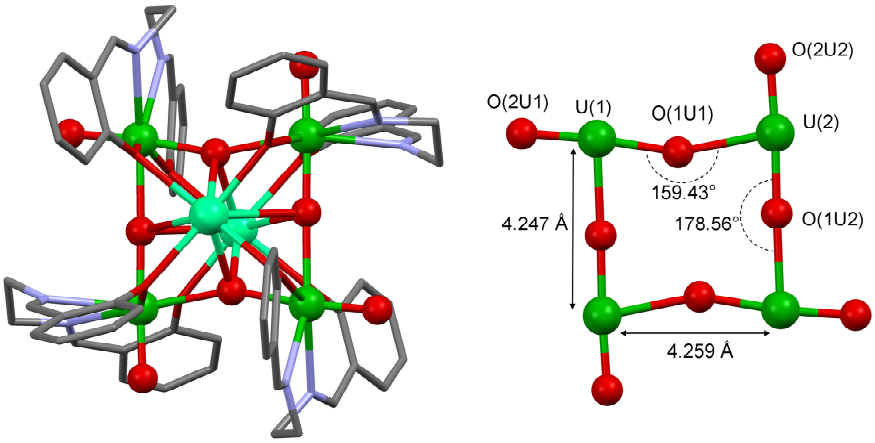

Figure II-21 Mercury view of **17** (left) and detail of the tetranuclear core (right). (Co-crystallised dichloromethane molecule and H were omitted; ligands are represented with pipes for clarity, C are represented in grey, O in red, N in blue Ca in turquoise and U in green)

Notably , in contrast with the alkaline ions centred tetramers which consist of isolated pairs of ions, in **17** the double positive charges of the central calcium ions balance the charges of the four uranyl(V) salen moieties, to give an overall neutral cluster. Similarly to the previously described clusters, the structure of **17** consists of a centrosymmetric tetrameric cluster built from UO_2^+ cations coordinated to each other in a monodentate fashion to form a square plane with two crystallographically non-equivalent uranyl complexes with two symmetry related calcium ions found respectively above and below the plane of the UO_2^+ tetrameric core. The mean values of the Ca-O_{yl} and of the Ca-O_{salen} distances (2.55(15) Å and 2.41(1) Å) are

shorter than the respective mean values of the Na-O_{yl} and of the Na-O_{salen} distances (2.82(30) Å and 2.52(7) Å). However, these shorter Ca-O values do not imply a more constrained tetrameric core, the U-U distances being longer (4.247(1) and 4.259(1) Å) for **17** than in those found in the $[UO_2(salen)]_4[\mu_8\text{-}Na]_2^{2-}$ anion in **14** (4.197(1) and 4.214(1) Å). This phenomenon can be explained by the closer distance between the calcium cation and the mean plane defined by the four uranium centres (Ca-mean plane distance = 1.82 Å) with respect to **14** (1.93 Å), leading to a less distorted core in the calcium complex. The two crystallographically independent U atoms in **17** are seven-coordinated, with slightly distorted pentagonal bipyramidal geometry, by two *trans* oxo groups, two nitrogens and two oxygens from the Schiff base ligand and one bridging oxygen from the adjacent uranyl complex. As observed for the previously reported cation-cation complexes, the $UO_2^{+\cdots}UO_2^{+}$ interaction results in a significant lengthening of the U=O bond distance for the uranyl oxygens involved in this interaction (mean U-O_{yl} 1.95(2) Å) with respect to the oxygens which do not participate to the $UO_2^{+\cdots}UO_2^{+}$ (mean U-O_{yl} 1.79(1) Å) interaction with a similar mean difference between the two U=O bonds of about 0.15 Å.

The proton NMR spectrum of solutions of **1** in pyridine displays similar features to those observed for the K and Rb adducts in agreement with the retention of the tetranuclear structure (Figure A-6). The Fourier-transform infrared (FTIR) spectrum of **17** in KBr pellets contains a band at 756 cm^{-1} assigned to U-O stretches that are weakened with respect to the uranyl(VI) analogue $[UO_2(salen)(py)]$ complex **4** (asymmetric U-O stretch at 892 cm^{-1}). These data support the pentavalent oxidation state of the isolated compound

II.2.1.5.2 ***Synthesis of $[\{[UO_2(salen)]_2Mn(py)_3\}_6]$***

Using the same synthetic strategy, the reaction of two equivalents of the monomeric uranyl(V) complex $[UO_2(salen)(py)][Cp^*_2Co]$ with one equivalent of $Mn(NO_3)_2$ in pyridine afforded a highly insoluble dark violet micro-crystalline powder. The presence of Mn(II) results in a lower solubility and stability with respect to complex **17** and attempts to re-crystallize it from dichloromethane resulted in partial decomposition as indicated by the NMR spectrum showing the presence of uranyl(VI) salen in the resulting solution. Nevertheless, crystals suitable for XRD studies were obtained by slow diffusion of a solution of one equivalent of $Mn(NO_3)_2$ in pyridine to a solution of two equivalents of $[UO_2(salen)(py)][Cp^*_2Co]$ in pyridine. Elemental analysis and magnetic data (see below) confirmed that the same species is obtained using the two methods (slow diffusion and direct reaction). X-ray diffraction studies revealed the presence of a dodecanuclear uranyl(V)

complex containing six manganese(II) centres [{[UO_2(salen)]$_2$Mn(py)$_3$}$_6$], **18** with a new wheel topology (Scheme II-13).

Scheme II-13 Synthesis of **18**

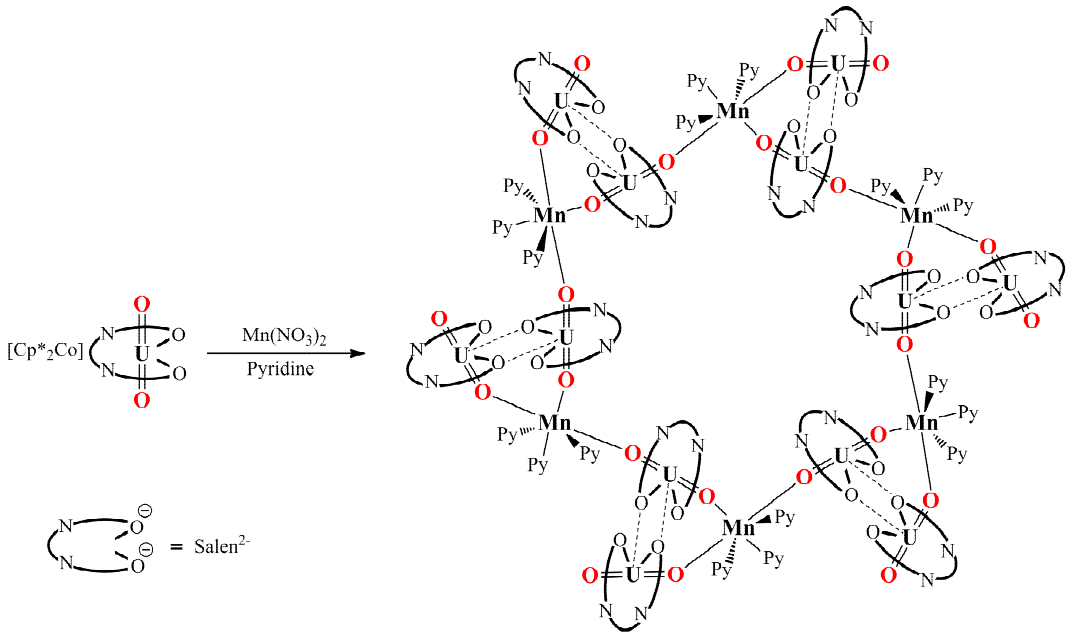

The structure of complex **18**, presented Figure II-22, totally differs from the previously reported tetramers, and represents the largest uranyl(V) cluster reported to date and the first one containing UO_2^+-Mn cation-cation interaction. Moreover, differently from all the uranyl(V) clusters previously reported **18** does not contains UO_2^+- UO_2^+ cation-cation interactions. The structure of **18** can be described as a centrosymmetric hexamer assembled from six triangles consisting of two salen bound UO_2^+ cations mutually coordinated through two salen-phenolate bridges which are both coordinated through the uranyl oxygen with the same Mn^{2+} ion. The 12 U and the 6 Mn ions are coplanar (mean deviation from the mean plane = 0.19 Å) and are arranged in a large circular array with a diameter of around 2 nm. The 2:1 UO_2^+: Mn^{2+} ratio ensures the balance of charges and affords a neutral cluster. The six triangles are connected together to yield the final $U_{12}Mn_6$ wheel through the cation-cation interaction of the manganese ion from one triangle with the uranyl oxygen of an adjacent triangle. As a result both uranyl oxygens are bound by a Mn(II) ion for six uranyl(V) complexes while for the remaining six only one of the two uranyl oxygens is Mn bound. Each Mn(II) ions is six-coordinated by three pyridine nitrogen and by three uranyl(V) oxo groups from three different uranyl(V)-salen complexes, of which two belong to the same triangle.

The overall geometry of the wheel results in a mean value of the U-U distances (3.92(1) Å) slightly shorter than those found in the tetrameric assemblies.

The original topology of the structure of **18** compared to the previously obtained dinuclear and tetranuclear cation-cation complexes is most likely the result of a combination of two structure directing parameters, the divalent charge of the Mn^{2+} ion associated to the strong preference of divalent manganese for an octahedral geometry in the present reaction conditions. The UO_2^+: Mn^{2+} cation-cation interaction plays here the structure directing role. Moreover, the used 2:1 UO_2^+: Mn^{2+} ratio likely plays a role in the geometry of the complex. This complex represents the first example of uranyl(V)-Mn(II) cluster compound. In contrast to previously reported uranyl(V) tetramers compound **18** does not contains UO_2^+-UO_2^+ interactions but is exclusively built from the functionalization of the uranyl-oxo group by a Mn(II) ion. This provides more insight into the structure directing parameters and open new routes of access to a rich variety of new topologies. Moreover **18** is the largest uranyl(V) cluster reported to date with an original wheel topology which complements the previously reported structures.

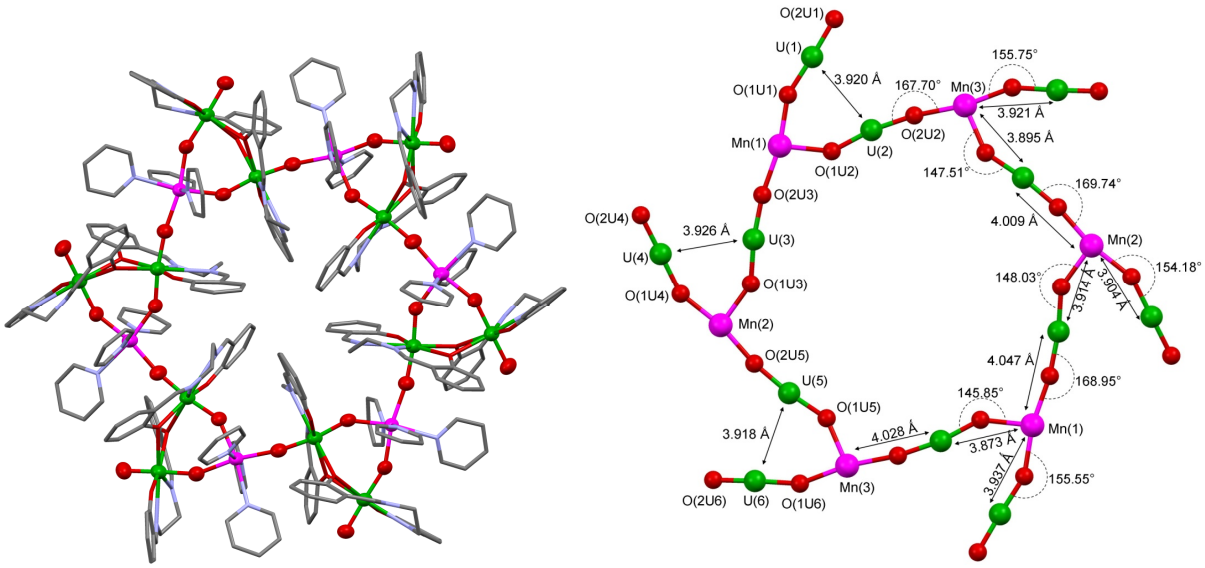

Figure II-22 Solid state structure of [{[UO_2(salen)]$_2$Mn(py)$_3$}$_6$], **18.** Ellipsoid plots at 50 % probability of **18** (top) and detail of the core (bottom). (Co-crystallised pyridine molecules and H were omitted and ligands are represented with pipes for clarity, C are represented in grey, O in red, N in blue Mn in pink and U in green)

The FTIR spectrum in KBr pellets of X-ray quality crystals of **18** prepared by the slow diffusion method is identical to the one of the bulk dark violet microcrystalline powder. The spectrum shows similar features to the previously reported tetramers with a band at 752 cm^{-1} assigned to uranyl(V) U-O stretches.

II.2.1.6 Solid state structural studies of the tetrameric cation-cation complexes

We have carried out a structural comparison between the many cation-cation complexes isolated in this work, in order to identify trends in the structural parameters in function of the ligand and counterion used. Moreover, these data give insight on the CC intermediates involved in the disproportionation of uranyl(V) and provide interesting information to relate the structure of the CC intermediate to the stability of the complexes.

II.2.1.6.1 *Tetrameric complexes*

The structural parameters of the 8 uranyl(V) tetramers described in the previous section are compared in Table II-6.

Table II-6 Selected bond distances (Å) and angles (°) in complexes **14**, **3**, **15**, **17, 6**, **8**, **10** and **7**

Distance (Å)	14	3	15	17	6	7	8	10
U(1)-O(1U1)	1.961(12)	1.936(5)	1.928(9)	1.962(13)	1.937(11)	1.912(11)	1.942(3)	1.893(18)
U(1)-O(2U1)	1.833(12)	1.841(5)	1.836(10)	1.797(13)	1.853(12)	1.768(11)	1.871(4)	1.848(17)
U(1)-O(1U2)	2.361(13)	2.421(5)	2.414(9)	2.317(10)	2.344(9)	2.373(9)	2.404(3)	2.417(18)
U(1)-O(1)	2.356(13)	2.358(6)	2.356(11)	2.361(11)	2.366(13)	2.373(9)	2.295(3)	2.290(18)
U(1)-O(2)	2.347(14)	2.342(6)	2.321(11)	2.379(10)	2.341(12)	2.374(9)	2.346(3)	2.317(17)
U(1)-N(1)	2.599(18)	2.671(7)	2.614(11)	2.544(13)	2.629(15)	2.401(10)	2.598(4)	2.63(2)
U(1)-N(2)	2.640(17)	2.594(7)	2.625(7)	2.545(16)	2.572(15)	2.558(10)	2.666(4)	2.66(2)
U(2)-O(1U2)	1.901(13)	1.909(5)	1.909(9)	1.930(10)	1.973(9)	1.909(10)	1.954(3)	1.972(18)
U(2)-O(2U2)	1.822(12)	1.840(5)	1.882(8)	1.786(13)	1.858(11)	1.799(9)	1.818(3)	1.827(16)
U(2)-O(2U1)	2.350(12)	2.374(5)	2.419(9)	2.365(12)	2.403(11)	2.375(9)	2.374(3)	2.321(18)
U(2)-O(21)	2.350(12)	2.348(6)	2.351(12)	2.369(10)	2.372(12)	2.375(9)	2.365(3)	2.294(18)
U(2)-O(22)	2.336(14)	2.386(6)	2.334(11)	2.396(10)	2.367(13)	2.405(11)	2.370(3)	2.334(17)
U(2)-N(21)	2.378(13)	2.630(7)	2.721(12)	2.535(17)	2.542(16)	2.408(11)	2.617(4)	2.682(19)
U(2)-N(22)	2.575(15)	2.631(6)	2.625(14)	2.579(18)	2.444(15)	2.550(13)	2.660(4)	2.68(2)

Angle(°)	14	3	15	17	6	7	8	10
O(1U1)-U(1)-O(2U1)	177.4(6)	176.9(2)	175.3(3)	177.1(7)	177.4(5)	179.3(4)	175.37(14)	177.4(8)
O(2U2)-U(2)-O(1U2)	174.9(5)	176.2(2)	177.1(5)	174.6(5)	179.3(5)	179.2(4)	174.72(15)	177.6(7)
U(1)-O(1U1)-U(2)	162.6(6)	171.0(3)	171.2(6)	178.5(8)	175.0(7)	173.4(5)	154.39(18)	178.2(8)
U(2)-O(1U2)-U(1)#1	153.4(7)	165.6(3)	171.2(4)	159.4(7)	172.2(6)	173.4(4)	155.33(16)	173.4(10)

#1 = Element generated by the symmetry operation -x+1,-y,-z+2

II.2.1.6.1.a Variation of the counterion

Four uranyl(V) salen tetramers with different central counterions were isolated, and allow the evaluation of the influence of the central ion on the final structure parameters. The comparison of the structural parameters of the core defined by the four uranyl moieties is given in Figure II-23. These data, and especially the average U-U distances, indicates that the ionic radius of the central counterion clearly influence the U-U distance within the tetrameric assembly. This is especially visible when comparing the tetramers **14**, **3** and **15**, with respective Na+, K^+ and Rb^+ counterions, with an average decrease of the U-U distance of around 0.05 Å when going from Rb^+ to K^+ or of 0.1 Å from K^+ to Na^+. However, the only comparison of the U-U distances does not seem accurate enough to provide quantitative information on the strength of the CCI, since distortion from planarity of the tetrameric core can significantly change the U-U distances. This observation is particularly relevant when comparing the Na^+ tetramer with its Ca^{2+} analogue. While the ionic radius of Ca^{2+} is smaller than the Na^+ one, the U-U distances are slightly longer in the case of the tetramer **17.** Thus, the comparison of the metric parameters of the bridging oxos appears to be a more accurate parameter to describe the strength of the CCI.

As indicated above, for all CC complexes**,** the $UO_2^{+\cdots}UO_2^+$ interaction results in a significant lengthening of the U=O bond distance for the uranyl oxygens involved in this interaction (noted here U=O--). The distance between that oxygen and the adjacent uranyl moiety (noted here U=O--) can also significantly vary depending of the strength of the interaction (Table II-7). These values clearly show that a decrease of the ionic radius (or an increase of the density of charge) of the central ion implicate a lengthening of the U=O-- bonds accompanied by a shortening of the U=O-- bonds, which can be interpreted as a strengthening of the CCI. This fact is likely to be one of the factors explaining the disproportionation observed in presence of Li^+ counterions described in part II.2.1.3.4.

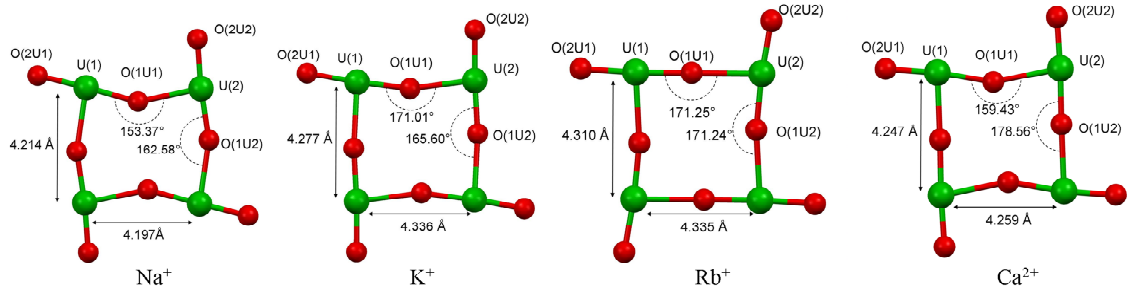

Figure II-23 Metric Comparison of the tetrameric core with different counterions showing the interacting UO_2^+/UO_2^+ with associated distances and angles. From left to right, **14**, **3**, **15** and **17**. The structures are represented along the axis formed by the two potassium ions which are in apical positions with respect to the plane of the uranium atoms.

Table II-7 Comparison of the ionic radius, density of charges[274] of the central cations with the average uranium-oxygen distances involved in the CCI

Angle(°)	**14 (Na^+)**	**3(K^+)**	**15(Rb^+)**	**17(Ca^{2+})**
Ri (´)	1.18	1.51	1.61	1.12
ρ (e*C/ ´3)	0.145	0.069	0.045	0.17
Av U=O--	1,931	1,923	1,919	1,946
Av U=O--	2,356	2,398	2,417	2,341

II.2.1.6.1.b Variation of the ligand

The isolation of four tetrameric uranyl(V) complexes with analogous potassium centered cores and decorated by the Schiff bases ligands acacen, salen, salophen and dophen have been described above. These complexes allow the comparison of the core parameters in function of the ligand employed. The tetrameric core of the complexes **6 , 3, 8** and **10** are presented in Figure II-24, and are ranked, from left to right, from the less aromatic acacen to the fully delocalised dophen ligand. It appears at the first sight of these structures that no trend can be easily established to explain the metric parameters of the uranyl core. While the tetrameric cores of the acacen, salen and dophen tetramers **6 , 3** and **10** possess similar parameters, the tetrameric core of the salophen complex **8** appears much more distorted and present shorter U-U distances. Moreover, differently to what has been observed in part II.2.1.6.1.a the comparison of the bridging oxygen-uranium distances given in Table II-8 does not allow a better rationalisation of the phenomenon observed.

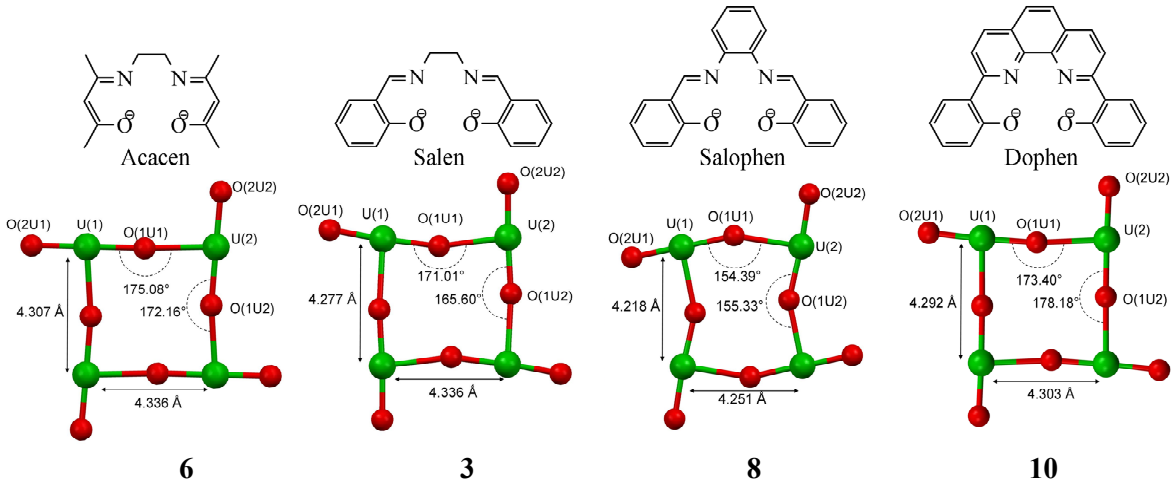

Figure II-24 Metric comparison of the tetrameric core with different ligands showing the interacting UO_2^+/UO_2^+ with associated distances and angles. From left to right, **6** , **3**, **8** and **10**. The structures are represented along the axis formed by the two potassium ions which are in apical positions with respect to the plane of the uranium atoms.

Table II-8 Comparison of the average uranium-oxygen distances involved in the CCI

Angle(°)	6 (acacen)	3 (salen)	8 (salophen)	10 (dophen)
Av U=O--	1,955	1,923	1,948	1,9325
Av U=O--	2,3735	2,398	2,389	2,369

However, several factors could explain the difference found in the metric parameter of the square core of **8** with respect to the tetrameric complexes **6 , 3** and **10**. The shorter U-U distance in **8** can be related to the presence of two additional potassium ions bridging the uranyl groups in **8** with respect to the other complexes (Figure II-9). As a result of the potassium coordination the core geometry in **8** is significantly distorted from a square. The distortion of the core observed in **8** could play a role in the low stability of the pentavalent uranyl in such tetrameric cation-cation complex resulting in its rapid disproportionation. Moreover, a large number of other factors can come into play here, such as the ligand geometry: while the salophen and the acacen ligands adopt a so-called “boat” conformation [270, 271], the salen and dophen coordination in the tetrameric complexes is almost planar.

One of the main contribution to the stability and structural properties of these complexes may result from different electronic structures for these complexes; in particular partial π-back donation from uranyl(V) to the ligand had been observed in recent DFT studies.[272] Future work will thus be directed to investigate the electronic structure of these complexes.

II.2.1.7 Homometallic assemblies

In all the structures presented previously, or in the few examples described in the literature, the reported CCI complexes of pentavalent uranyl are all heterobimetallic with the uranyl oxygens coordinated to alkali,[172] lanthanides[178] or d-block metal cations[177] which play an important role in determining the structure and the stability of the final complex.

In order to avoid the presence of additional counterions, the ligand used to coordinate the uranyl(V) ion should not possess more than one negative charge per uranyl ion. This requirement could be achieved by using monoanionic ligands, that should also meet the requirements formulated in part II.2.1.1, with an optimal tetradentate coordination pocket, in order to leave one coordination site available for CCI.

II.2.1.7.1 *Synthesis of {[UO_2(L)]$_3$*

These studies were carried out in collaboration with Lucile Chatelain, who carried out her M2 internship in our lab in 2011. The reaction of the UO_2^+ precursor $[(UO_2py_5)(KI_2py_2)]_n$,[170] with the potassium salt of the tetradentate aza β-diketiminate ligand, LK (L=2-(4-Tolyl)-1,3-bis(quinolyl)malondiiminate)[275] in pyridine leads to the immediate formation of the insoluble complex of pentavalent uranyl $[UO_2L]_3$, **19** as a dark red powder (Scheme II-14).

Scheme II-14 Synthesis of **19**

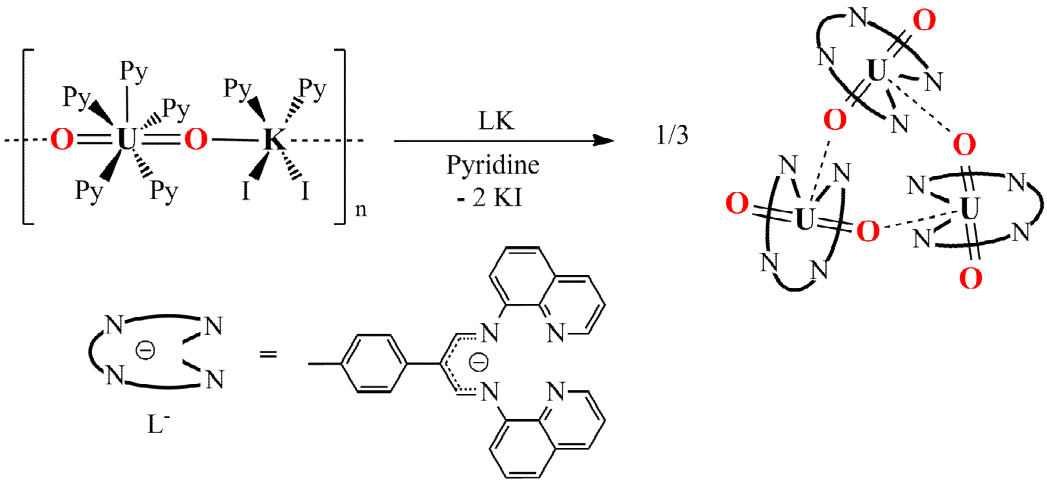

The crystal structure of **19**, determined by single crystal X-ray diffraction, is presented in Figure II-25. The crystal structure of **19** presents a trimeric unit consisting of uranyl moieties coordinated to each other to form an equilateral triangle of sides 4.19(2) Å long with a mean U-O-U angle of 156.1(11). Each uranium atom in the trimer has a pentagonal-bipyramidal

coordination with the four nitrogen atoms from the aza β-diketiminate ligand (mean U-$N_{dikeiminate}$ 2.53(1) Å; mean U-$N_{quinoline}$ 2.62(1) Å) and the bridging uranyl oxygen from the adjacent uranyl group (mean U-O 2.37(1) Å) in the equatorial plane. The environments of the three uranium atoms are equivalent with a pseudo threefold axis located in the centre of the equilateral triangle. This is the first example of a triangular geometry for cation-cation complexes of pentavalent uranyl. A similar triangular geometry has been previously reported only for the trimeric complex of uranyl(VI) $[UO_2(hfa)_2]_3$[145] and the neptunyl(V) oxalate complex $NH_4[NpO_2(C_2O_4)]$ both containing a cation-cation interaction.[46]

The uranyl groups in **19** remain nearly linear (mean O-U-O angle 176.6(2) °)) with terminal uranyl bond distances (mean U-O2 distance 1.84(1) Å) shorter than the bridging uranyl bonds (mean U-O1= 1.92(2) Å) similarly to that found in the previously reported CCI complexes. The trimer formation does not result in a significant modification of the aza β-diketiminate ligand geometry with respect to the mononuclear uranyl(VI) analogue $[UO_2LCl]$ (presented in part II.2.1.7.2).

The mean U-U distance in the triangle (4.19(1) Å) is in the same range than the mean U-U distance found in the T-shaped cores of the salen tetramer decorated with sodium cation **14** (4.20(5) Å) but is significantly longer than the U-U distances reported for the asymmetric diamond-shaped $(UO_2)_2$ cores found in the dimers $[UO_2(dbm)_2K(18C6)]_2$ (dbm^- = dibenzoylmethanate) and in the $[UO_2(pacman)_2Sm(py)]_2$[178] complexes (U-U =3.462 Å for the dbm complex and 3.471 Å for the pacman complex).

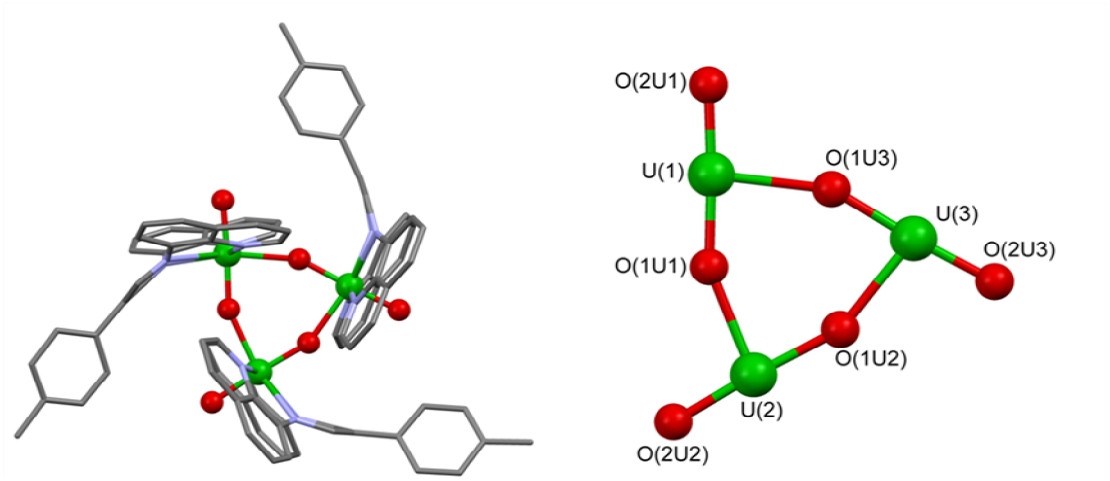

Figure II-25 Mercury plots of **19** (left) and of its uranyl core (right). (Ligands were represented in pipes, H and co-crystallised solvent molecules were omitted for clarity, C atoms are represented in grey, O in red, N in light blue and U in green.) Selected bonds lengths (Å) and angles (°): U(1)–O(1U1).1.842(10), U(1)–O(2U1) 1.905(10), U(1)–O(1U3) 2.374(8) ; O(1U1)–U(1)–O(2U1) 176.7(4);O(1U1)-U1-O(1U3) 84.2(3), O(2U1)-U1-O(1U3) 99.0(3); U(1)- O(1U1)- U(2) 157.1(5).

Proton NMR of the complex in pydine-d_5 revealed the presence of 10 isolated peaks in the area -13 – 9 ppm, accounting for the 10 protons of the ligand in a symmetrical environment.

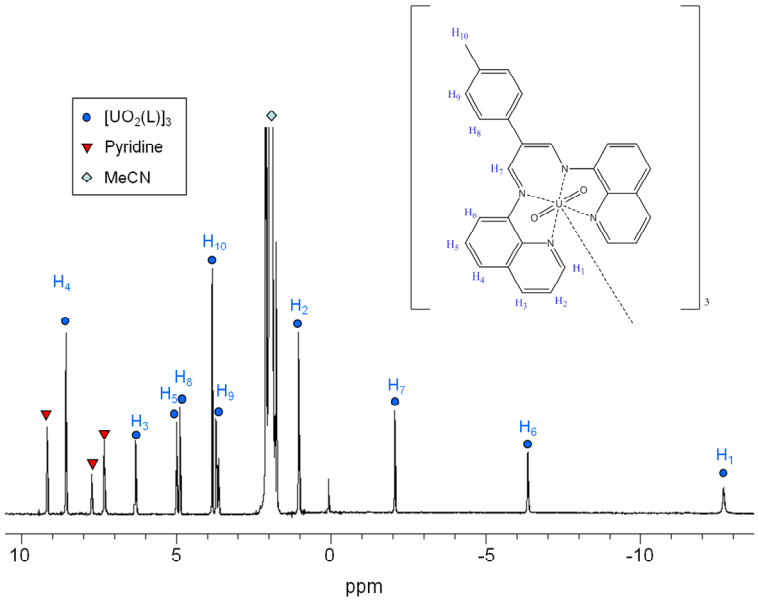

Figure II-26 Proton NMR spectra at 400 MHz and 298 K of **19** in d_3- acetonitrile.

ESI-MS spectroscopy (m/z = 2051,0 corresponding to the protonated complex $[UO_2(L)]_3H^+$) is in agreement with the presence of a trinuclear complex in gas phase (Figure II-27). Pulsed-Field Gradient STimulated Echo (PFGSTE) diffusion NMR was used to measure the diffusion coefficient (D) of **19** in pyridine solution using the mononuclear $[UO_2(L)Cl]$ complex in pyridine as an external reference.[276] The spherical hydrodynamic radii calculated from the measured diffusion coefficient using the Stokes-Einstein equation indicate that complex **19** retains its trinuclear form in pyridine solution (Table II-9).

Table II-9 Diffusion coefficient values of **19** and **20** and estimated spherical radii.

Solvent	Compound	D [$m^2.s^{-1}$]	r_{sph} [Å]$_{exp}$	r_{sph} [Å] (evaluated from crystal structure)
Pyridine η=0.879 mPa.s	**19**	$4.91(10).10^{-10}$	5.1	6.04
	20	$10.11(3)\ 10^{-10}$	2.5	3.31

This suggests that the mutual coordination of the uranyl ions is competing with the coordinating pyridine solvent. This differs from what had been observed with the Schiff base ligands in part I.1.1.1 showed that CCIs leading to polymetallic compounds occurred only in

the presence of alkali metal ions. In the absence of alkali metal ions only the formation of mononuclear complexes was observed. The stronger cation-cation interaction found in **19** arises probably from the higher positive charge on the metal centre in this neutral complex with respect to the anionic Schiff base complexes presented in part I.1.1.1.

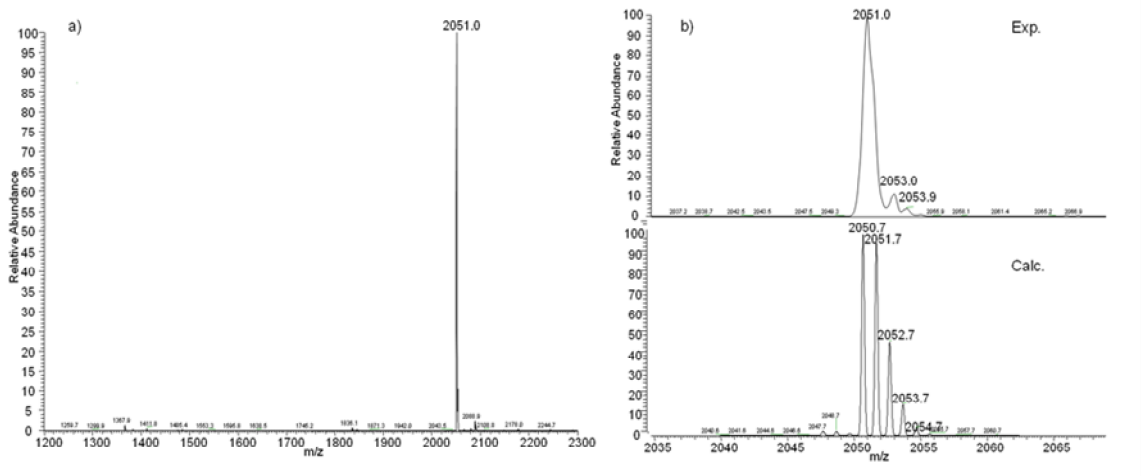

Figure II-27 ESI/MS spectra of **19** in acetonitrile (a), and (b) zoom on the molecular peak compared with the theoretical isotopic profile calculated for $\{[UO_2(L)]_3\text{-}H^+\}$

When **19** is dissolved in the more coordinating dmso solvent, a new set of signals appears in the proton NMR spectrum which were assigned to the monomeric dmso adduct $[UO_2(L)(dmso)]$ (Figure II-28). This indicates that dmso partially disrupts the trimeric assembly by competing with the uranyl oxo group for the coordination of the uranyl moiety in the equatorial plane. However, this monomer is only stable in dmso, and when the sample in dmso is taken to dryness and redissolved in acetonitrile or pyridine, the original proton NMR spectra of $[UO_2(L)]_3$ is restored, indicating that the dissociation process is reversible.

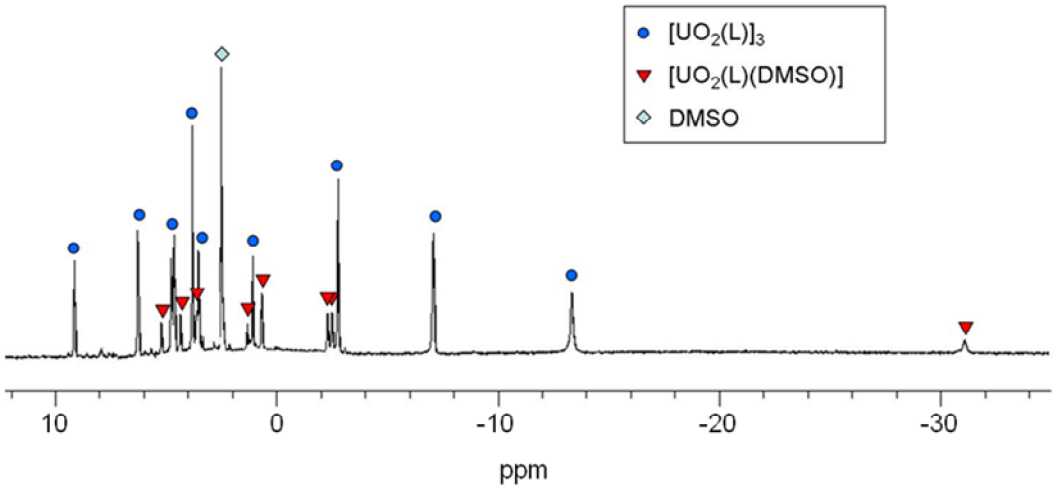

Figure II-28 Proton NMR spectra of $[UO_2(L)]_3$, **19** at 200 MHz and 298 K in dmso after 5 minutes (0.5 mM).

Since complex **19** is highly stable with respect to the disproportionation process it is particularly suited for reactivity studies. Preliminary studies show that complex **19** is highly reactive towards oxidizing agents.

II.2.1.7.2 *Synthesis of [UO_2LCl]*

Complex **19** reacts very rapidly with CH_2Cl_2 to form the hexavalent complex [UO_2LCl], **20** probably through chloride abstraction from the solvent. Complex [UO_2LCl] can be isolated in 86 % yield as dark brown needles suitable for single crystal X-ray diffraction, by slow diffusion of hexane on a dichloromethane solution of **19.**

The crystal structure of complex **20** was determined by X-ray diffraction and is shown in Figure II-29. It shows a uranium ion in a slightly distorted pentagonal bipyramidal geometry with the two uranyl groups in axial position (U=O distances =1.757(9) and 1.785(8) Å) and the chloride and the four nitrogen atoms from the azadiketiminate ligand (mean U-$N_{dikeiminate}$ 2.47(1)Å; mean U-$N_{quinoline}$ 2.62(1)Å) in equatorial position.

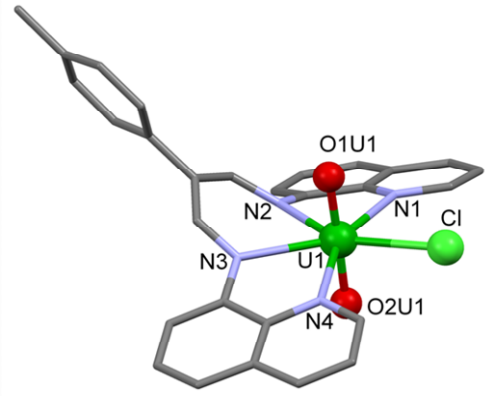

Figure II-29 Mercury plots of **20.** (Ligands were represented in pipes, H and co-crystallised dichloromethane molecule were omitted for clarity, C atoms are represented in grey, O in red, N in light blue Cl in light green and U in green.) Selected bond lengths (Å) and angles (°): U(1)–O(1U1).1.757(9), U(1)–O(2U1) 1.785(8), U(1)-Cl = 2.689(3) and O(1U1)–U(1)–O(2U1) 178.4(4).

Proton NMR indicated that the oxidation occurs within minutes after the introduction of the chlorinated solvent to yield the uranyl(VI) complex **20** as the only product (Figure II-30).

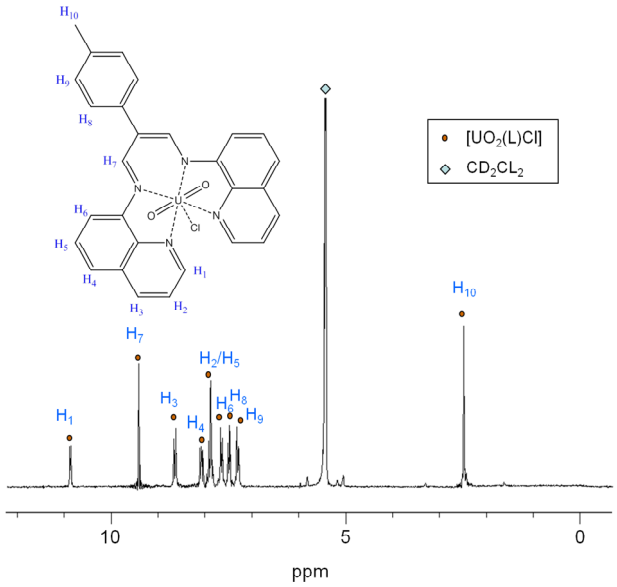

Figure II-30 Proton NMR spectra of $[UO_2(L)]_3$, at 200 MHz and 298 K in CD_2Cl_2 after 10 minutes (1 mM) yielding the U(VI) complex $[UO_2(L)Cl]$, **20**

II.2.1.7.3 *Synthesis of {[UO₂(L)]₂[μ₂-O]}*

Polynuclear assemblies are of high interest for the activation of small molecules, due to their ability to provide several electrons simultaneously. This type of reactivity is especially relevant for the reaction on substrates requiring multiple electrons transfer, such as dioxygen, and has been proven the subjects on numerous studies with transition metal complexes.[277]

The reactivity of the trinuclear uranyl(V) complex with dioxygen was thus investigated. Complex **19** thus reacts with dioxygen in acetonitrile solution to yield after two days standing under a dry O_2 atmosphere the dinuclear complex $\{[UO_2(L)]_2[\mu_2\text{-}O]\}$, **21** (Scheme II-15). Complex **21** is obtained reproducibly as dark red crystals suitable for single crystal X-ray diffraction in 72% yield.

Scheme II-15 Synthesis of **21**

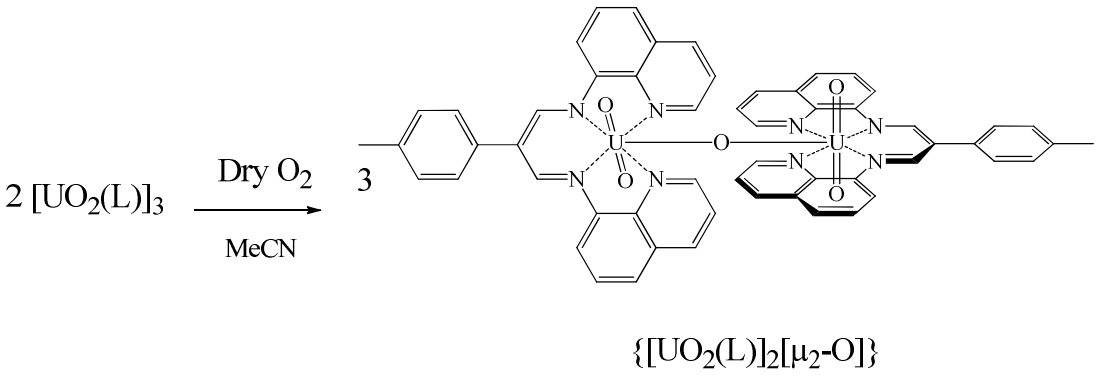

Analysis of the crystal structure of complex **21** revealed two oxo-bridged uranyl(VI) complexes arranged almost perpendicular to each other, probably to reduce steric interactions, resulting in an overall pseudo C_2 symmetry (Figure II-31). Bond valence sum calculation on the dimer confirmed the +VI oxidation states of the uranium centres and the presence of a bridging oxo.

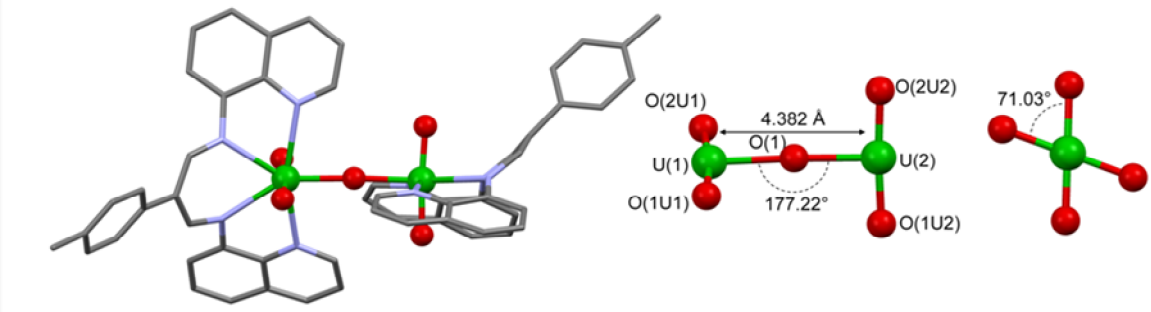

Figure II-31 Mercury plots of **21** (left) and of its uranyl core view along the b (centre) or c (right) cell axes. (Ligands were represented in pipes, H and co-crystallised acetonitrile molecules were omitted for clarity, C atoms are represented in grey, O in red, N in light blue and U in green.) Selected bonds lengths (Å) and angles (º): U(1)–O(1) 2.19(1), U(1)–O(1U1) 1.79(1), U(1)–O(2U1) 1.79(1), U(2)–O(1) 2.19(1), U(2)–O(1U2) 1.80(1), and U(1)–O(2U2) 1.82(1), O(2U1)- U(1)- O(1U1) 176.2(5); O(2U1)- U(1)- O(1) 91.7(5).

The proton NMR of **21** shows only one set of 20 signals in the diamagnetic region suggesting the presence of a rigid C_2 symmetric species in solution in agreement with the solid state structure (Figure II-32). The formation of complex **21** is also observed in moist air, but together with other products observed by NMR, which remain to be identified.

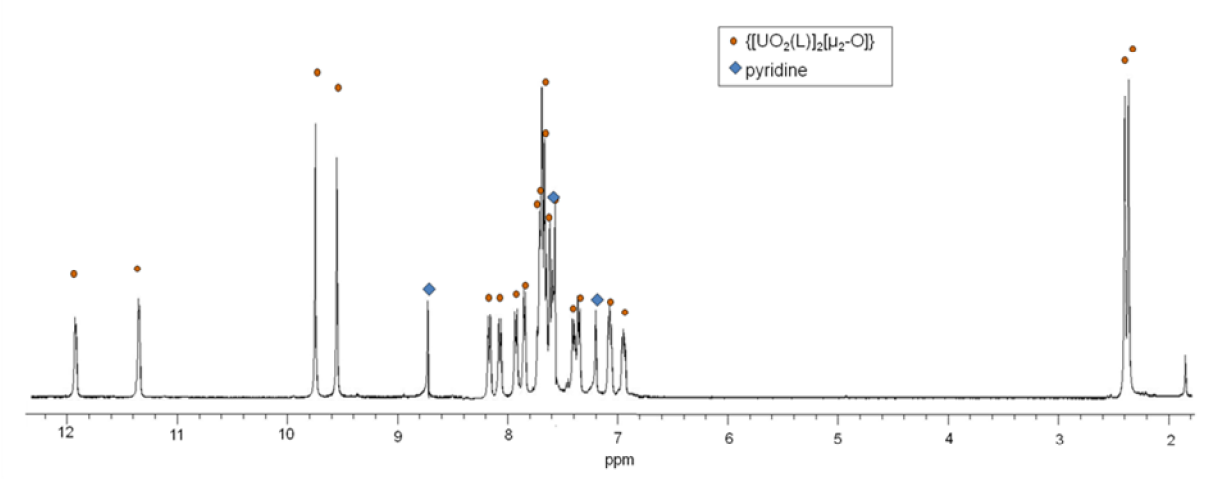

Figure II-32 Proton NMR spectra at 400 MHz and 298 K of **21** in d_5- pyridine (20 mM).

Only a few examples of uranyl oxo compounds containing μ_2-O bridging groups have been reported.[278, 279] These complexes were obtained as minor products of uranyl(VI) hydrolysis or uranyl(V) disproportionation reactions. Several well characterized examples of U(IV) μ-

oxo complexes have also been reported which were obtained from the reaction of U(III) complexes with CO_2[95], N_2O[197] or H_2O[280, 281]. Interestingly, the reaction of **19** with oxygen provides a synthetic route to uranyl(VI) oxo bridged species and shows a possible reaction pathway, which does not involve disproportionation, for the conversion of pentavalent uranyl into hexavalent uranyl in aerobic environment. Future studies will be directed to investigate the formation and the reactivity of this oxo species.

II.3 Magnetic properties

II.3.1 Electronic energy states

The ground-state electronic configuration of uranium(V) is [Rn]$5f^1$, preventing any interelectronic interaction in its open shell, and resulting in a spin orbit free ground state ^2F. This sevenfold degenerated ground state is split into two states by the spin orbit effect, a fourfold degenerate $^2F_{7/2}$ and a fivefold degenerate $^2F_{5/2}$ state, the latter possessing the lower energy according to Hund's rule[282] (Scheme II-16). Both experimental and calculations confirmed this free ion separation scheme. [283-286] Consideration of crystal field usually results in a further splitting of the $^2F_{5/2}$ and $^2F_{7/2}$ degenerated levels; which are six- and eightfold degenerated respectively[282], but keeping in mind that the half integer value of J for this $5f^1$ system implies the use of the "double group" representations to determine the irreducible representations of these states[287].

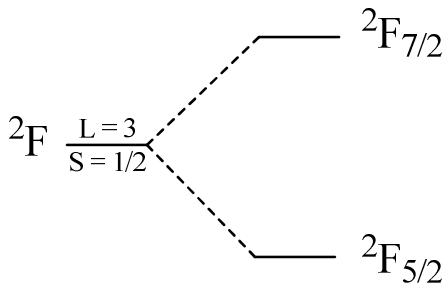

Scheme II-16 Schematic energy levels splitting from spin-orbit interaction for a $5f^1$ system.

In the case of dioxo uranium species UO_2^{n+}, the uranyl group is best considered a molecule ion which has strong intermixing of oxygen and uranium orbitals, rendering the picture not quite so simple. However, simple models for the determination of uranyl(V) ground state have been built on the basis of the model established for the UO_2^{2+} group by simple molecular orbital (MO) considerations. These calculation of the MO energy levels of uranyl were carried out using rough estimates of overlap integrals of oxygen and uranium atomic orbitals[288, 289], but these early models appeared to be quite close to the more sophisticated ones[290, 291]. As described in the MO diagram presented Figure II-33, the U-O bound in a uranyl moiety can be described simply, with strong σ bonds formed from the O 2pπ orbitals with a small participation of the uranium 5fπ and 6dπ orbitals[289]. This scheme results in a MO configuration for these bonding orbital of $\sigma_g^2\sigma_u^2\pi_g^4\pi_u^4$, all very close in energy, with a main contribution from the O 2p orbitals. The corresponding antibonding orbitals are thus mainly based on the uranium 5f and 6d orbitals, the 5fπ being the lowest in energy[288]. Of first

interest in the case of uranyl(V), in between lie the lowest unoccupied MO 5fδ and 5fφ, with a nonbonding character due to symmetry consideration with respect to the oxygen MO, and at higher energies the antibonding 5fπ and 6dδ can be observed. A very simple scheme can thus be drawn in absence of spin orbit contribution, with a theoretical triple U-O bond with one σ and two π bonds to each oxygen and the remaining electron in a 5fδ configuration for uranyl(V), most of its physical properties arising from this single electron in a pure 5f nonbonding orbital.

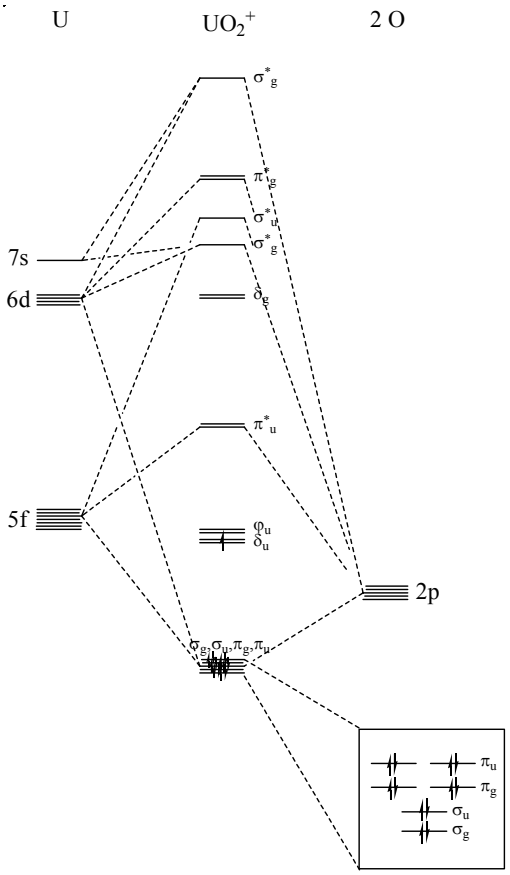

Figure II-33 Uranyl(V) spin free molecular orbital diagram

However, the 5fδ and 5fφ orbitals are very close in energy, and this spin free 5fδ configuration has no real meaning and should better be described as a $5f(\delta,\varphi)^1$ orbital. In order to determine the splitting between these orbitals, weak-field coupling interactions must be taken into account, and a number of more accurate calculations have proven that these interactions have a non negligible influence. The splitting between these orbitals is sensitive to different interactions, ranked by order of magnitude by Matsika[290]:

Axial field > electronic repulsion > spin-orbit > equatorial field

Considering this ordering for the different interactions, the case of uranyl(V) appears to be simplified, since the $5f^1$ configuration avoids the consideration of electron repulsion. Thus,

the most important interaction to consider is the spin-orbit interaction, resulting in a more important δ character of the ground state[292]. However, recent Ab Initio[293, 294] or DFT[176, 272] theoretical studies have proven that the uranyl(V) ground state can be both a 5fδ or a 5fφ orbital, depending of the equatorial ligand field interaction.

Moreover, recent calculations carried out in our laboratory have proven that depending on the ligand coordinated to the uranyl centre, the unpaired f^1electron could even be partially involved in a mixed f-π delocalized orbital arising from the ligand coordination, giving rise to a more complex description of the uranyl(V) electronic properties[272].

II.3.2 Magnetism of polynuclear uranium(V) complexes

As described in the previous section, the unique f electron in uranium(V) complexes simplifies the interpretation of their magnetic data, and this parameter has motivated the magnetic studies of several pentavalent uranium or uranyl complexes. Moreover, as stated above, the analysis of the U(V) magnetic properties could give insight into the understanding of the $5f^1$ localisation.

In addition, uranium(V) complexes possess interesting properties for the design of SMM, since the single f electron of uranium(V) implies that the degeneracy of the ground state is maintained in absence of a magnetic field (Kramer doublet). However, the S=1/2 configuration of uranium(V) is not sufficiently high to ensure a high magnetic moment to be maintained at temperatures where only the ground state is significantly populated. For this reason, we have directed our studies to polynuclear complexes presenting magnetic interactions between the metal centres.

Moreover, unambiguous evidence of magnetic communication between uranium(V) centres is rare, and limited to six examples of dimeric uranium(V) complexes[197, 204, 225, 226], which include one uranyl(V) complex.[168, 178]

This lack of magnetic studies for polynuclear uranium(V) complexes other than dinuclear, together with the potential applications for SMMs motivated the magnetic studies of the complexes presented above.

II.3.3 Magnetic properties of the tetrameric complexes

II.3.3.1 Uranyl(V) salen tetramers

Temperature dependent magnetic data were collected in the temperature range 2-300 K for all the tetramers described in the previous section. The influence of the central counterion on the magnetic properties was investigated by comparing the magnetic properties of the potassium, rubidium and calcium tetramers **3**, **15** and **17**.

The plot of χ_M versus *T* of the complexes **3**, **15** and **17** is given in Figure II-34. For these three tetramers, The χ_M versus T values increase with decreasing temperature up to a maximum reached at 5 K of the potassium tetramer **3**, at 11 K for the rubidium tetramer **15** and at 7 K for the calcium analogue **17**, and decrease with decreasing temperature under this value. These behaviours clearly indicate the presence of antiferromagnetic couplings[226] between the f^1 ions. These complexes represent the first examples of tetranuclear complex showing unambiguous magnetic coupling, although the presence of magnetic coupling at temperature lower than 2K had been suspected for the dbm tetramer isolated previously in our group.[168] At 300 K **3**, **15** and **17** display close effective magnetic moment of 1.93, 1.97 and 1.86 μ_B per uranium respectively. These values are lower than the theoretical value calculated for the free f^1 ion in the L-S coupling scheme (μ_{eff} = 2.54 μ_B) but within the range of the values reported for U(V) compounds.[168, 295, 296]

The variation of the Néel temperature with the different central cations could be the results of small differences in the structural or electronic parameters of the tetrameric core, and anticipates the possibility of establishing the first magnetostructural correlation in actinides. However, the determination of the EPR of these complexes both in solid state and solution did not allow determining their g-factors, rendering difficult the interpretation of the magnetic data.

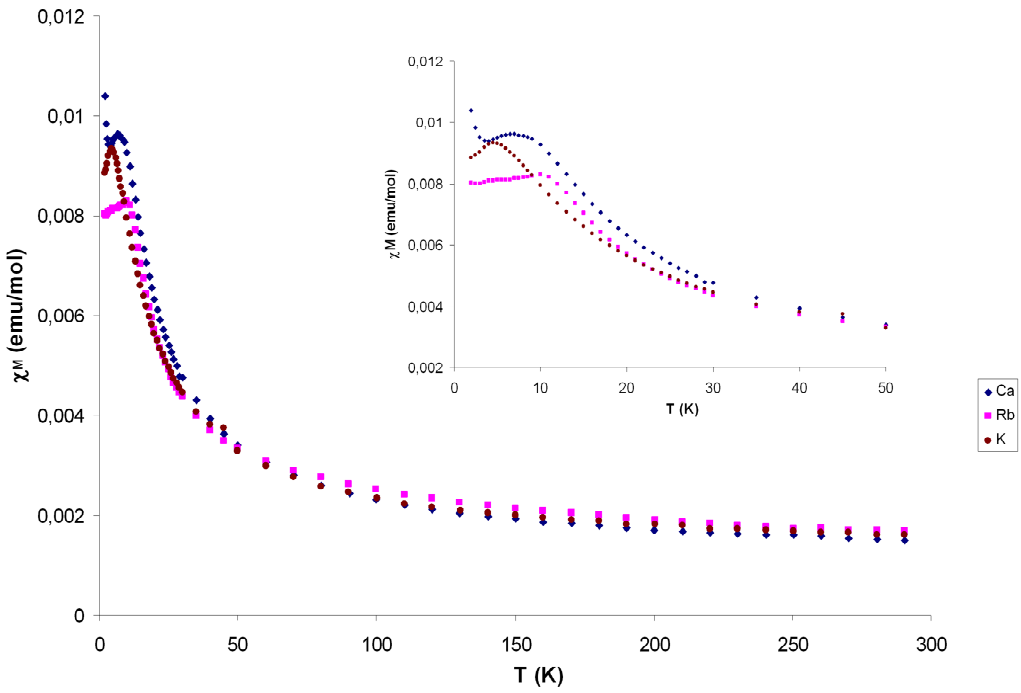

Figure II-34 Temperature-dependent magnetic susceptibility data for **3** (brown dots), **15** (pink square) an**d 17** (blue diamonds) in the range of 2-300 K and zoom of the region 2K-50K (inset). The susceptibility value is given per U(V) centre.

To characterize the relaxation of the magnetization at low temperature, we have performed a.c. magnetic susceptibility measurements on polycrystalline samples of **3** and **17** in the temperature window 2K-300K, but the data clearly indicated the absence of slow magnetic relaxation as anticipated from the antiferromagnetic character of the U-U interaction.

In order to gain insights on the coupling phenomenon within the tetrameric core, the magnetic susceptibility of the mixed valent 3U(V)/U(VI) complex **5** were measured and compared with the pentavalent precursor **3** (Figure II-35). While the magnetic behaviour of these two complexes are very similar up from 300 K to 30 K, with a very close effective magnetic moment at 300 K (1.92 μ_B per U(V) centres for **5**), a very different behaviour is observed below 30 K. While the magnetic susceptibility of the pentavalent tetramer **3** presents the signature of an antiferromagnetic coupling, the mixed valent 3 U(V)/ 1 U(VI) complex does not present a similar inflexion, and its magnetic susceptibility continues to increase with decreasing temperature. This unexpected behaviour highlights the fact that subtle electronic changes could influence the overall magnetic behaviour of the compound, which will be analysed through future DFT studies.

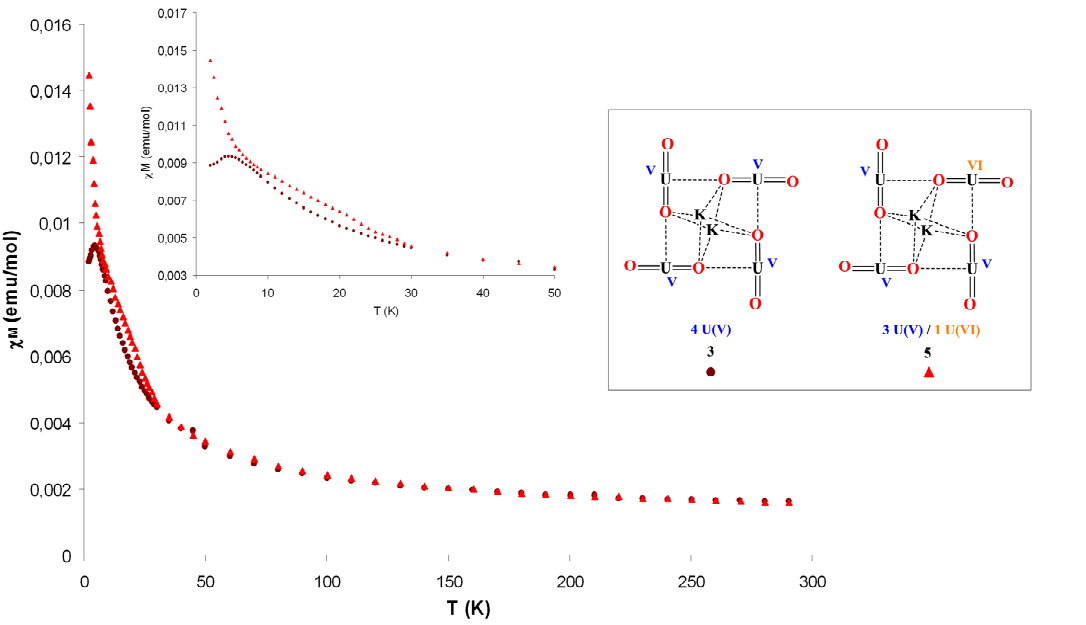

Figure II-35 Temperature-dependent magnetic susceptibility data for **3** (brown dots), and **5** (red triangles) in the range of 2-300 K and zoom of the region 2K-50K (inset). The susceptibility value is given per U(V) centre.

II.3.3.2 Uranyl(V) salophen tetramer

The magnetic behaviour of the salophen uranyl(V) tetramer **8** is essentially the same than for its salen analogue **3**, and the magnetic susceptibility measurements reveal the presence of an antiferromagnetic coupling with a Néel temperature of 5 K (Figure II-36). Despite the slightly different geometry of the cluster core in **8** with respect to **3** (average U-U distances 0.1 Å smaller and larger distortion of the square core in **8**), the two complexes seems to have very similar magnetic properties. A μ_{eff} value of 1.89 μ_B per uranium centre was measured for **8**, in the range of the previously measured tetrameric complexes.

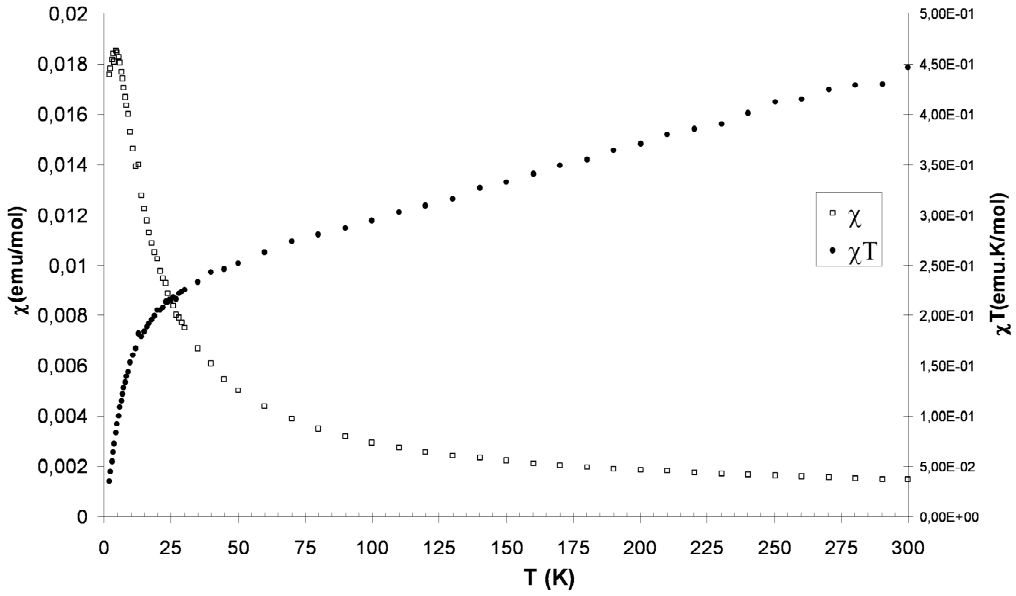

Figure II-36 Temperature-dependent magnetic susceptibility data for the tetrameric complex **8** in the range of 2-300 K. A μeff of 1.89 μB per uranium at 300 K was calculated for **8** (X_{dia} = -1.48 × 10^{-3} emu.mol^{-1}, *m=9.2* mg, *M* =4575.4 g.mol^{-1}).

II.3.3.3 Summary of the magnetic properties of the tetrameric complexes

In order to easily compare the magnetic properties of the tetrameric uranyl(V) complexes previously described, their magnetic properties, along with selected structural properties of the tetrameric core and electronic properties of the counterions is given in Table II-10. As observed from this summary table, no simple trend can be given for the analysis of the magnetic behaviour observed within this tetrameric family. Moreover, we observed that all these complexes are EPR silent, which complicates the potential fit and analysis of their magnetic properties. However, future DFT studies will be directed to identify a magneto-structural correlation in these systems.

Table II-10 Summary of selected magnetic and structural properties of complexes **3**, **5**, **8**, **15** and **17** (C indicates the charges of the central counterions, Ri and ρ their ionic radius and density of charges [274] (e=1.60218.10^{-19} C) and T_N the Néel temperature).

Complex	C (eC)	Ri (Å)	ρ (e.C/Å^3)	T_N (K)	μ_{eff}(300K) (μ_B)	Average dU-U (Å)	U-O-U angles max-min(°)
3 (K, salen)	+1	1,51	0,069	5	1.93	4.30(4)	**171.0-165.6**
5, (K, salen)	+1	1,51	0,069	x	1,92	4.28(5)	**175.1-168.9**
8 (K, salophen)	+1	1,51	0,069	5	1,89	4.23(2)	**155.3-154.4**
15 (Rb, salen)	+1	1,61	0,057	11	1,97	4.32(1)	**171.3-171.2**
17 (Ca, salen)	**+2**	**1,12**	**0,17**	**6,5**	**1.86**	**4.25(1)**	**178,6-159,4**

II.3.4 Magnetic properties of the trimer 19

The four tetramers presented above presented antiferromagnetic coupling behaviours that most probably arises from the pairwise coupling of the uranyl(V) groups along the CCIs, as schematised Scheme II-17. Assuming that T-shaped CCI give rise to antiferromagnetic coupling between the interacting uranyl(V) moiety, a symmetric triangular system could give rise to a spin frustrated system, since the full spin compensation is not achieved as a result of an odd number of spin centres, as represented Scheme II-17.[297] Triangular antiferromagnetic spin coupled motifs have been the subject of considerable attention over the past few years due to their propensity to adopt unusual, even exotic magnetic ground states which remain poorly understood and leading to unusual electronic properties.[298-302]

Scheme II-17 Schematic spin orientations for antiferromagnetically coupled centres in triangular and square based lattices

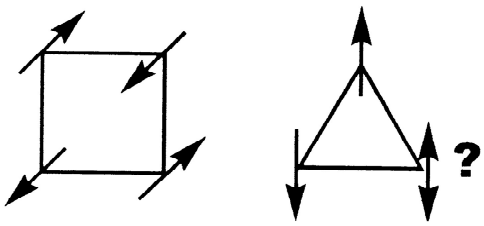

Temperature dependent magnetic susceptibility was measured for the triangular shaped complex **19** in the temperature range 2-300 K. At 300 K **19** displays an effective magnetic moment of 1.88 μ_B per uranium which is lower than the theoretical value calculated for the free f^1 ion in the L-S coupling scheme (μ_{eff} = 2.54 μ_B) but within the range of the values reported above for the U(V) tetramers. The plot of χ versus T (Figure II-37) clearly indicates the presence of an antiferromagnetic coupling between the f^1 ions with a maximum at 12 K. This is the first example of magnetic coupling in a triangular oxo bridged uranyl complex. Moreover, the maximum in the plot of χ versus T occurs at higher temperatures in the trimer **19** than in all other uranyl(V) oxo bridged complexes, suggesting a stronger coupling between the uranium ions and comparable to that found in the bis(imido) uranium(V) dimeric complex $[\{U(N^tBu)_2I(^tBu_2bipy)\}_2]$ presented in part I.4.2.2.4 presenting a short U-U distance of 3.57 Å (maximum at 13 K).[226] Interestingly, from these results it appears that the strength of the coupling in CCI complexes cannot be clearly correlated to the U-U distances since weaker coupling was observed in complexes with shorter U-U distances (shorter U-U distances are found in the $[UO_2(dbm)_2K(18C6)]_2$ complex).[168] Two parameters are likely to play a role in the enhancement of the coupling strength with respect to the previously reported tetrameric

CCI complexes: the smaller UOU angle in the trimeric complex (average 156.1(3) ° in **19**) could have a strong influence on the coupling, especially in the case of a superexchange coupling. The increased negative charge localized on the terminal uranyl oxygen atoms in the absence of coordinated cations and the electronic structure of the ligand are also likely to play an important role in the magnetic properties of **19**.

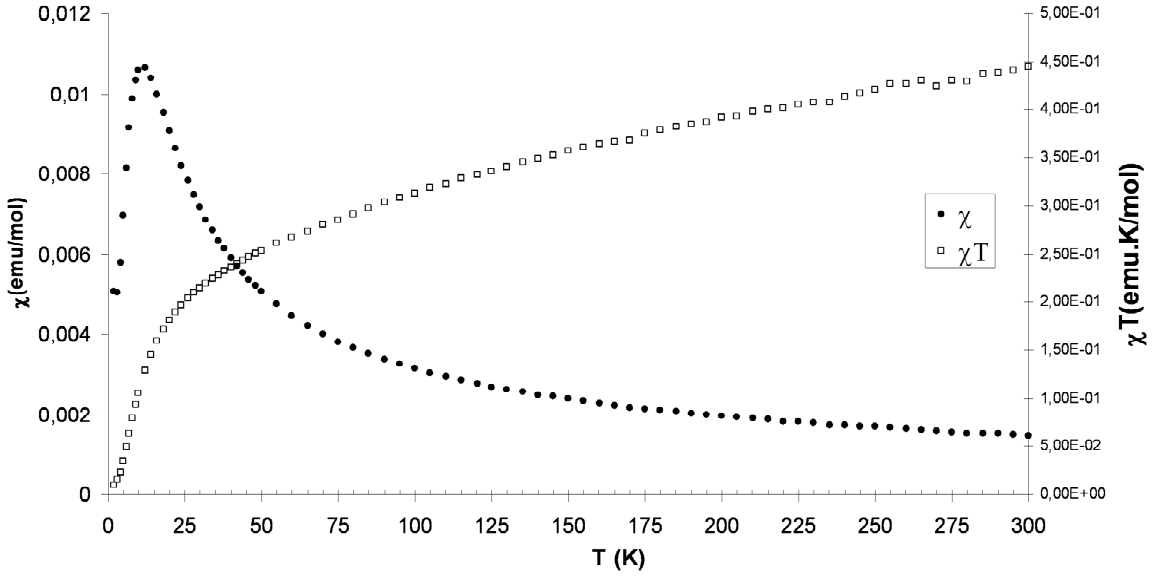

Figure II-37 Temperature-dependent magnetic susceptibility data for **19** in the range of 2-300 K. A μeff of 1.88 μB per uranium at 300 K was calculated for **19** (X_{dia} = -1.19 × 10^{-3} emu.mol^{-1}, *m=6.8* mg, *M* =2050 g.mol^{-1}).

The absence of supporting cations, the new triangular topology and the strength of the magnetic coupling renders this complex particularly suitable for investigating the mechanism and origins of the magnetic coupling.

There is a clear interest on cyclic-trinuclear metal complexes because these systems can be regarded as geometrically frustrated and offer the opportunity to test magnetic exchange models. Future work, including detailed EPR and DFT studies, will be directed to investigate the magnetic coupling in this trinuclear complex.

II.3.5 Magnetic properties of the uranyl(V)/Mn wheel shaped complex

The molecular wheel **18**, constituted of 12 uranyl(V) bound through 6 Mn bridging ions, possess the two requirements for potential SMM properties that are a high total spin with a significant magnetic anisotropy of the metal centres. Indeed, in octahedral geometry, the Mn(II) ions are very likely to be in the high spin S = 5/2 configuration, affording a potential S = 21 total spin for one wheel while the uranyl(V) atoms could provide magnetic anisotropy to the system.

The a.c. and d.c. magnetic properties of the $U_{12}Mn_6$ wheel were measured and interpreted in collaboration with the group of Pr. Caciuffo, at the ITU Karlsruhe.

Temperature dependent magnetic susceptibility was measured for the molecular wheel **18** in the temperature range 2-300 K after zero field cooling (Figure II-38). At 300 K **18** displays an effective magnetic moment of 13.5 μ_B that is 5.5 μ_B per each triangular unit which is about half the one expected for a system formed by one Mn^{II} and two U^{V} free ions. This value thus suggests that the overall exchange and ligand field splitting is much larger than 300 K.

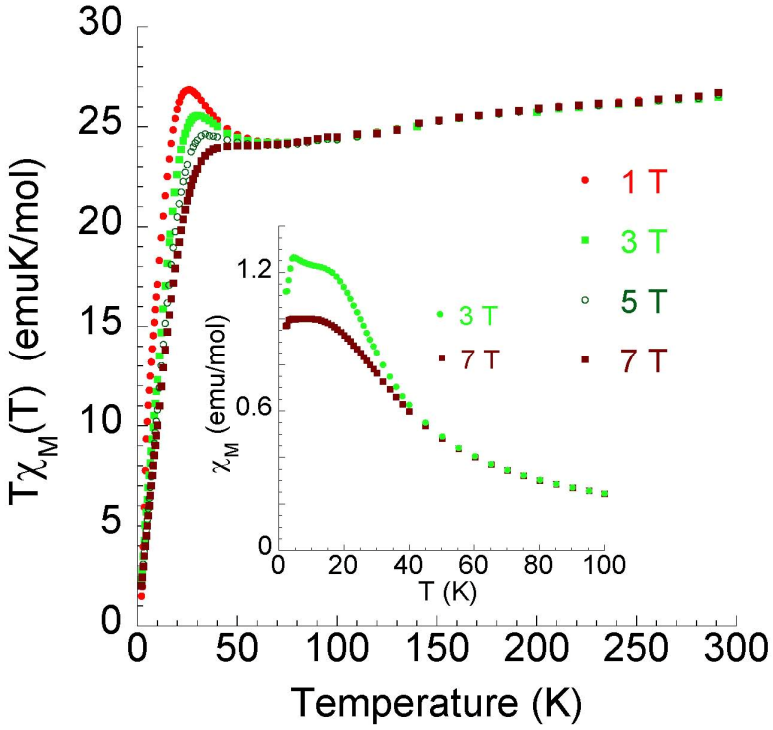

Figure II-38 Temperature-dependent magnetic susceptibility data for **18** in the range of 2-300 K The $T\chi_M(T)$ data have been collected after zero-field cooling in a magnetic field of 1 T (red dots), 3 T (green squares), 5T (open olive circles), and 7 T (brown squares). The inset shows the $\chi_M(T)$ curve between 2 and 100 in a field of 3 and 7 T. A contribution due to a ferromagnetic impurity $M_{imp} = 6.7\times10^{-3}$ μ_B/molecule has been subtracted.

The plot of χT versus T (Figure II-38) revealed three different domains. Between 300 K and 60 K the curve follows a classical Curie behaviour, but deviates below 60 K, with first an

increase of the χT value between 60 and 30 K followed by a decrease below 30 K. This magnetic response is very similar to the one reported for the triangular-shaped $\{Np^{VI}O_2Cl_2\}\{Np^{V}O_2Cl(thf)_3\}_2$ complex.[118] In that case, the observed behaviour was described as a combination of ligand field and superexchange interactions between the 5f centres. A similar scenario, applied to the compound **18** would implicate that the ground-state degeneracy of the exchange-coupled ions is lifted by the magnetic field, leading to a higher energy state with parallel U and Mn magnetic moments and a lower energy state with antiparallel orientations (Scheme II-18). The susceptibility first increases with decreasing temperature because of the higher-energy level contribution, then drops down when only the lower-energy level is thermally populated. The finite value of χT at low temperature suggests a magnetic ground state for the wheel, which is expected in presence of strong antiferromagnetic (AF) interactions between the U^{V} and the Mn^{II} centres and a weaker AF interaction between the two U^{V} centres within a triangle. However, no quantifiquation of the ligand field and exchange interactions have been proposed because the complexity of the system. Only the synthesis of an isostructural analogue with Mn replaced by a diamagnetic ion and its magnetic characterization could allow a further understanding of the phenomenon involved in this system.

Scheme II-18 Schematic representation of the field lifted degeneracy for one triangular unit (left) and of the postulated magnetic ground state of the wheel assuming strong U-Mn AF couplings (U centres are represented in green, Mn centres in pink).

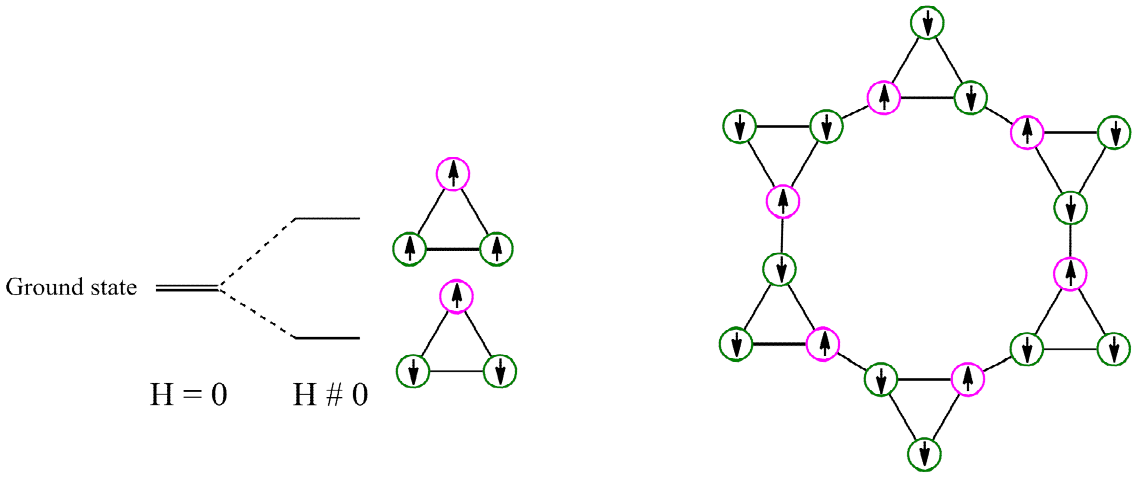

The presence of a magnetic ground state is confirmed by the observation of magnetic hysteretic loops below 4.5 K. As shown in Figure II-39, magnetic bistability is observed in the

magnetization versus applied d.c. field scan taken at 4 K. With decreasing temperature the coercivity increases, reaching a value of about 1.5 T at 2.25 K. This behaviour is typical of a single-molecule magnet below its blocking temperature T_B. [303-305] Magnetic bistability has been observed in bridged binuclear lanthanide and uranium complexes,[112, 119] and in a mononuclear Np complex.[117], but this is the first time that magnetic bistability is observed in a 5f-3d system and that magnetization loops exhibiting a non-zero coercive field and quantum steps of the magnetization are reported for a 5f system.

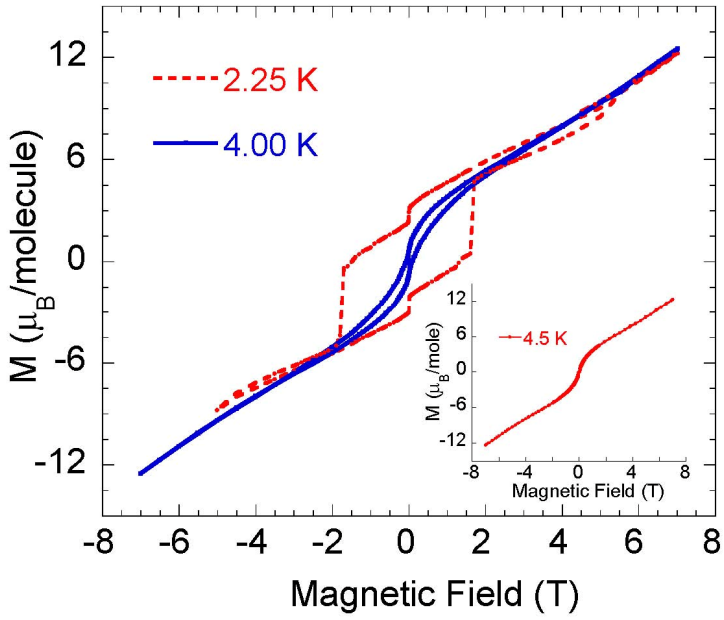

Figure II-39 Magnetization versus applied d.c. field scan measured at 2.25 and 4 K while sweeping the field from 7 to -7 T and back, with a sweep rate of 0.004 T/s. Step-like changes at periodic field values are due to quantum tunnelling of the magnetization. Data collected at 4.5 K are shown in the inset

To characterize the relaxation of the magnetization at low temperature, we have performed a.c. magnetic susceptibility measurements on polycrystalline samples in a 10 Oe a.c. field oscillating at a frequency f varying between 18 and 9887 Hz. Data have been collected either as a function of temperature, T, for a given f (Figure I-44). The in- phase component of the a.c. susceptibility, χ_M' , shows a peak at a frequency-dependent temperature reaching about 10 K at ~1 kHz, accompanied by a maximum in the out-of-phase component, χ_M'', clearly indicating the occurrence of slow magnetic relaxation. The values corresponding to the lowest temperatures, T = 4.5 K and T = 5 K, have been obtained by fitting to a single stretched exponential behaviour the time dependence of the d.c. magnetization measured with the SQUID (Figure A-13).

The relaxation behaviour can be fitted to an Arrhenius relation, $\tau = \tau_0 \exp(U_{eff}/k_BT)$, corresponding to a thermally activated regime, and a linear regression of the experimental data points provides a barrier to relaxation $U_{eff} = 142 \pm 7$ K (Figure I-44 c), close to the largest ones observed so far. [112]

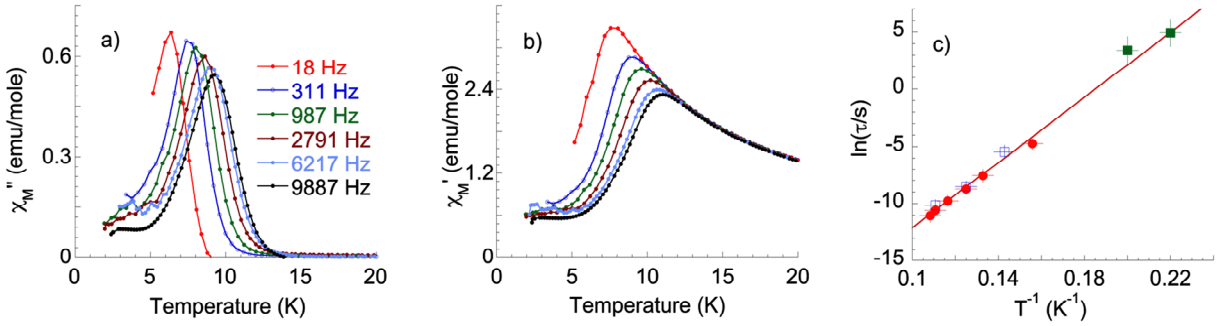

Figure II-40 Temperature dependence of the out-of-phase (χ_M'', a) and in-phase (χ_M', b) components of the a.c. magnetic susceptibility measured in a 10 G a.c. field oscillating at the indicated frequencies, under zero d.c. field. The temperature dependence of the magnetic relaxation time τ under zero-dc field is shown as ln(τ) versus T^{-1} (c), as obtained from data collected in temperature (filled circles) and frequency (open square) variation regimes. The values for the two lowest temperatures (filled square) have been obtained from time relaxation measurements of the d.c. magnetization assuming a mono-modal distribution of the characteristic relaxation rate. The straight line is a fit to the Arrhenius relation, giving a thermal energy barrier for the relaxation $U_{eff} = 142 \pm 7$ K

This $U_{12}Mn_6$ wheel is the first 5f-3d based molecular complex exhibiting single molecule magnet properties with an open magnetic hysteresis loop at low temperature, with a non-zero coercive field. Moreover, its relaxation barrier is one of the highest among any previously reported manganese wheel and among the few characterized uranium single-molecule magnet systems. The interesting magnetic properties of this $U_{12}Mn_6$ cluster suggest that the use of the anisotropy of uranium ions is a very promising path in the quest for single molecule magnets with improved properties.

II.4 Conclusions

In this chapter we have demonstrated that CCI can be a very convenient tool for the assembly of uranium(V) polynuclear assemblies. Thus, the isolation of the first stable uranyl(V) CC assembly confirmed that contrary to the common belief CCI do not necessarily lead to the disproportionation of the pentavalent precursors, and validated the use of tetradentate ligands to promote the formation of CC complexes.

Based on these observations, we have carried out a fine study of the parameters ruling the CC assembly formation on an isostructural family of uranyl(V) tetramers synthesised by a careful tuning of the ligand and counterions properties. The synthesis of this large family of tetrameric complexes of uranyl(V), and the comparison of their solution stability and structural properties laid the groundwork for a rational design of new polynuclear uranyl(V) architectures. Moreover, these tetrameric assemblies have made it possible to investigate and better understand the disproportionation mechanism in organic media, and have pointed at the critical role of protons.

Given this information, new assemblies containing three, four and twelve uranyl(V) centres have been rationally isolated through a subtle variation of the ligand and reaction conditions. A major step forward has been achieved using these new synthetic routes with the isolation of the first uranyl(V)-transition metal polynuclear assembly. Thus, the largest uranyl(V) assembly has been isolated under the original form of a $U_{12}Mn_6$ wheel shaped complex. This new architecture has been built using the preferential geometries of transition metal ions to drive the final assembly shape. Our results demonstrate that cation-cation interactions between actinyl complexes and 3d transition metal cations provide an effective way to build large heterometallic 5f-3d assemblies.

The magnetic properties of all these polynuclear assemblies were investigated, given the fact that systems with a single 5f-electron constitute the simplest examples to explore magnetic properties. Most of the complexes presented above show unambiguous magnetic couplings. The interpretation of the magnetic properties of these complexes will pave the way for the analysis of more complex systems and the elaboration of a magneto-structural correlation for uranyl(V). Moreover, the combination of the magnetic anisotropy of uranium with the high

spin number of a transition metal has lead to the synthesis of the first 5f-3d single molecule magnet, presenting a relaxation barrier among the highest reported so far, and an open magnetisation hysteretic loop below 4 K.

The isolation of uranyl(V) complexes, especially polynuclear, had been largely limited by a poor knowledge of the parameters controlling the disproportionation of uranyl(V). We have demonstrated here that a strict control of the ligand and counterion properties in organic media enable the isolation of stable polynuclear uranyl(V) complexes. Moreover, we have rationalised the parameters involved in the formation of these assemblies to build a effective synthetic route to large polynuclear uranyl(V) complexes with the ability to incorporate transition metal ions. This strategy allowed the synthesis of a single molecule magnet combining the best of 5f and transition metals elements.

Polynuclear assemblies of uranium from redox reactivity of low valent precursors

CHAPTER III. Polynuclear assemblies of uranium from redox reactivity of low valent precursors

III.1 Context

As highlighted in part I the redox reactivity of low valent uranium complexes with small molecules, solvent or simple ligand systems can lead to the isolation of polymetallic assemblies of uranium. These phenomenon of aggregations through redox processes is also observed in the environment, in geological media and during the reprocessing of spent nuclear fuel[44, 67, 70], but few rational approaches for the synthesis of uranium clusters have been developed so far. The precursor's studies of controlled hydrolysis of the cationic complex $U(tpa)^{3+}$ in organic media carried out in our laboratory allowed the isolation of an oxo uranium trimer, paving the way for larger uranium clusters synthesis through controlled hydrolysis of trivalent uranium precursors.

In the light of this result, systematic studies were carried out in our laboratory on the trivalent uranium triflate precursor $[U(OTf)_3(CH_3CN)_3]_n$ and have proven that varying the ligand and water stoichiometries could lead to the isolation of uranium oxo clusters of different nuclearities, up to 12 uranium centre per cluster. However, these synthesis were still not fully predictable, and in some cases lead to a mixture of different products. Many reaction parameters had still to be tested in order to develop a rational approach for the synthesis of uranium oxo clusters.

Our approach will thus follow two main directions: the functionalization of uranyl(V) oxos and the hydrolysis of low valent uranium precursors in presence of simple polydentate ligands

III.2 Functionalization of uranyl oxos

III.2.1 Preventing cation-cation interactions with steric bulk

As described in part II or in recent literature[177, 178], the binding of alkali, earth alkaline, d metal ions, lanthanide, or hexavalent uranyl to the pentavalent uranyl oxygen were found to play an important role in the structure, stability and properties of pentavalent complexes. However, the coordination of U(IV) to the uranyl oxygens has never been investigated, despite the importance of An(V)/An(IV) interactions in nuclear reprocessing and in actinide migration in the environment. Thus, we aim to investigate the functionalization of uranyl(V) oxo groups with uranium(IV) ions, and to use this strategy to isolate new uranium oxo clusters. Nevertheless, as described in chapter II, the presence of cations in the media also promotes the formation of CC assemblies. In order to first focus only on the uranyl(V) oxo functionalization, ligand systems preventing CCI should be used.

Strategies to prevent cation-cation interactions have been developed in the team of Hayton and in our group with the objective of isolating stable uranyl(V) monomeric complexes. Given the current understanding of the importance of cation-cation interaction in the disproportion mechanism and the electrochemical studies of uranyl(V), the directing idea to stabilize uranyl complexes followed by these two groups was to prevent the approach of uranyl(V) units through steric protection provided by sterically encumbered ligands. This would result in a kinetic stability of the uranyl(V) complex given by the increase of the cation-cation transition state's energy.

Bidentate bulky β-diketiminate Ar_2nacnac ((2,6-^{i}Pr$_2$C$_6$H$_3$)NC(Me)CHC(Me)N(2,6-^{i}Pr$_2$C$_6$H$_3$)) ligands were proposed by the group of Hayton to increase the steric hindrance and therefore prepare a more stable uranyl(V) complexes [173]. These ligands are indeed easy to synthesise, and the aryl groups, being orthogonal to the equatorial plane, provide a steric protection for the oxo ligands. The association of the Ar_2nacnac ligand with a bulky phosphine-oxide ligand lead to the uranyl(VI) $[UO_2(Ar_2nacnac)(OPPh_2Me)_2](OTf)$ complex. The reduction of this complex with cobaltocene generated the uranyl(V) complex $[UO_2(Ar_2nacnac)(OPPh_2Me)_2]$, drawn in Scheme III-1. This complex however exhibited a finite lifetime in solution, the easy loss of $MePPh_2O$ explaining that observed instability. In order to find a better co-ligand, and considering the capacity of the bidentate β-diketonate class of ligand to support uranyl(V), mixed-ligand uranyl(V) β-diketiminate/ β-diketonate complexes were envisaged by the

Hayton group. Three different UO_2^{2+} complexes were studied, with different diketonate co-ligands were thus synthesised (Scheme III-1) [174], and were successfully reduced to the corresponding uranyl(V) complexes with Cp_2Co or Cp^*_2Co. However the resulting uranyl(V) complexes still showed limited solution stability. Moreover, reactivity studies are more difficult in systems with a multiple ligand set.

Scheme III-1 Chemical structures of $[UO_2(Ar_2nacnac)(OPPh_2Me)_2]$ (left) and mixed-ligand uranyl(V) β-diketiminate/β-diketonate complexes (right)

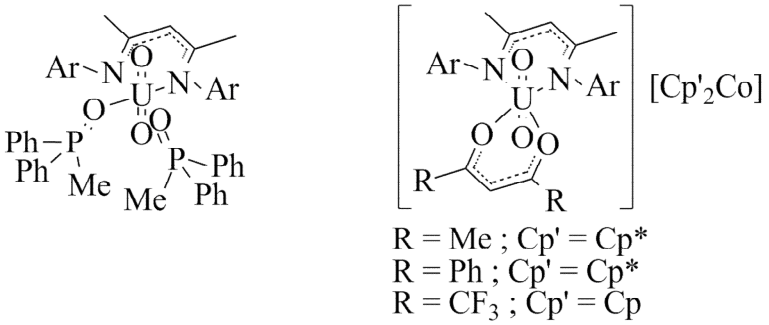

The use of high denticity ligands as opposed to bidentate ligands appears thus crucial to prevent the decomposition through a pathway requiring ligand dissociation. Interesting seminal work carried out in our group demonstrated that fully stable monomeric uranyl(V) compounds (with respect to the disproportionation reaction) could be obtained using Schiff-base derivatives and aminophenolates ligands presenting bulky groups on their phenol moieties. Coordinated to uranyl, these ligands would provide a steric protection by encumbering the equatorial plane of the uranyl moiety. The uranyl(V) complexes $[UO_2(salan\text{-}^tBu_2)(py)K]$ [175] and $[UO_2(salophen\text{-}^tBu_2)(py)K]$ [176] were thus synthesized by reaction of their respective potassium salts with the uranyl(V) precursor $[(UO_2py_2)(KI_2py_2)]$ (Scheme III-2).

Scheme III-2 Chemical structures of the uranyl(V) salan-$^tBu_2$ and salophen-$^tBu_2$ anionic complexes

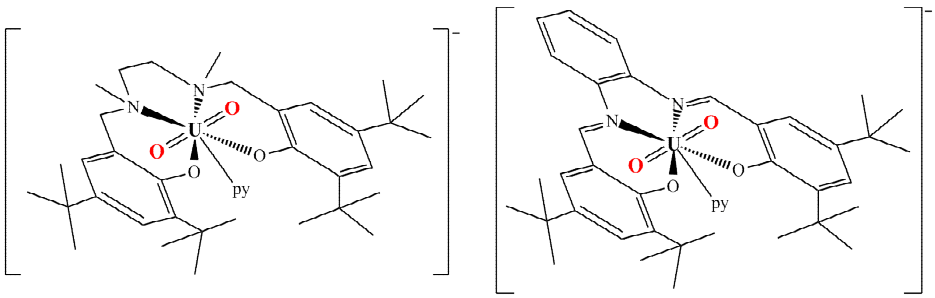

The crystal structures of these two complexes are presented in Figure III-1, and confirm the steric encumbrance of the equatorial plane of the uranyl(V) units and justify the choice of these ligands. These complexes were the first uranyl(V) complexes stable in solutions, and

demonstrated that the combination of a high denticity ligand with a fine tuning of its steric bulk could fully prevent the formation of cation-cation interactions.

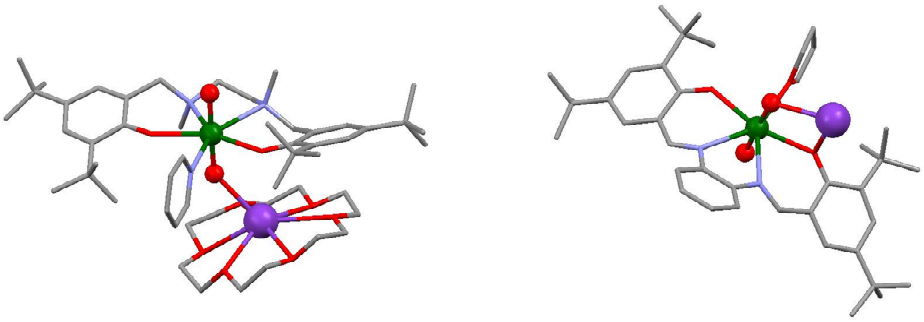

Figure III-1 Mercury views of the complexes $[UO_2(salan\text{-}^tBu_2)(py)(K(18C6)]$ (left), and $[UO_2(salophen\text{-}^tBu_2)(thf)K]$ (right). (Co-crystallised solvent molecules and H atoms were omitted. Ligands were represented in pipes for clarity, C are represented in grey, O in red, N in blue, K in purple and U in green).

III.2.2 Synthesis of a pentacoordinated uranyl complex

In order to prevent cation-cation interactions between uranyl moieties, and to only focus on the functionalization of the uranyl oxo, we also designed a model uranyl(V) complex according to an alternative approach. We target to prevent CCI via a saturation of the coordination sphere of the uranyl(V) moiety. Considering the usual pentacoordination of uranyl(V) in its equatorial plane, our strategy aimed to coordinatively saturate the UO_2^+ equatorial plane by using a pentadentate ligand. The formation of CCI for such a coordinatively saturated complex would require a ligand decoordination step, and thus a large energy.

Indeed, the reaction of the pentadentate Schiff base ligand Mesaldien ($MesaldienH_2$ = N,N'-(2-aminomethyl)diethylenebis(Salicylideneimine)) with the uranyl(V) polymer **1** afforded an uranyl(V) complex where the equatorial plane of the uranyl was fully surrounded by the ligand. The stable complex $\{[UO_2(Mesaldien)]K\}_n$, **22**, is thus prepared in 94% yield by reacting the uranyl(V) precursor $[(UO_2py_5)(KI_2py_2)]$ with one equivalent of the potassium salt $MesaldienK_2$ in pyridine (Scheme III-3).

Scheme III-3 Synthesis of **22**

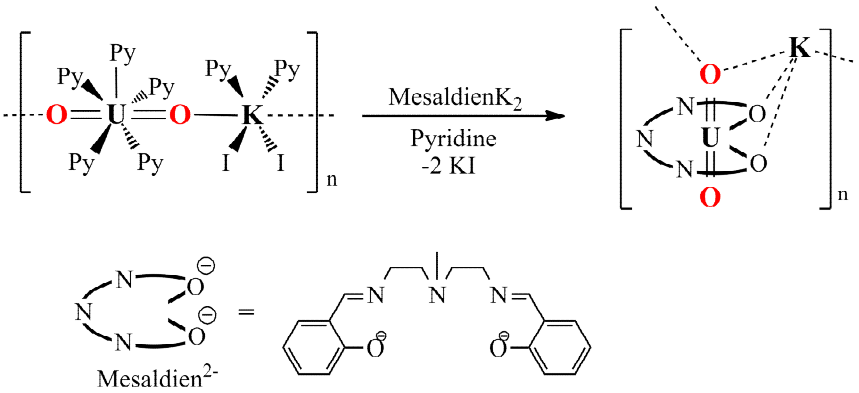

X-ray quality crystals of **22** were obtained as dark blue needles by slow diffusion of thf in a pyridine solution of **22**, and its crystal structure was determined by single crystal X-ray diffraction. A Mercury diagram of the structure is presented in Figure III-2.

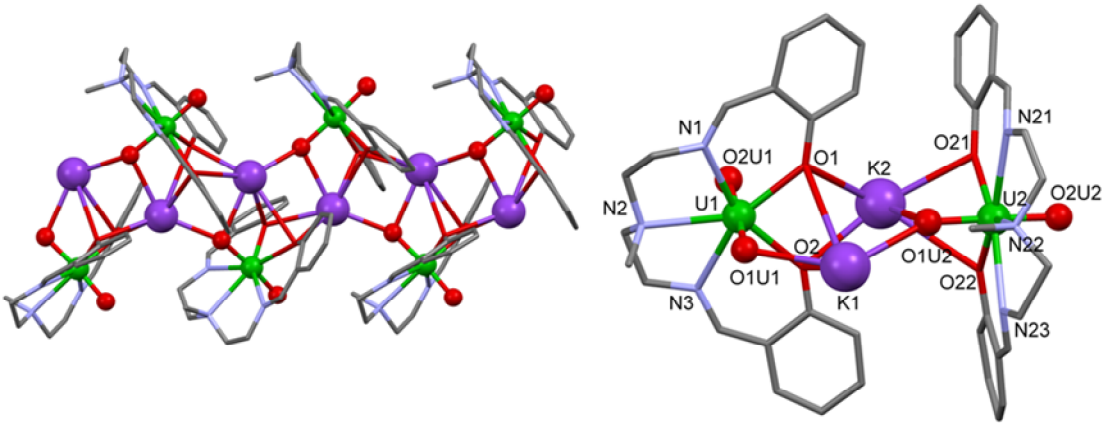

Figure III-2 Mercury plots of the polymeric complex **22** (left) and a detail showing the coordination environment of the two crystallographically independent uranium ions (right). (Ligands were represented in pipes, H and co-crystallised pyridine molecules were omitted for clarity, C atoms are represented in grey, O in red, K in purple, N in light blue and U in green.) Selected bonds lengths (Å): U(1)-O(1U1) 1.862(2), U(1)-O(2U1) 1.79(2), O(1U1)-K(2) 2.632(18), O(1U1)-K(1) 2.804(19).

The structure of the polymer **22** consists of $[UO_2(Mesaldien)]^-$ anions connected through potassium cations binding two uranyl oxygens from adjacent complexes to form a ladder-like chain with two crystallographically non-equivalent uranyl complexes. The two crystallographically independent U atoms in **22** are seven-coordinated, with a slightly distorted pentagonal bipyramidal geometry, by two trans oxo groups, three nitrogens and two oxygens from the Schiff base ligand. In this complex**,** the mean U=O bond distances lies in the range of the values observed for uranyl(V) complexes, with the $UO_2^{+\cdots}K^+$ interaction resulting in a slight lengthening of the U=O bonds (average U=O = 1.84(1) Å) with respect to the unbound oxygens (average U=O = 1.79(1) Å).

Due to the absence of coordinated solvent molecule to the uranyl moiety, complex **22** is soluble and stable in a wide range of solvents, including dimethylsulphoxide, acetonitrile, pyridine and in the presence of up to 10 equivalents of water. Proton NMR of **22**, with 10 independent signals, is in agreement with a rigid complex of C_{2v} symmetry in solution (Figure A-7).

The Fourier-transform infrared (FTIR) spectrum of **22** in KBr pellets (Figure A-8) contains a band at 804 cm^{-1} assigned to U-O stretches that was weakened with respect to the uranyl(VI) analogue [UO_2(Mesaldien)(py)] complex (asymmetric U-O stretch at 896 cm^{-1}). These data support the pentavalent oxidation state of the isolated compound.

III.2.3 U(IV) induced disproportionation

III.2.3.1 Synthesis of {[UO_2(Mesaldien)-(U(Mesaldien)]$_2$(μ-O)}

In order to investigate the reactivity of the pentavalent precursor **22** with uranium(IV), the reaction of one equivalent of the U(IV) salt [$UI_4(Et_2O)_2$] with two equivalents of **22** in pyridine was carried out, in the presence of (Mesaldien)K_2 to prevent ligand exchange. The addition of [$UI_4(Et_2O)_2$] led to an immediate colour change to dark red indicating a partial disproportionation of **22** to afford the linear tetramer presenting $UO_2^{+}\cdots U^{4+}$ interactions {[UO_2(Mesaldien)-(U(Mesaldien)]$_2$(μ-O)}, **23,** as dark red needle which were suitable for X-Ray diffraction in 76% yield. Slow diffusion of hexane on the filtrate collected after filtration of **23** affords the U(VI) complex [UO_2(Mesaldien)], **24**, in 88% yield (Scheme III-4). The different solubility of the two complexes allows their separate crystallization in a pure form affording a convenient synthetic route to the mixed valent U(V)/U(IV) tetranuclear complex **23**. Compound **23** can also be prepared as a microcrystalline powder by reacting directly the preformed [U(Mesaldien)I_2]·MeCN, **25**, complex with **22**. The compounds obtained by the two routes were found to have the same formula and structure, confirmed by elemental analysis and identical IR spectra.

Scheme III-4 Synthesis of **23**

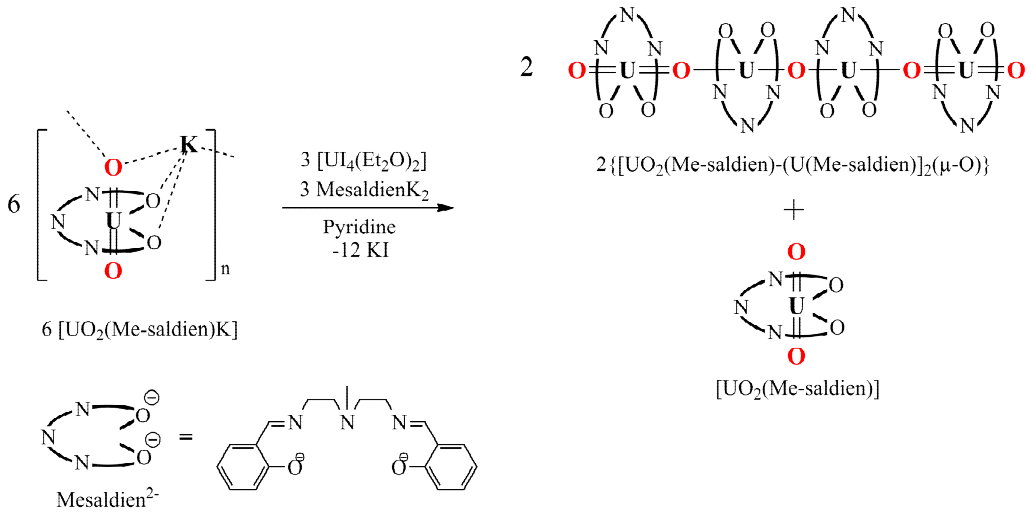

The structure of **23** consists of two [UO_2(Mesaldien)-(U(Mesaldien)] fragments bridged by an oxo group in a linear manner (Figure III-3). A crystallographic symmetry centre located on the oxo group relates the two fragments. In each fragment the oxo group of the pentavalent uranyl complex binds the U(IV) centre. The four uranium and five oxo atoms are coplanar with a maximum deviation of 0.06 A˚, the metal centres being almost linear, with U(2)-O(1U)-U(1) and U(1)#1-O(2U)-U(1) angles being equal to 162.8(7)° and 180.0°. This linear arrangement of the uranium ions is similar to the one found in the U(IV) oxo tetramer $[\{U(OTf)(terpy)_2(\mu\text{-}O)(\mu\text{-}OTf)U(terpy)]\}_2(\mu\text{-}OTf)_2(\mu\text{-}O)]^{4+}$.[306]

The two crystallographically independent U atoms in **23** are seven-coordinated, with a slightly distorted pentagonal bipyramidal geometry, by two trans oxo groups, three nitrogens and two oxygens from the Schiff base ligand. The value of the U-O_{oxo} bond lengths are significantly different for U1 and U2 and are consistent with the presence of UO_2^+ (U2) and U(IV) (U1) ions. The U1-O(2U) distance (2.085 Å) is in the range of the values reported for uranium(IV) oxo complexes.[182, 197, 307, 308]. The $UO_2^+\cdots U^{4+}$ interaction results in an appreciable lengthening of the U=O bond (U(2)-O(1U) = 2.003(13) Å) with respect to the unbound oxygen which presents a U=O distance (U(2)-O(3U) = 1.816(14) Å) very close to that of the unbound uranyl(V) oxygen in **22**. This lengthening is larger than what is normally found for uranyl groups involved in $UO_2^+\cdots UO_2^+$ or $UO_2^+\cdots$cation interactions as shown in complexes **3**-**18**, but similar distances were found in the mixed valent $UO_2^+\cdots UO_2^{2+}$ tetramer **5** (2.02(1) Å). The U(2)-O(1U) bond distance (2.003(13) Å) remains significantly shorter than the U1-O(1U) distance (2.198(13)Å). The bond valence sum analysis, performed using the empirical expression and constants proposed by Brown,[264] is in agreement with the presence of two pentavalent uranium (U(2)) and two localised tetravalent uranium centres (U(1)) in **23**.

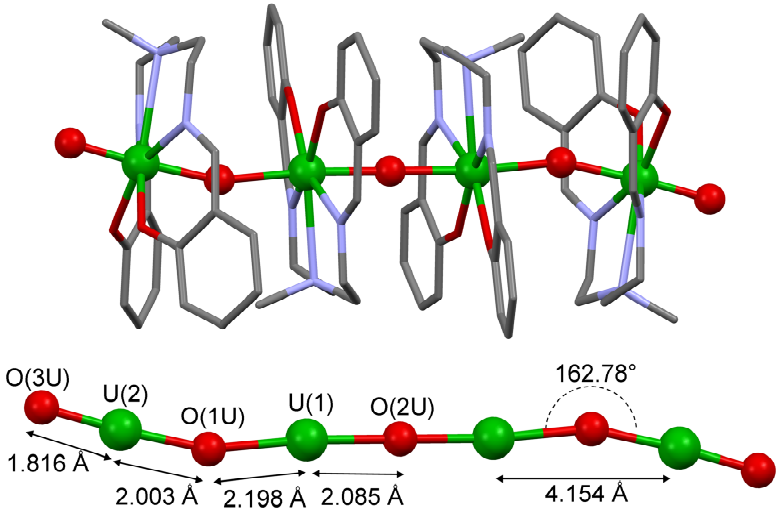

Figure III-3 Mercury diagrams of the complex **23** (top) and detail of the linear core (bottom). (Ligands were represented in pipes, co-crystallised pyridine molecules and H were omitted for clarity, C are represented in grey, O in red, N in blue and U in green) Selected angles (deg): O(3U)-U(2)-O(1U) 176.5(6), O(2U)-U(1)-O(1U) 175.3(3), U(1)#1-O(2U)-U(1) 180.0.

The infrared spectrum of **23** shows a strong band at 530 cm^{-1} that is not present in the infrared spectra of the starting materials **22** and **25** (figure S6). This peak was assigned to the U-O-U stretch, in comparison with the U-O-U vibration reported for the linear chains ···O-U-O-U-O··· in U_3O_8 .[309]

Due to the high insolubility of **23**, the uranyl(VI) by-product **24** was easily isolated in pure form by the crystallisation of the filtrate collected after filtration of the crystals of **23**. The structure of **24** consisted of a typical uranyl(VI) Schiff base complex, with two crystallographically inequivalent uranyl(VI) cations coordinated by the three nitrogen and the two oxygen atoms of the ligand in their equatorial plane, the uranium atoms being at the centre of a slightly distorted pentagonal bipyramid. In this complex, the mean value of the U=O bond distances (1.77(1) Å) were in the range of the typical values observed for uranyl(VI) complexes.

While the pentavalent uranyl complex **22** was fully stable in solution, the addition of U(IV) instantly promoted the partial disproportionation of complex **22**. The first step of the reaction was likely due to the replacement of the bound potassium in **22** by the U(IV) complex which is favoured by elimination of KI, resulting in a complex of lower stability than **22**. A U(IV) oxo fragment formed in the disproportionation reaction was trapped by unreacted uranyl(V) to form the stable but highly insoluble tetramer **23**. This result was quite unexpected and opens up the question of the possibility of an alternative disproportionation mechanism that does not involve UO_2^{+}···UO_2^{+} dimeric intermediates.

III.2.3.2 Isolation of {[UO_2(salen)][U(salophen-^{t}Bu$_2$)]$_2$[(U(salen)]$_2$(μ-O)$_3$(μ$_3$-O)}

We carried out similar studies with the sterically hindered complex [UO_2(salophen-^{t}Bu$_2$)(py)K], introduced in part III.2.3 [176]. . Similarly, the addition of the U(IV) complex [U(salen)Cl_2(thf)$_2$] to a pyridine solution of UO_2(salophen-^{t}Bu$_2$)(py)K] resulted in an immediate colour change of the solution indicating a partial disproportionation of the pentavalent precursor. However, in this case the reaction led to a complicated mixture of disproportionation products such as UO_2^+, U(IV) and UO_2^{2+} species, as observed by proton NMR of the crude reaction mixture (Figure A-9).

Crystals of the oxo cluster {[UO_2(salen)][U(salophen-^{t}Bu$_2$)]$_2$[(U(salen)]$_2$(μ-O)$_3$(μ$_3$-O)}, **26** were reproducibly isolated from this reaction mixture and a Mercury view of **26** is given in Figure III-4. The structure of **26** consists of five crystallographically independent uranium centres connected to each other by 5 bridging μ-oxo groups in a quasi-planar arrangement. An additional triply bridging oxo group was also found at the centre of the distorted pentagon connecting U3, U4 and U5. This U_2O_4 core defined by U3 and U5 has also been recently observed in an oxo complex of uranium(V) [204]. The overall charge count for this complex indicated the presence of 2 U(V) and 3 U(IV) ions. The calculated bond valence sum was in agreement with a localized valence of +V for U4 and +IV for U1 and U2, however such assignment was more ambiguous for U3 and U5. Except for U4, which keeps an uranyl(V) character, the U-O_{oxo} bond distances were all larger than 2 Å, suggesting that the uranyl moieties have been disrupted to yield a mixed-valent uranium oxo cluster with a new geometry. Although some double bond characters remain, the cluster formed cannot be described as uranyl-type, since the U-O_{oxo} distances were of those that were typical for uranium oxo clusters.

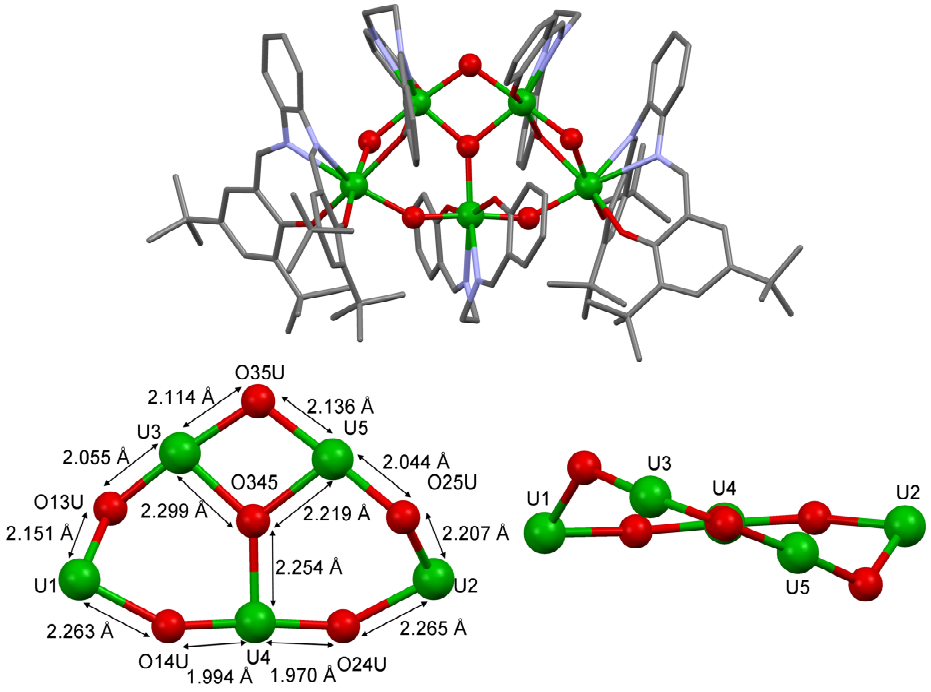

Figure III-4 Mercury plots of the complex **26** (top) and details of the core of complex **26** (bottom, left and right). (Co-crystallised acetonitrile molecules, and H were omitted. Ligands were represented in wireframe for clarity, C are represented in grey, O in red, N in blue and U in green) Selected angles (deg): O(13U)-U(3)-O(35U) 177.2(7), O(24U)-U(4)-O(14U) 174.7(6), O(25U)-U(5)-O(35U) 174.5(7).

The proton NMR of **26** revealed a complicated spectrum (Figure A-10) which was not possible to assign.

This result demonstrated that U(IV) species can promote the disproportionation of complexes of pentavalent uranyl otherwise stable in organic solution, and that the reaction between pentavalent uranyl and tetravalent uranium complexes can result in the formation of new original mixed-valent polynuclear oxo clusters. Future studies will be directed to investigate the mechanism of the U(IV) mediated disproportionation and towards the characterization of new cluster compounds through this new synthetic route.

III.2.4 Disproportionation of uranyl(V) promoted by organic acids

The former examples have demonstrated that the disproportionation of uranyl(V) induced by uranium(IV) precursors can lead to the isolation of polynuclear uranium oxo clusters. The formation of uranium oxo aggregates from disproportionation of uranyl(V) precursors has also been observed during the microbial bioreduction of uranyl(VI). Specialist anaerobic bacteria are thus able to reduce the soluble UO_2^{2+} to an insoluble U(IV) compound, UO_2,[4, 26, 58, 157, 310].

This reductive precipitation could effectively remove uranium from a large range of uranium-contaminated water, and can potentially be used for the environmental remediation of uranium-polluted sites. Precipitation of uranium as the result of enzymatic U(VI) reduction in sedimentary environments by bacteria may thus be an important sink for this compound and may also lead to the formation of certain uranium ores. The potential of using microbial U(VI) reduction for the removal of uranium from contaminated water leads to the investigation of the enzymatic and chemical mechanism for U(VI) reduction. The reduction of UO_2^{2+} by anaerobic microorganisms is thought to proceed via an unstable uranyl(V) species which then rapidly undergoes acid mediated disproportionation to yield UO_2^{2+} and U(IV) products[60]. However, the nature of these species has not to date, been identified and experimental validation of the proposed mechanism is lacking.[25, 26, 60] Humid acids have been found to enhance the bioreduction of U(VI) yielding insoluble forms of U(IV) such as colloidal nanoparticles and molecular-scale clusters but the potential role of an UO_2^{+} intermediate was not discussed in these studies.[4, 18, 62, 63] The combination of the acid induced disproportionation of uranyl(V), described in part II, with environmentally relevant ligand could be an original route to the synthesis of polynuclear oxo clusters with original topologies. Thus the reaction of uranyl(V) in the presence of biologically relevant organoacids, notably benzoic acid, which is found in large quantities in cells, as well as in humic acids, was further investigated.

The reaction of the uranyl(V) precursor $[(UO_2py_5)(KI_2py_2)]$, **1** with two equivalents of benzoic acid in pyridine immediately yielded a 1:1 mixture of the uranium(IV) cluster $[U_6O_4(OH)_4(C_6H_5COO)_{12}(py)_3]$, **27**, and of the uranyl(VI) complex $[UO_2(C_6H_5COO)_2(py)_2]$, **28** as shown in Scheme III-5. The difference in the solubility of the two complexes and their tendency to form crystalline material allow a clean separation: complete crystallisation of cluster **27** was performed in acetonitrile, and complex **28** was isolated from pyridine by slow diffusion of hexane. The two reaction products **27** and **28** were crystallized in 45 and 40%

yield respectively, accounting approximately for the total amount of the uranium in the starting material.

Scheme III-5 The disproportionation reaction of uranyl(V) in presence of benzoic acid.

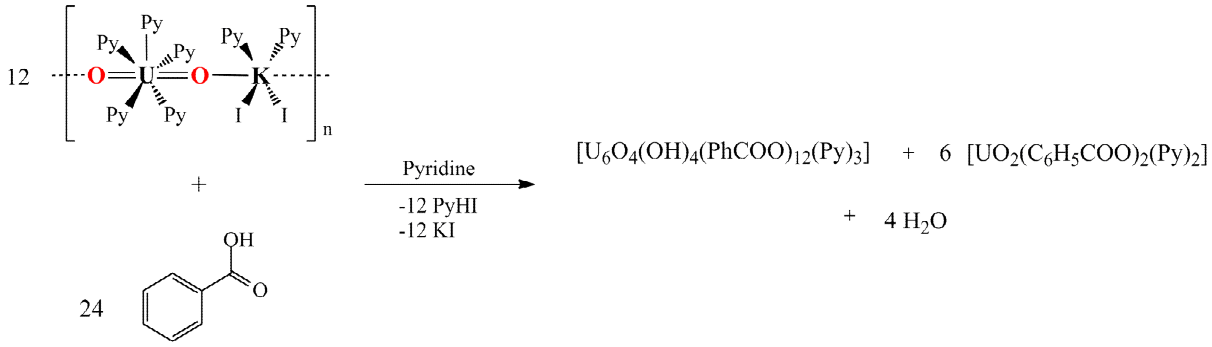

The X-ray crystal structure of the complex **27** showed the presence of a U(IV) cluster constituted of six uranium ions arranged at the corners of an octahedron (U–U distances ranging from 3.823(3) to 3.858(3) Å) as presented in Figure III-5. Each one of the eight triangular faces is capped by a triply bridging oxygen resulting in a U_6O_8 core. For the four oxygens from the hydroxo groups, the value of the U–O distances ranged from 2.419(2) to 2.455(15) Å and are in agreement with the presence of μ_3-OH groups while the four others ranged from 2.228(20) to 2.271(13) Å, again in agreement with the presence of μ_3-O^{2-} groups.

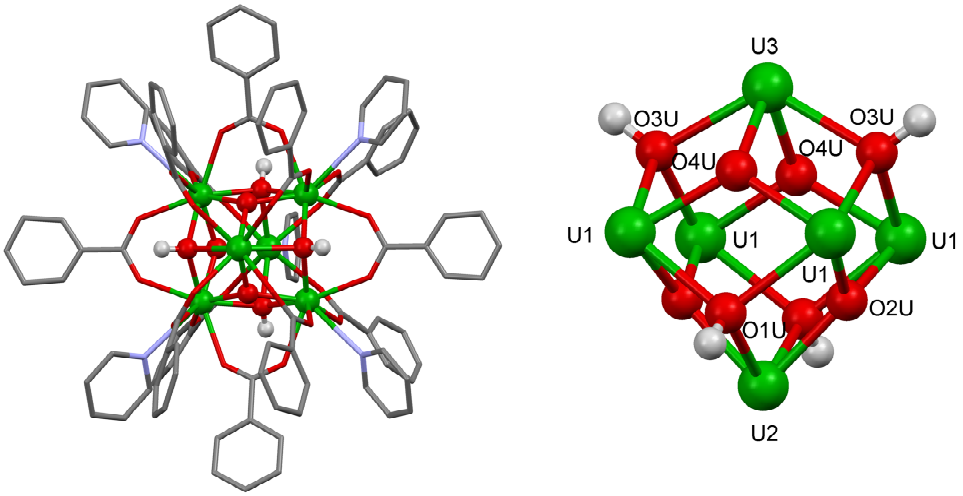

Figure III-5 Mercury Diagram of the structure of the cluster $[U_6(OH)_4O_4(PhCOO)_{12}(py)_3]$, **27** (left), and of the cluster $O_6O_4(OH)_4$ core (right) (Co-crystallised acetonitrile molecule, disorder on one benzoate aromatic ring and H were omitted. Ligands were represented in wireframe for clarity, C are represented in grey, O in red, N in blue and U in green).

The bond valence calculation carried out for the oxygen atoms using Brown's parameters were also in agreement with the presence of 4 oxo and 4 hydroxo groups bridging six U(IV) ions. The presence of well defined hydroxo groups was confirmed by the presence of two well defined vibration band at 3585 and 3629 cm^{-1} in the infrared spectrum of **27** (Figure III-6). These oxo and hydroxo groups are arranged in two interwoven tetrahedrons to form a distorted square antiprism. Each uranium ion is also coordinated by two bidentate benzoates acting as bridging ligands between adjacent uranium ions. Five uranium atoms are coordinated to a pyridine molecule, with various occupancies of the pyridine molecules. Dependent on the crystal analysed, the pyridine occupancy was proved to vary from 3 to five per cluster. Surprisingly, no electronic density was found in apical position of U(3), indicating no coordinated pyridine molecule, and resulting in a distortion of the hexanuclear core, U(3) being closer (2.692 Å) to the plane defined by the four symmetry relating U(1) than U(2) (2.740 Å). This distortion has also been previously observed in a reported oxo/hydroxo U_6 clusters [50, 189, 311] while the pure oxo U_6 clusters did not present this distortion[189, 202, 203, 312, 313]

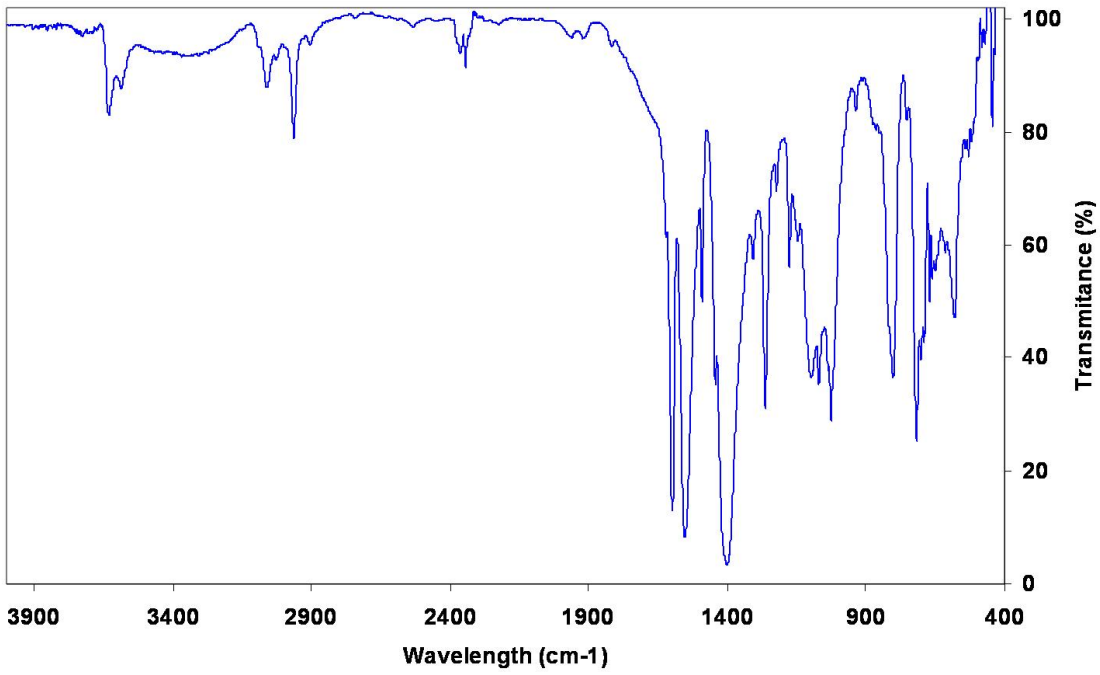

Figure III-6 FTIR spectra of **27** in KBr

The X-ray crystal structure of **28** showed an uranyl(VI) cation with a slightly distorted hexagonal bipyramidal geometry, and coordinated in the equatorial plane by two bidentate benzoate ligands and two pyridine molecules (Figure III-7). The uranyl ion has the typical linear geometry (O(1)-U(1)-O(2) = 180°). The U=O bond lengths (U(1)-O(1) = 1.769(5) Å)

and the U-$O_{carboxylate}$ bond distances (2.478(5) and 2.476(5) Å) are in the range of other structurally characterized uranyl(VI) carboxylato complexes.[37]

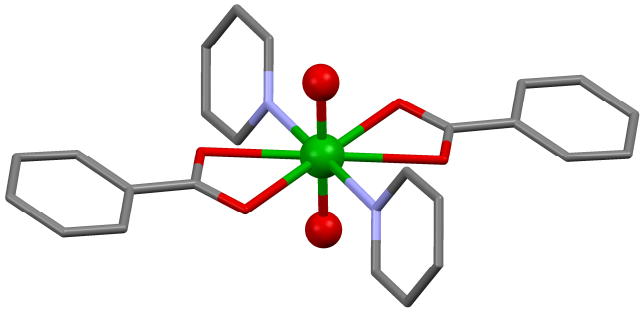

Figure III-7 Mercury Diagram of the structure of the complex $[UO_2(C_6H_5COO)_2(py)_2]$, **28** (H were omitted, ligands were represented in wireframe for clarity, C are represented in grey, O in red, N in blue and U in green).

The two compounds were obtained analytically pure and characterised by proton NMR. While complex **28** presents two broad signals overlapping with the pyridine peaks(Figure III-8, a)), the hexanuclear cluster **27** showed a well resolved spectrum presenting three signals corresponding to the three inequivalent protons of the benzoate bridging ligands (Figure III-8, b)).

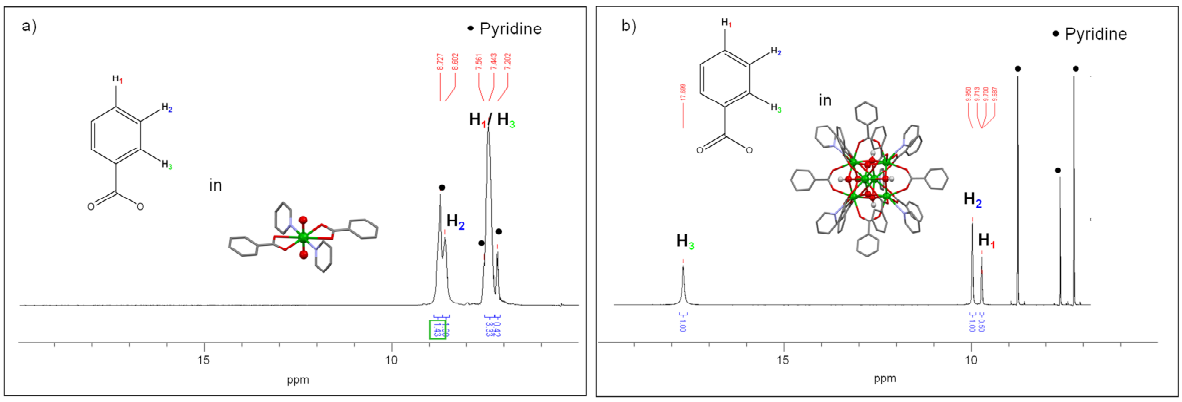

Figure III-8 Proton NMR spectrum of **28** (2.5mM) (a) and **27** (1.7mM) (Bruker Advance 500MHz).

The two compounds also presented very different UV/Vis spectra, with the respective signatures of U(IV) f-f transitions and uranyl(VI) vibrational bands (Figure III-9).

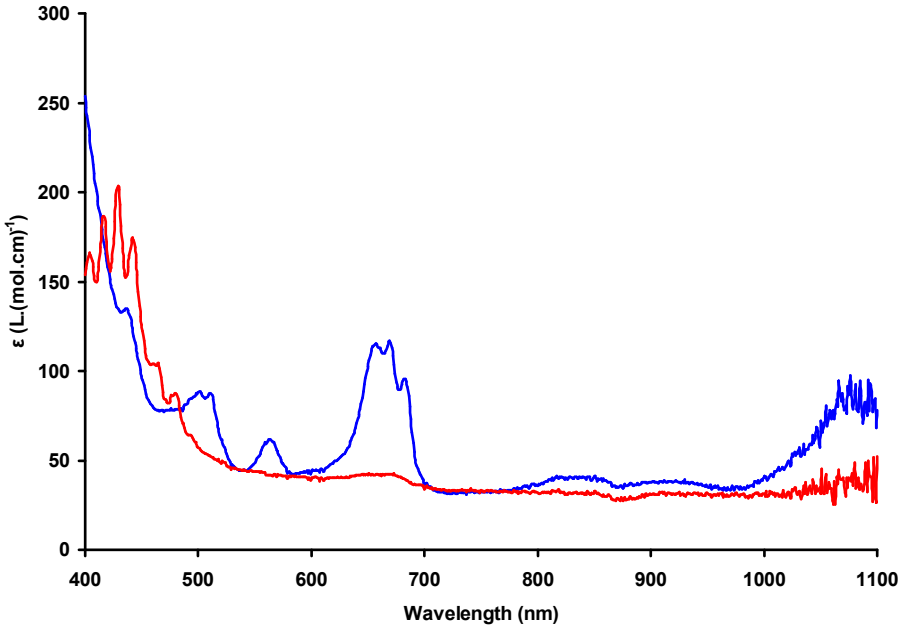

Figure III-9 UV-Visible spectra of **27** (blue) and **28** (red) in pyridine solution (Epsilon given per U centre)

PFGSTE diffusion NMR was used to measure the diffusion coefficient (D) of **27** and **28** in 1 mM pyridine solutions.[260] The D value measured for **27** with respect to **28** was in agreement with the presence of a hexanuclear cluster in solution (Table III-1). NMR and UV-Vis studies showed that cluster **27** was stable in acetonitrile and pyridine solution for more than one month. Moreover, addition of more than 50 molar equivalents of water did not lead to cluster decomposition. The high stability of this cluster contrasts with the low stability of the dibenzoylmethanate (dbm) cluster which consists of the same $U_6O_4(OH)_4$ core, and has been reported to dissociate to a mononuclear U(IV) species over time.[311]

Table III-1 Diffusion coefficient values of **27** and **28** and estimated spherical radii.

Solvent	Compound	D [$m^2.s^{-1}$]	r_{sph} [Å]$_{exp}$	r_{sph} [Å] (evaluated from crystal structure)
Pyridine η=0.879 mPa.s (298K)	**27**	3.29(4) 10^{-10}	7.5	8.5
	28	5.74(7) 10^{-10}	4.3	4.6

The characteristic proton NMR and UV-Vis spectra of the two species allowed following of the reaction in situ, and the two techniques revealed that the disproportionation reaction is in fact very fast, and that the cluster compound is formed within minutes after the addition of

benzoic acid to **1**. The presence of **28** was also detected in the reaction mixture by an ESI/MS experiment, but the cluster **27** was not observed by this technique.

An approximate 1:1 ratio was evaluated from the integral determination of the NMR spectrum of the crude reaction mixture (Figure III-10). The integral determination in situ was however not straightforward, since the presence of water broadens the signals, and the ratio of the two species were determined by peak deconvolution of the spectra using a mixed Lorentzian-Gaussian model (see Appendix for details). Water was formed during the reaction, and its presence in the reaction mixture has been unambiguously identified by ^{1}H NMR studies. The unusually shifted peak of water (Figure III-10) arises from the exchange with pyridinium protons [314]. The water formed during the disproportionation reaction most likely arises from the protonation of the uranyl(V). The formation of water molecules, the oxo and hydroxo groups in **27** and **28** accounted for all the uranyl oxygens in the starting material.

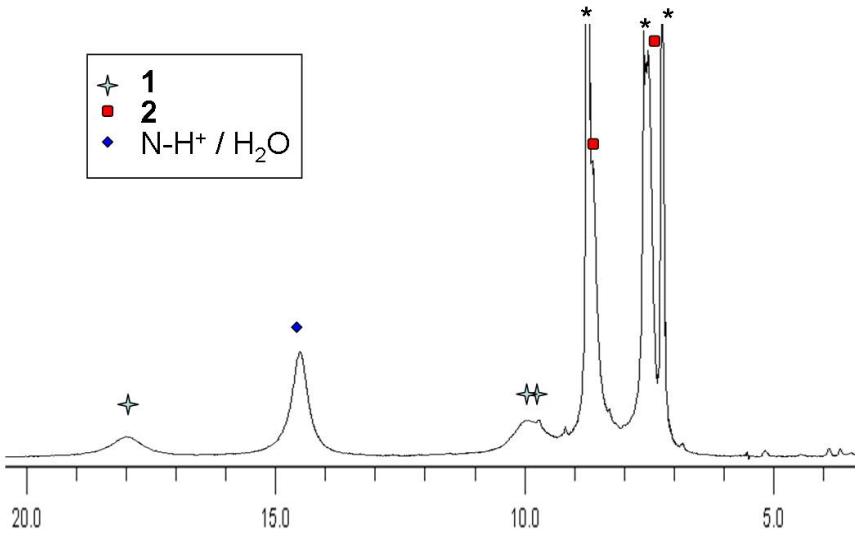

Figure III-10 Proton NMR spectra of the reaction mixture (Bruker Advance 200MHz, *: pyridine residual peaks, units in ppm).

In order to investigate the role of the proton source during the disproportionation reaction, we carried out the reaction of the uranyl(V) polymer with a separate source of protons, py.HCl, and the deprotonated potassium benzoate salt. The formation of cluster was never observed (by NMR and UV-Vis studies) when both reagents were added separately, as summed up in Scheme III-6, indicating that the coordination of the benzoate to the pentavalent uranyl precursor could play an important role in the outcome of the acid promoted disproportionation reaction.

The formation of the cluster **27** likely follows a two step mechanism: in a first step, according to the disproportionation mechanism of Steel and Taylor described in part I.3.1.2.1, the

disproportionation of uranyl(V) in presence of protons affords a uranyl(VI) complex and a uranium(IV) bis hydroxo complex. In a second reaction step, this uranium(IV) bis hydroxo complexes aggregates via oxolation reactions to afford the cluster **27** and water (see section I.3.1.3 for details on oxolation reaction).

Scheme III-6

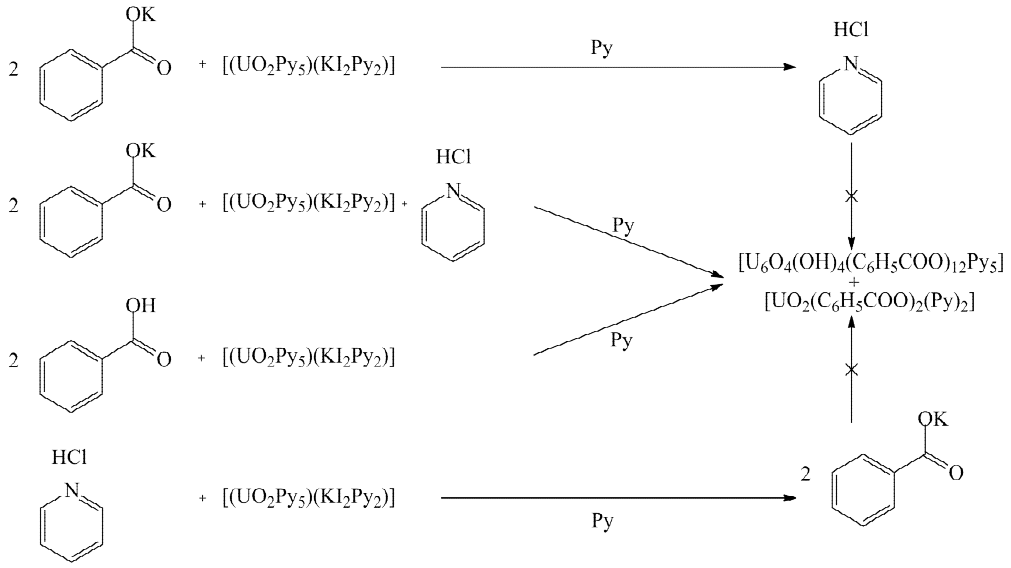

In the present case, the high stability of the cluster **27** is particularly convenient for the isolation of all the disproportionation products. This result demonstrated for the first time that the acid mediated disproportionation process results in the formation of polymetallic species which are here stabilized by the benzoate ligand. This observation has two direct implications: on one hand, the observed cluster formation is likely to be a missing link between the pentavalent uranyl intermediate in uranium bioreduction and the formation of colloidal nanoparticles involved in the transport of actinides in ground water. On the other hand, the results presented here confirmed the hypotheses postulated in section II.3 concerning the fate of oxygen atoms during the course of disproportionation reaction in aprotic media The formation of such complex polyoxo species thus provides a reasonable explanation for the difficulties encountered in the characterization of the products of the disproportionation of previously described pentavalent uranyl complexes.[168, 170, 172, 173]. However, despite the strong environmental implications of the synthesis of uranium clusters through proton induced disproportionation, this synthetic method does not seem appropriate for a systematic study of uranium clusters. The two compounds produced during the course of the disproportionation reaction complicate the isolation procedures, thus synthetic routes yielding single products should be preferred.

III.2.5 Controlled hydrolysis of low valent uranium complexes

As discussed in part I, the controlled hydrolysis of trivalent uranium complexes in organic media allowed the isolation of several oxo uranium clusters in our team, their nuclearity being related to the ligand used and the reaction conditions. However, in contrast with the structural diversity of U(VI) peroxide clusters, all these U clusters have a hexanuclear structure,[50, 189, 201-203, 311-313] with the only exception being a dodecanuclear cluster reported in our group in 2007.[189] Although oxo/hydroxo clusters provide reasonable models for the actinide nanoparticles implicated in actinide migration, their reactivity remains unexplored. In particular, the possibility of using these small clusters as building blocks for the isolation of larger cluster has to be investigated.

III.2.5.1 Alternative synthesis of 27

The highly stable cluster obtained by disproportionation of uranyl(V) with benzoate ligand encouraged us to investigate the controlled hydrolysis of uranium(III) in the presence of benzoate ligands. The U(IV) benzoate cluster **27** was also independently prepared in 75% yield by stoichiometric addition of water to a 1:2 acetonitrile solution of $[UI_3(thf)_4]$ and potassium benzoate (Scheme III-7) and subsequent recrystallisation from pyridine/acetonitrile. Crystals of **27** were also obtained with a similar procedure from the hydrolysis of the U(IV) analogue $[UI_4(PhCN)_4]$, although in this case other minor unidentified U(IV) species were also formed. This second synthetic route thus justified the relevance of cluster synthesis from U(III) for understanding the environmental mobility of actinides.

Scheme III-7 Synthesis of cluster **27** from $UI_3(thf)_4$.

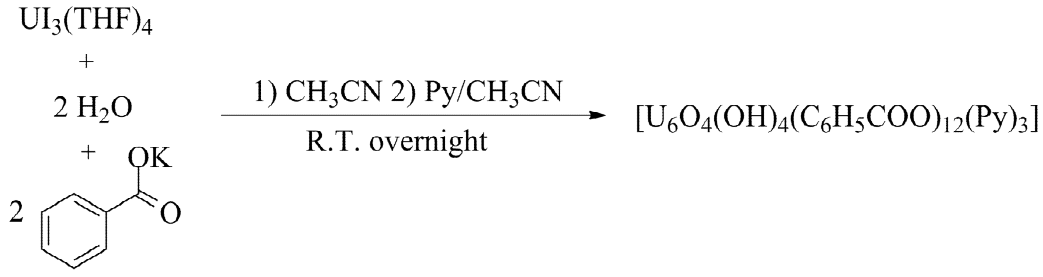

Proton NMR studies showed that cluster **27** was the only product in the reaction, and also that the formation of the cluster by controlled hydrolysis followed a much slower kinetic

mechanism than for the disproportionation reaction, since 12 h were required for the quantitative formation of **27** by this route, whereas the reaction was completed within minutes in the case of the disproportionation reaction. While the strong change in the UV-Vis spectrum observed instantly after the addition of water indicated that the oxidation of U(III) to U(IV) is very fast, formation of the uranium(IV) bis hydroxo complex is probably the kinetic limiting step, and can account for the slower reaction in this case. This observation also gives clues about the mechanism of disproportionation observed in part I.1.1.

III.2.5.2 Synthesis of $[U_{10}O_8(OH)_6(C_6H_5COO)_{14}I_4(H_2O)_2(MeCN)_2]$

The monitoring of the reaction presented in Scheme III-7 by proton NMR showed that the addition of pyridine to the acetonitrile reaction mixture leads to large changes in the NMR spectrum (changing from broad to well defined signals assigned to the U_6O_8 cluster) suggesting that pyridine has an important role in the formation/isolation of the U_6O_8 benzoate cluster. In order to investigate the nature of the species present in acetonitrile before addition of pyridine, slow diffusion of diisopropylether on the reaction mixture was carried out, and resulted in the isolation of X-Ray quality green crystals of a new decanuclear uranium oxo cluster, $[U_{10}O_8(OH)_6(C_6H_5COO)_{14}I_4(H_2O)_2(MeCN)_2]$, **29** in 80% yield (Scheme III-8).

Scheme III-8 Synthesis of cluster **29** from $UI_3(thf)_4$.

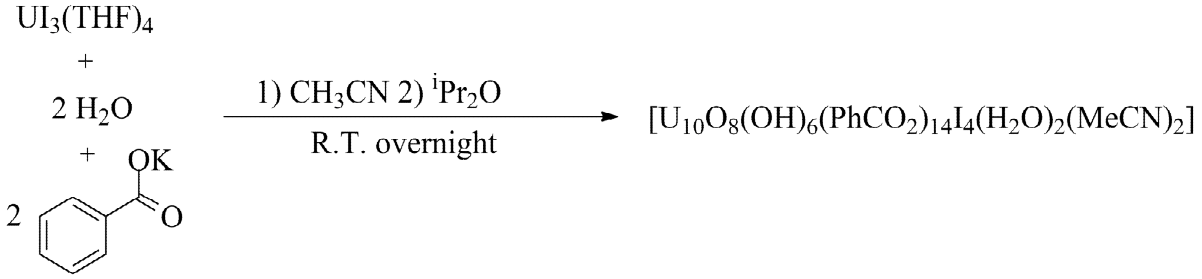

The X-ray crystal structure of **29** (Figure III-11, left) reveals the presence of a discrete decanuclear oxo/hydroxo cluster with a $U_{10}O_{14}$ core. The $U_{10}O_{14}$ topology consists of two U_6O_8 cages that are fused through two shared U and two shared O atoms with an inversion centre located in the middle of the common edge (Figure III-11, right). As in the U_6O_8 topology, the O atoms are located above the faces of the octahedrons. Three triply bridging oxides and three triply bridging hydroxides cap alternatively six faces of each octahedron. The four remaining faces share two μ_4 oxides bridging the two adjacent octahedrons. The

calculated bond valence sum (BVS) is in agreement with the presence of 6 hydroxide and 8 oxides. The value of the mean U-O distances are 2.23(5) Å for the μ_3-O, 2.43(6) Å for the μ_3-OH and 2.40(1) Å for the two μ_4-O. Six benzoate ligands bridge six external edges of each octahedron while two additional benzoates bridge the U1 and U3 atoms connecting the two octahedrons. A bridging iodide connects U1 and U3 at the vertex of each octahedron (a second iodide bridges the symmetry related U1A and U3A atoms). The presence of 8 oxo ligands, 6 hydroxo ligands, 14 benzoates, and 4 iodides adds up to an overall charge of - 40 for complex **29** which distributed over 10 uranium centres gives an average positive charge of +4. The calculated BVS is in agreement with the presence of 10 U(IV) ions. One acetonitrile molecule is also found in the coordination sphere of U2 and U2A, and a water molecule in that of U5 and U5A(2).

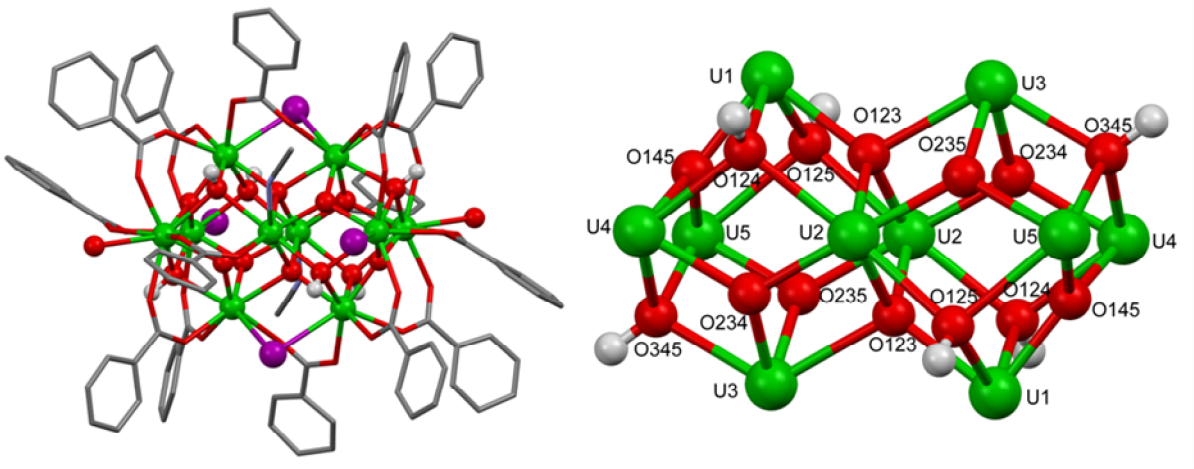

Figure III-11 Mercury Diagram of the structure of the cluster $[U_{10}O_8(OH)_6(C_6H_5COO)_{14}I_4(H_2O)_2(MeCN)_2]$, **29** (left), and of the cluster $U_{10}O_8(OH)_6$ core (right) (Co-crystallised acetonitrile molecule and H atoms were omitted. Ligands were represented in wireframe for clarity, C are represented in grey, H in white, O in red, N in blue, I in purple and U in green). Average bond lengths (Å): U-Oxo = 2.20(10), U-OH = 2.43(6), U-O benzoate = 2.37(3), U-U = 3.83(6)

Crystals of clusters with $U_{10}O_8(OH)_6$ core were obtained reproducibly from the hydrolysis reaction of $UI_3(thf)_4$ with stoichiometric amounts of water even in the presence of different benzoate:uranium ratios suggesting that only U_{10} clusters were present in acetonitrile solution. However, in presence of a lower benzoate ratio, a second type of cluster was isolated from the acetonitrile reaction mixture, differing from the structure of **29** by a lower benzoate ligand to uranium ratio, with a formula of $[U_{10}O_8(OH)_6(C_6H_5COO)_{12.82}I_{3.18}(H_2O)_4(MeCN)_3]I_2 \cdot 5MeCN$, **30**. The only difference in the structure of **30** with respect to **29** was due to the disorder from the partial occupation of iodide and benzoate ligands, suggesting the presence of a mixture of

clusters in the solid state with a $U_{10}O_{14}$ core having a variable ratio of benzoate/iodide ligands.

Contrary to **27**, presenting a clear proton NMR spectrum, **29** only presented very broad signals, and was not able to be characterised from its NMR spectra. However, different features between **27** and **29** were distinguished by FTIR spectroscopy. The presence of coordinated water molecules in **29** was confirmed by the appearance of two well defined vibrations at 3203 and 3293 cm^{-1} (characteristics of the OH stretches) and of a strong absorption band at 1592 cm^{-1} due to the coordinated HOH bending[315] (Figure III-12). However, the well defined hydroxo OH stretches vibration bands observed in **27** were broader in **29** with a weak band at 3558 cm^{-1}, which might be explained by the close proximity of acetonitrile molecule and iodine atoms in the crystal structure.

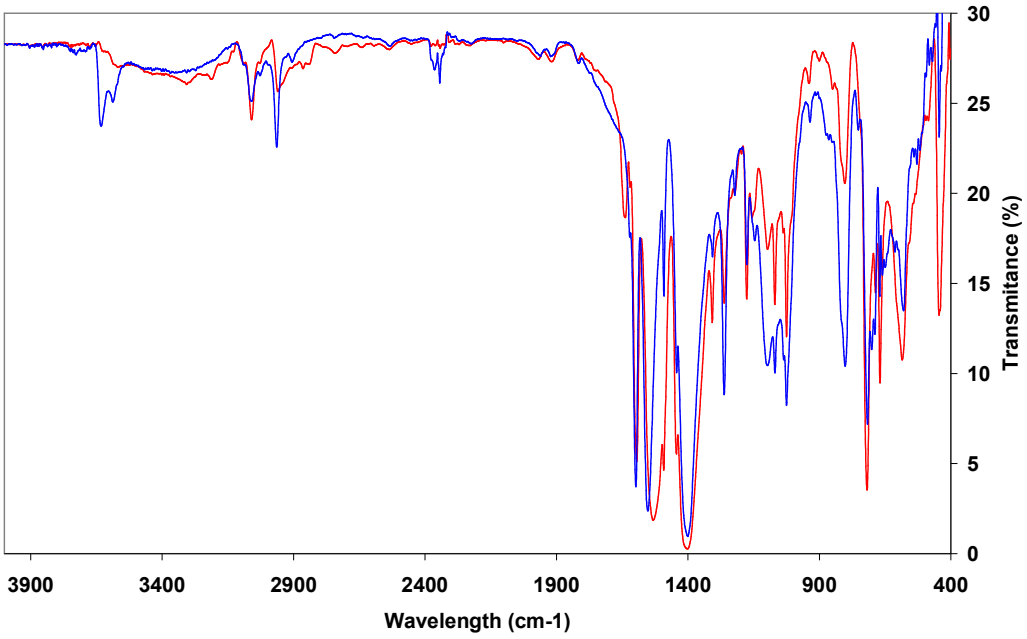

Figure III-12 FTIR spectra of **27** (blue line) and **29** (red line) in KBr

The comparison of the crystal structures of **29** and **27**, obtained in acetonitrile, before and after addition of pyridine allowed differentiation of the two different roles played by pyridine in the formation of the$[U_6O_4(OH)_4(C_6H_5COO)_{12}(py)_3]$ cluster from the $U_{10}O_8(OH)_6$ clusters. The higher coordinating ability of pyridine with respect to acetonitrile is likely to favour smaller size clusters. Moreover, the basicity of pyridine is postulated to play an important role in favouring the deprotonation of coordinated water molecules to yield hydroxo and oxo groups.

III.2.5.3 Synthesis of $\{[K(MeCN)]_2[U_{16}O_{22}(OH)_2(C_6H_5COO)_{24}]\}.4MeCN$

In order to evaluate the importance of the basicity of the media, a strong organic base, TMEDA (tetramethylethylenediamine), was added (1.5-3 equivalents) to the hydrolysis reaction mixture of $UI_3(thf)_4$ in presence of stoichiometric amounts of water (1.5-2 eq.) and potassium benzoate in acetonitrile, leading to the isolation of green crystals of the U_{16} cluster $\{[K(MeCN)]_2[U_{16}O_{22}(OH)_2(C_6H_5COO)_{24}]\}.4MeCN$, **31**. This U_{16} cluster is the largest uranium cluster reported to date, and can be isolated in 80% yield as green microcrystals by the reaction of 1.5 equivalents of water with $UI_3(thf)_4$ followed by addition of 1.5 equivalents of potassium benzoate and TMDEA (Scheme III-9).

Scheme III-9 Synthesis of **31**

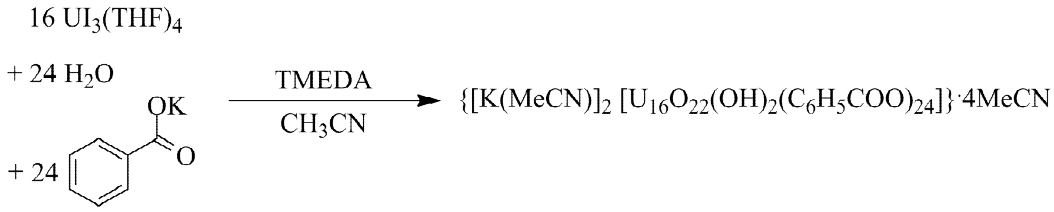

The structure of **31** is presented Figure III-13, and consists of a discrete oxo/hydroxo hexadecanuclear uranium cluster with a $U_{16}O_{22}(OH)_2$ core and with a 1.5/1 benzoate/uranium ratio. The geometrical arrangement of the 16 uranium atoms can be described as consisting of four fused octahedrons with 8 crystallographically independent uranium atoms related to their symmetry equivalents by an inversion centre located in the middle of the U1-U1 edge. The two external octahedrons share one edge with each one of the two adjacent octahedrons. Each octahedron shares one edge with all neighbouring octahedrons (Figure III-13, bottom-right). The overall cluster size is approximately 24 x 24 x 26 Å while the core structure is 11.13 Å wide (U6-U6 distance) and 8.38 Å tall (U8-U8 distance).

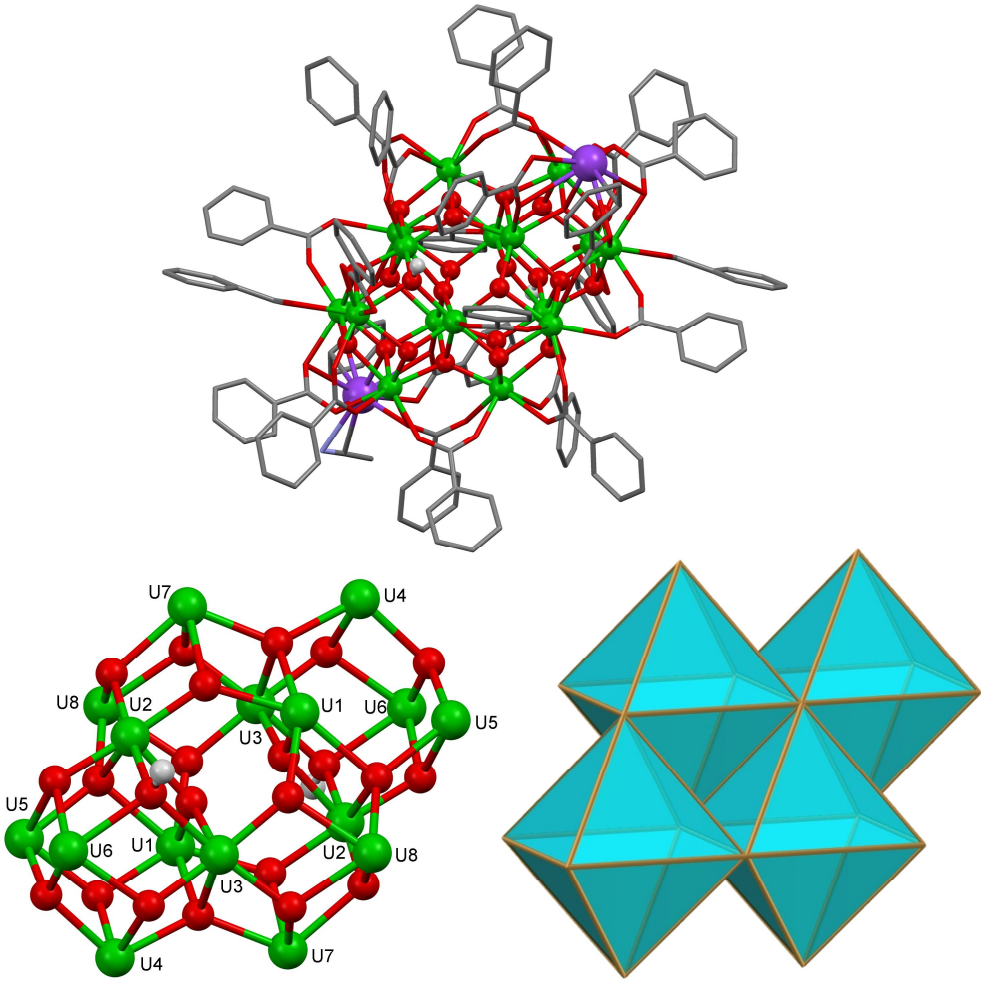

Figure III-13 Mercury Diagram of the structure of the cluster $\{[K(MeCN)]_2[U_{16}O_{22}(OH)_2(C_6H_5COO)_{24}]\}$ 4MeCN, **31** (top), of the $U_{16}O_{22}(OH)_2$ core (bottom, left) and its idealized structure represented with tetrahedrons, each edge accounting for one uranium centre (bottom, right) (Co-crystallised acetonitrile molecule and H atoms were omitted. Ligands were represented in wireframe for clarity, C are represented in grey, H in white, O in red, N in blue, K in purple and U in green). Average bonds lengths (Å): U-Oxo = 2.30(10), U-O benzoate = 2.42(6), U-U = 3.71(7).

The U1, U2, U3 atoms are 7-coordinated with a distorted monocapped trigonal prism geometry while the remaining uranium ions are 8-coordinated with a distorted square antiprism geometry. The uranium atoms are connected by 22 oxo, 2 hydroxo and 24 benzoate ligands. 16 μ_3-O ligands 2 μ_3- OH ligands and 6 μ_4-O ligands are capping the 28 triangular faces of the octahedrons, four of the μ_4-O linking together two or three adjacent octahedrons (Figure III-14). Only the four triangular faces in the core of the structure are not capped by oxo groups, probably due to steric constraints inside the cluster core. As a result, the geometry of two core octahedrons is highly distorted with the U1-U1 edge much longer (4.89 Å) than the other edges (mean value of 3.72(7) Å). Finally, two μ_4-O groups each bridges three uranium atoms (U1, U4, U5) and a potassium cation. The mean U-O distances is 2.3(1) Å for

the μ_3-O groups, 2.4(1) Å for the μ_4-O groups and 2.29(9) Å for the μ_3-OH. The position of the two hydroxo groups in the crystal structure has been assigned on the basis of the geometric parameters. Bond valence sum calculation were carried out on the cluster core, and indicated that the valence was localised in the structure, with 12 U ions in the +IV oxidation state and 4 U ions in the +V oxidation state (in yellow in Figure III-14).

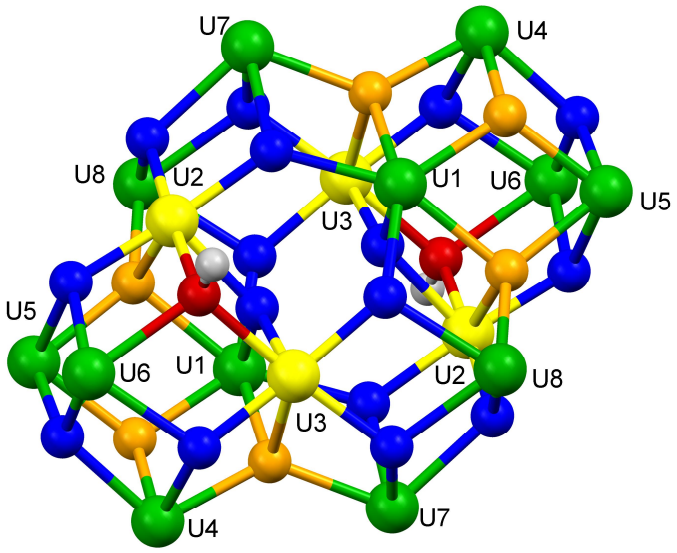

Figure III-14 Mercury diagram of the geometrical arrangement of the uranium atoms in **31** showing the four +V uranium atoms in yellow, the 16 μ_3-oxo groups in blue, the 2 μ_3-hydroxo in red and the 6 μ_4-oxo groups in orange.

This localized valence is not common in uranium oxo clusters; while mixed valent U(IV)/U(V) clusters with $U_{12}O_{20}$ and U_6O_8 cores have been previously isolated in our group[189], this is the first time the calculated BVS clearly suggests the presence of a localized valence for uranium. The calculated BVS value for the oxygen atoms indicated that the two oxygen atoms determined, belonged to the hydroxo groups which possess a rather high BVS value (1.7), but lower than the other oxygen atoms of the structure (BVS = 1.9 - 2.2). The 1.7 value might thus be ascribed to a delocalization of the position of the hydroxo hydrogens in the structure. The presence of two potassium cations in the structure added to the +70 charge arising from the uranium centres is consistent with the presence of 2 hydroxo and 22 oxo groups in the neutral complex.

Proton NMR spectroscopy of the cluster was carried out, but the compound did not present any signal in the temperature range -40/+50°C.

Similarly to **27**, the presence of hydroxo groups was confirmed by the IR spectrum, showing a well defined low intensity band centred at 3599 cm^{-1} assigned to the O-H stretching[315] (Figure III-15).

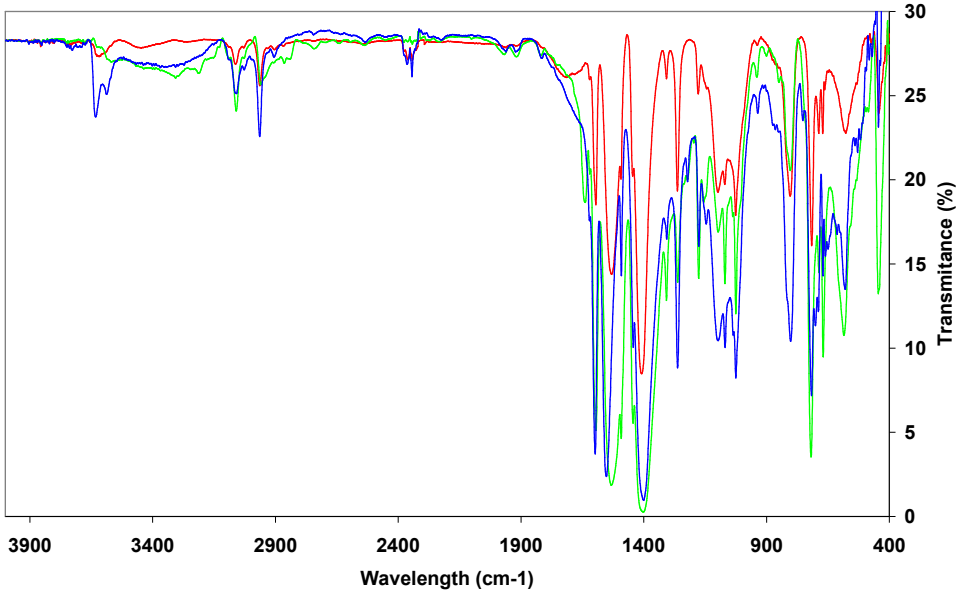

Figure III-15 FTIR spectra of **27** (blue line), **29** (green line) and **31** (red line) in KBr

The UV-Vis spectrum of **31** confirmed the presence of U(IV) with the presence of the typical band at around 690 nm [316]also present in the spectra of **27** and **29**. Despite this common transition observed, the fine feature observed within that band for the three UV-Vis spectra allowed a clear identification of the compounds by UV-Vis experiments (Figure III-16).

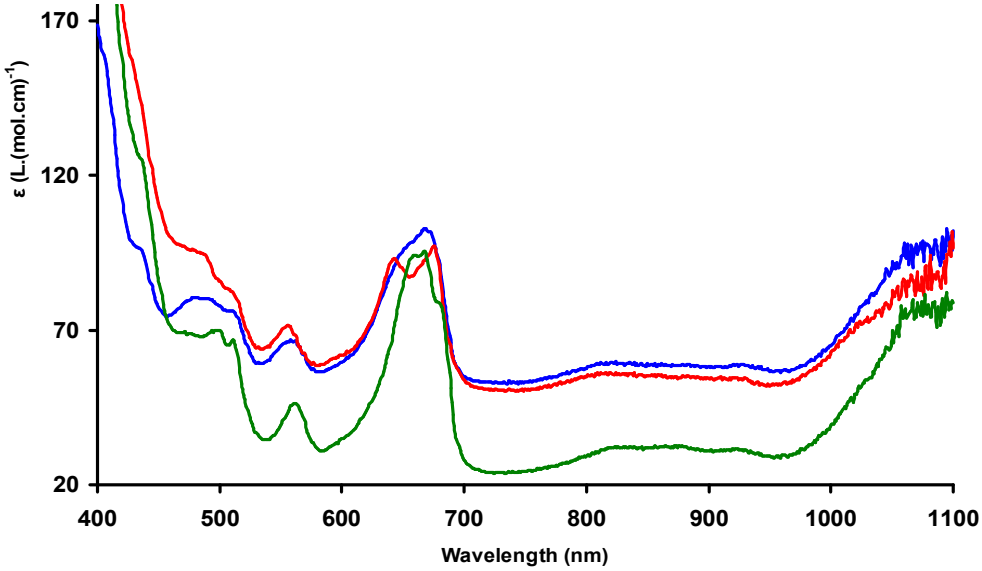

Figure III-16 UV-Visible spectra of **27** (green line), **29** (red line) and **31** (blue line) in acetonitrile solution (Epsilon given per U centre).

III.2.5.4 Reactivity studies

While the formation of the $U_{16}O_{22}(OH)_2$ cluster **31** and of the $U_6O_4(OH)_4$ cluster **27** from $UI_3(thf)_4$ hydrolysis in the presence of TMDEA or pyridine respectively demonstrated the important role of the base in the outcome of the hydrolysis reaction, the inverse reaction, using large cluster and reacting them with protons was investigated.

Proton NMR and UV-Vis spectroscopic studies thus showed that the $U_{16}O_{22}(OH)_2$ cluster **31** can be converted into the $U_6O_4(OH)_4$ cluster **27** after addition of py.HCl (0.6 equivalents) to a pyridine solution of **31** in the presence of potassium benzoate (Scheme III-10, Figure III-17 and Figure A-11).

Scheme III-10 Reaction of **31** with py.HCl and C_6H_5COOK in pyridine

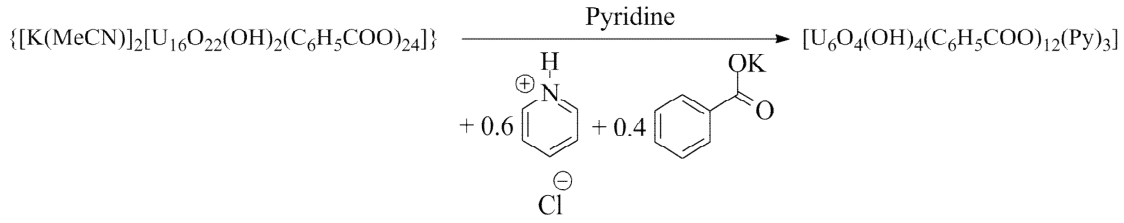

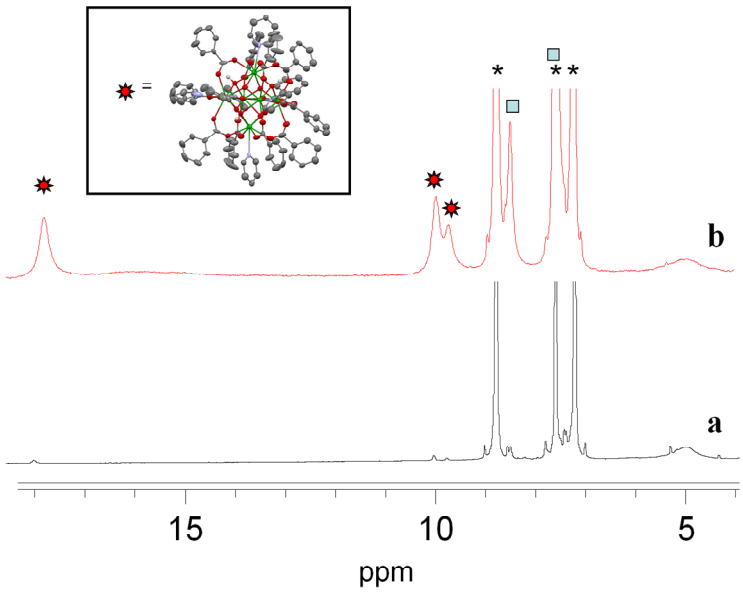

Figure III-17 Proton NMR spectrum (298 K, Unity 400MHz) of isolated complex **31** in py-d_5 before (a) and after (b) addition of 0.4 equivalents of potassium benzoate and 0.6 eq of py.HCl; red dots: $[U_6O_4(OH)_4(C_6H_5COO)_{12}(py)_3]$; green squares: excess benzoate.

This observation demonstrated that acidic conditions and coordinating solvents favoured the formation of smaller clusters, while the formation of larger cluster is favoured by strong bases promoting the deprotonation of hydroxo groups to afford oxo ligands. These results also showed how organic bases can be used to control the size and topology of the cluster assembly, as summed up in Figure III-18, providing a tool for the nanoscale control of uranium materials.

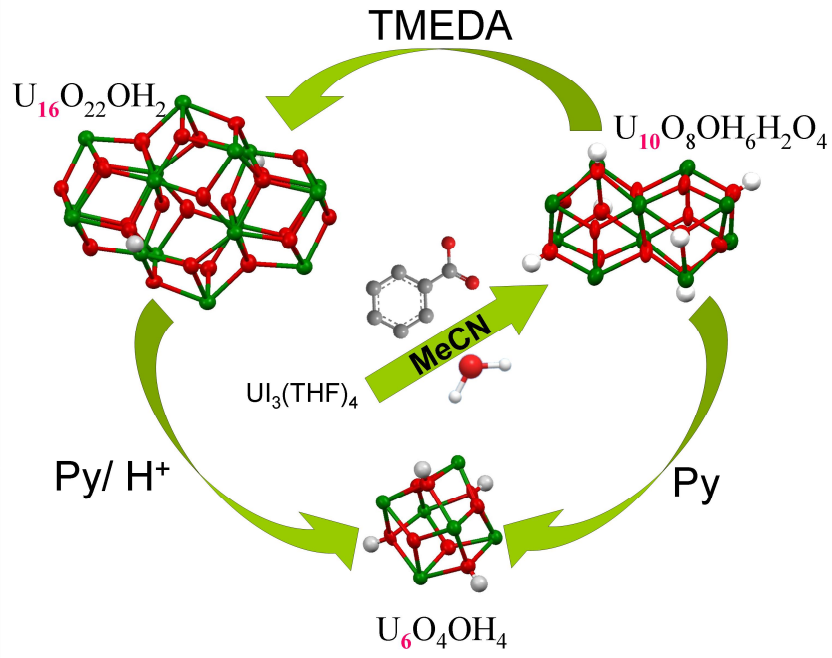

Figure III-18 Schematic representation of the size control of uranium benzoate clusters.

III.2.5.5 Structural comparisons

As shown in Figure III-19, the three clusters described in the previous section are all built of two or three fused octahedral U_6O_8 units. These octahedral U_6O_8 units can be found in natural uraninite, which consists in a fluorite type crystalline network with the overall UO_2 formula, and can thus be described as an infinite assembly of octahedral U_6O_8 units. This fact highlights that the three clusters **27**, **29** and **31** constitute as accurate models of the elemental bricks leading to the formation of bulk uraninite.

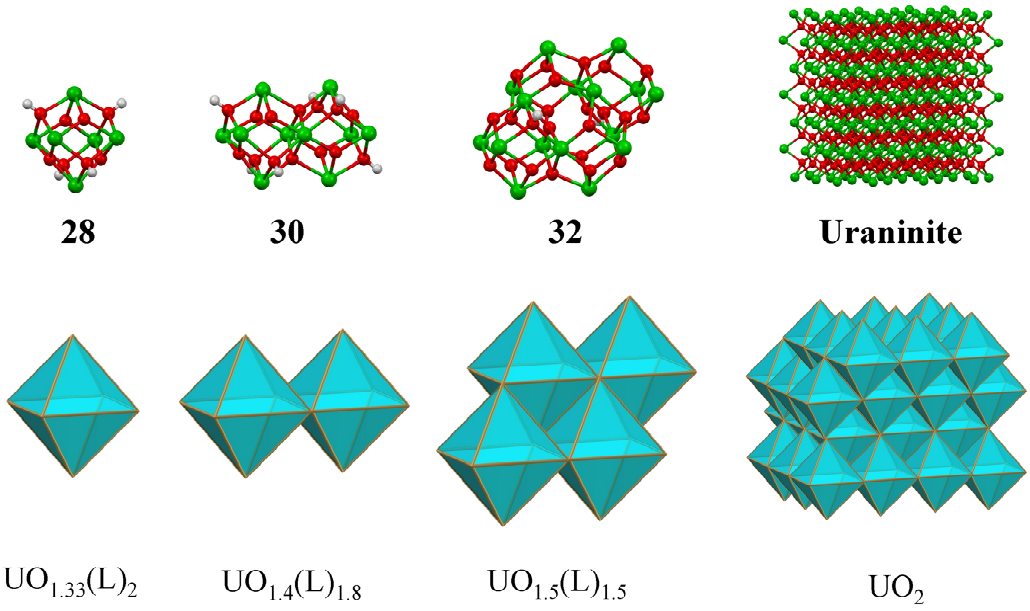

Figure III-19 Top: Mercury plot of the cluster cores and of bulk uraninite; Bottom: Schematic polyhedron representations of the assemblies (each polyhedron edge accounting for one uranium centre) and simplified formulas.

From the simplified formulas given in Figure III-19 it is observed that the ratio O vs. U increases with increasing cluster size, while the ratio L vs. U decrease. The formula of the cluster gets closer to the bulk uraninite formula UO_2 with the increase of the cluster size. The observation of these trends allows for the rational design of larger uranium clusters by increasing the water to uranium ratio, and by decreasing the ligand stoichiometry. However, there are limitations by experimental factors such as by the solubility of the large assemblies which is inversely proportional to their size; this tends to limit the isolation of very large clusters in a crystalline form. Moreover, in view of our results, the influence of the bases and the choice of the ligand is found to largely influence the final cluster structure

III.3 Magnetic properties

As discussed in part II.4, the magnetic properties of polynuclear uranium complexes do not only have a fundamental interest, but has also lead to the design of single molecules magnets. While part II.4 focused on uranium(V) polynuclear complexes, this chapter will deal with the magnetic properties of uranium clusters containing U(IV) atoms ($5f^2$ configuration) or a mixture of U(IV) and U(V) centres.

III.3.1 Electronic energy states

The ground state arising from the $5f^2$ configuration is $^3H_4$ (Scheme III-11) and the effect of a crystal or ligand field is to split both that and excited states further. In the case of U(IV) $5f^2$ systems, the crystal or ligand field splitting of this ground state is often large, resulting in wide gaps between the ground state and the first excited states, crystal field splitting of around 2000 cm^{-1} being commonly observed in U(IV) systems [4, 5, 317]. This large gap result in the typical feature observed with U(IV) compound which often exhibits Temperature Independent Paramagnetism (TIP) at low temperature. When the ground state and the first excited state are separated by an energy difference greater than kT in a particular temperature range, only the lowest state will be populated and the overall susceptibility will be independent of temperature (which formally correspond to a first order Zeeman term equal to zero in the Van Vleck equation). When the crystal field is such that the first excited state is separated from the ground state with an energy close to kT (which correspond to a very small first order Zeeman effect), the temperature dependence is reduced, and the susceptibility shows an inflexion below a certain temperature. However, the presence of several uranium centres in our polymetallic assemblies strongly complicates the interpretation of the magnetic data, the combination of different oxidation states and the possibility of magnetic exchange rendering the analysis of the raw data extremely complex.

Scheme III-11 Schematic energy levels splitting from electrostatic and spin-orbit interaction for a $5f^2$ system. The energy level obtained will be further degenerated by the effect of crystal field.

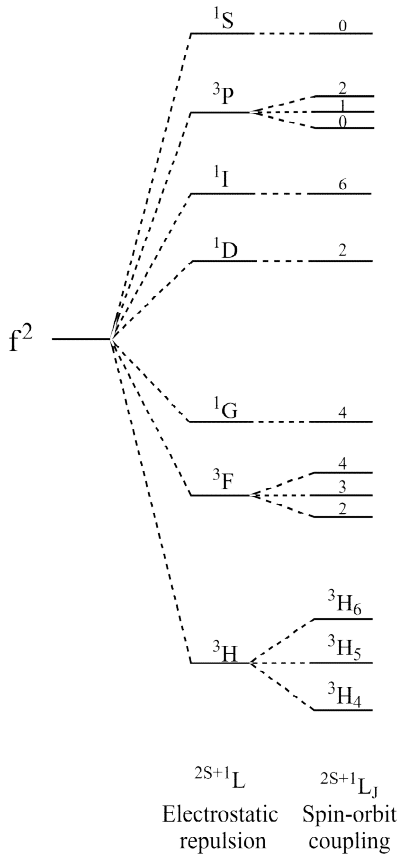

III.3.2 Magnetic properties of {[UO_2(Mesaldien)-(U(Mesaldien)]$_2$(μ-O)}

Temperature dependent magnetic susceptibility was measured for the mixed valent U(IV)/U(V) cluster **23** in the temperature range 2-300 K. The plot of χ versus T (Figure III-20) presents an inflexion around 18K in the slope of the magnetic susceptibility, and might indicate a superimposition of the paramagnetism of the U(V) centres with a TIP behaviour of the U(IV) enter below this temperature.

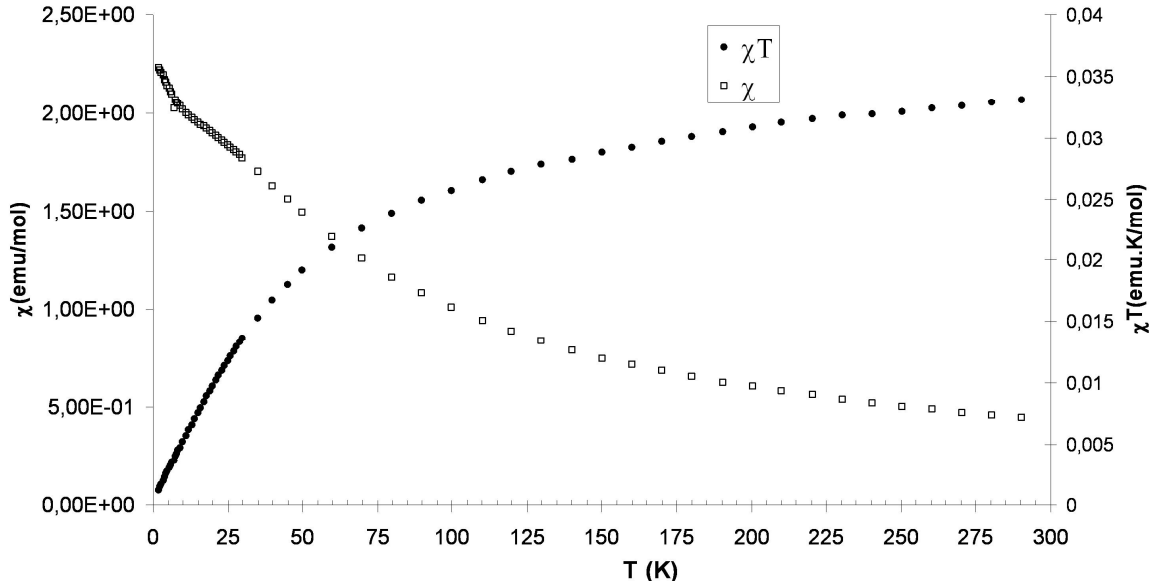

Figure III-20 Temperature-dependent magnetic susceptibility data for **23** in the range of 2-300 K in a 1 T field. (X_{dia} = -9.56 × 10^{-4} emu.mol^{-1}, *m=20.6* mg, *M* =2255.17 g.mol^{-1}).

The 1/χ versus T data are linear in the range 50K-300K, allowing Curie-Weiss fitting χ=C/T-θ. Parameters per uranium ion obtained from a linear fit of the 1/χ versus T data in this range are C=0.62 emu.K.mol^{-1} and θ=-54K (Figure III-21). From these value, an effective magnetic moment of 2.06 μ_B per uranium was calculated for **23**, which is lower than the value calculated for 2 U(IV) and 2 U(V) in the L-S coupling scheme behaving as independent paramagnets (μ_{eff} = 3.05 μ_B per U centre) but similarly low values had been observed for the mixed valence cluster [$U_{12}(\mu_3\text{-}OH)_8(\mu_3\text{-}O)_{12}I_2(\mu_2\text{-}OTf)_{16}(CH_3CN)_8$] containing ten U(IV) and two U(V) [189]. However, the magnetic data obtained from DC measurement for these polynuclear complexes did not allow a full interpretation of their magnetic properties, and theoretical models are lacking to expand their understanding.

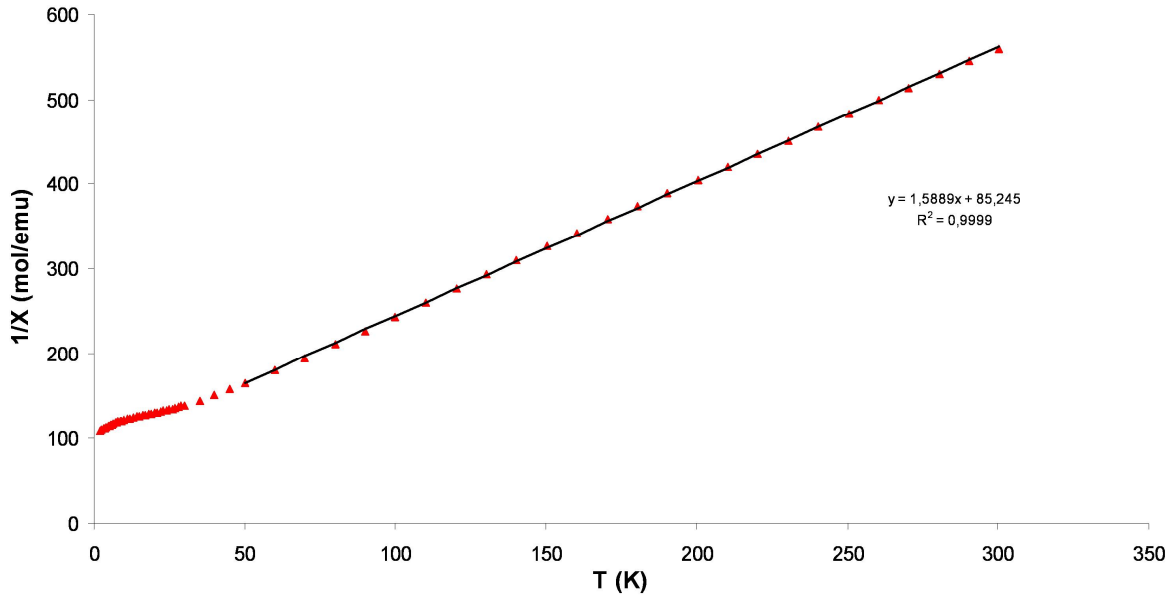

Figure III-21 1/χ vs. T data for **23** in a field of 1 T plotted per uranium ion and linear fit of the 50-300 K section. Curie–Weiss parameters extracted from linear fit: C = 0.62 emu.K.mol^{-1}, θ = -54 K.

III.3.3 Magnetic properties of $[U_6O_4(OH)_4(C_6H_5COO)_{12}(py)_3]$

Temperature-dependent magnetic susceptibility data were collected for **27** in the temperature range from 2 to 300 K (Figure III-22). The χ versus T values increase with decreasing temperature but the temperature dependence is reduced below 10 K. This behaviour could be the result of a very small first order Zeeman effect, typical of molecular U(IV) complexes, could be explained by a TIP behaviour hindered by magnetic coupling within the cluster. The current understanding of U(IV) magnetic properties does not allow an unambiguous assignment of this behaviour.

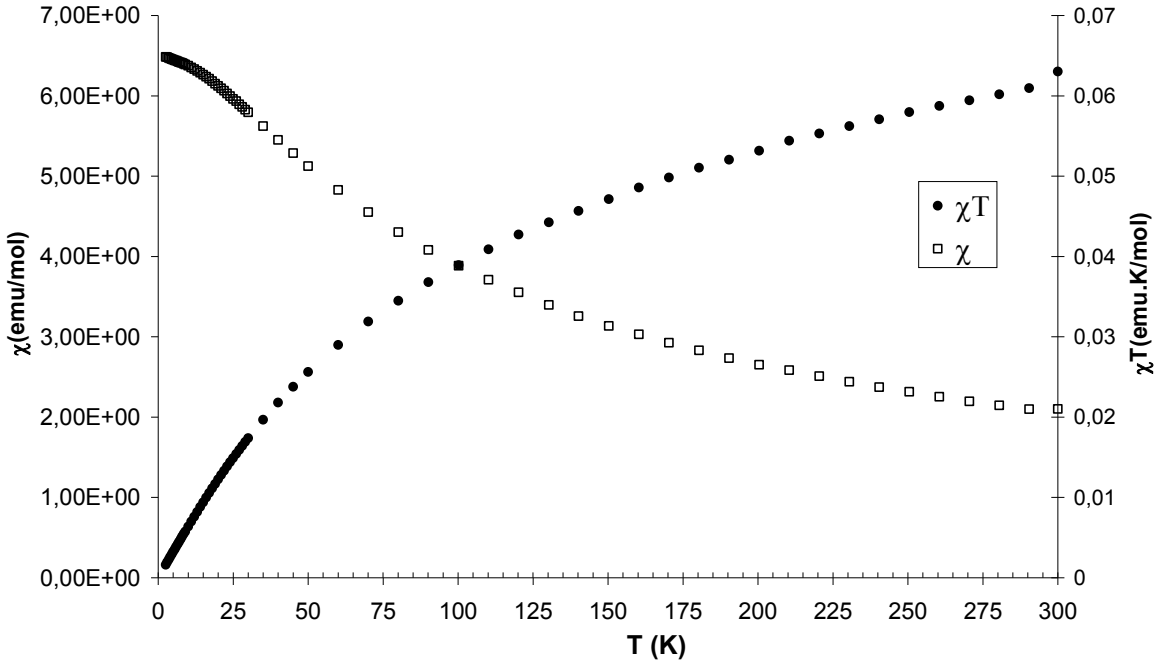

Figure III-22 Temperature-dependent magnetic susceptibility data for **27** in the range of 2-300 K in a 1 T field. (X_{dia} = -1.37 × 10^{-3} emu.mol^{-1}, *m=11.8* mg, *M* =3409.09 g.mol^{-1}).

The 1/χ versus T data are linear in the range 50K-300K, allowing Curie-Weiss fitting. Parameters per uranium ion obtained from a linear fit of the 1/χ versus T data in this range are C=1.49 emu.K.mol^{-1} and θ=-125.2 K (Figure III-23). From these value, an effective magnetic moment of 2.90 μ_B per uranium was calculated for **27**, which is lower than the value calculated for 6 U(IV) in the L-S coupling scheme behaving as independent paramagnets (μ_{eff} = 3.57 μ_B per U centre) but in the range of the values previously reported for mononuclear U(IV) complexes (2.5–3.55 μ_B). [197, 318-320] These magnetic data provide strong evidence that complex **27** contained only U(IV) ions.

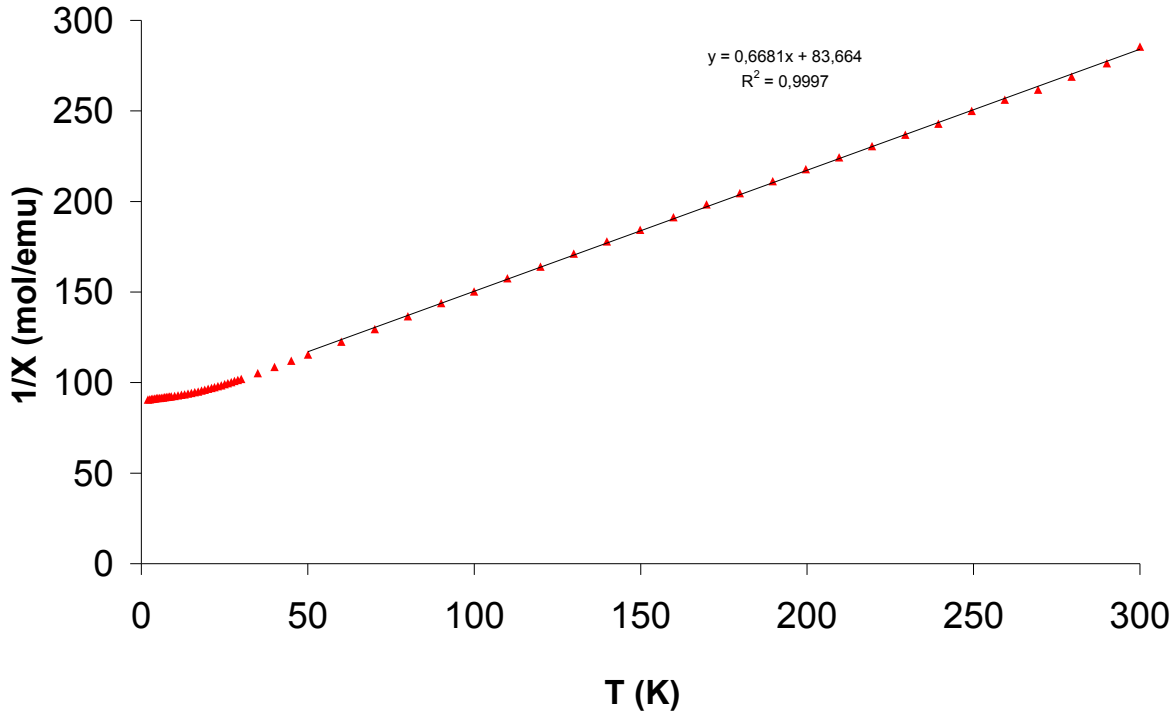

Figure III-23 1/χ vs. T data for **27** in a field of 1 T plotted per uranium ion and linear fit of the 50-300 K section. Curie–Weiss parameters extracted from linear fit: C = 1.49 emu.K.mol^{-1}, θ = -125.2 K.

To characterize the relaxation of the magnetization at low temperature, and to investigate the possibility of single molecule magnet properties of **27**, we have performed a.c. magnetic susceptibility measurements on polycrystalline samples of **27** in a 10 Oe a.c. field oscillating at a frequency f varying between 18 and 9887 Hz. Data have been collected as a function of temperature, T, for a given f (Figure III-24). The in-phase and out-of-phase components of the a.c. susceptibility, do not present any maximum in the temperature window 2K-300K clearly indicating the absence of slow magnetic relaxation. This together with the absence of any hysteresis in the magnetisation versus field curve up to 1.8 K ruled out the use of **27** as a potential single molecule magnet.

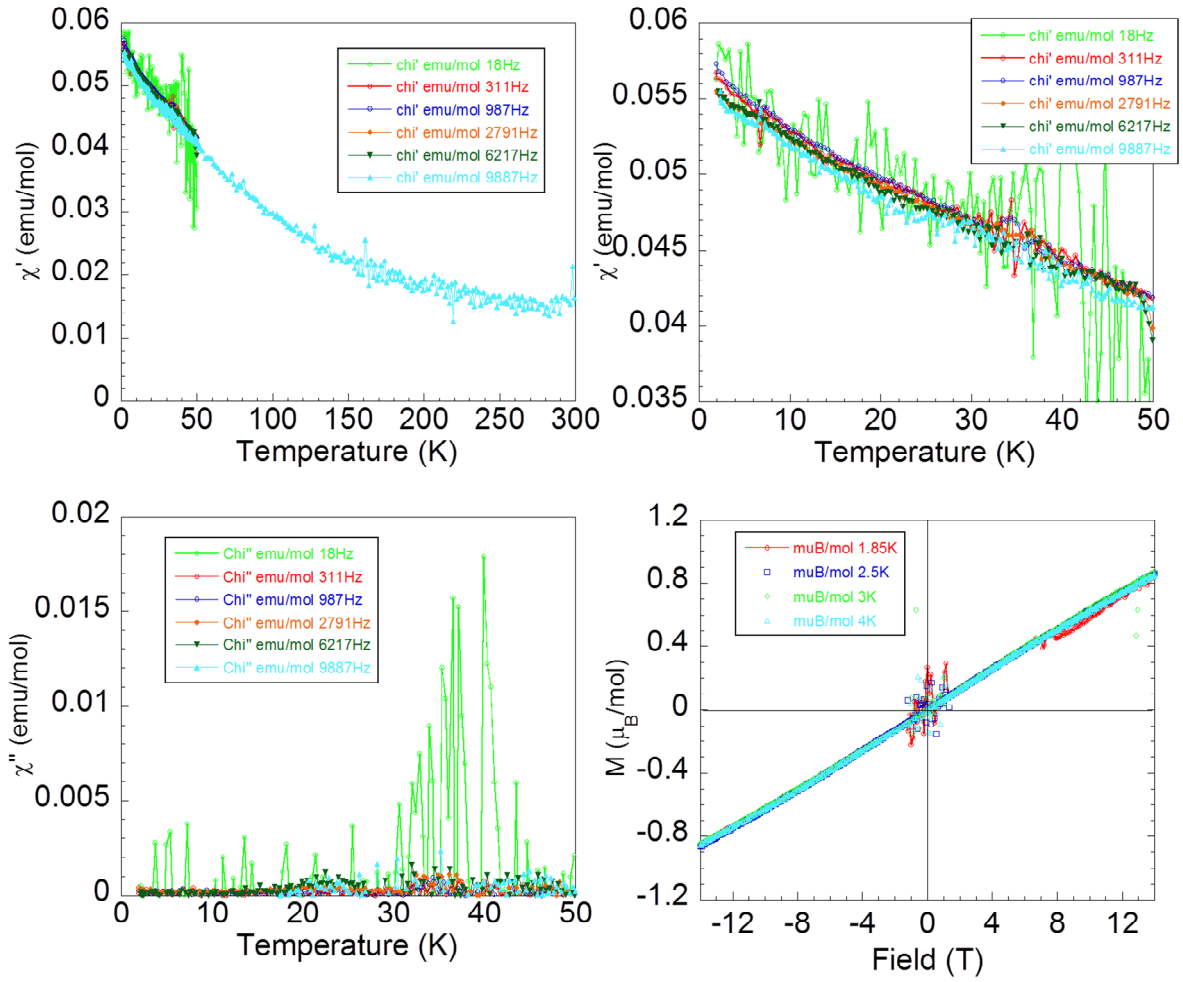

Figure III-24 Temperature dependence for **27** of the in-phase (χ_M', top) and out-of-phase (χ_M", left, bottom) components of the a.c. magnetic susceptibility measured in a 10 G a.c. field oscillating at the indicated frequencies, under zero d.c. field, and magnetisation versus field in the -14-14 Tesla domain (right, bottom).

III.3.4 Magnetic properties of $\{[K(MeCN)]_2[U_{16}O_{22}(OH)_2(C_6H_5COO)_{24}]\}$

The solid state magnetic susceptibility χ_M of **31** was measured in the temperature range 2-300 K in a 1 T field, and is plotted vs. T in Figure III-25. The χ versus T values increase with decreasing temperature but differently to the clusters **23** and **27** this variation does not present any inflexion at low temperature. Thus, the common feature observed with U(IV) complexes, with a plateau or an inflexion in the χ vs. T observed at low temperature due to TIP is not observed here, and might be the result of the presence of the paramagnetic U(V) centres or due to magnetic couplings within the cluster core.

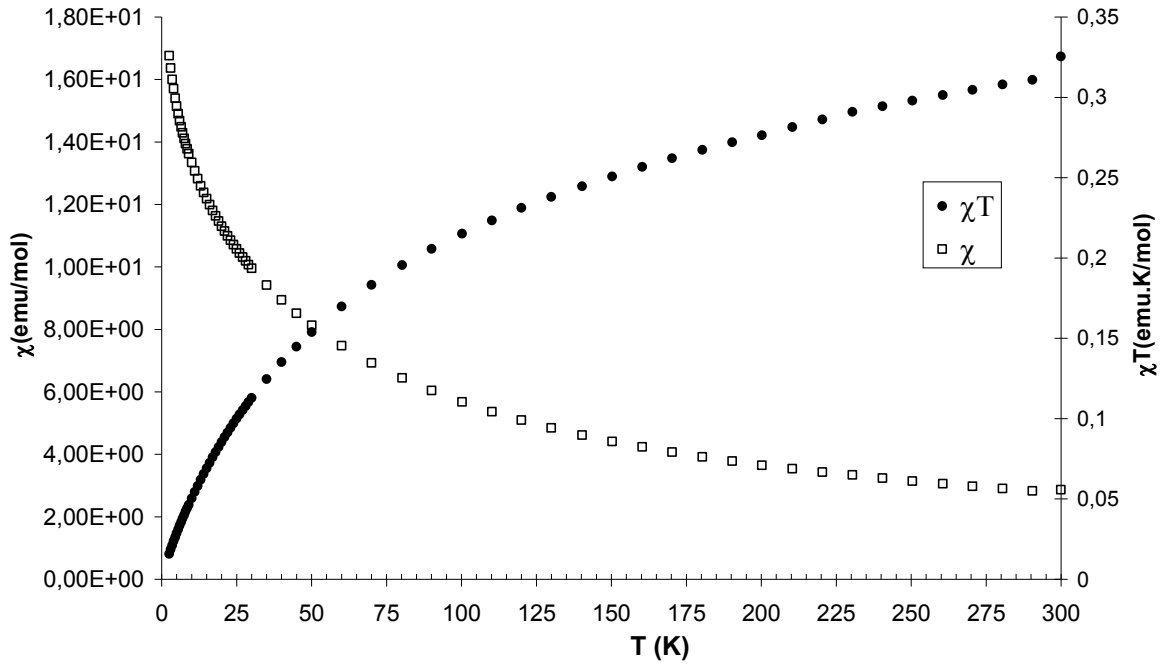

Figure III-25 Temperature-dependent magnetic susceptibility data for **31** in the range of 2-300 K in a 1 T field. (X_{dia} = -2.36 × 10^{-3} emu.mol^{-1}, *m=17.6* mg, *M* =7425.75 g.mol^{-1}).

The 1/χ versus T data are linear in the range 100K-300K, allowing Curie-Weiss fitting. Parameters per uranium ion obtained from a linear fit of the 1/χ versus T data in this range are C=1.41 emu.K.mol^{-1} and θ=-103.9 K (Figure III-26). From these values, an effective magnetic moment at 300 K of 2.89 μ_B per uranium was calculated, which is equal to the value obtained with the pure U(IV) cluster **27** and could question the presence of 4 U(V) centres in **31**. However, this value is slightly lower than the value calculated for 12 U(IV) and 4 U(V) which behaves as independent paramagnets (μ_{eff} = 3.32 μ_B per U centre),but is similar to the magnetic moment (2.79 μ_B) reported for the mixed valence cluster $[U_{12}(\mu_3\text{-}OH)_8(\mu_3\text{-}O)_{12}I_2(\mu_2\text{-}OTf)_{16}(CH_3CN)_8]$ which contained ten U(IV) and two U(V). The value itself does not allow a

full determination of the oxidation states, but its combination with the structural factors tend to confirm the presence of four U(V) centres within the cluster core.[189]

This large size mixed valent cluster is a good potential candidate for single molecule magnets properties, and a.c. magnetic susceptibility measurements should be carried out in the near future.

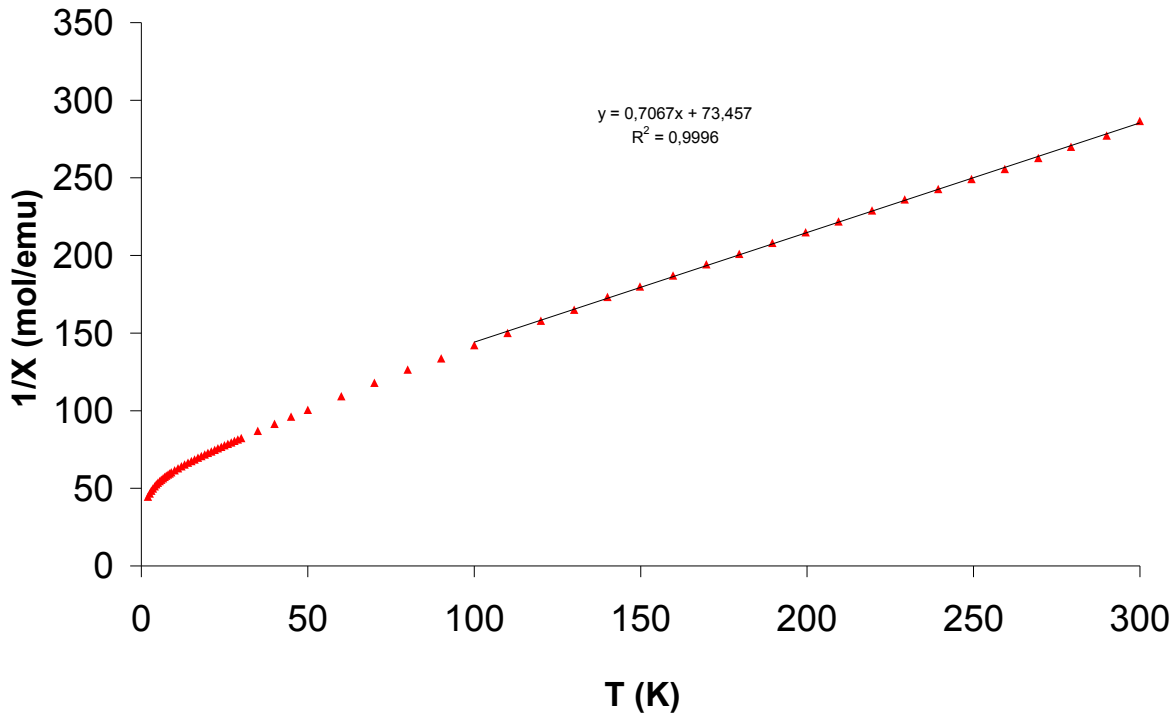

Figure III-26 1/χ vs. T data for **31** in a field of 1 T plotted per uranium ion and linear fit of the 100-300 K section. Curie–Weiss parameters extracted from linear fit: C = 1.41 emu.K.mol^{-1}, θ = -103.9 K.

The three examples discussed in this part highlight that the magnetic exchange coupling of these kind of clusters, despite their high relevance in the design of nanomagnets require an accurate analysis of the magnetic properties, and is beyond current understanding of the interplaying effects of temperature independent paramagnetism, crystal field splitting, spin–orbit-coupling, and orbital angular momentum quenching in such complex uranium systems. However, this lack of theoretical analysis of the magnetic properties of these polynuclear structures should not prevent the empirical observation of their properties which will provide insight to the design and the understanding of 5f single molecule magnets.

III.4 Conclusion and perspectives

The work presented in this chapter focused on the preparation of polynuclear uranium oxo clusters. Two different synthetic routes have been investigated, and resulted in the design of uranium clusters with unprecedented geometries and nuclearities. The first route developed exploited disproportionation of uranyl(V) precursors induced by uranium(IV) complexes or organic acids to build new polynuclear architectures. We have demonstrated for the first time that the reaction between pentavalent uranyl and tetravalent uranium complexes results in the formation of new original mixed-valent polynuclear oxo clusters which are relevant for the understanding of the uranium environmental speciation and are of potential interest for the study of magnetic communication between uranium ions. Future studies will be directed to investigate the mechanism of the U(IV) mediated disproportionation and to the characterization of new cluster compounds.

Moreover, the formation of hexanuclear U(IV) oxo-clusters has been observed in the disproportionation of pentavalent uranyl promoted by organic acids. This synthetic route conceptually reproduces the aggregation phenomena observed in environmental and microbial uranium reduction.

The second synthetic approach to uranium oxo clusters exploited a method developed in the laboratory for the synthesis of uranium oxo clusters, by the hydrolysis of low valent precursors. The application of this synthetic method in the presence of biologically relevant organic ligand lead to the isolation of three stable uranium cluster, including the biggest one isolated to date. This very large cluster has been isolated through a fine tuning of the reaction condition, providing new approaches for the isolation of larger assemblies.

The results reported here suggest that the reactivity of UO_2^+ in the presence of different ligands provides a convenient tool for understanding oxo-cluster formation and for the growth of aggregates with new geometries. The isolation of aggregates with $U_{10}O_{14}$ and $U_{16}O_{24}$ cores clearly demonstrates that polyoxometalates containing U(IV) and U(V) are not limited to the U_6O_8 topology and that a wide variety of different new topologies are yet to be discovered.

In the near future, two main directions should be exploited in order to isolate uranium oxo clusters with new geometries and nuclearities. The U(IV) induced disproportionation route highlights that the denticity of the organic ligand drive the dimension of the cluster, our example illustrating the synthesis of a 1D cluster with pentadentate ligands and a planar 2D

cluster in the presence of tetradentate ligands. This denticity influence should be investigated, in order to isolate clusters with new geometries.

We have observed along the second synthetic route through the hydrolysis of low valent precursors that the solubility of uranium oxo clusters is inversely proportional to their size, and thus limits the isolation of very large assemblies. In order to maintain the solubility of the final clusters, reaction with more soluble ligands should be investigated, and might lead to the isolation of very large uranium assemblies.

General conclusion

CHAPTER IV. General conclusion

The global objective of this thesis work was the development of rational methods for the synthesis of discrete polynuclear uranium architectures designed to explore the electronic structure, the reactivity and the magnetic exchange in compounds containing the uranium in oxidation state lower than +VI. The access to well defined model complexes by using these routes is crucial in the understanding of actinide migration in the environment and in nuclear fuel related concerns. This work contributed to the elaboration of controlled synthetic strategies to afford original polynuclear uranium clusters with interesting properties.

The first part of this thesis work was dedicated to the investigation of uranyl(V) polynuclear assemblies connected via CCI. The factors controlling the formation and the stability of uranyl(V) cation-cation assemblies have been investigated, and have resulted in the rational isolation of the first uranyl(V) assembly fully stable towards disproportionation. Several tetranuclear Schiff bases ligands were employed in analogous syntheses, and afforded a large family of tetranuclear assemblies with various stabilities, and have set the foundations for a better understanding of the structure/stability relationship. Moreover, the isolation of a fully stable polynuclear assembly with salen ligand has allowed the design of a new synthetic route based on the reduction of the hexavalent uranyl salen complex with an organometallic reductant. This allowed to the study of the counteraction influence on the final uranyl assembly shape and stability. The synthesis of a family of isostructural tetranuclear complexes centred on alkaline (Na^+, K^+, Rb^+) or earth-alkaline (Ca^{2+}) cations demonstrates the validity of this new synthetic method and provided a rare opportunity to compare structural parameters in isostructural CC complexes with various counterions. Notably, the disproportionation observed in presence of lithium ions provided insights on the parameters controlling the stability of the CC complexes. This synthetic method, applied to transition metal cations, provided the largest 5f-3d cluster isolated to date and proved that very original topologies can be obtained by the combination of cation-cation interactions with the geometrical preferences of 3d metal ions. Further developments stemming from this synthetic route may be anticipated, especially considering the large number of transition metal ions that could potentially be used.

Moreover, the remarkable role played by the counterion in these assemblies prompted an investigation into developing a “cation free” system. The use of a single charged tetradentate

ligand afforded a trinuclear homometallic uranyl(V) complex, and proved that stable CC complexes could be formed without the need of a additional metal cation.
Finally, the investigation of the magnetic properties of these complexes was carried out, and the observation of clear magnetic coupling has laid the groundwork for the establishment of a magnetostructural correlation for uranyl complexes. Moreover, the combination of 5f and 3d metals magnetic properties has been proven to be an efficient way to generate molecules with SMM properties.

The second aim of this work was to provide new synthetic routes towards low valent uranium oxo/hydroxo clusters. The first direction investigated was based on the synthetic methods developed in the team for the synthesis of oxo/hydroxo uranium clusters by the hydrolysis of low valent precursors. This synthetic route provided polynuclear clusters with high nuclearity, but necessitated to be improved to rationally access larger assemblies. A fine tuning of the reaction conditions during the hydrolysis of trivalent uranium in presence of the biologically relevant benzoate ligands allowed the synthesis of uranium oxo clusters of different topologies. Notably, large U_{10} and U_{16} clusters were synthesised through the variation of the media basicity.
Using similar organic acids, the formation of hexanuclear U(IV) oxo-clusters has been observed in the disproportionation of pentavalent uranyl giving insight on the aggregation phenomena observed in the environment.
Finally we demonstrated that uranyl(V) complexes can be exploited to generate uranium oxo clusters through U(IV) induced disproportionation. This synthetic route afforded uranium clusters with original topologies, shaped by the organic ligands of the pentavalent uranium precursor.

In this work, we developed several well defined synthetic routes to polynuclear assemblies of uranium. These synthetic methods have strong fundamental implications, and contribute to a better understanding of the specific coordination chemistry of the actinides. The isolation of well defined polynuclear species provides simple models to the understanding of the much more complex actinide behaviour in the environment and in nuclear industry. The polynuclear uranium clusters synthesised in this work have been proven to be highly promising for the design of magnetic materials, and the synthetic approaches developed in this work open a very large avenue in the quest for uranium based single molecule magnets.

Experimental part

CHAPTER V. Experimental part

V.1 Materials and methods

V.1.1 Solvents and starting materials

V.1.1.1 General

All manipulations were carried out under an inert argon atmosphere using Schlenk techniques and an MBraun glovebox equipped with a purifier unit. The water and oxygen level were always kept at less than 1 ppm. The solvents were purchased from Aldrich in their anhydrous form conditioned under argon and were vacuum distilled from K/benzophenone (pyridine, thf, dme, diisopropylether and toluene), sodium dispersion (hexane, eicosane) or CaH_2 (CH_2Cl_2, acetonitrile, benzonitrile, dmso and methanol) and degassed by three freeze-thaw cycles. dmso was stored over activated 3Å molecular sieves. Anhydrous O_2 gas was purchased from Fischer Scientific and further dried over P_2O_5 for 48 hours. Deuterated solvent were prepared identically, except pyridine-d_5 and dmso-d_6 both obtained by drying commercial, degassed three time and further dried over 3Å molecular sieves preliminary heated at 200°C under high vacuum. Water solutions were prepared from distilled and degassed MilliQ water and anhydrous solvents.

Depleted uranium turnings were purchased from the "Société Industrielle du Combustible Nucléaire" of Annecy (France). $CaCl_2$(DME) was synthesised from $CaCl_2 \cdot 2\ H_2O$ according to literature procedure [321] while $Mn(NO_3)_2$ was obtained by drying the hydrated salt in presence of P_2O_5 followed by high vacuum drying at 40°C. Cp^*_2Co, pyridine N-oxide, 18-crown-6, I_2, benzoic acid were purchased from Aldrich and sublimated prior to use. Pyridine hydrochloride was recrystallized from ethyl acetate/diethyl ether and dried under high vacuum. Dibenzo-18-crown-6 was recrystallized twice from toluene and dried under high vacuum for 7 days. TMEDA was vacuum distilled from Na/benzophenone. The $[Bu_4N][PF_6]$ electrolyte was recrystallized from warm toluene, conditioned under argon and dried under high vacuum (10^{-7} mmHg) prior to use. Unless otherwise specified, all the reagent and ligands were dried under high vacuum (10^{-7} mBar) for minimum 3 days. The glassware was systematically oven dried at 200°C over minimum 10h followed by 3 vacuum/ argon cycles.

Elemental analyses were performed under argon by Analytische Laboratorien GMBH at Lindlar, Germany.

V.1.1.2 Starting materials

The starting materials $[(UO_2py_5)(KI_2py_2)]$ [170], $[UO_2I_2py_3]$ [170] $[UI_4(Et_2O)]$ [322], $[UI_4(PhCN)_4]$ [316],$[UCl_4]$ [323], $[UI_3(thf)_4]$[324], $[U(salen)Cl_2(thf)_2]$ [325] and $[UO_2(salophen\text{-}^tBu_2)(py)K]$ [176] were prepared according to literature procedures.

V.1.2 Characterizations

V.1.2.1 Magnetic measurements

Static magnetic properties were measured using a Quantum Design SQUID MPMS-XL 5.0 susceptometer. Ultra-Low Field Capability ±0.05 G for the 5 T magnets. Continuous Low Temperature Control/Temperature Sweep Mode (CLTC) - Sweep rate: 0.001 - 10 K/min. Temperature range: 2K to 300K.

The magnetic measurements of uranyl(V) compounds are complex, due to three specificities:

-The high anisotropy of uranium complexes induce relatively strong torquing during the magnetic measurement and the samples should be restrained mechanically or through the use of a frozen liquid.

-The uranium complexes in the oxidation states lower than +VI are often exceedingly air sensitive, and the sample should be protected from air to avoid sample oxidation.

-The magnetic signal of uranyl(V) complexes is usually low, due to their $5f^1$ configuration. The sample holder should possess a very low signal, at least two orders of magnitude lower than the complex signal.

During the course of this PhD, several sample holders were tested and improved, including, Kel-F®, aluminium and Suprasil® quartz, under vacuum, Argon or Helium. Samples were

restrained either by pressing in the sample holder of by using a frozen inert liquid such as cyclohexane or eicosane.

We found that the method below gave the best results:
The samples were crushed in an agate mortar and pressed under argon into a quartz Suprasil® container which was then introduced under argon in a 5mm Suprasil-Quartz tube with a Teflon cap or were introduced in a 5mm Suprasil-Quartz tube, covered with cyclohexane or eicosane and sealed under vacuum. Contribution to the magnetization from quartz container and tube were measured independently and subtracted from the total measured signal to be corrected. Diamagnetic corrections were made using Pascal's constants. For each compound, the measurements were performed at several fields. Reproducibility of the magnetic measurement was checked for each compound by the independent measurement of three recrystallized samples from three different synthetic batches.

V.1.2.2 Electrochemistry

Cyclic voltammetry experiments were performed using a PAR 273 potentiostat. All experiments were performed in a glovebox. The working electrode consisted of a platinum disk embedded in PTFE (1 mm diameter or 2.5 mm diameter), a Pt counter electrode, and an Ag/AgCl reference electrode. Solutions employed during cyclic voltammetry studies were typically 2.5 mM for the uranium complex and 0.1 M for $[Bu_4N][PF_6]$. All potentials are reported versus the $[Cp_2Fe]^{0/+}$ couple.

V.1.2.3 FTIR spectra.

FTIR spectra were recorded with a Perkin Elmer Spectrum 100 Series FTIR spectrophotometer in KBr pellets and were routinely corrected for baseline.

V.1.2.4 NMR studies.

V.1.2.4.1 ***General considerations***

^{1}H NMR spectra were recorded on Varian MERCURY 400 MHz and Bruker Advance DMX 200 MHz and 500 MHz spectrometers at 298 K. NMR chemical shifts are reported in ppm with solvent as internal reference; the signals were assigned to the corresponding protons using COSY and NOESY experiments. Abbreviations used for describing multiplicity of the NMR signals are: s (singlet), d (doublet), dd (doublet of doublet), t (triplet), dt (doublet of triplet), q (quadruplet) and m(multiplet) and br (broad).

V.1.2.4.2 ***Diffusion coefficients measurements***

The diffusion NMR experiments were performed using a Pulsed-Field Gradient STimulated Echo (PFGSTE) sequence, using bipolar Gradients, at 298 K and no spinning was applied to the NMR tube. [326-328]

The following BPP-LED (**B**ipolar **P**ulse **P**air – **L**ongitudinal **E**ddy-current **D**elay) pulse sequence was applied[327]:

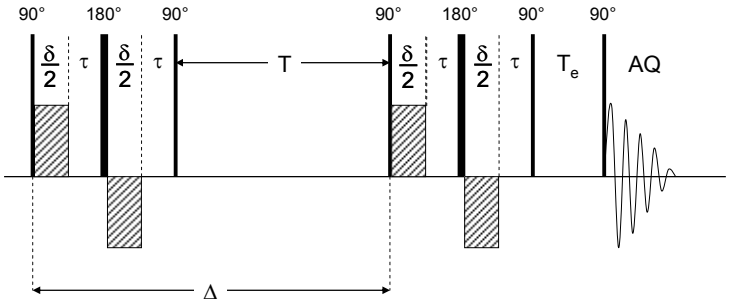

δ= 2 ms. τ = 0.5 ms.

The diffusion times T were optimized for each complex/solvent couple, with values ranking in the range 80-180 ms. The evolution of the pulsed-field gradient during the NMR diffusion experiments was established in 25 steps, applied linearly between 2.7 and 41.6 G.cm^{-1}.

In the present sequence the intensity of the signal is given by the following equation: [327]

$$I(q) = I(0).\exp\left[-D.q^2.\left(\Delta - \frac{\delta}{3} - \frac{\tau}{2}\right)\right] \quad \text{with } q = \gamma.\delta.g$$

and D : diffusion coefficient (m².s^{-1}), Δ: time between the two gradient pulse sequences (s), δ : bipolar gradient duration (s), τ : pulse separation delay (s), γ : magnetogyric ratio of the observed nucleus (s^{-1}.T^{-1}) and finally g : gradient strength (T.m^{-1}).

The diffusion coefficient is then the slope of the line obtained by plotting $\ln(I/I_0)$ against $q^2.\left(\Delta - \frac{\delta}{3} - \frac{\tau}{2}\right)$

V.1.2.4.3 ***Spherical hydrodynamic radius***

The spherical hydrodynamic radius (called Stokes radius) of the molecule was calculated from the Stokes-Einstein equation and compared to the value obtained from the solid state structure and with a similar reference compound in the same solvent:

$$r_{sph} = \frac{k_B.T}{6\pi.\eta.D}$$

r_{sph}

η (Pa.s) = viscosity of the medium ; k_B ($m^2.kg.s^{-2}.K^{-1}$) = Boltzmann constant.

T : absolute temperature (K); D : diffusion coefficient ($m^2.s^{-1}$)

The hydrodynamic radii calculated from the measured coefficient diffusion values were compared with the spherical radii evaluated from the crystal structure by considering the volume of the ellipsoid determined by the three main dimensions and calculating the radius of a sphere of the same volume.

V.1.2.5 UV/Vis-NIR studies

UV-Visible measurements were carried out with a Varian Cary 50 Probe spectrophotometer while Visible-NIR spectra were recorded a Lambda 9 Perkin Elmer spectrophotometer in quartz cells (optical path lengths: 1 mm and 1cm) adapted with J. Young valves.

V.1.2.6 Mass spectrometry

Mass spectra were acquired on a LXQ-linear ion trap (Thermo Scientific, San Jose, CA,USA), equipped with an electrospray source in a pyridine/acetonitrile mixture (1:1 to 1:5) which was prepared and filtered on microporous filters in the glove-box and maintained under argon until injection in the spectrometer. Electrospray full scan spectra, in the range of *m/z* 50 –3000 amu, were obtained by infusion through fused silica tubing at 2 – 10 μL min^{-1}.

The solutions were analysed in positive mode. The LXQ calibration (*m/z* 50-2000) was achieved according to the standard calibration procedure from the manufacturer (mixture of caffeine/MRFA and Ultramark 1621). The LXQ calibration (*m/z* 2000-4000) was performed with ES tuning mix (Agilent). The temperature of the heated capillary of the LXQ was set to the range of 180-220 °C, the ion spray voltage was in the range of 1-3 kV with an injection time of 5-100 ms. The experimental isotopic profile was compared in each case to the theoretical one.

V.1.2.7 X-Ray crystallography

Diffraction data were taken using a Oxford-Diffraction XCallibur S kappa geometry diffractometer (Mo-Kα radiation, graphite monochromator, λ = 0.71073 Å). To prevent evaporation of co-crystallised solvent molecules the crystals were coated with light hydrocarbon oil and the data were collected at 150 K. The cell parameters were obtained with intensities detected on three batches of 5 frames. The crystal-detector distance was 4.5 cm. The number of settings and frames has been established taking in consideration the Laue symmetry of the cell by CrysAlisPro CCD Oxford-diffraction software. The data were collected for 1° increments in ω with a different exposure time for each crystal depending on the intensities measured during the first three batches of 5 frames. Unique intensities detected on all frames using the Oxford-diffraction CrysalisPro Red program were used to refine the values of the cell parameters. The substantial redundancy in data allows empirical absorption corrections to be applied using multiple measurements of equivalent reflections with the ABSPACK Oxford-diffraction program. Space groups were determined from systematic absences, and they were confirmed by the successful solution of the structure. The structures were solved by direct methods using the SHELXTL 6.14 [329] package and for all structures all atoms, including hydrogen atoms, were found by difference Fourier synthesis. All non-hydrogen atoms were anisotropically refined whereas hydrogen atoms were fixed in ideal position. Details of the data collections and crystal parameters are given in appendix.

V.1.2.8 Bond Valence Sum calculation

Bond valences for each U–X (X = O, N, I) bond were calculated using the formula: s_{ij} = exp[(r_{ij} - d_{ij})/b) (where d_{ij} is the experimental bond length while r_{ij} and b are empirically determined constants for the given *i-j* bond) proposed by Brown[264] for al U–X bonds. From the parameters published on the Web (http://www.ccp14.ac.uk/ccp/web-mirrors/i_d_brown/bond_valence_param) we have chosen r_{ij} = 2.075 and b = 0.37 for U^{V}–O and U^{VI}–O bonds. We have used r_{ij} = 2.112 and b = 0.37 for calculating the valences of U^{IV}–O bonds. For U–N bond we used for both U^{VI}–N and U^{V}–N bonds r_{ij} = 1.93 and b = 0.35, which was proposed for calculating valences of U^{VI}–N bonds only, as there were no parameters proposed for U^{V}–N bonds. However, we expect it could only slightly affect bond

valence sum for U^{V} as valences of U–N do not contribute considerably to the sum of bond valence of uranium. For the U^{IV}–N bonds we used r_{ij} = 2.18 and b = 0.37. Browns parameters were preferred with respect to Burns parameters [265-267] because they include values for U-N and U-I bonds. The sum of bond valences for compounds **3**, **4**, **5**, **12**, **21**, **23**, **26**, **27**, **29** and **31** are presented in appendix.

V.2 Synthesis

V.2.1 Ligands and ligand potassium salts syntheses

V.2.1.1 Schiff bases

The two ligands N,N'-ethylene-bis(salicylideneimine) (salenH_2) and N,N'-phenylene-bis(salicylideneimine) (salophenH_2), were prepared according to the literature procedures [330] [331]and dried under high vacuum for a week prior to use.

V.2.1.1.1 *Synthesis of acacenH_2*

Diethylamine (1.36 g, 1.52 mL, 22.5 mmol, 1 eq.) was added dropwise to a solution of acetylacetone (5g, 5.15 mL, 50 mmol, 2.2 eq.) in toluene (150 mL) in a three neck flask connected to a Dean-Stark apparatus. The resulting solution was refluxed for 24h. 0.7 mL of H_2O was collected from the Dean-Stark. Off white crystals formed while cooling to room temperature. These crystals were filtered, dissolved in dichloromethane boiled to reflux in presence of charcoal. After filtration on a Celite pad, the volatiles were removed in vacuo, and the residue was recrystallized from a dichloromethane/pentane mixture to afford 2.96 g of white crystals of acacenH_2 (13.5 mmol, 60 %).

^{1}H NMR: (CD_3Cl, 298K, 200MHz): 1.90 (s, 6H); 1.99 (s, 6H); 3.41 (m, 2H); 4.99 (s, 2H); 10.89 (br s, 2H).

V.2.1.1.2 *Synthesis of MesaldienH_2*

4.68 g (5.15 mL, 40 mmol, 1 eq.) of N-methyldiethylenetriamine were added dropwise to a boiling solution of salicylaldehyde (10 g, 11.6 mL, 80 mmol, 2 eq.) in 100 mL EtOH, resulting in a colour change to deep yellow. The resulting solution was kept under reflux 18 h,

and the volatiles were removed in vacuo to afford 14.5 g of bright yellow crystals (0.039 mmol, 98%)

^{1}H NMR: (CD_3Cl, 298K, 200MHz): 2.41 (s, 3H); 2.81 (m, 4H); 3.75 (m, 4H); 6.86 (td, 2H); 6.93 (dd, 2H); 7.17 (dd, 2H); 7.33 (dd, 2H); 8.32 (s, 2H); 13.40 (s, 2H).

V.2.1.1.3 ***General synthesis of (ligand)K_2:***

A solution of (ligand)H_2 (>1 eq.) in thf (3 mL) was added to a suspension of KH (2 eq.) in thf (1 mL). The mixture was stirred until the end of gas evolution (up to 4 h) and subsequent 3 hours leading to a white precipitate in the case of (acacen)K_2 and to a yellow precipitate for (salen)K_2, (Mesaldien)K_2 and (salophen)K_2. After removal of the excess of KH by filtration, the precipitates were washed 3 times with 3 mL of thf.

AcacenK$_2$:(acacen)H_2 (525.0 mg, 2.34 mmol, 1 eq), KH (160 mg, 3.99 mmol, 1.70 eq) Yield (acacen)K_2: (592 mg , 97 %) ^{1}H NMR: (Pyridine-d_5, 298K, 200MHz): 1.61 (s, 6H); 2.09 (s, 6H); 3.46 (s, 2H); 5.02 (s, 2H); 6.80 (s, 1H).

SalenK$_2$: (salen)H_2 (215.0 mg, 0.80 mmol, 1 eq), KH (60.5 mg, 1.51 mmol, 1.88 eq) Yield (salen)K_2: (192.1 mg , 73.9 %) ^{1}H NMR: (dmso-d_6, 298K, 200MHz): 3.53 (s, 2H); 5.75 (m, 1H); 6.03 (m, 1H); 6.70 (t, 1H); 7.27 (d, 1H); 8.55 (s, 1H).

SalophenK$_2$: (salophen)H_2 (167.2 mg, 0.53 mmol, 1eq), KH (40.10 mg, 1.00 mmol, 1.90 eq) Yield (salophen)K_2: (170 mg , 82.0 %) ^{1}H NMR: (dmso-d_6, 298K, 400MHz): 5.84 (t, 1H); 6.11 (d, 1H); 6.78 (m, 2H); 7.01 (m, 1H); 7.26 (d, 1H); 8.39 (s, 1H).

(Mesaldien)K$_2$: (Mesaldien)H_2 (860.0 mg, 2.64 mmol, 1 eq), KH (211 mg, 5.28 mmol, 2 eq) Yield (Mesaldien)K_2: (899 mg , 84 %) ^{1}H NMR: (dmso-d_6, 298K, 200MHz): 2.43 (s, 3H); 2.79 (m, 4H); 3.75 (m, 4H); 6.83 (td, 2H); 6.91 (dd, 2H); 7.17 (dd, 2H); 7.30 (dd, 2H); 8.25 (s, 2H).

V.2.1.2 Synthesis of 2-(4-Tolyl)-1,3-bis(quinolyl)malondiimine (HL)

The synthesis of 2-(4-Tolyl)-1,3-bis(quinolyl)malondiimine described in the literature [275] in our hands did not yield the desired compound in significant yield, but resulted in a mixture of

compounds difficult to separate. We describe here a more convenient synthetic route inspired from the synthesis of β-diketiminate ligands described by Power and co-workers [332]
HL is light sensitive, and therefore the reaction mixture should be protected from light.
A round-bottom flask in an ice bath was charged with 8-aminoquinoline (0.919 g, 6.38 mmol), and ethanol was added up to its entire solubilisation (5 mL). Concentrated HCl (270 µL, 3.19 mmol) was added, affording an orange suspension. To this suspension a solution of 2-(4-tolyl)malondialdehyde (0.517 g (3.19 mmol) in ethanol (20 mL) was added drop-wise maintaining the flask below 0°C. The resulting red solution was stirred 16h at room temperature and then 150 mL of dichloromethane were added. The resulting solution was neutralised at 0°C with 50 mL of a $NaHCO_3$ saturated aqueous solution. The organic layer was separated, dried over Na_2SO_4 and the volatiles were removed by vacuum distillation to provide 880mg of an orange solid (2.13 mmol, 67%).
^{1}H NMR (200MHz, dmso-d_6, 298K): δ=13.97 (t, 1H), 8.83 (dd, 2H); 8.58 (d, 2H); 8.39 (dd, 2H) 7.84 (dd, 2H); 7.66 (m, 4H); 7.58 (d, 2H); 7.50 (d, 2H); 7.22 (d, 2H), 2.33 (s, 3H, -CH_3).

V.2.1.3 Synthesis of potassium 2-(4-Tolyl)-1,3-bis(quinolyl)malondiiminate (LK)

To a solution of 2-(4-Tolyl)-1,3-bis(quinolyl)malondiimine (62mg, 0.15mmol, 1 equiv) in thf (2mL) was added a suspension of KH (6 mg, 0.15mmol, 1 equiv) in thf (1mL) and the resulting reaction mixture was stirred at room temperature for 12 hours. The resulting dark violet suspension was filtered out and was washed with thf (4x1mL) and dried under vacuum to yield 53.9mg of LK (0.12mmol, 80%). The residual content of thf was evaluated for each sample by NMR.
^{1}H NMR (200MHz, CD_3CN, 298K): δ=8.74 (s, 4H); 8.16 (d, 2H, J^3_{H-H}=8.03Hz); 7.95 (s, 2H); 7.39 (m, 4H); 7.26 (d, 2H, J^3_{H-H}=7.5Hz); 7.05 (s, 2H); 7.01 (s, 2H); 2.28 (s, 3H, -CH_3).

V.2.1.4 Synthesis of potassium benzoate

A solution of benzoic acid (330 mg, 2.69 mmol, 1.1 eq) in thf (6 mL) was added to a suspension of KH (98.50 mg, 2.65 mmol, 1 eq) in thf (2 mL). The mixture was stirred 24 h

until the gaseous clearing was complete. The solution was filtered under suction and washed three times with 2 mL thf. The white precipitate filtered off was dried under vacuum to yield 375 mg (2.35 mmol, 92 %) of potassium benzoate salt.

^{1}H NMR (200MHz, dmso-d_6, 298K): δ=8.12 (s, 2H); 7.62 (s, 2H); 7.45 (s, 1H).

V.2.2 Synthesis of uranium complexes

V.2.2.1 [(UO_2)(salen)K(py)]·1.4KI, 2

$[(UO_2py_5)(KI_2py_2)]_n$, **1** (150 mg, 0.134 mmol) was added to a suspension of salenK_2 (47.3 mg, 0.134 mmol,1 eq.) in pyridine (2 mL) affording a dark blue solution. After stirring this solution for 4h at room temperature, a violet powder was formed. The violet solid was filtered, washed 3 times with pyridine (3 mL) and dried under vacuum to yield 70 mg (0.077 mmol, 58%) of light purple powder.

Elemental analysis (%) calcd for [UO_2(salen)K(py)] 1.4 KI ($C_{21}H_{19}I_{1.4}K_{2.4}N_3O_4U$, M_r = 886.83) C 28.44, H 2.16, N 4.74; found C 28.42, H 2.55, N 4.92.

^{1}H NMR (dmso-d_6; 298 K; 200MHz): δ=0.41 (br, 1H, -NCH_2-); 1.06 (br. d, 1H, J^3_{H-H} = 8.5 Hz, -CH-$_{aromatic}$); 2.80 (br. d, 1H, -NCH_2-); 5.13 (t, 1H, J^3_{H-H} = 6.3 Hz, -CH-$_{aromatic}$); 5.87 (br. t, 1H, -CH-$_{aromatic}$); 6.05 (d, 1H, J^3_{H-H} = 6.6 Hz, -CH-$_{aromatic}$); 12.31 (s, 1H, -HC=N-).

V.2.2.2 [UO_2(salen)]$_4$[μ_8-K]$_2$[K(18C6)py]$_2$, 3

To a suspension of **2** (39.0 mg, 0.0439 mmol) in pyridine (1.5 mL), 17 mg of 18C6 (0.065 mmol, 1.5 eq.) were added. After stirring for 3h at room temperature the violet suspension turned into a clear dark blue solution. The slow diffusion of hexane into this solution yielded 37.9 mg of **3** (0.0103 mmol, 94%) as X-ray quality deep blue crystals.

ESI/MS m/z = 1111.4 $\{[UO_2(Salen)]_2[\mu_8\text{-K}]\}_2^{2-}$.

Elemental analysis (%) calcd for $\{[UO_2(salen)]_4[\mu_8\text{-K}]_2\}(K(18C6)py)_2$ ($C_{88}H_{104}K_4N_8O_{28}U_4$, M_r = 2830.33) C 37.34, H 3.70, N 3.96; found C 37.48, H 4.04, N 4.22 .

^{1}H NMR (no changes observed over 30 days) (pyridine-d_5; 298 K; 500MHz): δ=-0.09 (br, 1H, -NCH_2-); 1.87 (d, 1H, J^3_{H-H} = 8.5 Hz, -CH-$_{aromatic}$); 3.36 (br, 1H, -NCH_2-); 3.67 (s, 18-c-6);

5.40 (t, 1H, -CH-$_{aromatic}$); 6.14 (d, 1H, J^3_{H-H} = 8.5 Hz, -CH-$_{aromatic}$); 6.38 (t, 1H, -CH-$_{aromatic}$); 11.78 (s, 1H, -HC=N-).

^{1}H NMR (dmso-d_6; 298 K; 200MHz): δ=0.41 (br, 1H, -NCH_2-); 1.06 (br. d, 1H, J^3_{H-H} = 8.5 Hz, -CH-$_{aromatic}$); 2.80 (br. d, 1H, -NCH_2-); 3.56 (s, 18-c-6); 5.13 (t, 1H, J^3_{H-H} = 6.3 Hz, -CH-$_{aromatic}$); 5.87 (br. t, 1H, -CH-$_{aromatic}$); 6.05 (d, 1H, J^3_{H-H} = 6.6 Hz, -CH-$_{aromatic}$); 12.31 (s, 1H, -HC=N-).

μ_{eff} (dmso, 298 K) = 1.94(9) μ_B.

V.2.2.3 [(UO_2)(salen)(py)], 4

N,N-diisopropylethylamine (1mL, 5.20 mmol, 2 equiv) was added to a stirred solution of salenH_2 (697.5mg, 2.60 mmol, 1 equiv) in MeOH (25mL) and $CHCl_3$ (25mL). Under vigorous stirring $UO_2(NO_3)_2(H_2O)_6$ (1.306g, 2.60 mmol, 1 equiv) was added to this solution resulting in a change of colour from yellow to bright orange. The reaction mixture was brought to reflux (80°C) for 3h and slowly cooled down to room temperature without stirring resulting in the formation of a bright orange solid. This orange precipitate was filtered out and washed with cold MeOH/$CHCl_3$ (20 mL). This filtrate was dissolved in pyridine and brought to reflux for 1 hour. Slow diffusion of *n*.hexane to the orange solution resulted in the formation of orange cubic crystals of [(UO_2)(salen)(py)] that were washed with n-hexane and dried under high vacuum to yield 1.304g of the desired compound (2.12 mmol, 82%).

^{1}H NMR (pyridine-d_5; 298 K; 400MHz): δ=4.47 (s, 2H, -NCH_2-); 6.85 (t, 1H, J^3_{H-H} = 7.5 Hz, -CH-$_{aromatic}$); 7.35 (d, 1H, J^3_{H-H} = 8.3 Hz, -CH-$_{aromatic}$); 7.69 (m, 2H, -CH-$_{aromatic}$); 9.38 (s, 1H, -HC=N-).

Elemental analysis (%) calcd for [$U^{VI}O_2$(salen)(py)] ($C_{21}H_{19}N_3O_4U$, M_r = 615.42) C 40.98, H 3.11, N 6.83; found C 40.60, H 3.25, N 6.88.

V.2.2.4 {[UO_2(salen)μ-K(18C6)][UO_2(salen)]$_3$[μ_8-K]$_2$}, 5

To a suspension of **2** (49.0 mg, 0.055 mmol, 3 eq.) in pyridine (2mL), a solution of **4** (11.5 mg, 0.018 mmol, 1 eq.) in pyridine (1 mL) was added. After stirring for 1h, a pyridine solution (0.5 mL) of 18C6 (42.8 mg, 0.162 mmol, 9 eq.) was added to this mixture. The clear

brown solution obtained after 18h stirring was evaporated under vacuum to the ¼ of the initial volume. Slow diffusion of *n*.hexane afforded complex **5** as deep brown crystals (21 mg, 0.0083 mmol, 46%).

ESI/MS: 2222.8, $\{[UO_2(Salen)]_2[\mu_8\text{-}K]\}_2^-$. Elemental analysis (%) calcd for $\{[UO_2(salen)\mu\text{-}K(18C6)][UO_2(salen)]_3\}[\mu_8\text{-}K]_2$ ($C_{76}H_{80}K_3N_8O_{22}U_4$, M_r = 2525.63) C 36.12, H 3.19, N 4.43; found C 36.31, H 3.41, N 4.62.

^{1}H NMR of $\{[UO_2(salen)\mu\text{-}K(18C6)][UO_2(salen)]_3\}[\mu_8\text{-}K]_2$: The complex **5** is selectively obtained as a pure crystalline solid. However, when this solid is dissolved in pyridine, it quickly undergoes a rearrangement to yield a mixture of complexes **5**, **3** and **4**. The proton NMR spectrum of a 14 mM solution of **5** in pyridine shows a mixture of **5**, **4** and **3** in 10:3.5:5 ratios. The lower solubility of complex **5** with respect to **4** and **3** in pyridine allows the isolation of **5** in good yield and in a pure form.

It should be noted than **5** can also be synthesised in good yield through the addition of one equivalent of CuI to **3:**

1 mL of a 1 mM solution of CuI in d_5-py was added to a solution of 3 mg (0.001 mmol) of **3** in 0.7 mL d_5-py. The solution, initially green, turns in 5 minutes to dark brown. ^{1}H NMR of the solution was identical to compound **5**.

^{1}H NMR (pyridine-d_5; 298 K; 500MHz) of **5**: δ= 0.46 (br, 1H, -NCH_2-); 2.83 (br d, 1H, $J^3_{H\text{-}H}$ = 7.5 Hz, -NCH_2-); 3.58 (s, 18-c-6); 5.79 (br t, 1H, $J^3_{H\text{-}H}$ = 8.5 Hz,-$CH\text{-}_{aromatic}$); 6.54 (br d, 1H, $J^3_{H\text{-}H}$ = 7.3 Hz,-$CH\text{-}_{aromatic}$); 6.65 (br t, 1H, -$CH\text{-}_{aromatic}$); 7.47 (t, 1H, $J^3_{H\text{-}H}$ = 7.5 Hz, -$CH\text{-}_{aromatic}$); 11.43 (s, 1H, -HC=N-).

V.2.2.5 $\{[UO_2(acacen)]_4(\mu_8\text{-}K)_2][K(18C6)]_2\}$ 2py, 6

70 mg (0.062 mmol) of $[(UO_2py_5)(KI_2py_2)]_n$, **1** were added to a suspension of acacenK_2 (18.8 mg, 0.062 mmol, 1 eq.) in pyridine (2 mL) resulting in a dark red solution with a small amount of an off-white precipitate. After 1h stirring at room temperature, the reaction mixture was filtered and 18C6 (34 mg, 0.124 mmol, 2 eq) was added to the resulting solution. After 48h stirring at room temperature the solution colour turns to pink. Slow diffusion of diisopropyl ether (6mL) into this solution yielded after 2 days 15 mg of X-ray quality deep red crystals of the tetrameric $\{[UO_2(acacen)]_4[\mu_8\text{-}K]_2[K(18C6)(py)]_2\}$, **6** complex (0.0054 mmol, 34%) (The crystallization was stopped at an early stage to avoid the co-crystallisation

of K(18C6)I [*], which explains the low yield of the reaction). These crystals are not very stable and easily loose the two pyridine molecules present in the unit cell when they were dried under vacuum for the elemental analysis.

Elemental analysis (%) calcd for $\{[UO_2(acacen)]_4[\mu_8\text{-}K]_2[K(18C6)]_2\}$ $C_{72}H_{120}N_8O_{28}K_4U_4$, M_r = 2654.29) C 32.58, H 4.56, N 4.22; found C 32.47, H 4.77, N 4.53.

^{1}H NMR (no changes observed over 30 days) (pyridine-d_5; 298 K; 200MHz): δ(ppm) -3.83 (s, 3H, -CH_3); -3.22 (s, 3H , -CH_3); 0.26 (br s, 1H, -NCH_2-); 1.09 (d, 2H, C-HC=C-); 3.80(s, 24H, 18C6).

[*] (Higher yields (82%) can be obtained with a longer crystallisation time (10 days) but the final compound presents 2 co-crystallized K(18C6)I. Elemental analysis (%) calcd for $\{[UO_2(acacen)]_4[\mu_8\text{-}K]_2[K(18C6)]_2\}\cdot 2[K(18C6)I]$ $C_{96}H_{168}N_8O_{40}K_4U_4$, M_r = 2654.29) C 32.80, H 4.82, N 3.19; found C 32.79, H 4.61, N 3.39.)

V.2.2.6 $\{[UO_2(acacen)]_4[\mu_8\text{-}K]\}$ 2[K(222)py], 7

50 mg (0.044 mmol, 1 eq.) of $[(UO_2py_5)(KI_2py_2)]_n$, **1** were added to a suspension of acacenK_2 (13.5 mg, 0.044 mmol, 1 eq.) in pyridine (2 mL) resulting in a dark red solution with a small amount of an off-white precipitate. After 1h stirring at room temperature, the reaction mixture was filtered and 50.6 mg (0.134 mmol, 3 eq.) of [2,2,2]cryptand were added to the resulting solution. After 2h stirring at room temperature the solution colour turns to clear brown. Slow diffusion of diisopropyl ether (7mL) into this solution yielded 17.8 mg of X-ray quality deep red crystals of the tetrameric $[UO_2(acacen)]_4[\mu_8\text{-}K]\cdot 2[K(222)(py)]$complex (0.0058 mmol, 53%). These crystals are not very stable and partially loose the pyridine molecules present in the unit cell when they were dried under vacuum for the elemental analysis.

Elemental analysis (%) calcd for $[UO_2(acacen)]_4[\mu_8\text{-}K]\cdot 2[K(222)]\cdot 1.7(py)$ $C_{92.5}H_{1552.5}N_{13.7}O_{28}K_4U_4$, M_r = 3013.14) C 36.87, H 5.10, N 6.37; found C 36.84, H 4.92, N 5.98.

^{1}H NMR (no changes observed over 30 days) (pyridine-d_5; 298 K; 500MHz): δ(ppm) -3.75 (s, 3H, -CH_3); -3.22 (s, 3H , -CH_3); 0.46 (br s, 1H, -NCH_2-); 1.16 (s, 1H, C-HC=C-); (2.38, 3.39, 3.44, s, [2,2,2] cryptand); 6.80 (s, 1H, -NCH_2-). ESI-MS: 1023.2 (M^{2+}); 2046.9 (M^+).

V.2.2.7 {[UO_2(salophen)]$_4$[μ_8-K]$_2$[μ_5-KI]$_2$[(K(18C6)]}·2[K(18C6)(thf)$_2$]·2I, 8

To 100.0 mg (0.090 mmol, 1 eq.) of [(UO_2py$_5$)(KI_2py$_2$)]$_n$, **1** a solution of salophenK_2 (36.0 mg, 0.090 mmol, 1 eq.) and 18C6 (78.1 mg, 0.296 mmol) in py (3.0 ml) was added resulting instantly in a clear green solution. The solution was stirred for 2 hours and then filtered. The filtrate was concentrated under *vacuum* (0.5 ml). Addition of $^{i}Pr_2O$ (7 ml) to the resulting solution yielded a green oil which was filtered, triturated in $^{i}Pr_2O$ (5 x 3 ml) and dried under *vacuum* to yield 125.0 mg of a light green powder. This powder was recrystallized from thf (10 mL) to yield the title compound as dark blue crystals (73 mg, 0.011 mmol, 51 %). The compound co-crystallizes with K(18C6)I which couldn't be separated by further recrystallisation.

Elemental analysis (%) calcd for [UO_2(salophen)]$_4$[μ_8-K]$_2$[μ_5-KI]$_2$[(K(18C6)]·2[K(18C6)(thf)$_2$]I ($C_{208}H_{312}I_9K_{13}N_8O_{75}U_4$, M_r = 6727.32) C 37.14, H 4.67, N 1.67, I 16.98; found C 36.84, H 4.92, N 2.06, I 17.28.

^{1}H NMR of the green powder (Pyridine-d$_5$; 298 K; 400MHz,) δ(ppm) 0.69 (br d., 1H), 2.06 (br, 1H); 3.86 (s, 18C6) (4.65 (br d. 1H), 4.78 (br t., 1H); 6.04 (br. 1H); 6.26 (s, 1H); 7.01 (br t. 1H).

V.2.2.8 [UO_2(salophen)(py)][Cp^*_2Co], 9

To a suspension of 2.5 mg of Cp^*_2Co (0.007 mmol, 1 eq.) in 0.5 mL of pyridine-d$_5$, a bright orange solution of 5.0 mg (0.008 mmol, 1eq.) of [UO_2(Salophen)(thf)] in py-d$_5$ (0.5 mL) was added resulting in a fast colour change to deep green. The solution was stirred overnight at room temperature. The ^{1}H NMR spectrum of the resulting dark green solution reveals the presence of a uranyl(V) complex of salophen.

^{1}H NMR (Pyridine-d$_5$; 298 K; 200MHz, no changes observed over 15 days): δ(ppm) 0.35 (br d, 1H), 1.53 (br, 1H); 4.57 (br. d, 1H), 4.62 (br t, 1H); 5.78 (s, 1H); 5.88 (br., 1H); 7.03 (br t. 1H), 8.38 (br., around 20H $Cp^*_2Co^+$/Cp^*_2Co). This complex is stable in pyridine but its isolation was prevented by its lower stability after addition of non-solvents (necessary for the crystallization) such as n.hexane.

V.2.2.9 {[UO_2(dophen)]$_4$[μ_8-K(py)]$_2$[μ_4-K(py)$_2$]$_4$[μ_2-I]$_2$}, 10

To 61.3 mg (0.055 mmol, 1 eq.) of [(UO_2py_5)(KI_2py_2)]$_n$, **1** a solution of dophenK_2 (24.2 mg, 0.055 mmol, 1 eq.) in py (2.0 ml) was added resulting instantly in a dark green solution. The solution was stirred for 3 hours and then filtered. The filtrate was layered with hexane (5 ml) affording after slow diffusion of the counter solvent the title compound as dark green crystals (42 mg, 0.010 mmol, 77 %).

^{1}H NMR (pyridine-d_5; 298 K; 500MHz): δ= 3.54 (br d, 2H); 6.28 (t, 2H, J^3_{H-H} = 7Hz); 6.60 (d, 2H, J^3_{H-H} = 7.6 Hz); 6.92 (m, 4H); 8.84 (s, 2H); 9.52 (d, 2H, J^5_{H-H} = 8.9 Hz).

V.2.2.10 [UO_2(salen)(py)][Cp*$_2$Co], 11

A 0.5 mL pyridine solution of 5 mg of **4** (0.081 mmol) was added to a 0.5 mL pyridine suspension of 2.7 mg of Cp*$_2$Co (0.081 mmol), resulting after 3h stirring at room temperature in a green solution.

ESI/MS: 536.3 (M^+), 1072.1 ($2M^+$).

^{1}H NMR (Pyridine-d_5; 298 K; 200MHz): δ=-8.16 (s, 2H, -NCH_2-); -0.45 (d, 1H, J^3_{H-H} = 8.5 Hz, -CH-$_{aromatic}$); 4.06 (d, 1H, J^3_{H-H} = 7.5 Hz, -CH-$_{aromatic}$); 4.66 (t, 1H, J^3_{H-H} = 7.3 Hz, -CH-$_{aromatic}$); 4.94 (s, 1H, -HC=N-), 6.13 (t, 1H, J^3_{H-H} = 8.7 Hz, -CH-$_{aromatic}$).

The addition of a solution of K(18C6)I or of K([2,2,2] cryptand)I (1eq.) in pyridine to a solution of the compound obtained by the reduction of [$U^{VI}O_2$(salen)(py)] with Cp*$_2$Co results in the formation of complex **3**, as monitored by ^{1}H NMR, UV spectroscopy and ESI/MS.

V.2.2.11 [UO_2(salen)(py)]$_2$[Cp*$_2$Co], 12

6.5 mg of Cp*$_2$Co (0.0195 mmol, 1 eq.) were added to a pyridine solution of **4** (10.8 mg, 0.0395 mmol, 2 eq.) in py (1 mL) and the resulting suspension was stirred for 3 hours. The solution became dark green after few minutes and did not change further with time. The solution was filtered and *n.*hexane was layered on the top of the filtrate (4 mL) to afford after 2 days 12 mg of green crystals (0.0081mmol, 92 %).

Elemental analysis (%) calcd for [UO2(salen)(py)]2 [Cp*2Co]$C_{57}H_{63}N_5O_8CoU_2$, M_r = 1481.15) C 46.22, H 4.29, N 4.73; found C 46.16, H 4.33, N 4.89.

^{1}H NMR (pyridine-d_5; 298 K; 500MHz,) δ(ppm) -3.36 (br S, 1H), -0.24 (br, 1H); 1.86 (br. s, 30H, $Cp^*_2Co^+$), 3.68 (s, 1H); 5.83 (s, 1H); 6.25 (s, 4H); 6.61 (s, 1H), 6.74 (br s, 1H), 7.69 (d, 1H), 8.10 (s, 1H), 10.62(s, 1H), 11.99(s, 1H).

V.2.2.12 Isolation of $[UO_2(salen)(py)]_2[Me_4N]$, 13

2.9 mg of Cp^*_2Co (0.0088 mmol, 1 eq.) were added to a pyridine solution of **4** (5.4 mg, 0.0195 mmol, 2 eq.) and Me_4NI (2.7 mg, 0.0132 mmol, 1.5 eq.) in py (1 mL) and the resulting suspension was stirred for 12 hours. The solution became dark green after few minutes and did not change further with time. The solution was filtered and n.hexane was layered on the top of the filtrate (4 mL) to afford after 1 days green crystals of **13**.

V.2.2.13 $[UO_2(salen)]_4[\mu_8\text{-}Na]_2[Na(18C6)(py)_2]_2$, 14

A suspension of Cp^*_2Co (21.4 mg, 0.065 mmol, 1 eq.) in pyridine was added to an orange solution of **4** (40 mg, 0.065 mmol, 1 eq.) in pyridine (3 mL), resulting in a dark-green suspension which was stirred for ½ hour. A suspension of NaI (9.7 mg, 6.5 µmol, 1 eq.) in pyridine (1 mL) was then added to the dark-green filtrate. Immediately a violet precipitate started to form. This suspension was stirred overnight at room temperature. The violet precipitate was filtered and washed with pyridine (7 x 1mL) and n-hexane (1 mL). The violet powder of $[UO_2(salen)]_4Na_4$ was then suspended in a pyridine solution of 18C6 (17.2 mg, 13 µmol, 2 eq.). After 5 hours stirring the dark blue solution was filtered and set for crystallisation by slow diffusion of n-hexane into the solution to yield large dark blue crystals of $\{[UO_2(salen)]_4[\mu_8\text{-}Na]_2[Na(18C6)(py)_2]_2\}$ (27.5 mg, 8.9µmol, 55%).

Elemental analysis (%) calculated for $\{[UO_2(salen)]_4[\mu_8\text{-}Na]_2[Na(18C6)(py)_2]_2\}$ ($C_{108}H_{124}N_{12}Na_4O_{28}U_4$ 3082;28 g;mol^{-1}) C 42.08, H 4.05 and N 5.45, found C 42.35, H 4.12 and N 5.67.

^{1}H NMR (no changes observed over 30 days) (pyridine-d_5; 298 K; 500MHz): δ=-0.16 (br, 1H, -NCH_2-); 1.89 (d, 1H, $J^3_{H\text{-}H}$ = 8.5 Hz, -$CH\text{-}_{aromatic}$); 3.36 (br, 1H, -NCH_2-); 3.67 (s, 18-c-6);

5.40 (t, 1H, -CH-$_{aromatic}$); 6.14 (d, 1H, J^3_{H-H} = 8.5 Hz, -CH-$_{aromatic}$); 6.38 (t, 1H, -CH-$_{aromatic}$); 11.65 (s, 1H, -HC=N-).

V.2.2.14 {[UO_2(salen)]$_4$[μ_8-Rb]$_2$[Rb(18C6)]$_2$}, 15

A suspension of Cp*$_2$Co (17.2 mg, 0.052 mmol, 1 eq.) in pyridine was added to a bright orange solution of **4** (40 mg, 0.052 mmol, 1 eq.) in pyridine (3 mL), resulting in a dark-green suspension which was stirred for ½ hour. A suspension of RbI (11 mg, 0.052 mmol, 1 eq.) in pyridine (1 mL) was added to the dark-green filtrate. Immediately a violet precipitate started to form. This suspension was stirred for 3 hour at room temperature, and the violet precipitate was collected by centrifugation and washed with pyridine (7 x 1 mL). A solution of 13.8 mg (0.052 mmol, 1 eq.) of 18C6 in pyridine (5 mL) was added to the resulting solid, to yield, after 16h stirring at room temperature, a dark blue solution. The solution was filtered and the filtrate was layered with n.hexane (5 mL) to yield after 2 days 32 mg (0.016 mmol, 81%) of dark blue crystals of {[UO_2(salen)]$_4$[μ_8-Rb]$_2$[Rb(18C6)]$_2$}, **15** suitable for X-ray.
The ^{1}H NMR (pyridine-d_5; 298 K; 500MHz) is identical to the ^{1}H NMR of **2**.
Elemental analysis (%) calculated for {[UO_2(salen)]$_4$[μ_8-Rb]$_2$[Rb(18C6)]$_2$} ($C_{88}H_{104}N_8Rb_4O_{28}U_4$ 3015.81 g;mol^{-1}) C 35.05, H 3.48 and N 3.72, found C 34.82, H 3.34 and N 3.99.

V.2.2.15 Isolation of {[UO_2(salen)]$_4$[μ_4-O]$_2$[μ_4-Li]$_4$}, 16

[UO_2(salen)][Cp*$_2$Co] was prepared "in situ" by the addition of 5.7 mg of Cp*$_2$Co (0.017 mmol, 1 eq.) to a solution of **4** (10.4 mg, 0.017 mmol, 1 eq.) in py (1 mL). 2.3 mg of LiI (0.017 mmol, 1 eq.) were added to the resulting dark green solution. The addition leads to an immediate colour change to dark red. The solution was stirred another 72 h and then filtered. Slow diffusion of ^{i}Pr$_2$O (3 mL) affords after 7 days red brown crystals of {[UO_2(salen)]$_4$[μ_4-O]$_2$[μ_4-Li]$_4$}, **16** as well as a significant quantity of intractable red precipitate.

V.2.2.16 Reaction of 3 with py·HCl

A solution of py·HCl (1.4 mg, 0.012 mmol, 4 eq) in pyridine-d_5 (0.5 mL), was added to a solution of **3** (7.5 mg, 0.003 mmol, 1 eq.) in pyridine-d_5 (2 ml) resulting in an immediate colour change of the solution, from dark blue to yellow. The ^{1}H NMR spectrum of this solution clearly indicated the presence of three species, $[UO_2(salen)(py)]$ $[U(salen)_2]$ and $[UCl_2(salen)]$, identified by comparison with the separately synthesized complexes. These three complexes were crystallized from this solution by slow diffusion of hexane. The presence of water as a reaction product was clearly identified by ^{1}H NMR spectroscopy.

V.2.2.17 $\{[UO_2(salen)]_4Ca_2\}$, 17

A dark brown solution of Cp^*_2Co (107mg, 0.325 mmol, 1 equiv) in pyridine (2 mL) was added under stirring to a bright orange solution of $[UO_2(salen)(py)]$ (200mg, 0.325 mmol, 1 equiv) in pyridine (3 mL), resulting in a dark green solution, which was stirred over 1h. The dark green solution was filtered, and a solution of $CaCl_2$(DME) (32.7 mg, 0.162 mmol, 0.5 equiv) in pyridine (7 mL) was added dropwise to the filtrate under stirring, resulting in the precipitation of a violet powder. The suspension was stirred over 3h at room temperature, and the light violet precipitate was filtered out and washed with pyridine (4 x 2 mL) and n-hexane (2 x 2 mL) and dried under vacuum to afford a violet powder. This powder was extracted from CH_2Cl_2 to afford the title compound as dark red crystals suitable for X-ray of $\{[UO_2(salen)]_4Ca_2\}\cdot CH_2Cl_2$ that were dried under vacuum to yield 166mg of a violet powder of $\{[UO_2(salen)]_4Ca_2\}$ (0.074 mmol, 90%)

Elemental analysis(%) calculated for $\{[UO_2(salen)]_4Ca_2\}$ ($C_{64}H_{56}N_8Ca_2O_{16}U_4$ 2225.46g/mol) C 34.54, H 2.54 and N 5.04, found C 34.80, H 2.56 and N 5.13.

^{1}H NMR (pyridine-d_5; 298 K; 500MHz): δ=0.92 (br, 1H, -NCH_2-); 2.50 (d, 1H, $J^3_{H\text{-}H}$ = 8.5 Hz, -CH-$_{aromatic}$); 4.88 (br, 1H, -NCH_2-); 5.30 (t, 1H, -CH-$_{aromatic}$); 5.74 (br d, 1H, -CH-$_{aromatic}$); 6.38 (t, 1H, -CH-$_{aromatic}$); 12.82 (s, 1H, -HC=N-).

V.2.2.18 [{[UO_2(salen)]$_2$Mn(py)$_3$}$_6$], 18

A dark brown solution of Cp*$_2$Co (53.5 mg, 0.162 mmol, 1 equiv) in pyridine (1 mL) was added under stirring to a bright orange solution of [UO_2(salen)(py)], **4** (100mg, 0.162 mmol, 1 equiv) in pyridine (2 mL), resulting in a dark green solution, which was stirred over 1h. The dark green solution was filtered, and a solution of $Mn(NO_3)_2$ (14.5 mg, 0.081 mmol, 0.5 equiv) in pyridine (5 mL) was added drop-wise to the filtrate under stirring, resulting in the precipitation of a dark violet powder. The suspension was stirred over 3h at room temperature, and the dark violet precipitate was filtered out and washed with pyridine (10 x 1.5 mL) and dried thoroughly under vacuum to yield 82 mg of a violet powder of [{[UO_2(salen)]$_2$Mn(py)$_3$}$_6$], **18** (0.010 mmol, 74%).

Elemental analysis(%) calculated for [{[UO_2(salen)]$_2$Mn(py)$_3$}$_6$] ($C_{282}H_{258}N_{42}Mn_6O_{48}U_{12}$ 8189.38 g/mol) C 41.36, H 3.18 and N 7.18, found C 41.02, H 3.18 and N 7.08.

Synthesis of X-ray quality crystals of [{[UO_2(salen)]$_2$Mn(py)$_3$}$_6$]$_2$

A dark brown solution of Cp*$_2$Co (21.4 mg, 0.065 mmol, 1 equiv) in pyridine (1 mL) was added under stirring to a bright orange solution of [UO_2(salen)(py)], **4** (40 mg, 0.065 mmol, 1 equiv) in pyridine (3 mL), resulting in a dark green solution, which was stirred for 1h. The dark green solution was filtered and introduced in one of the two sections of a slow diffusion H tube. A solution of $Mn(NO_3)_2$ (6.6 mg, 0.032 mmol, 0.5 equiv) in pyridine (4 mL) was introduced into the other section of the H tube, and the two sections were layered with pyridine (10 mL) to allow the two sides to be connected with solvent. After two weeks diffusion; dark violet crystals of [{[UO_2(salen)]$_2$Mn(py)$_3$}$_6$], **18** suitable for X-ray crystallised at the interface. The dark violet crystals were collected by filtration and washed with pyridine (3 x 1.5 mL) and dried under vacuum to yield 39 mg of a dark violet crystals of [{[UO_2(salen)]$_2$Mn(py)$_3$}$_6$] (0.0047 mmol, 87 %)

Elemental analysis(%) calculated for [{[UO_2(salen)]$_2$Mn(py)$_3$}$_6$]·2py ($C_{292}H_{268}N_{44}Mn_6O_{48}U_{12}$ 8347.59 g/mol) C 42.01, H 3.24 and N 7.26, found C 41.89, H 3.05 and N 7.38.

The complexes isolated by the two methods described above possess identical IR and magnetic properties.

V.2.2.19 $[UO_2L]_3$, 19

A dark violet suspension of LK (64 mg, 0.14 mmol, 1 equiv) in pyridine (2 mL) was added to a light orange suspension of $[UO_2(py)_5][KI_2(py)_2]$, **1** (160 mg, 0.14 mmol, 1equiv.) in pyridine (2 mL). The reaction mixture was stirred over 12h, resulting in a dark red suspension. In order to remove the KI formed during the course of the reaction, dibenzo-18-crown-6 (100 mg, 0.28 mmol, 2 equiv.) was added to the reaction mixture which was then stirred for an additional 2 hours. The resulting suspension was centrifuged, and the dark reddish solid was collected, and washed with pyridine (10 x 1.5 mL), rinsed with diisopropylether (2 x 1.5 mL) and dried under reduced pressure to yield 90.1 mg (0.043 mmol, 93%) of $[UO_2(L)]_3$, **19** as a dark red solid. While the ligand is light sensitive, complex **19** is not sensitive to light over a month period. Crystals of **19** suitable for X-ray diffraction were obtained by slow diffusion of diisopropylether into a saturated solution (3.6 $x10^{-4}$ M) of **19** in acetonitrile.

^{1}H NMR (400MHz, CD_3CN, 298K): δ=9.17 (d, 2H, J^3_{H-H} = 7 Hz); 6.20 (d, 2H, J^3_{H-H} = 7 Hz); 4.98 (t, 2H, J^3_{H-H} = 7.7 Hz); 4.86 (d, 2H, J^3_{H-H} = 7.9 Hz); 3.85 (s, 3H,); 3.67 (d, 2H, J^3_{H-H}= 8 Hz); 0.98 (m, 2H); -2.23 (s, 2H); -6.50 (d, 2H, J^3_{H-H} = 8 Hz), -12.99 (br s, 2H).

ESI-MS: 2051 ($M-H^+$).

Elemental analysis (%) calculated for $[UO_2(L)]_3$ ($C_{84}H_{63}N_{12}O_6U_3$ 2050.56g/mol) C 49.20, H 3.10 and N 8.20, found C 49.39 H 3.27 N 8.46.

The absence of iodine and potassium was confirmed using silver nitrate and flame tests.

V.2.2.20 $[UO_2(L)Cl]$, 20

14 mg (0.0068 mol) of $[UO_2(L)]_3$ were suspended in 3 mL of CD_2Cl_2, resulting, after 5 minutes stirring, in a clear brown solution. Proton NMR spectroscopy revealed the presence of only one set of diamagnetic signals. Slow diffusion of hexane in this solution afforded 14 mg (0.019 mmol, 93 %) of $[UO_2(L)Cl]\cdot CD_2Cl_2$, **20**$\cdot CD_2Cl_2$ as dark brown needles suitable for single crystal X-ray diffraction.

^{1}H NMR (200MHz, CD_2Cl_2, 298K): δ=10.83 (d, 2H, J = 6.1 Hz); 9.36 (s, 2H); 8.59 (d, 2H, J = 8.5 Hz); 8.03 (m, 2H); 7.80 (m, 4H); 7.59 (d, 2H, J = 7.3 Hz); 7.43 (d, 2H, J = 7.3 Hz); 7.24 (d, 2H, J = 8.5 Hz); 2.43 (s, 3H).

Elemental analysis (%) calculated for $[UO_2(L)Cl]\cdot 0.2CD_2Cl_2$, ($C_{28.2}H_{21.4}N_4O_2UCl_{1.4}$ 735.97 g/mol) C 46.02, H 2.93 and N 7.61, found C 45.76 H 3.18 N 7.36.

V.2.2.21 {$[UO_2(L)]_2[\mu_2\text{-}O]$}, 21

Dry O_2 (1 atm.) was added to a dark red suspension of $[UO_2(L)]_3$, **19** (24 mg 0.011 mmol, 1 eq) in MeCN (3 mL) resulting in a colour change of the solution to brown. After letting stand the solution at room temperature for 2 days, dark red crystals of {$[UO_2(L)]_2[\mu_2\text{-}O]$} suitable for single crystal X-ray diffraction formed. The crystals were filtered, washed with cold MeCN (2*2 mL) and dried under vacuum to yield 17.6 mg of the title compound (0.012 mmol, 72%).

^{1}H NMR (400MHz, py, 298K): δ=11.93 (d, 2H, J = 4.9 Hz); 11.37 (d, 2H, J = 4.9 Hz); 9.76 (s, 2H); 9.57 (s, 2H); 8.17 (d, 2H, J = 8.6 Hz); 8.08 (d, 2H, J = 8.6 Hz); 7.94 (d, 2H, J = 8.6 Hz); 7.86 (d, 2H, J = 8.6 Hz); 7.70 (m, 6H); 7.62 (m, 6H); 7.41 (d, 2H, J = 7.9 Hz); 7.37 (d, 2H, J = 7.9 Hz); 7.09 (dd, 2H, J = 7.9, 4.9 Hz); 6.98 (dd, 2H, J = 7.9, 4.9 Hz); 2.41 (s, 3H), 2.38 (s, 3H).

Elemental analysis (%) calculated for $\{[UO_2(L)]_2[\mu_2\text{-}O]\}\cdot 2MeCN$ ($(C_{60}H_{48}N_{10}O_5U_2$ 1465.17;g/mol) C 49.19, H 3.30 and N 9.56, found C 49.50, H 3.41 and N 9.68.

ESI-MS: 1384.1 ($\{[UO_2(L)]_2[\mu_2\text{-}O]\}\text{-}H^+$)

V.2.2.22 {$[UO_2(Mesaldien)]K\}_n$, 22

A suspension of MesaldienK_2 (49.6 mg, 0.123 mmol, 1 eq.) in pyridine (2 mL) was added to a suspension of $[(UO_2py_5)(KI_2py_2)]_n$ (138 mg, 0.123 mmol, 1 eq.) in 1 mL of pyridine resulting in a dark blue solution. After 3h stirring at room temperature, an off-white precipitate of KI formed. The precipitate was filtered out and thf was slowly diffused into the filtrate to yield after two days blue needles suitable for X-Ray single crystal diffraction. The solid was filtered, washed 3 times with 3 ml of cold thf and dried under vacuum to afford 73.5 mg of the **22**·0.1 py (0.116 mmol, 94%).

^{1}H NMR (MeCN-d_3; 298 K; 200MHz): δ=-5.45 (s, 3H, -NCH_3); -4.61 (s, 2H,-NCH_2-);-3.70 (s, 2H,-CH_2-); -3.70 (br s, 2H,-CH_2-);0.65 (d, 2H, $J^3_{H\text{-}H}$ = 8.54 Hz, -$CH\text{-}_{aromatic}$); 1.28 (br. s,

2H,-NCH_2-); 5.02 (t, 2H, J^3_{H-H} = 7.32 Hz, -CH-$_{aromatic}$); 5.31 (d, 2H, J^3_{H-H} = 7.21 Hz, -CH-$_{aromatic}$); 6.13 (t, 2H, J^3_{H-H} = 7.32 Hz, -CH-$_{aromatic}$); 9.46 (s, 2H, -HC=N-).

Elemental analysis (%) calcd for $\{[UO_2(Mesaldien)]K\}_n \cdot 0.1$ py ($C_{19.5}H_{21.5}KN_{3.1}O_4U$, M_r = 640.42) C 36.57, H 3.38, N 6.78; found C 36.69, H 3.49, N 6.84.

V.2.2.23 {[UO_2(Mesaldien)-(U(Mesaldien)]$_2$(μ-O)}, 23

To a suspension of $[(UO_2py_5)(KI_2py_2)]_n$ (92.7 mg, 0.083 mmol, 2 eq.) of pyridine (1 mL), a suspension of MesaldienK_2 (50 mg, 0.124 mmol, 3 eq.) in pyridine (2 mL) was added resulting in a dark blue solution. After 3h stirring at room temperature, a solution of $UI_4(Et_2O)_2$ (37.1 mg, 0.041 mmol, 1 eq.) in pyridine (1 mL) was added, resulting in a colour change of the solution to dark red. The resulting solution was stirred for 15 minutes, filtered, and the filtrate was left standing to afford **23** as red needles which were collected, washed and dried to yield 52.5 mg of **23**·2.5 py (0.0208 mmol and 76%). Evaporation of this solution and re-crystallisation of the residue from py/hexane afforded 7.2 mg (0.0121 mmol, 88%) of [UO_2(Mesaldien)].

The low solubility of the isolated complex **23** prevents its NMR characterization.

Elemental analysis (%) calcd for {[UO_2(Mesaldien)(U(Mesaldien)]$_2$(μ-O)·2.5 py ($C_{88.5}H_{96.5}N_{14.5}O_{13}U_4$, M_r = 2523.19) C 42.13, H 3.86, N 8.05; found C 42.13, H 4.12, N 8.39.

Compound **23** can also prepared by reacting directly the preformed [U(Mesaldien)I_2]·MeCN complex with **22** according to the following procedure.

A dark blue solution of **22** (13.5 mg, 0.021 mmol, 2 eq.) in pyridine (1 mL) was added to a dark brown solution of [U(Mesaldien)I_2]·MeCN (9.13 mg, 0.011 mmol, 1 eq) in pyridine (1 mL) under vigorous stirring, resulting in the formation of a red brown precipitate. The suspension was stirred over 24h, and the light orange filtrate was separated from the red-brown precipitate by centrifugation. Proton NMR of the mother liquor shows the presence of the uranyl(VI) complex **23**. The red-brown powder was washed twice with pyridine (2*1.5 mL), and dried under vacuum to afford 15.8 mg (0.0059 mmol, 84%) of the title compound as a light brown powder. IR spectrum of this powder is identical to the spectrum of **23** synthesised from the first route.

Elemental analysis (%) calcd for {[UO_2(Mesaldien)(U(Mesaldien)]$_2$(μ-O)·4py ($C_{96}H_{104}N_{16}O_{13}U_4$, M_r = 2641.69) C 43.65, H 3.97, N 8.48; found C 43.65, H 4.10, N 8.58.

V.2.2.24 [UO_2(Mesaldien)], 24

MesaldienH_2 (802.1 mg, 2.4 mmol, 1 eq.) was dissolved in 50 mL of a 1/1 methanol/chloroform mixture in a three neck flask. To this yellow solution diisopropylethylamine (859 µL, 4.9 mmol, 2 eq.) was added, and the solution was stirred over 5 min. Uranyl nitrate hexahydrate (1.240 g, 2.4 mmol, 1 eq.) was added portionwise to this solution, resulting in the formation a deep red solution. The solution was heated under reflux over 2 h, during which time a bright orange solid precipitate. The solution was then cooled in a water/ice bath, and the orange solid was filtered and rinsed twice with cold methanol/chloroform (10 mL). The solid was dried under vacuum prior to be extracted into warm pyridine (6 mL) using a Soxlet apparatus, resulting in a red crystalline compound, that was kept over 3 days at 45°C under high vacuum, to yield 980 mg of the title compound (1.65 mmol, 68%).

^{1}H NMR (MeCN-d_3; 298 K; 200MHz): δ=3.20 (s, 3H, -NCH_3); 3.55 (dd, 2H,-NCH_2-);3.86 (td, 2H,-CH_2-); 4.52 (dd, 2H,-CH_2-);5.02 (tq, 2H, ,-NCH_2-); 6.73 (t, 2H, J^3_{H-H} = 7.01 Hz, -CH-$_{aromatic}$); 6.99 (d, 2H, J^3_{H-H} = 8.24 Hz, -CH-$_{aromatic}$); 7.56 (d, 2H, J^3_{H-H} = 7.62 Hz, -CH-$_{aromatic}$); 9.49 (s, 2H, -HC=N-).

Elemental analysis (%) calcd for [UO_2(salen)] ($C_{19}H_{21}N_3O_4U$, M_r = 593.42) C 38.46, H 3.57, N 7.08; found C 38.41, H 3.62, N 7.28.

V.2.2.25 [U(Mesaldien)I_2]·MeCN, 25

A solution of 57.7 mg of $UI_4(PhCN)_4$ (0.049 mmol) in acetonitrile (1.5 mL) was added to a suspension of 20 mg of saldienK_2 (0.049 mmol) in 1.5 mL of acetonitrile yielding after 5 minutes a dark red solution, that was filtered and set for crystallisation. 28.2 mg of dark red crystals suitable for X-Ray of [U(Mesaldien)I_2]·MeCN were collected after one night (0.033 mmol, 67%).

^{1}HNMR (200 MHz, py-d5, 298 K): δ = 96.53 (s, 2H), 42.42 (s, 2H), 29.86 (s, 2H), 23.10 (d, 4H), 16.62 (s, 2H), 13.65 (s, 2H), -2.92 (s, 3H) , -29.08 (s, 2H), -40.36 (s, 2H).

Elemental analysis (%) calcd for [U(Mesaldien)I_2]·MeCN: $C_{21}H_{24}I_2N_4O_2U$: C, 29.46; H, 2.83; N, 6.54. Found: C, 29.54; H, 2.81; N, 6.64

V.2.2.26 Isolation of {[UO_2(salen)][U(salophen-^{t}Bu$_2$)]$_2$[(U(salen)]$_2$(μ-O)$_3$(μ_3-O)}, 26

A dark green solution of [UO_2(salophen-^{t}Bu$_2$)(py)K] (12.9 mg, 0.0139 mmol, 2 eq.) in pyridine (0.5 mL) was added to a light green solution of [U(salen)Cl_2(thf)$_2$] (5 mg, 0.0069mmol, 1 eq.) in pyridine (0.5 mL), resulting in an immediate colour change to dark red. Proton NMR of the mother liquor shows the presence of a complicated mixture of uranium(IV)/(V)/(VI) compounds. The solution was stirred over 12h, taken to dryness and the brown solids were dissolved in acetonitrile to yield after 2 days standing dark brown crystals suitable for X-ray diffraction of **26** (4 mg collected).

V.2.2.27 [$U_6O_4(OH)_4(C_6H_5COO)_{12}(py)_3$], 27

From uranyl(V):

A solution of 21.9 mg of benzoic acid (0.179mmol, 2 eq) in 1.5 mL of pyridine was added to a red suspension of 100 mg of [(UO_2py_5)(KI_2py_2)] (0.089 mmol, 1 eq) in 1.5 mL pyridine, yielding after 10 minutes stirring a clear green solution. The resulting solution was stirred overnight, and concentrated under vacuum (0.5 mL). 2.5 mL of MeCN were added to the resulting green slurry and KI was removed by filtration. The resulting solution was left standing to yield after 2 days a yellow-green crystalline solid (22 mg, 48%) and a green solution (**b**).

The elemental analysis carried out reproducibly on these crystals is in agreement with the formula [$UO_4(OH)_4(C_6H_5COO)_{12}py_6$].MeCN: Elemental analysis (%) calcd for $C_{116}H_{97}N_7O_{32}U_6$, ($M_r$ = 3529.14) C 39.48, H 2.77, N 2.78; found C 39.48, H 2.97, N 2.38.

^{1}H NMR of the isolated cluster (pyridine-d_5; 298 K; 500MHz,) 17.69 (s, 2H), 9.95(br T, 2H), 9.70 (T, J = 6.45 Hz, 1H). Peaks were assigned by COSY experiment

Block shaped crystals suitable for X-ray studies of [$U_6O_4(OH)_4(C_6H_5COO)_{12}(py)_3$].2MeCN, **27**.2MeCN, were obtained by recrystallisation from pure acetonitrile. Recrystallisation from pyridine/acetonitrile in 1:3 ratios also produces crystals. X-ray analysis is this case in agreement with the formula [$U_6O_4(OH)_4(C_6H_5COO)_{12}(py)_5$].2MeCN.

From U(III):

An acetonitrile (0.5 mL) solution of potassium benzoate (7.1 mg, 0.044 mmol) was reacted with an acetonitrile solution (0.5 ml) of $UI_3(thf)_4$ (20.0 mg, 0.022 mmol). 88 µL of a 0.5 M solution of water (0.044 mmol) in acetonitrile was added to the resulting green colour solution. The resulting dark green solution was stirred over 1 day at room temperature, filtered and then evaporated to dryness under vacuum. The resulting green solid was dissolved in pyridine (1 mL) and diisopropyl ether (1 mL) was added, causing the formation of white precipitate of KI which was removed after 2 days by filtration. The resulting green solution was evaporated to dryness and the residue was recrystallized in acetonitrile, X-ray quality crystals of **27**·2MeCN were obtained over 6-7 hours in 75 % yield.

From U(IV):

Crystals of **27** were also obtained starting from $[UI_4(PhCN)_4]$ by reacting a pyridine solution (0.5 mL) of potassium benzoate (5.5 mg, 0.034 mmol) with a solution of $UI_4(PhCN)_4$ (20.0 mg, 0.017 mmol) in pyridine (0.5 ml). 68 µL of a 0.5(M) water solution in pyridine (0.034 mmol) was added to this mixture to yield, after 1 day stirring at room temperature, a green solution with an off-white precipitate. The precipitate was filtered out and the resulting green solution was evaporated under reduced pressure to yield a light green solid, which was recrystallized in acetonitrile. The structure of cluster **27** was confirmed by X-Ray diffraction.

V.2.2.28 $[UO_2(C_6H_5COO)_2(py)_2]$, 28

The green solution **b** obtained during the synthesis of **27** was evaporated under vacuum and the solid residue was dissolved in pyridine. Slow diffusion of hexane into the resulting light green solution afforded 23 mg (0.032 mmol, 38%) of $[UO_2(C_6H_5COO)_2py_2]$, **28**, as light yellow crystals of block shape suitable for X-Ray.

Elemental analysis (%) calcd for **28**·0.27 KI ($C_{24}H_{20}N_2O_6UK_{0.27}I_{0.27}$, M_r = 715.29) C 40.30, H 2.82, N 3.92; found C 40.30, H 2.98, N 4.30.

^{1}H NMR of the uranyl(VI) complex **28** (pyridine-d_5; 298 K; 200MHz,) 8.65 (br s, 2H), 7.46(br s, 3H). ESI/MS of the crude mixture (main peak m/z = 671.2 $\{UO_2(C_6H_5COO)_2py_2\}H^+$)

V.2.2.29 $[U_{10}O_8(OH)_6(C_6H_5COO)_{14}I_4(H_2O)_2(MeCN)_2]$, 29

220 µL of a 0.5 M solution of water (0.110 mmol) in acetonitrile were added drop-wise under vigorous stirring to a dark green solution of $UI_3(thf)_4$ (50 mg, 0.055 mmol) in 4 mL of MeCN, resulting in a colour change to light green after 5 minutes stirring. A suspension of potassium benzoate (17.6 mg, 0.110 mg) in MeCN (1 mL) was added to the solution. The light green resulting solution was stirred over 16 h. 1 mL of $^{i}Pr_2O$ was added to the solution, resulting in the precipitation of a white solid, that was filtered out. The filtrate was collected and the volatiles were removed in vacuo. The residue was extracted in 2 mL MeCN, filtered, and the filtrate was layered with 4 mL of $^{i}Pr_2O$. After 1 week 22 mg of green crystals of **29** were collected (0.0044 mmol, 80%).

Elemental analysis (%) calcd for $[U_{10}O_8(OH)_6(C_6H_5COO)_{14}I_4(H_2O)_2(MeCN)_2]$, ($C_{106}H_{82}N_4O_{42}U_{10}I_4$, M_r = 4971.71) C 25.61, H 1.66, N 1.13; found C 25.72, H 1.79, N 1.37.

V.2.2.30 $\{[K(MeCN)]_2[U_{16}O_{22}(OH)_2(C_6H_5COO)_{24}]\}$.4MeCN, 31

660 µL of a 0.5 M solution of water (0.33 mmol) in acetonitrile were added dropwise under vigorous stirring to a dark green solution of $UI_3(thf)_4$ (200 mg, 0.22 mmol) in 4 mL of MeCN, resulting in a colour change to light green after 5 minutes stirring. A suspension of potassium benzoate (53.0 mg, 0.33 mmol) in acetonitrile (2 mL) was added to the solution. The light green reaction mixture was stirred over 16 h and then filtered to remove KI. 100 µL of TMEDA (tetramethylethylenediamine) were added to the resulting solution, resulting in a fast precipitation of a light green microcrystalline powder. The microcrystalline powder was isolated by centrifugation, and washed twice with 1.5 mL of acetonitrile, to yield after drying 82 mg of the complex **31** (0.011 mmol, 80%). X-rays quality crystals were obtained either by letting stand a dilute acetonitrile solution of **31** (0.3 mmol) or by slow diffusion of an acetonitrile solution of TMEDA into a solution of $UI_3(thf)_4$ reacted with H_2O (1.5 eq) and potassium benzoate (1.5 eq).

The measured IR spectra of the microcrystalline and single crystals are identical.

Elemental analysis (%) calcd for **31** ($C_{180}H_{140}N_6O_{72}K_2U_{16}$, Mr = 7425.66) C 29.12, H 1.90, N 1.13; found C 28.99, H 2.00, N 1.16.

Bibliography

Bibliography

[1] M. H. Klaproth, *Chemische Annalen* **1789**, *2*, 387.
[2] E. M. Péligot, *Annales de Chimie et de Physique* **1842**, *5*, 5.
[3] H. Bequerel, *Comptes Rendus de L Academie Des Sciences* **1896**, *1*, 420.
[4] L. R. Morss, N. M. Edelstein, J. Fuger, *The Chemistry of the Actinide and Transactinide Elements*, Springer, Dordrecht, **2006**.
[5] S. Cotton, *Lanthanides and Actinides*, MacMillan Education, London, **1991**.
[6] L. Karmazin, M. Mazzanti, C. Gateau, C. Hill, J. Pecaut, *Chemical Communications* **2002**, 2892.
[7] C. Den Auwer, M. C. Charbonnel, M. G. B. Drew, M. Grigoriev, M. J. Hudson, P. B. Iveson, C. Madic, M. Nierlich, M. T. Presson, R. Revel, M. L. Russell, P. Thuery, *Inorganic Chemistry* **2000**, *39*, 1487.
[8] D. L. Clark, S. S. Hecker, G. D. Jarvinen, M. P. Neu, *The Chemistry of the Actinide and Transactinide Elements*, Springer, Dordrecht, **2006**.
[9] G. R. Choppin, *Radiochimica Acta* **1983**, *32*, 43.
[10] D. L. Clark, D. E. Hobart, M. P. Neu, *Chemistry Review* **1995**, *95*, 25.
[11] J. K. Bates, J. P. Bradley, A. Teetsov, C. R. Bradley, M. B. Tenbrink, *Science* **1992**, *256*, 649.
[12] B. Guillaume, G. M. Begun, R. L. Hahn, *Inorganic Chemistry* **1982**, *21*, 1159.
[13] N. J. Stoyer, D. C. Hoffman, R. J. Silva, *Radiochimica Acta* **2000**, *88*, 279.
[14] Vitorge, Pierre, *Chimie des actinides, Vol. BN2*, Techniques de l'ingénieur, Paris, FRANCE, **1999**.
[15] B. J. Masters, L. L. Schwartz, *Journal of the American Chemical Society* **1961**, *83*, 2620.
[16] G. Gordon, H. Taube, *Journal of Inorganic & Nuclear Chemistry* **1961**, *16*, 272.
[17] W. S. Jung, Y. Ikeda, H. Tomiyasu, H. Fukutomi, *Bulletin of the Chemical Society of Japan* **1984**, *57*, 2317.
[18] Y. Suzuki, S. D. Kelly, K. M. Kemner, J. F. Banfield, *Nature* **2002**, *419*, 134.
[19] F. R. Duke, R. C. Pinkerton, *Journal of the American Chemical Society* **1951**, *73*, 2361.
[20] H. G. Heal, *Transactions of the Faraday Society* **1949**, *45*, 1.
[21] D. M. H. Kern, E. F. Orlemann, *Journal of the American Chemical Society* **1949**, *71*, 2102.
[22] K. A. Kraus, F. Nelson, G. L. Johnson, *Journal of the American Chemical Society* **1949**, *71*, 2510.
[23] T. W. Newton, F. B. Baker, *Inorganic Chemistry* **1965**, *4*, 1166.
[24] A. Ekstrom, *Inorganic Chemistry* **1974**, *13*, 2237.
[25] H. Steele, R. J. Taylor, *Inorganic Chemistry* **2007**, *46*, 6311.
[26] M. Sundararajan, A. J. Campbell, I. H. Hillier, *Journal of Physical Chemistry A* **2008**, *112*, 4451.
[27] M. Sundararajan, R. S. Assary, I. H. Hillier, D. J. Vaughan, *Dalton Transactions* **2011**, *40*, 11156.
[28] Landress.G, Duyckaer.G, *Analytica Chimica Acta* **1972**, *58*, 369.
[29] J. Nadjo, J. M. Saveant, *Electrochimica Acta* **1971**, *16*, 887.
[30] Mastrago.M, J. M. Saveant, *Electrochimica Acta* **1968**, *13*, 751.
[31] P. C. Burns, *Comptes Rendus Chimie* **2010**, *13*, 737.

[32] W. Runde, G. S. Goff, *Radionucleides in the Environment*, John Wiley & Sons, Chichester, West Sussex, **2010**.
[33] W. Runde, *Los Alamos Science* **2000**, *26*, 392.
[34] G. R. Choppin, J. N. Mathur, *Radiochimica Acta* **1991**, *52-3*, 25.
[35] S. Ahrland, *Acta Chemica Scandinavica* **1949**, *3*, 374.
[36] C. L. Cahill, D. T. de Lill, M. Frisch, *Crystengcomm* **2007**, *9*, 15.
[37] J. Leciejewicz, N. W. Alcock, T. J. Kemp, in *Structure and Bonding, Vol. 82*, **1995**, pp. 43.
[38] C. J. Burns, *Science* **2005**, *309*, 1823.
[39] P. Thuery, M. Nierlich, B. Souley, Z. Asfari, J. Vicens, *Journal of the Chemical Society, Dalton Transactions: Inorganic Chemistry* **1999**, 2589.
[40] C. E. Rowland, C. L. Cahill, *Inorganic Chemistry* **2010**, *49*, 8668.
[41] R. N. Sylva, M. R. Davidson, *Journal of the Chemical Society-Dalton Transactions* **1979**, 465.
[42] K. A. H. Kubatko, K. B. Helean, A. Navrotsky, P. C. Burns, *Science* **2003**, *302*, 1191.
[43] P. C. Burns, K. A. Hughes, *American Mineralogist* **2003**, *88*, 1165.
[44] P. C. Burns, K. A. Kubatko, G. Sigmon, B. J. Fryer, J. E. Gagnon, M. R. Antonio, L. Soderholm, *Angewandte Chemie-International Edition* **2005**, *44*, 2135.
[45] C. R. Armstrong, M. Nyman, T. Shvareva, G. E. Sigmon, P. C. Burns, A. Navrotsky, *Proceedings of the National Academy of Sciences of the United States of America* **2012**, *109*, 1874.
[46] N. N. Krot, M. S. Grigoriev, *Russian Chemical Reviews* **2004**, *73*, 89.
[47] T. W. Newton, M. J. Burkhart, *Inorganic Chemistry* **1971**, *10*, 2323.
[48] K. Takao, S. Takao, A. C. Scheinost, G. Bernhard, C. Hennig, *Inorganic Chemistry* **2012**, *51*, 1336.
[49] H. Moriyama, T. Sasaki, T. Kobayashi, I. Takagi, *Journal of Nuclear Science and Technology* **2005**, *42*, 626.
[50] S. Takao, K. Takao, W. Kraus, F. Ernmerling, A. C. Scheinost, G. Bernhard, C. Hennig, *European Journal of Inorganic Chemistry* **2009**, 4771.
[51] A. P. Novikov, S. N. Kalmykov, S. Utsunomiya, R. C. Ewing, F. Horreard, A. Merkulov, S. B. Clark, V. V. Tkachev, B. F. Myasoedov, *Science* **2006**, *314*, 638.
[52] V. Neck, M. Altmaier, T. Fanghanel, *Comptes Rendus Chimie* **2007**, *10*, 959.
[53] E. J. O'Loughlin, S. D. Kelly, R. E. Cook, R. Csencsits, K. M. Kemner, *Environmental Science & Technology* **2003**, *37*, 721.
[54] D. M. Giaquinta, L. Soderholm, S. E. Yuchs, S. R. Wasserman, *Radiochimica Acta* **1997**, *76*, 113.
[55] S. Chakraborty, F. Favre, D. Banerjee, A. C. Scheinost, M. Mullet, J. J. Ehrhardt, J. Brendle, L. Vidal, L. Charlet, *Environmental Science & Technology* **2010**, *44*, 3779.
[56] J. K. Fredrickson, J. M. Zachara, D. L. Balkwill, D. Kennedy, S. M. W. Li, H. M. Kostandarithes, M. J. Daly, M. F. Romine, F. J. Brockman, *Applied and Environmental Microbiology* **2004**, *70*, 4230.
[57] E. V. F. K.E. German, V. F. peretrukhin, T. V. Khiznyak, M. Simonoff, *Radiochemistry* **2003**, *45*, 229.
[58] D. R. Lovley, E. J. P. Phillips, Y. A. Gorby, E. R. Landa, *Nature* **1991**, *350*, 413.
[59] M. Simonoff, C. Sergeant, S. Poulain, M. S. Pravikoff, *Comptes Rendus Chimie* **2007**, *10*, 1092.
[60] J. C. Renshaw, L. J. C. Butchins, F. R. Livens, I. May, J. M. Charnock, J. R. Lloyd, *Environmental Science & Technology* **2005**, *39*, 5657.

[61] E. J. Schofield, H. Veeramani, J. O. Sharp, E. Suvorova, R. Bernier-Latmani, A. Mehta, J. Stahlman, S. M. Webb, D. L. Clark, S. D. Conradson, E. S. Ilton, J. R. Bargar, *Environmental Science & Technology* **2008**, *42*, 7898.
[62] B. H. Gu, H. Yan, P. Zhou, D. B. Watson, M. Park, J. Istok, *Environmental Science & Technology* **2005**, *39*, 5268.
[63] W. Luo, B. Gu, *Environmental Science & Technology* **2009**, *43*, 152.
[64] G. J. Vazquez, C. J. Dodge, A. J. Francis, *Inorganic Chemistry* **2009**, *48*, 9485.
[65] D. R. Lovley, *Science* **2001**, *293*, 1444.
[66] R. Knopp, V. Neck, J. I. Kim, *Radiochimica Acta* **1999**, *86*, 101.
[67] R. E. Wilson, S. Skanthakumar, L. Soderholm, *Angewandte Chemie-International Edition* **2011**, *50*, 11234.
[68] T. G. Srinivasan, M. K. Ahmed, A. M. Shakila, R. Dhamodaran, P. R. V. Rao, C. K. Mathews, *Radiochimica Acta* **1986**, *40*, 151.
[69] J. Garraway, P. D. Wilson, *Journal of the Less-Common Metals* **1985**, *106*, 183.
[70] M. J. Sarsfield, R. J. Taylor, C. J. Maher, *Radiochimica Acta* **2007**, *95*, 677.
[71] L. M. Toth, H. A. Friedman, M. M. Osborne, *Journal of Inorganic & Nuclear Chemistry* **1981**, *43*, 2929.
[72] L. Soderholm, P. M. Almond, S. Skanthakumar, R. E. Wilson, P. C. Burns, *Angewandte Chemie-International Edition* **2008**, *47*, 298.
[73] A. C. Muscatello, J. D. Navratil, M. E. Killion, *Separation Science and Technology* **1983**, *18*, 1731.
[74] D. W. Ockenden, G. A. Welch, *Journal of the Chemical Society* **1956**, 3358.
[75] P. Thiyagarajan, H. Diamond, L. Soderholm, E. P. Horwitz, L. M. Toth, L. K. Felker, *Inorganic Chemistry* **1990**, *29*, 1902.
[76] R. J. Silva, H. Nitsche, *Radiochimica Acta* **1995**, *70-1*, 377.
[77] G. H. John, I. May, M. J. Sarsfield, D. Collison, M. Helliwell, *Dalton Transactions* **2007**, 1603.
[78] M. J. Sarsfield, A. D. Sutton, I. May, G. H. John, C. Sharrad, M. Helliwell, *Chemical Communications* **2004**, 2320.
[79] A. D. Sutton, I. May, C. A. Sharrad, M. J. Sarsfield, M. Helliwell, *Dalton Transactions* **2006**, 5734.
[80] A. M. Fedosseev, N. A. Budantseva, M. S. Grigoriev, K. E. Guerman, J. C. Krupa, *Radiochimica Acta* **2003**, *91*, 147.
[81] G. H. John, I. May, C. A. Sharrad, A. D. Sutton, D. Collison, M. Helliwell, M. J. Sarsfield, *Inorganic Chemistry* **2005**, *44*, 7606.
[82] A. R. Fox, S. C. Bart, K. Meyer, C. C. Cummins, *Nature* **2008**, *455*, 341.
[83] P. Roussel, W. Errington, N. Kaltsoyannis, P. Scott, *Journal of Organometallic Chemistry* **2001**, *635*, 69.
[84] P. Roussel, P. Scott, *Journal of the American Chemical Society* **1998**, *120*, 1070.
[85] G. Cloke, F. N., P. B. Hitchcock, *Journal of American Chemical Society* **2002**, *124*, 9352.
[86] W. J. Evans, S. A. Kozimor, J. W. Ziller, *Journal of the American Chemical Society* **2003**, *125*, 14264.
[87] A. L. Odom, P. L. Arnold, C. C. Cummins, *Journal of the American Chemical Society* **1998**, *120*, 5836.
[88] I. Korobkov, S. Gambarotta, G. P. A. Yap, *Angewandte Chemie-International Edition* **2002**, *41*, 3433.
[89] O. T. Summerscales, F. G. N. Cloke, P. B. Hitchcock, J. C. Green, N. Hazari, *Science* **2006**, *311*, 829.

[90] O. T. Summerscales, A. S. P. Frey, F. Geoffrey, N. Cloke, P. B. Hitchcock, *Chemical Communications* **2009**, 198.
[91] A. S. Frey, F. G. N. Cloke, P. B. Hitchcock, I. J. Day, J. C. Green, G. Aitken, *J. Am. Chem. Soc.* **2008**, *130*, 13816.
[92] P. L. Arnold, Z. R. Turner, R. M. Bellabarba, R. P. Tooze, *Chemical Science* **2011**, *2*, 77.
[93] S. M. Mansell, N. Kaltsoyannis, P. L. Arnold, *Journal of the American Chemical Society* **2011**, *133*, 9036.
[94] B. M. Gardner, J. C. Stewart, A. L. Davis, J. McMaster, W. Lewis, A. J. Blake, S. T. Liddle, *Proceedings of the National Academy of Sciences of the United States of America* **2012**, *109*, 9265.
[95] I. Castro-Rodriguez, K. Meyer, *Journal of the American Chemical Society* **2005**, *127*, 11242.
[96] O. P. Lam, S. C. Bart, H. Kameo, F. W. Heinemann, K. Meyer, *Chemical Communications* **2010**, *46*, 3137.
[97] I. Castro-Rodriguez, H. Nakai, L. N. Zakharov, A. L. Rheingold, K. Meyer, *Science* **2004**, *305*, 1757.
[98] O. P. Lam, C. Anthon, K. Meyer, *Dalton Transactions* **2009**, 9677.
[99] O. P. Lam, F. W. Heinemann, K. Meyer, *Angewandte Chemie-International Edition* **2011**, *50*, 5965.
[100] O. P. Lam, K. Meyer, *Polyhedron* **2012**, *32*, 1.
[101] A.-C. Schmidt, A. V. Nizovtsev, A. Scheurer, F. W. Heinemann, K. Meyer, *Chemical Communications* **2012**, *48*, 8634.
[102] P. L. Diaconescu, P. L. Arnold, T. A. Baker, D. J. Mindiola, C. C. Cummins, *Journal of the American Chemical Society* **2000**, *122*, 6108.
[103] P. L. Diaconescu, C. C. Cummins, *Journal of American Chemical Society* **2002**, *124*, 7660.
[104] Q. L. Zhao, T. D. Harris, T. A. Betley, *Journal of the American Chemical Society* **2011**, *133*, 8293.
[105] C. L. Hill, *Journal of Molecular Catalysis a-Chemical* **2007**, *262*, 2.
[106] C. L. Hill, *Chemical Reviews* **1998**, *98*, 1.
[107] B. Nohra, H. El Moll, L. M. Rodriguez Albelo, P. Mialane, J. Marrot, C. Mellot-Draznieks, M. O'Keeffe, R. Ngo Biboum, J. Lemaire, B. Keita, L. Nadjo, A. Dolbecq, *Journal of the American Chemical Society* **2011**, *133*, 13363.
[108] D. Gatteschi, R. Sessoli, J. Villain, *Molecular Nanomagnets*, Oxford University Press, Oxford, UK, **2006**.
[109] M. Murrie, *Chemical Society Reviews* **2010**, *39*, 1986.
[110] D. Schray, G. Abbas, Y. H. Lan, V. Mereacre, A. Sundt, J. Dreiser, O. Waldmann, G. E. Kostakis, C. E. Anson, A. K. Powell, *Angewandte Chemie-International Edition* **2010**, *49*, 5185.
[111] J. D. Rinehart, M. Fang, W. J. Evans, J. R. Long, *Journal of the American Chemical Society* **2011**, *133*, 14236.
[112] J. D. Rinehart, M. Fang, W. J. Evans, J. R. Long, *Nature Chemistry* **2011**, *3*, 538.
[113] M. Mazzanti, *Nature Chemistry* **2011**, *3*, 426.
[114] J. D. Rinehart, J. R. Long, *Journal of the American Chemical Society* **2009**, *131*, 12558.
[115] J. D. Rinehart, K. R. Meihaus, J. R. Long, *Journal of the American Chemical Society* **2010**, *132*, 7572.
[116] M. A. Antunes, L. C. J. Pereira, I. C. Santos, M. Mazzanti, J. Marcalo, M. Almeida, *Inorganic Chemistry* **2011**, *50*, 9915.

[117] N. Magnani, C. Apostolidis, A. Morgenstern, E. Colineau, J. C. Griveau, H. Bolvin, O. Walter, R. Caciuffo, *Angewandte Chemie-International Edition* **2011**, *50*, 1696.
[118] N. Magnani, E. Colineau, R. Eloirdi, J. C. Griveau, R. Caciuffo, S. M. Cornet, I. May, C. A. Sharrad, D. Collison, R. E. P. Winpenny, *Physical Review Letters* **2010**, *104*, 4.
[119] D. P. Mills, F. Moro, J. McMaster, J. van Slageren, W. Lewis, A. J. Blake, S. T. Liddle, *Nature Chemistry* **2011**, *3*, 454.
[120] C. J. Milios, A. Vinslava, W. Wernsdorfer, S. Moggach, S. Parsons, S. P. Perlepes, G. Christou, E. K. Brechin, *Journal of the American Chemical Society* **2007**, *129*, 2754.
[121] H. W. Roesky, I. Haiduc, N. S. Hosmane, *Chemical Reviews* **2003**, *103*, 2579.
[122] R. E. P. Winpenny, *Chemical Society Reviews* **1998**, *27*, 447.
[123] D. L. Long, E. Burkholder, L. Cronin, *Chemical Society Reviews* **2007**, *36*, 105.
[124] C. R. Armstrong, M. Nyman, T. Shvareva, G. E. Sigmon, P. C. Burns, A. Navrotsky, *Proceedings of the National Academy of Sciences of the United States of America* **2010**, *109*, 1874.
[125] J. M. Harrowfield, M. I. Ogden, B. W. Skelton, A. H. White, *Dalton Transactions* **2010**, *39*, 8313.
[126] X. Delaigue, C. D. Gutsche, J. M. Harrowfield, M. I. Ogden, B. W. Skelton, D. F. Stewart, A. H. White, *Supramolecular Chemistry* **2004**, *16*, 603.
[127] R. L. Lintvedt, M. J. Heeg, N. Ahmad, M. D. Glick, *Inorganic Chemistry* **1982**, *21*, 2350.
[128] S. Di, Z. Na, X. Qin-Juan, H. Rong-Bin, Z. Lan-Sun, *Inorganic Chemistry Communications* **2010**, *13*, 859.
[129] J. M. Harrowfield, B. W. Skelton, A. H. White, *Comptes Rendus Chimie* **2005**, *8*, 169.
[130] Z. T. Yu, G. H. Li, Y. S. Jiang, J. J. Xu, J. S. Chen, *Dalton Transactions* **2003**, 4219.
[131] G. Vandenbossche, M. R. Spirlet, J. Rebizant, J. Goffart, *Acta Crystallographica Section C-Crystal Structure Communications* **1987**, *43*, 383.
[132] A. J. Zozulin, D. C. Moody, R. R. Ryan, *Inorganic Chemistry* **1982**, *21*, 3083.
[133] M. J. Crawford, P. Mayer, H. Noth, M. Suter, *Inorganic Chemistry* **2004**, *43*, 6860.
[134] P. Thuery, B. Masci, *Polyhedron* **2004**, *23*, 649.
[135] P. Thuery, C. Villiers, J. Jaud, M. Ephritikhine, B. Masci, *Journal of the American Chemical Society* **2004**, *126*, 6838.
[136] P. C. Burns, *Canadian Mineralogist* **2005**, *43*, 1839.
[137] J. Ling, J. Qiu, P. C. Burns, *Inorganic Chemistry* **2012**, *51*, 2403.
[138] J. Qiu, J. Ling, A. Sui, J. E. S. Szymanowski, A. Simonetti, P. C. Burns, *Journal of the American Chemical Society* **2012**, *134*, 1810.
[139] J. Ling, M. Ozga, M. Stoffer, P. C. Burns, *Dalton Transactions* **2012**, *41*, 7278.
[140] G. E. Sigmon, P. C. Burns, *Journal of the American Chemical Society* **2011**, *133*, 9137.
[141] D. K. Unruh, J. Ling, J. Qiu, L. Pressprich, M. Baranay, M. Ward, P. C. Burns, *Inorganic Chemistry* **2011**, *50*, 5509.
[142] J. Ling, J. Qiu, G. E. Sigmon, M. Ward, J. E. S. Szymanowski, P. C. Burns, *Journal of the American Chemical Society* **2010**, *132*, 13395.
[143] D. K. Unruh, A. Burtner, L. Pressprich, G. E. Sigmon, P. C. Burns, *Dalton Transactions* **2010**, *39*, 5807.
[144] T. Z. Forbes, J. G. McAlpin, R. Murphy, P. C. Burns, *Angewandte Chemie-International Edition* **2008**, *47*, 2824.
[145] J. C. Taylor, A. Ekstrom, C. H. Randall, *Inorganic Chemistry* **1978**, *17*, 3285.
[146] M. P. Wilkerson, C. J. Burns, H. J. Dewey, J. M. Martin, D. E. Morris, R. T. Paine, B. L. Scott, *Inorganic Chemistry* **2000**, *39*, 5277.

[147] A. Cousson, S. Dabos, H. Abazli, F. Nectoux, M. Pages, G. Choppin, *Journal of the Less-Common Metals* **1984**, *99*, 233.
[148] M. S. Grigoriev, N. N. Krot, A. A. Bessonov, K. Y. Suponitsky, *Acta Crystallographica Section E-Structure Reports Online* **2007**, *63*, M561.
[149] I. A. Charushnikova, N. N. Krot, Z. A. Starikova, *Radiochimica Acta* **2007**, *95*, 495.
[150] I. Charushnikova, N. Krot, I. Polyakova, *Radiochemistry* **2006**, *48*, 223.
[151] A. Bessonov, N. Krot, M. Grigor'ev, V. Makarenkov, *Radiochemistry* **2005**, *47*, 468.
[152] S. M. Cornet, L. J. L. Haller, M. J. Sarsfield, D. Collison, M. Helliwell, I. May, N. Kaltsoyannis, *Chemical Communications* **2009**, 917.
[153] I. Charushnikova, E. Bosse, D. Guillaumont, P. Moisy, *Inorganic Chemistry* **2010**, *49*, 2077.
[154] T. W. Newton, F. B. Baker, *Inorganic Chemistry* **1962**, *1*, 368.
[155] A. Ikeda, C. Hennig, S. Tsushima, K. Takao, Y. Ikeda, A. C. Scheinost, G. Bernhard, *Inorganic Chemistry* **2007**, *46*, 4212.
[156] T. I. Docrat, J. F. W. Mosselmans, J. M. Charnock, M. W. Whiteley, D. Collison, F. R. Livens, C. Jones, M. J. Edmiston, *Inorganic Chemistry* **1999**, *38*, 1879.
[157] E. S. Ilton, A. Haiduc, C. L. Cahill, A. R. Felmy, *Inorganic Chemistry* **2005**, *44*, 2986.
[158] J. C. Sullivan, A. J. Zielen, J. C. Hindman, *Journal of the American Chemical Society* **1961**, *83*, 3373.
[159] C. Miyake, T. Kondo, S. Imoto, H. Ohyanishiguchi, *Journal of the Less-Common Metals* **1986**, *122*, 313.
[160] K. Mizuguchi, Y. Y. Park, H. Tomiyasu, Y. Ikeda, *Journal of Nuclear Science and Technology* **1993**, *30*, 542.
[161] K. Mizuoka, S. Tsushima, M. Hasegawa, T. Hoshi, Y. Ikeda, *Inorganic Chemistry* **2005**, *44*, 6211.
[162] K. Mizuoka, S. Y. Kim, M. Hasegawa, T. Hoshi, G. Uchiyama, Y. Ikeda, *Inorganic Chemistry* **2003**, *42*, 1031.
[163] K. Takao, S. Tsushima, S. Takao, A. C. Scheinost, G. Bernhard, Y. Ikeda, C. Hennig, *Inorganic Chemistry* **2009**, *48*, 9602.
[164] K. Mizuoka, Y. Ikeda, *Inorganic Chemistry* **2003**, *42*, 3396.
[165] S. Y. Kim, T. Asakura, Y. Morita, Y. Ikeda, *Journal of Alloys and Compounds* **2006**, *408*, 1291.
[166] S. Y. Kim, T. Asakura, Y. Morita, G. Uchiyama, Y. Ikeda, *Radiochimica Acta* **2005**, *93*, 75.
[167] S. Y. Kim, H. Tomiyasu, Y. Ikeda, *Journal of Nuclear Science and Technology* **2002**, *39*, 160.
[168] G. Nocton, P. Horeglad, J. Pecaut, M. Mazzanti, *Journal of the American Chemical Society* **2008**, *130*, 16633.
[169] J. C. Berthet, M. Nierlich, M. Ephritikhine, *Angewandte Chemie-International Edition* **2003**, *42*, 1952.
[170] L. Natrajan, F. Burdet, J. Pecaut, M. Mazzanti, *Journal of the American Chemical Society* **2006**, *128*, 7152.
[171] J. C. Berthet, G. Siffredi, P. Thuery, M. Ephritikhine, *Chemical Communications* **2006**, 3184.
[172] F. Burdet, J. Pecaut, M. Mazzanti, *Journal of the American Chemical Society* **2006**, *128*, 16512.
[173] T. W. Hayton, G. Wu, *Journal of the American Chemical Society* **2008**, *130*, 2005.
[174] T. W. Hayton, G. Wu, *Inorganic Chemistry* **2008**, *47*, 7415.
[175] P. Horeglad, G. Nocton, Y. Filinchuck, J. Pécaut, M. Mazzanti, *Chemical Communication* **2009**, 1843.

[176] G. Nocton, P. Horeglad, V. Vetere, J. Pecaut, L. Dubois, P. Maldivi, N. M. Edelstein, M. Mazzanti, *Journal of the American Chemical Society* **2010**, *132*, 495.
[177] P. L. Arnold, D. Patel, C. Wilson, J. B. Love, *Nature* **2008**, *451*, 315.
[178] P. L. Arnold, E. Hollis, F. J. White, N. Magnani, R. Caciuffo, J. B. Love, *Angewandte Chemie-International Edition* **2011**, *50*, 887.
[179] D. P. Mills, O. J. Cooper, F. Tuna, E. J. L. McInnes, E. S. Davies, J. McMaster, F. Moro, W. Lewis, A. J. Blake, S. T. Liddle, *Journal of the American Chemical Society* **2012**, *134*, 10047.
[180] P. C. Leverd, M. Nierlich, *European Journal of Inorganic Chemistry* **2000**, 1733.
[181] L. Salmon, P. Thuery, M. Ephritikhine, *Polyhedron* **2006**, *25*, 1537.
[182] J. C. Berthet, M. Nierlich, Y. Miquel, C. Madic, M. Ephritikhine, *Dalton Transactions* **2005**, 369.
[183] P. Charpin, G. Folcher, M. Nierlich, M. Lance, D. Vigner, A. Navaza, C. Derango, *Acta Crystallographica Section C-Crystal Structure Communications* **1990**, *46*, 1778.
[184] L. Salmon, P. Thuery, M. Ephritikhine, *Polyhedron* **2004**, *23*, 623.
[185] L. Moisan, T. Le Borgne, P. Thuery, M. Ephritikhine, *Acta Crystallographica Section C-Crystal Structure Communications* **2002**, *58*, m98.
[186] J. Lukens, Wayne W., S. M. Beshouri, L. L. Blosh, R. A. Andersen, *Journal of the American Chemical Society* **1996**, *118*, 901.
[187] P. C. Blake, M. F. Lappert, R. G. Taylor, J. L. Atwood, H. Zhang, *Inorganica Chimica Acta* **1987**, *139*, 13.
[188] L. Karmazin, M. Mazzanti, J. Pecaut, *Inorganic Chemistry* **2003**, *42*, 5900.
[189] G. Nocton, F. Burdet, J. Pecaut, M. Mazzanti, *Angewandte Chemie-International Edition* **2007**, *46*, 7574.
[190] M. Ephritikhine, *New Journal of Chemistry* **1992**, *16*, 451.
[191] M. Ephritikhine, *Dalton Transactions* **2006**, 2501.
[192] W. J. Evans, S. A. Kozimor, *Coordination Chemistry Reviews* **2006**, *250*, 911.
[193] M.-R. Spirlet, J. Rebizant, C. Apostolidis, E. Dornberger, B. Kanellakopulos, B. Powietzka, *Polyhedron* **1996**, *15*, 1503.
[194] J.-C. Berthet, J.-F. Le Maréchal, M. Nierlich, M. Lance, J. Vigner, M. Ephritikhine, *Journal of Organometallic Chemistry* **1991**, *408*, 335.
[195] L. R. Avens, D. M. Barnhart, C. J. Burns, S. D. McKee, W. H. Smith, *Inorganic Chemistry* **1994**, *33*, 4245.
[196] P. Roussel, R. Boaretto, A. J. Kingsley, N. W. Alcock, P. Scott, *Journal of Chemical Society, Dalton Transaction* **2002**, 1423.
[197] O. P. Lam, F. W. Heinemann, K. Meyer, *Chemical Science* **2011**, *2*, 1538.
[198] S. Fortier, J. L. Brown, N. Kaltsoyannis, G. Wu, T. W. Hayton, *Inorganic Chemistry* **2012**, *51*, 1625.
[199] I. Korobkov, S. Gambarotta, G. P. A. Yap, *Organometallics* **2001**, *20*, 2552.
[200] C. P. Larch, F. G. N. Cloke, P. B. Hitchcock, *Chemical Communications* **2008**, 82.
[201] P. B. Duval, C. J. Burns, D. L. Clark, D. E. Morris, B. L. Scott, J. D. Thompson, E. L. Werkema, L. Jia, R. A. Andersen, *Angewandte Chemie-International Edition* **2001**, *40*, 3357.
[202] L. M. Mokry, N. S. Dean, C. J. Carrano, *Angewandte Chemie-International Edition* **1996**, *35*, 1497.
[203] J. C. Berthet, P. Thuery, M. Ephritikhine, *Chemical Communications* **2005**, 3415.
[204] P. L. Arnold, G. M. Jones, S. O. Odoh, G. Schreckenbach, N. Magnani, J. B. Love, *Nature Chemistry* **2012**, *4*, 221.
[205] J. G. Reynolds, A. Zalkin, D. H. Templeton, N. M. Edelstein, L. K. Templeton, *Inorganic Chemistry* **1976**, *15*, 2498.

[206] J. G. Reynolds, A. Zalkin, D. H. Templeton, N. M. Edelstein, *Inorganic Chemistry* **1977**, *16*, 599.
[207] J. G. Reynolds, A. Zalkin, D. H. Templeton, N. M. Edelstein, *Inorganic Chemistry* **1977**, *16*, 1858.
[208] J. L. Stewart, R. A. Andersen, *New Journal of Chemistry* **1995**, *19*, 587.
[209] I. Korobkov, S. Gambarotta, G. P. A. Yap, L. Thompson, P. J. Hay, *Organometallics* **2001**, *20*, 5440.
[210] T. Le Borgne, M. Lance, M. Nierlich, M. Ephritikhine, *Journal of Organometallic Chemistry* **2000**, *598*, 313.
[211] J. L. Kiplinger, J. A. Pool, E. J. Schelter, J. D. Thompson, B. L. Scott, D. E. Morris, *Angewandte Chemie-International Edition* **2006**, *45*, 2036.
[212] E. J. Schelter, R. L. Wu, B. L. Scott, J. D. Thompson, D. E. Morris, J. L. Kiplinger, *Angewandte Chemie-International Edition* **2008**, *47*, 2993.
[213] M. J. Monreal, S. I. Khan, J. L. Kiplinger, P. L. Diaconescu, *Chemical Communications* **2011**, *47*, 9119.
[214] S. A. Kozimor, B. M. Bartlett, J. D. Rinehart, J. R. Long, *Journal of the American Chemical Society* **2007**, *129*, 10672.
[215] J. D. Rinehart, S. A. Kozimor, J. R. Long, *Angewandte Chemie-International Edition* **2010**, *49*, 2560.
[216] W. J. Evans, S. A. Kozimor, J. W. Ziller, *Science* **2005**, *309*, 1835.
[217] G. Nocton, J. Pecaut, M. Mazzanti, *Angewandte Chemie-International Edition* **2008**, *47*, 3040.
[218] J. C. Berthet, M. Lance, M. Nierlich, J. Vigner, M. Ephritikhine, *Journal of Organometallic Chemistry* **1991**, *420*, C9.
[219] W. J. Evans, K. A. Miller, J. W. Ziller, J. Greaves, *Inorganic Chemistry* **2007**, *46*, 8008.
[220] J. G. Brennan, R. A. Andersen, A. Zalkin, *Journal of American Chemical Society* **1988**, *110*, 4554.
[221] E. M. Broderick, N. P. Gutzwiller, P. L. Diaconescu, *Organometallics* **2010**, *29*, 3242.
[222] J. C. Berthet, P. Thuery, M. Ephritikhine, *Angewandte Chemie-International Edition* **2008**, *47*, 5586.
[223] J.-C. Berthet, C. Rivière, Y. Miquel, M. Nierlich, C. Madic, M. Ephritikhine, *European Journal of Inorg Chemistry* **2002**, 1439.
[224] J. G. Brennan, R. A. Andersen, *Journal of the American Chemical Society* **1985**, *107*, 514.
[225] R. K. Rosen, R. A. Andersen, N. M. Edelstein, *Journal of the American Chemical Society* **1990**, *112*, 4588.
[226] L. P. Spencer, E. J. Schelter, P. Yang, R. L. Gdula, B. L. Scott, J. D. Thompson, J. L. Kiplinger, E. R. Batista, J. M. Boncella, *Angewandte Chemie-International Edition* **2009**, *48*, 3795.
[227] D. Patel, F. Moro, D. P. Mills, J. McMaster, W. Lewis, A. J. Blake, S. T. Liddle, *Angewandte Chemie-International Edition* **2011**, *50*, 10388.
[228] A. R. Fox, P. L. Arnold, C. C. Cummins, *Journal of the American Chemical Society* **2010**, *132*, 3250.
[229] D. M. King, F. Tuna, E. J. L. McInnes, J. McMaster, W. Lewis, A. J. Blake, S. T. Liddle, *Science* **2012**, *337*, 717.
[230] P. C. Blake, M. F. Lappert, R. G. Taylor, J. L. Atwood, W. E. Hunter, H. M. Zhang, *Journal of the Chemical Society-Chemical Communications* **1986**, 1394.
[231] O. J. Cooper, D. P. Mills, J. McMaster, F. Moro, E. S. Davies, W. Lewis, A. J. Blake, S. T. Liddle, *Angewandte Chemie-International Edition* **2011**, *50*, 2383.

[232] F. A. Cotton, W. Schwotzer, *Organometallics* **1985**, *4*, 942.
[233] R. J. Francis, P. S. Halasyamani, J. S. Bee, D. O'Hare, *Journal of the American Chemical Society* **1999**, *121*, 1609.
[234] P. B. Hitchcock, M. F. Lappert, R. G. Taylor, *Journal of the Chemical Society-Chemical Communications* **1984**, 1082.
[235] W. W. Lukens, S. M. Beshouri, L. L. Blosch, A. L. Stuart, R. A. Andersen, *Organometallics* **1999**, *18*, 1235.
[236] L. Maria, A. Domingos, I. Santos, *Inorganic Chemistry* **2003**, *42*, 3323.
[237] F. A. Cotton, W. Schwotzer, C. Q. Simpson, *Angewandte Chemie-International Edition in English* **1986**, *25*, 637.
[238] D. Baudry, P. Charpin, M. Ephritikhine, M. Lance, M. Nierlich, J. Vigner, *Journal of the Chemical Society-Chemical Communications* **1987**, 739.
[239] W. J. Evans, K. A. Miller, A. G. DiPasquale, A. L. Rheingold, T. J. Stewart, R. Bau, *Angewandte Chemie-International Edition* **2008**, *47*, 5075.
[240] W. J. Evans, K. A. Miller, S. A. Kozimor, J. W. Ziller, A. G. DiPasquale, A. L. Rheingold, *Organometallics* **2007**, *26*, 3568.
[241] J. F. Lemarechal, C. Villiers, P. Charpin, M. Lance, M. Nierlich, J. Vigner, M. Ephritikhine, *Journal of the Chemical Society-Chemical Communications* **1989**, 308.
[242] J. G. Brennan, R. A. Andersen, A. Zalkin, *Inorganic Chemistry* **1986**, *25*, 1761.
[243] P. C. Leverd, T. Arliguie, M. Lance, M. Nierlich, J. Vigner, M. Ephritikhine, *Journal of the Chemical Society-Dalton Transactions* **1994**, 501.
[244] W. J. Evans, E. Montalvo, J. W. Ziller, A. G. DiPasquale, A. L. Rheingold, *Inorganic Chemistry* **2010**, *49*, 222.
[245] W. J. Evans, M. K. Takase, J. W. Ziller, A. G. DiPasquale, A. L. Rheingold, *Organometallics* **2009**, *28*, 236.
[246] T. Cantat, T. Arliguie, A. Noel, P. Thuery, M. Ephritikhine, P. Le Floch, N. Mezailles, *Journal of the American Chemical Society* **2009**, *131*, 963.
[247] D. L. Clark, J. C. Gordon, J. G. Huffman, J. G. Watkin, B. D. Zwick, *New Journal of Chemistry* **1995**, *19*, 495.
[248] P. C. Leverd, T. Arliguie, M. Ephritikhine, M. Nierlich, M. Lance, J. Vigner, *New Journal of Chemistry* **1993**, *17*, 769.
[249] T. Arliguie, M. Blug, P. Le Floch, N. Mezailles, P. Thuery, M. Ephritikhine, *Organometallics* **2008**, *27*, 4158.
[250] A. J. Gaunt, B. L. Scott, M. P. Neu, *Inorganic Chemistry* **2006**, *45*, 7401.
[251] T. Arliguie, P. Thuery, P. Le Floch, N. Mezailles, M. Ephritikhine, *Polyhedron* **2009**, *28*, 1578.
[252] T. Arliguie, M. Lance, M. Nierlich, J. Vigner, M. Ephritikhine, *Journal of the Chemical Society-Chemical Communications* **1994**, 847.
[253] P. L. Diaconescu, C. C. Cummins, *Journal of the American Chemical Society* **2002**, *124*, 7660.
[254] W. J. Evans, S. A. Kozimor, J. W. Ziller, N. Kaltsoyannis, *Journal of the American Chemical Society* **2004**, *126*, 14533.
[255] W. J. Evans, G. W. Nyce, J. W. Ziller, *Angewandte Chemie-International Edition* **2000**, *39*, 240.
[256] W. J. Evans, C. A. Traina, J. W. Ziller, *Journal of the American Chemical Society* **2009**, *131*, 17473.
[257] P. L. Diaconescu, C. C. Cummins, *Inorganic Chemistry* **2012**, *51*, 2902.
[258] K. Mizuoka, Y. Ikeda, *Radiochimica Acta* **2004**, *92*, 631.
[259] K. Takao, Y. Ikeda, *Inorganic Chemistry* **2007**, *46*, 1550.
[260] J. T. J. Edward, *Chemical Education* **1970**, *47*, 261.

[261] G. Nocton, P. Horeglad, J. Pécaut, M. Mazzanti, *Journal of the American Chemical Society* **2008**, *130*, 16633.
[262] T. A. Sullens, R. A. Jensen, T. Y. Shvareva, T. E. Albrecht-Schmitt, *Journal of the American Chemical Society* **2004**, *126*, 2676.
[263] E. V. Alekseev, S. V. Krivovichev, W. Depmeier, O. I. Siidra, K. Knorr, E. V. Suleimanov, E. V. Chuprunov, *Angewandte Chemie-International Edition* **2006**, *45*, 7233.
[264] I. D. Brown, D. Altermatt, , *Acta crystallographica Section B* **1985**, *B41*, 244.
[265] P. C. Burns, R. J. Finch, *American Mineralogist* **1999**, *84*, 1456.
[266] N. Belai, M. Frisch, E. S. Ilton, B. Ravel, C. L. Cahill, *Inorganic Chemistry* **2008**, *47*, 10135.
[267] F. C. Hawthorne, R. J. Finch, R. C. Ewing, *Canadian Mineralogist* **2006**, *44*, 1379.
[268] C. H. Lin, K. H. Lii, *Angewandte Chemie-International Edition* **2008**, *47*, 8711.
[269] M. J. Sarsfield, M. Helliwell, *Journal of the American Chemical Society* **2004**, *126*, 1036.
[270] G. Bandoli, D. A. Clemente, U. Croatto, M. Vidali, P. A. Vigato, *Journal of the Chemical Society-Dalton Transactions* **1973**, 2331.
[271] B. Zarli, R. Graziani, Forselli.E, U. Croatto, G. Bombieri, *Journal of the Chemical Society D-Chemical Communications* **1971**, 1501.
[272] V. Vetere, P. Maldivi, M. Mazzanti, *Comptes Rendus Chimie* **2010**, *13*, 876.
[273] P. C. Burns, J. F. Finch, *American Mineralogist* **1999**, *84*, 1456.
[274] R. D. Shannon, *Acta Crystallographica Section A* **1976**, *32*, 751.
[275] J. M. Fritsch, K. A. Thoreson, K. McNeill, *Dalton Transactions* **2006**, 4814
[276] A. R. Waldeck, P. W. Kuchel, A. J. Lennon, B. E. Chapman, *Progress in Nuclear Magnetic Resonance Spectroscopy* **1997**, *30*, 39.
[277] A. P. Cole, D. E. Root, P. Mukherjee, E. I. Solomon, T. D. P. Stack, *Science* **1996**, *273*, 1848.
[278] J. C. Berthet, M. Lance, M. Nierlich, M. Ephritikhine, *European Journal of Inorganic Chemistry* **2000**, 1969.
[279] M. J. Sarsfield, M. Helliwell, J. Raftery, *Inorganic Chemistry* **2004**, *43*, 3170.
[280] L. Karmazin, M. Mazzanti, J. Pécaut, *Inorganic Chemistry* **2003**, *42*, 5900.
[281] W. W. Lukens, S. M. Beshouri, L. L. Blosch, R. A. Andersen, *Journal of the American Chemical Society* **1996**, *118*, 901.
[282] J. Selbin, J. D. Ortego, *Chemistry Review* **1969**, *69*, 657.
[283] I. Infante, E. Eliav, M. J. Vilkas, Y. Ishikawa, U. Kaldor, L. Visscher, *Journal of Chemical Physics* **2007**, *127*, 12.
[284] C. Danilo, V. Vallet, J. P. Flament, U. Wahlgren, *Journal of Chemical Physics* **2008**, *128*, 9.
[285] V. Kaufman, L. J. Radziemski, *Journal of the Optical Society of America* **1976**, *66*, 599.
[286] W. Rudorff, H. Leutner, *Zeitschrift Fur Anorganische Und Allgemeine Chemie* **1957**, *292*, 193.
[287] F. A. Cotton, *Chemical applications of group theory*, Wiley, **1990**.
[288] J. C. Eisenstein, M. H. L. Pryce, *Proceedings of the Royal Society of London Series a-Mathematical and Physical Sciences* **1955**, *229*, 20.
[289] S. P. McGlynn, J. K. Smith, *Journal of Molecular Spectroscopy* **1961**, *6*, 164.
[290] S. Matsika, Z. Zhang, S. R. Brozell, J. P. Baudeau, Q. Wang, R. M. Pitzer, *Journal of Physical Chemistry A* **2001**, *105*, 3825.
[291] N. Kaltsoyannis, *Inorganic Chemistry* **2000**, *39*, 6009.
[292] S. Matsika, R. M. Pitzer, *Journal of Physical Chemistry A* **2000**, *104*, 4064.

[293] F. Ruiperez, C. Danilo, F. Real, J. P. Flament, V. Vallet, U. Wahlgren, *Journal of Physical Chemistry A* **2009**, *113*, 1420.
[294] V. Vallet, T. Privalov, U. Wahlgren, I. Grenthe, *Journal of the American Chemical Society* **2004**, *126*, 7766.
[295] S. C. Bart, C. Anthon, F. W. Heinemann, E. Bill, N. M. Edelstein, K. Meyer, *Journal of the American Chemical Society* **2008**, *130*, 12536.
[296] C. R. Graves, P. Yang, S. A. Kozimor, A. E. Vaughn, D. L. Clark, S. D. Conradson, E. J. Schelter, B. L. Scott, J. D. Thompson, P. J. Hay, D. E. Morris, J. L. Kiplinger, *Journal of the American Chemical Society* **2008**, *130*, 5272.
[297] O. Kahn, *Chemical Physics Letters* **1997**, *265*, 109.
[298] S. Karmakar, O. Das, S. Ghosh, E. Zangrando, M. Johann, E. Rentschler, T. Weyhermuller, S. Khanra, T. Kanti Paine, *Dalton Transactions* **2010**, *39*, 10920.
[299] Y.-B. Jiang, H.-Z. Kou, R.-J. Wang, A.-L. Cui, J. Ribas, *Inorganic Chemistry* **2005**, *44*, 709.
[300] S. Ferrer, F. Lloret, I. Bertomeu, G. Alzuet, J. Borrás, S. Gercia-Granda, M. Liu-González, J. G. Haasnoot, *Inorganic Chemistry* **2002**, *41*, 5821.
[301] M. U. Anwar, L. K. Thompson, L. N. Dawe, *Dalton Transactions* **2011**, *40*, 1437.
[302] R. D. Cannon, U. A. Jayasooriya, R. Wu, S. K. arapKoske, J. A. Stride, O. F. Nielsen, R. P. White, G. J. Kearley, D. Summerfield, *Journal of the American Chemical Society* **1994**, *116*, 11869.
[303] D. Gatteschi, *Advanced Materials* **1994**, *6*, 635.
[304] R. Sessoli, D. Gatteschi, A. Caneschi, M. A. Novak, *Nature* **1993**, *365*, 141.
[305] R. Sessoli, H. L. Tsai, A. R. Schake, S. Y. Wang, J. B. Vincent, K. Folting, D. Gatteschi, G. Christou, D. N. Hendrickson, *Journal of the American Chemical Society* **1993**, *115*, 1804.
[306] J.-C. Berthet, M. Nierlich, Y. Miquel, C. Madic, M. Ephritikhine, *Dalton Transaction* **2005**, 369.
[307] L. Natrajan, M. Mazzanti, J.-P. Bezombes, J. Pécaut, *Inorganic Chemistry* **2005**, *44*, 6115.
[308] C. J. Burns, A. P. Sattelberger, *Inorganic Chemistry* **1988**, *27*, 3692.
[309] M. Tsuboi, M. Terada, T. Shimanouchi, *Journal of Chemical Physics* **1962**, *36*, 1301.
[310] A. J. Francis, C. J. Dodge, *Environmental Science & Technology* **2008**, *42*, 8277.
[311] G. Nocton, J. Pecaut, Y. Filinchuk, M. Mazzanti, *Chemical Communications* **2010**, *46*, 2757.
[312] G. Lundgren, *Arkiv. Kemi.* **1952**, *5*, 349.
[313] J. C. Berthet, P. Thuery, M. Ephritikhine, *Inorganic Chemistry* **2011**, *49*, 8173.
[314] J. W. Shuppert, C. A. Angell, *Journal of Chemical Physics* **1977**, *67*, 3050.
[315] K. Nakamoto, 6 ed. (Ed.: J. W. Sons), **2009**.
[316] A. E. Enriquez, B. L. Scott, M. P. Neu, *Inorganic Chemistry* **2005**, *44*, 7403.
[317] M. Hirose, C. Miyake, J. G. H. Du Preez, B. Zeelie, *Inorganica Chimica Acta* **1988**, *150*, 293.
[318] E. A. M. Boudreaux, L. N., *Theory and Applications of Molecular Paramagnetism*, Wiley, New York, **1976**.
[319] I. Korobkov, S. Gambarotta, G. P. A. Yap, L. Thompson, P. J. Hay, *Organometallics* **2001**, *20*, 5440.
[320] I. Castro-Rodriguez, K. Meyer, *Chemical Communications* **2006**, 1353.
[321] D. B. Dell'Amico, C. Bradicich, L. Labella, F. Marchetti, *Inorganica Chimica Acta* **2006**, *359*, 1659.
[322] C. D. Carmichael, N. A. Jones, P. L. Arnold, *Inorganic Chemistry* **2008**, *47*, 8577.

[323] J. L. Kiplinger, K. D. John, D. E. Morris, B. L. Scott, C. J. Burns, *Organometallics* **2002**, *21*, 4306.
[324] L. R. Avens, S. G. Bott, D. L. Clark, A. P. Sattelberger, J. G. Watkin, B. D. Zwick, *Inorganic Chemistry* **1994**, *33*, 2248.
[325] F. Calderazzo, M. Pasquali, N. Corsi, *Journal of the Chemical Society-Chemical Communications* **1973**, 784.
[326] J. E. Tanner, *Journal of Chemical Physics* **1970**, *52*, 2523.
[327] D. H. Wu, A. D. Chen, C. S. Johnson, *Journal of Magnetic Resonance, Series A* **1995**, *115*, 260.
[328] C. S. Johnson, *Progress in Nuclear Magnetic Resonance Spectroscopy* **1999**, *34*, 203.
[329] G. M. Sheldrick, SHELXTL 6.14 ed., University of Göttingen, Germany, Germany, **2006**.
[330] T. G. Appleton, *Journal of Chemical Education* **1977**, *54*, 443.
[331] E. Y. Tshuva, I. Goldberg, M. Kol, *Journal of the American Chemical Society* **2000**, *122*, 10706.
[332] M. Stender, R. J. Wright, B. E. Eichler, J. Prust, M. M. Olmstead, H. W. Roesky, P. P. Power, *Journal of the Chemical Society-Dalton Transactions* **2001**, 3465.

Appendix

Appendix

A-Spectroscopic data

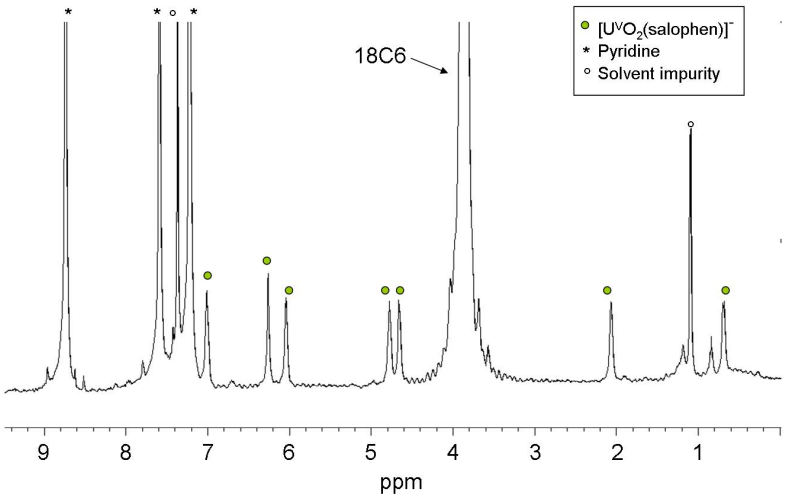

Figure A-1 ^{1}H NMR of the reaction mixture leading to the isolation of **8** in pyridine-d_5

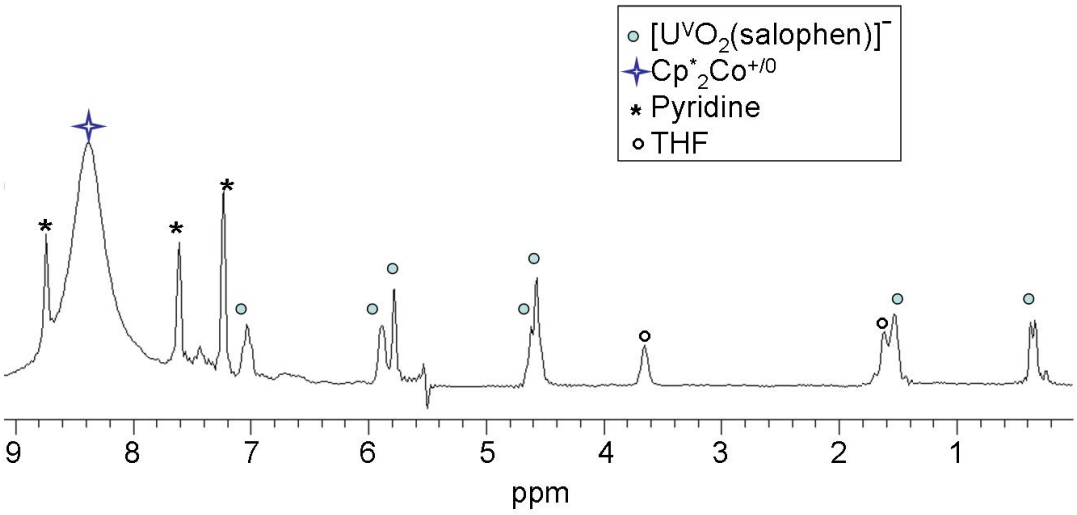

Figure A-2 ^{1}**H** NMR of **9** in pyridine-d_5

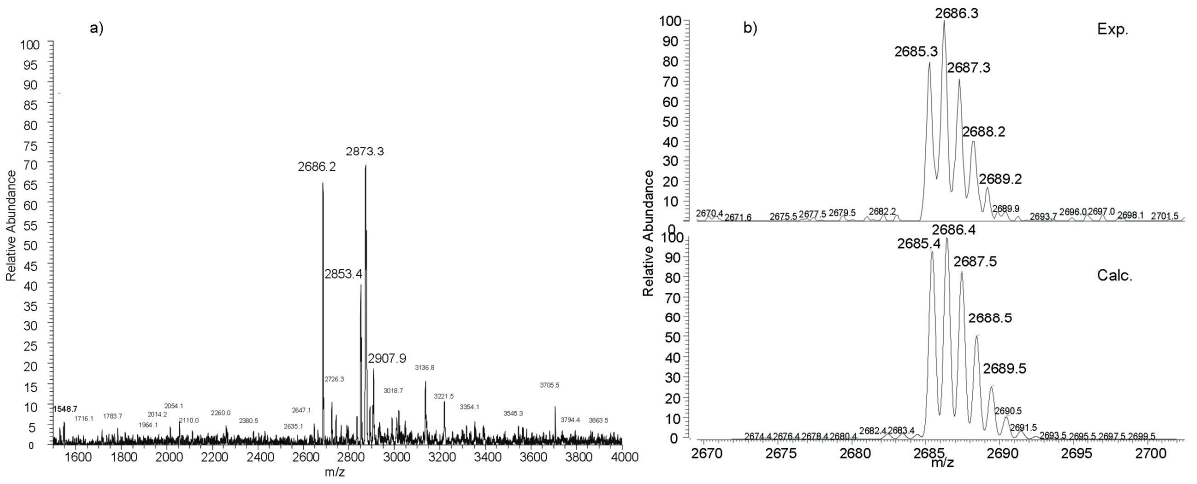

Figure A-3 ESI/MS spectra of complex **10** pyridine/acetonitrile 1:1 (a), and (b) zoom on the molecular peak compared with the theoretical isotopic profile calculated for $\{[UO_2(dophen)]_2[\mu_8\text{-}K]\}_2^{2-}$ H^+ adduct.

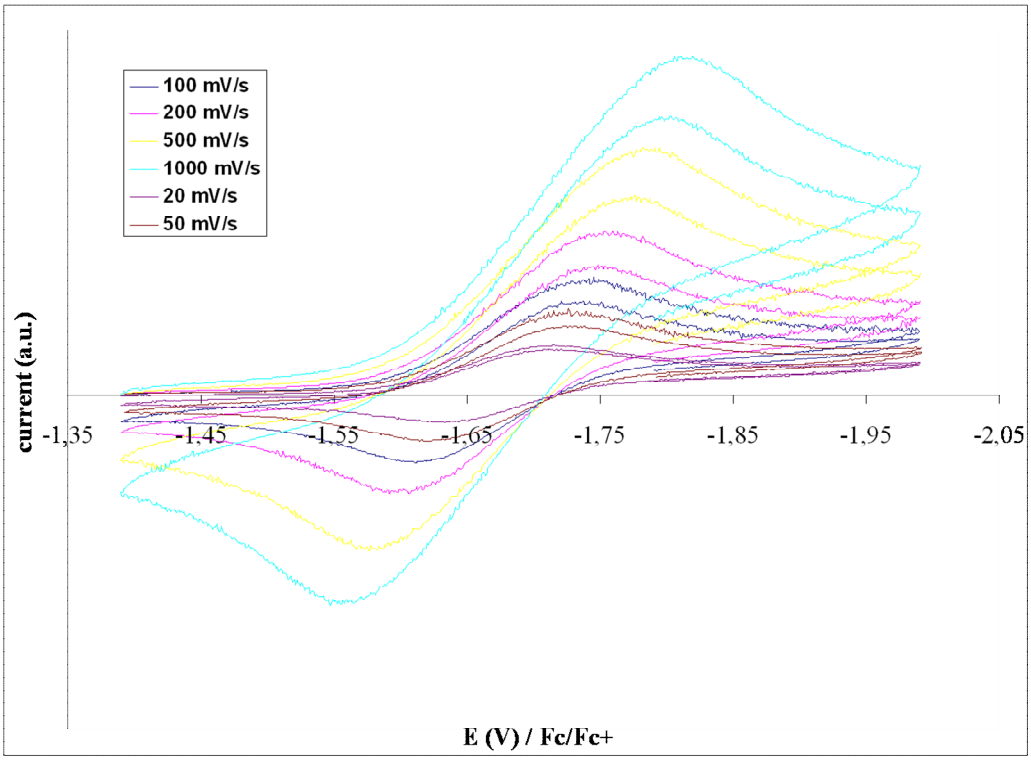

Figure A-4 Room temperature cyclic voltamogramm at different speed of **4** in pyridine (0.1 M $[NBu_4][PF_6]$ as supporting electrolyte). $E_{1/2}$ = -1.68 V vs. Fc/Fc^+.

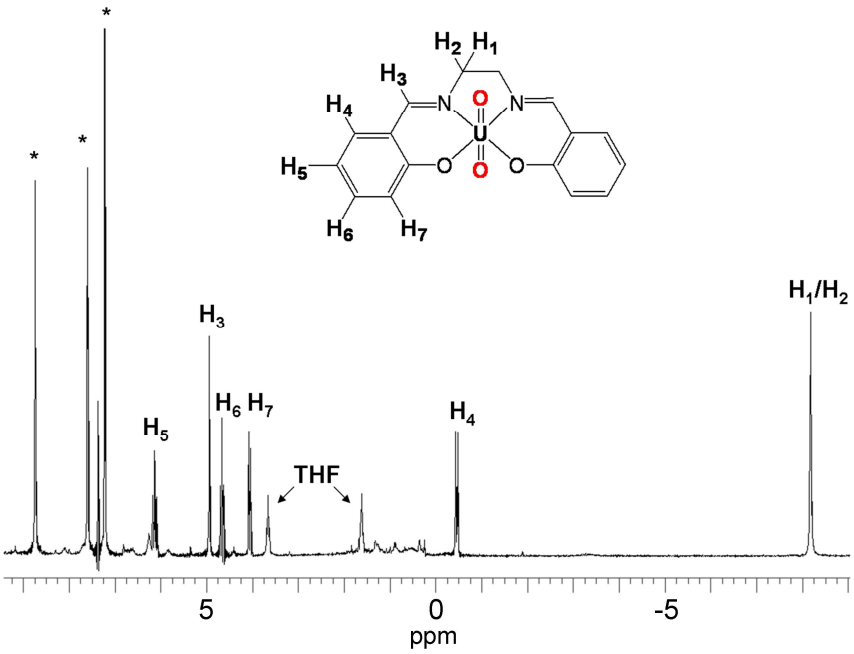

Figure A-5 ^{1}H NMR spectra of the reduction of **4** with $Cp^{*}_{2}Co$ in pyridine-d_5 (4.1 mM) (Bruker Advance 500MHz, * : solvent residual peaks)

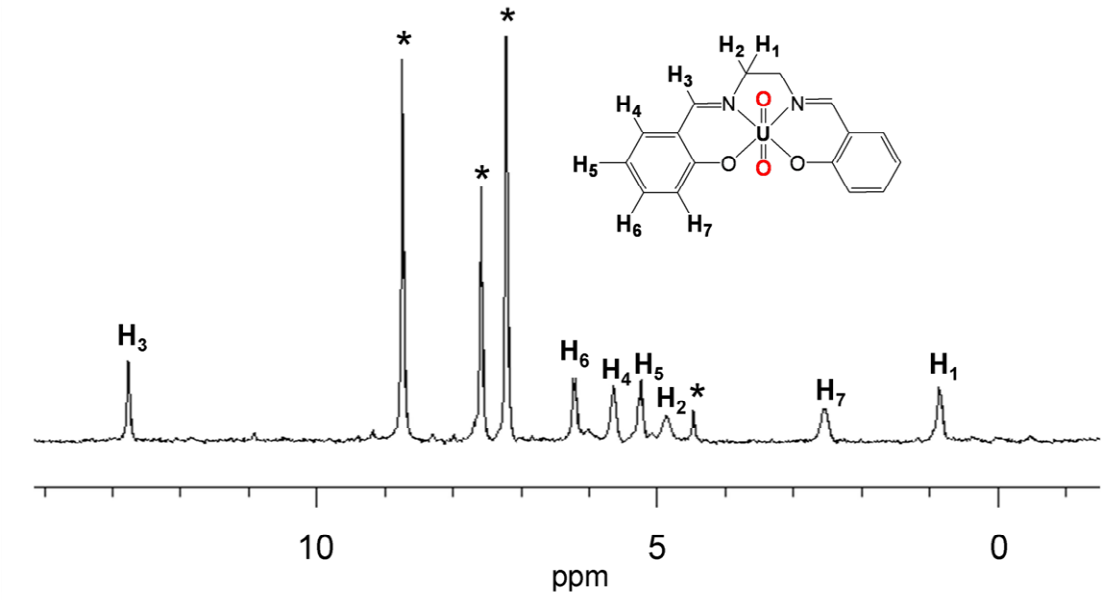

Figure A-6 ^{1}H NMR spectra of **17** in pyridine-d_5 (0.1 mM) (Bruker 200MHz, *: solvent residual peaks)

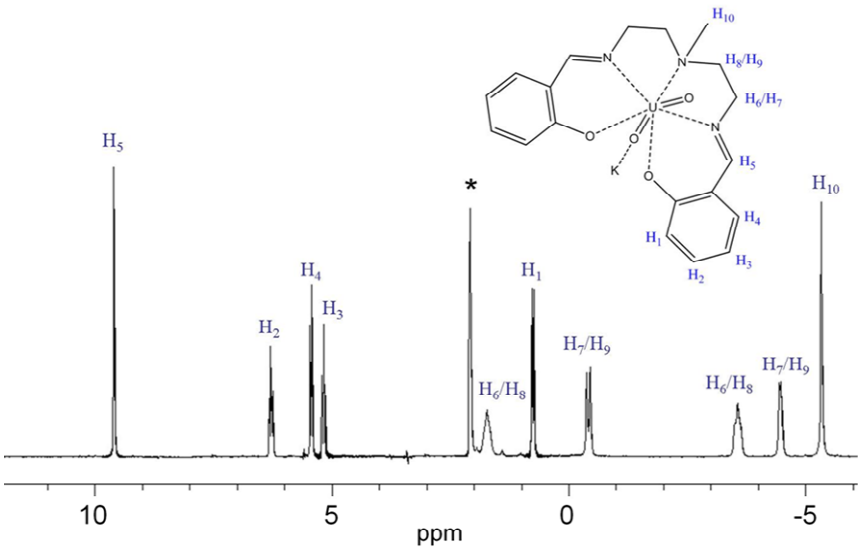

Figure A-7 Proton NMR spectrum of **22** in acetonitrile (1.5 mM, 200 MHz, *: solvent residual peak)

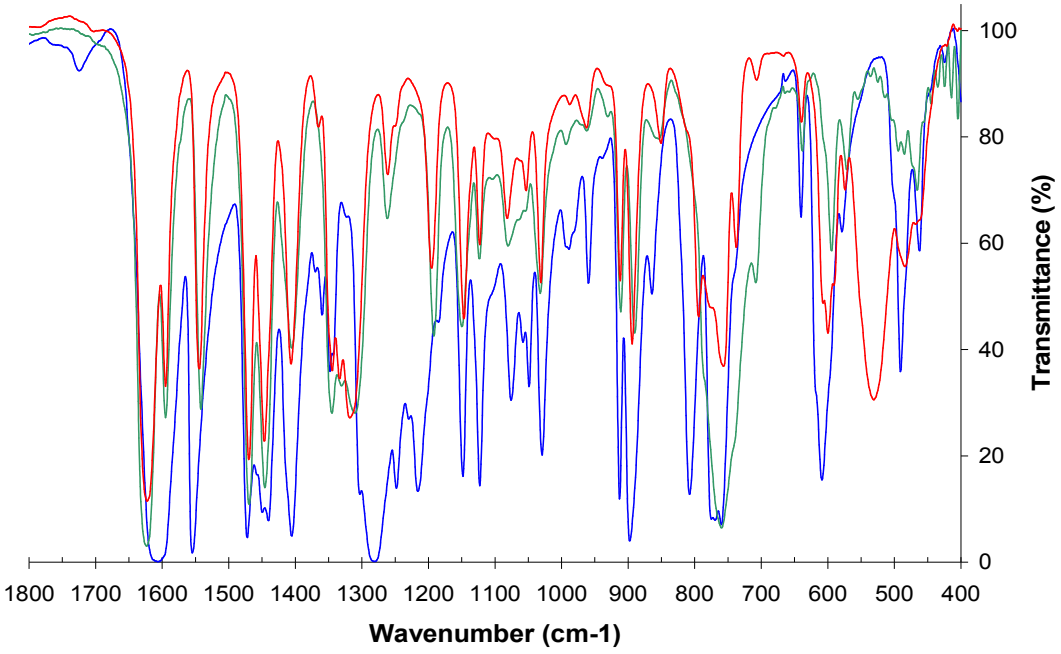

Figure A-8 Infrared spectra of **22** (green line), **23** (red line) and **25** (blue line).

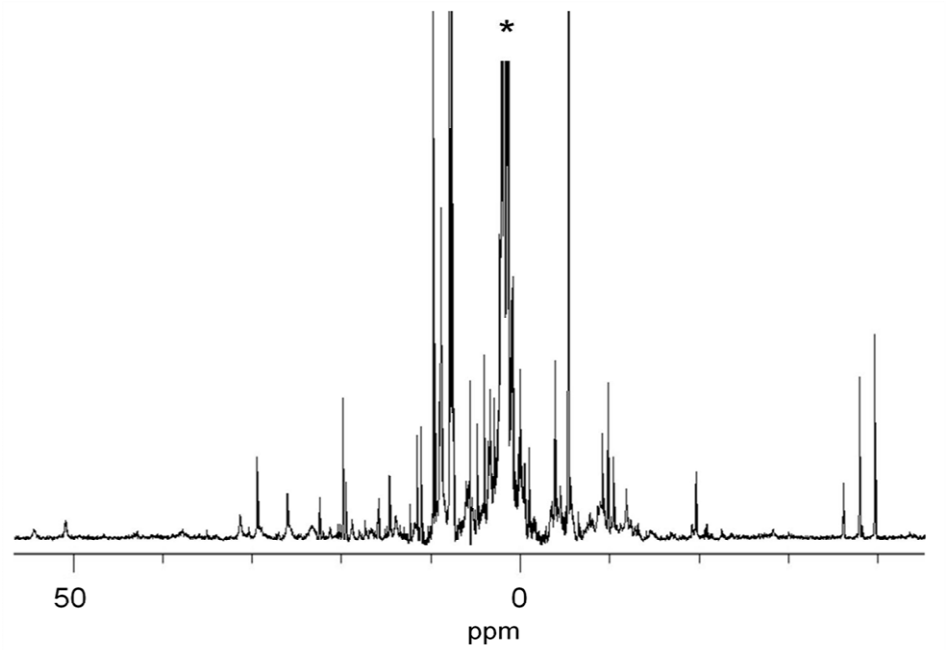

Figure A-9 Proton NMR spectrum of the reaction mixture during the course of the isolation of **26** in acetonitrile (200 MHz, *: solvent residual peak)

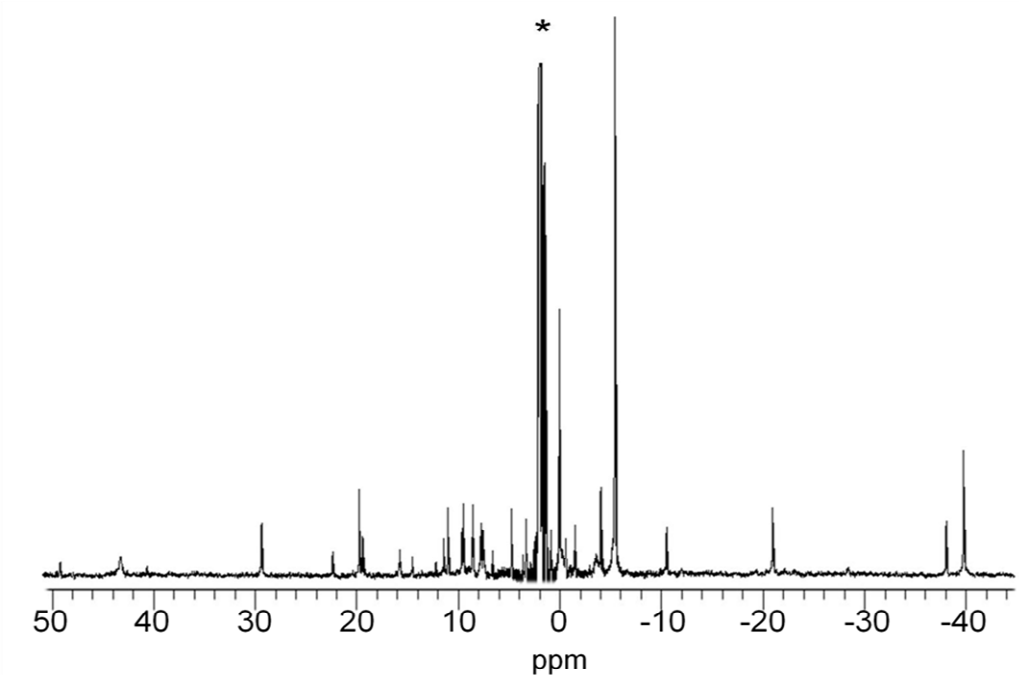

Figure A-10 Proton NMR spectrum of the crystals of **26** in acetonitrile (200 MHz, *: solvent residual peak)

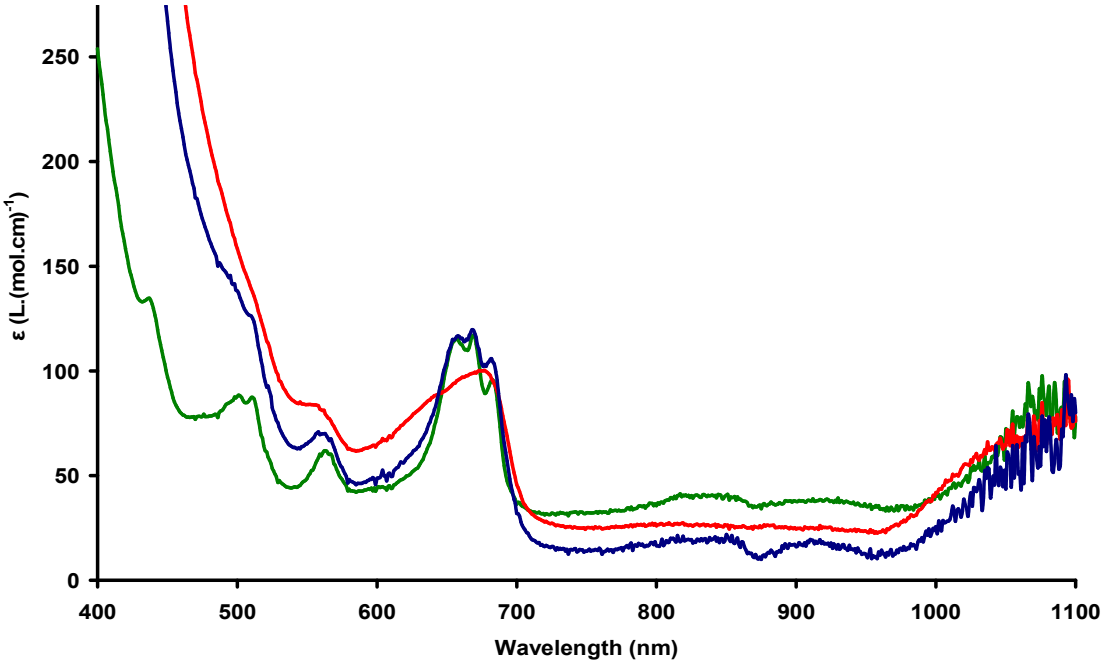

Figure A-11 UV-Vis spectra of complex **31** in py before (red line) and after (blue line) addition of 0.4 equivalent of potassium benzoate and 0.6 eq of py.HCl compared with $[U_6O_4(OH)_4(C_6H_5COO)_{12}(py)_3]$ in pyridine solution (green line) (Epsilon given per U center).

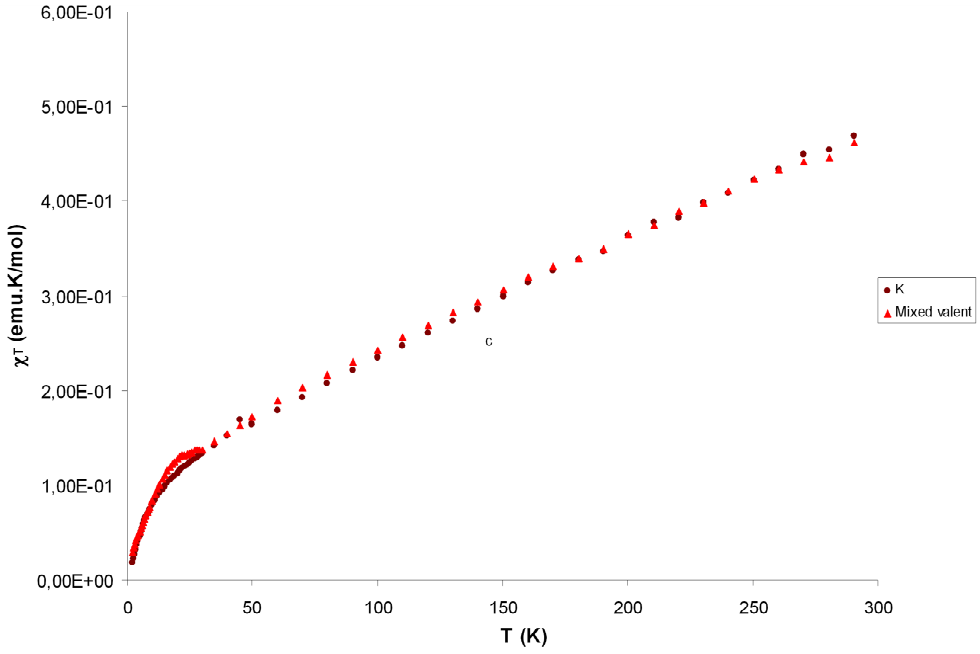

Figure A-12 Temperature-dependent χT data of **3** (brown dots) and **5** (red triangles) in the range of 2-300 K in a 1 T field.

Table A-1 Mass, molecular weight and diamagnetic contribution χ_{dia} calculated with Pascal constants.

	m (mg)	M (g.mol^{-1})	χ_{dia} (emu.mol^{-1})
3 (K, salen)	16.2	2830.33	-1.96x10^{-3}
5 (K, salen, mixed valent)	11.1	2526.92	-1.44x10^{-3}
8 (K, salophen)	22.5	4575.62	-1.48x10^{-3}
15 (Rb, salen)	13.5	3648.77	-2.10x10^{-3}
17 (Ca, salen)	9.2	4575.4	-1.47x10^{-3}
18 (Mn, salen)	49.1	8347.59	-2.94x10^{-3}
19 ([UO_2(diket)]$_3$)	16.8	2050.30	-1.19x10^{-3}

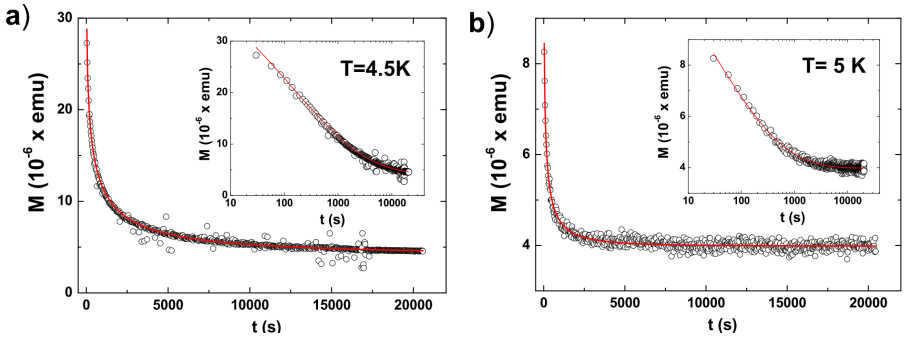

Figure A-13 Time dependence of the magnetization measured for **18** with the sample kept at 4.5 K (panel a) and 5 K (panel b) after cooling from 50 K in a d.c. field of 0.1 T. Data have been collected with a SQUID magnetometer at constant time intervals. The experimental data (open circles) can be fitted with a mono-modal stretched exponential decay. The insets show the same data and fits in log-log scale. The data have been fitted to a mono-modal stretched exponential function $M(t) = M_{eq} + [M(0)-M_{eq}]\exp[-(t/\tau)^{\beta}]$, where M_{eq} and $M(0)$ are the equilibrium and the initial magnetization. Results of the fit: τ = 140 s and β = 0.32 for T = 4.5 K, and τ = 30 s and β = 0.32 for T = 5 K.

V.2.3 Characterisation of water in the reaction mixture after the disproportionation reaction in presence of benzoic acid

A solution of 6.8 mg of benzoic acid (0.055 mmol, 2 eq) in 0.5 mL of pyridine-d_5 was added to a red suspension of 31 mg of [(UO_2py_5)(KI_2py_2)] (0.027 mmol, 1 eq) in 0.5 mL pyridine-d_5, yielding after 10 minutes stirring a clear green solution. The resulting solution was stirred an additional 2h, and was transferred in a NMR tube. The ^{1}H NMR spectra of the mixture presents the peaks of the species **27** and **28**, but also an additional broad peak at 14.51 ppm (Figure A-14). The addition of 0.5 equivalent of water to this sample led to the decrease of the

shift of this peak to 13.29 ppm together with an increase of its intensity , and no peak were observed at the usual place for water in pyridine (around 5 ppm) (Figure S4 -2). When this solution was taken to dryness and dissolved back in pyridine, the shift of the additional peak increased up to 17.50 ppm with a significant decrease of its intensity (Figure S4 -3). This behaviour is characteristic of the N-H^+ proton of pyridinium in pyridine in presence of water, and has been studied in detail.[314] The final peak observed at 17.50 ppm has been observed by Schuppert *et al.*[314] for the pure pyridinium proton, which also noticed that the addition of water to a pyridinium chloride solution in pyridine led to the decrease of the shift of the pyridinium proton and no peak at the usual shift for water.

Figure A-14: Proton NMR spectra of the reaction mixture: 1 - crude mixture; 2 - after addition of 0.5 eq of water; 3 - after drying under vacuum (Bruker 200MHz, *: pyridine residual peaks).

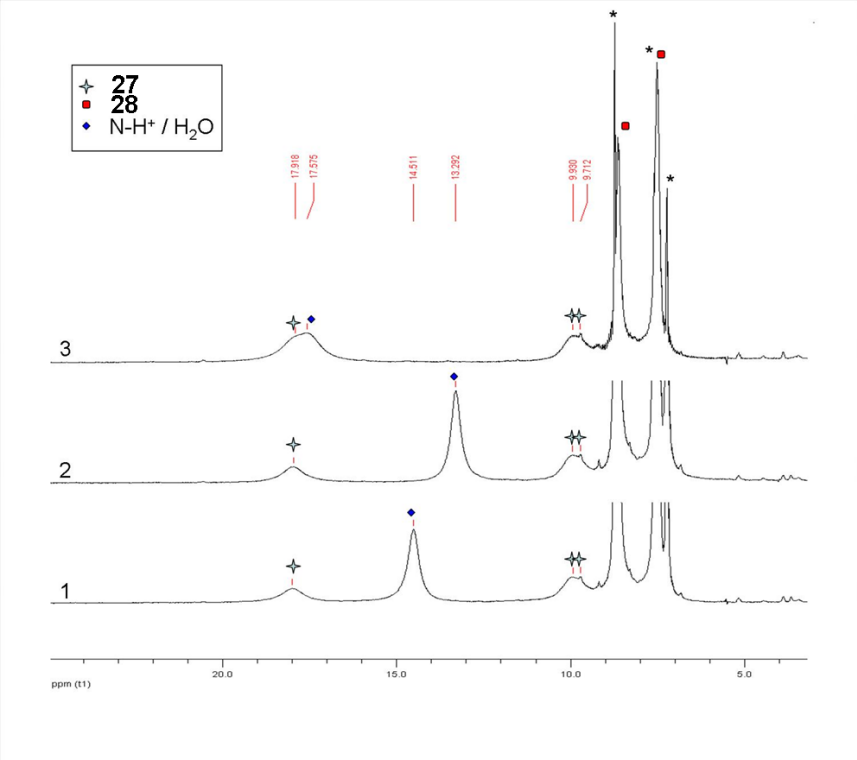

V.2.4 Bond valence sum calculations

Table A-2. Bond valence sum for compounds **3**, **4**, **5**, **12**, **21**, **23**, **26**, **27**, **29** and **31**. Numberin brackets refer to the numbering of the crystallographic structure.

Compound	U(1)	U(2)	U(3)	U(4)	U(5)	U(6)	U(7)	U(8)
3	4.95	5.00	–	–	–	–	–	–
4	6.02	–	–	–	–	–	–	–
5	6.00	5.23	4.85	4.85	–	–	–	–

12	6.12	4.97	–	–	–	–	–	–
21	6.02		–	–	–	–	–	–
23	4.16	5.25	–	–	–	–	–	–
26	4.06	4.07	4.66	5.20	4.23	–	–	–
27	3.98	4.04	4.10	4.12	3.93	–	–	–
29	4.27	3.87	4.12	4.16	3.96	–	–	–
31	4.06	4.84	4.70	4.04	4.20	4.00	3.99	4.05

V.2.5 Determination of the 27/28 ratio after the disproportionation reaction in presence of benzoic acid by peak deconvolution of the NMR spectra

The ^{1}H NMR of the reaction mixture was fitted using the deconvolution tool provided with the software Mestrec 4.8.6.0 in the windows 22-5 ppm. To minimize systematic errors arising from applying Lorentzian or Gaussian lineshapes, a mixed Lorentzian-Gaussian (Voight) lineshape model was used for the deconvolution. The experimental peaks were first fitted using the Levenberg-Marquardt non–linear least squares and Downhill Simplex (Nelder and Mead) algorithms for estimating peak parameters (position, intensity, line width and lineshape function).

A ratio **27** : **28** of 1:1.25 was finally determined with this refined model.

Table A-3 Parameters used to model the different peaks of the reaction mixture NMR with the Mestrec program(L/G: Lorentzian-Gaussian ratio of the Voight function)

Peak	ppm	Height	Width	L/G	Area	Normalised area	assignement
0	17,945	568	166	1	148107,244	1	**H3 cluster**
1	14,488	2886,55	73	1	330995,302	2,23	N-H+/H2O
2	9,91	937	145	1	213416,243	1,44	**H1/H2 cluster**
3	9,692	302	16	1	7590,088	0,05	
4	9,15	571	4	1	3587,699	0,02	pyridine ^{13}C satellite
5	8,716	35911	11,58	0,5	547936,311	3,69	pyridine
6	8,606	8600	14,3	1	193176,535	1,30	**H3 monomer**

7	7,571	9056	20,6	1	293037,715	1,97	pyridine
8	7,473	7099	22,5	1	250899,37	1,69	**H1/H2 monomer**
9	7,211	16018	11,6	1	291867,79	1,97	pyridine

Figure A-15: Graphical representation of the peaks represented in Table A-2.

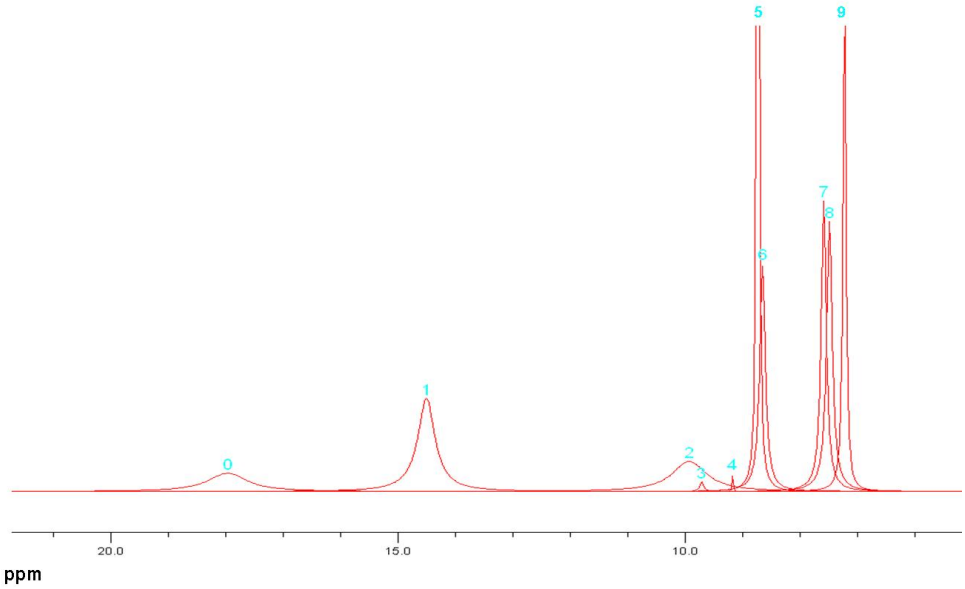

Figure A-16: Graphical representation of the peaks in Table S1 (grey line) and original NMR spectra (dark line).

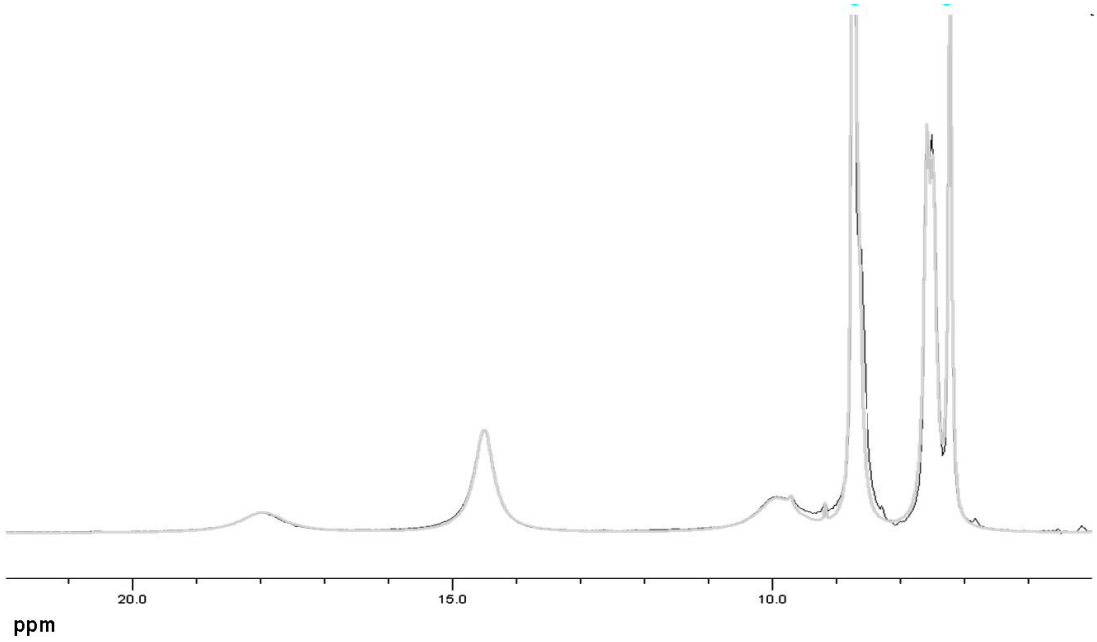

Figure A-17: Difference between the calculated and experimental spectrum (brown line), and experimental NMR spectra (dark line)

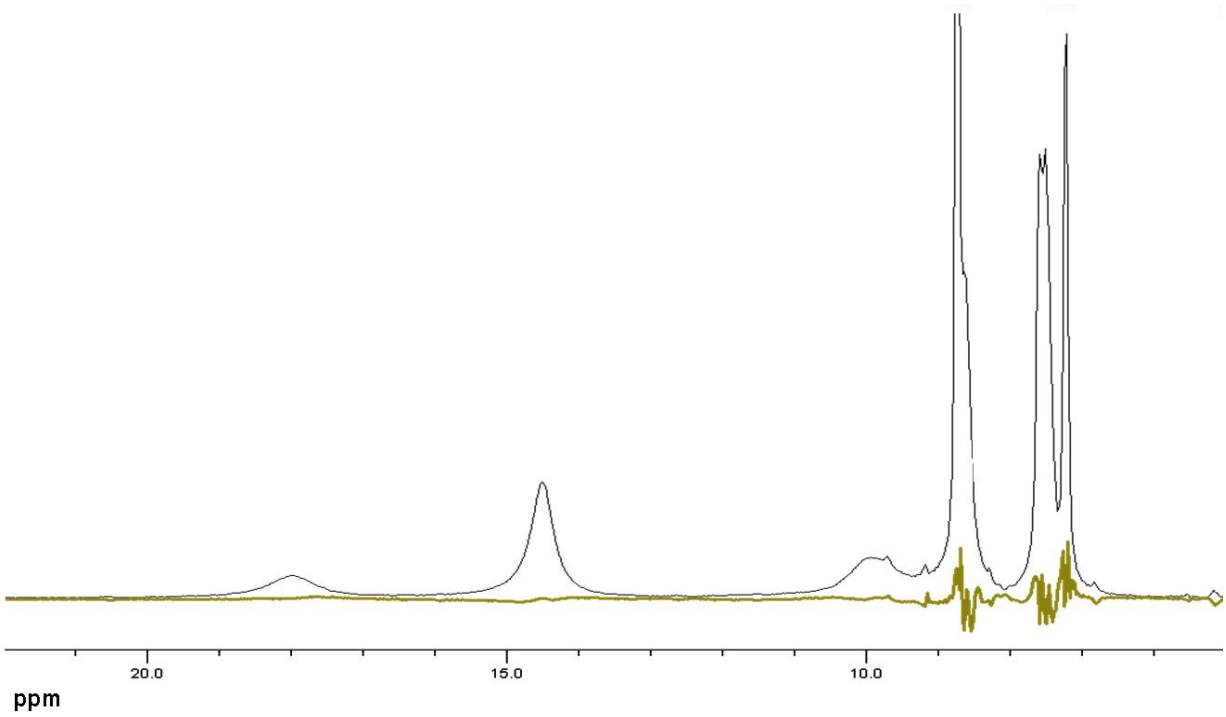
20.0
15.0
10.0
ppm

B-Crystallographic Tables

Table B-0-2:: Crystal data and structure refinement for $[UO_2(salen)]_4[\mu_8\text{-}K]_2[K(18C6)py]_2$, **3**

Empirical formula	C49 H57 K2 N5 O14 U2	
Formula weight	1494.26	
Temperature	150(2) K	
Wavelength	0.71073 A	
Crystal system	Monoclinic	
Space group	P 21/c	
Unit cell dimensions	a = 12.99521(19) A b = 15.4772(2) A c = 26.2194(4) A	alpha = 90 deg. beta = 90.9358(15) deg. gamma = 90 deg.
Volume, Z	5272.80(14) A^3, 4	
Density (calculated)	1.882 Mg/m^3	
Absorption coefficient	6.361 mm^-1	
F(000)	2880	
Crystal size	0.35 x 0.20 x 0.20 mm	
Theta range for data collection	3.06 to 29.08 deg.	
Limiting indices	-17<=h<=14, -19<=k<=21, -35<=l<=35	
Reflections collected	28323	
Independent reflections	12033 [R(int) = 0.0294]	
Absorption correction	Semi-empirical from equivalents	
Max. and min. transmission	1.00000 and 0.69396	
Refinement method	Full-matrix least-squares on F^2	
Data / restraints / parameters	12033 / 0 / 649	
Goodness-of-fit on F^2	0.875	
Final R indices [I>2sigma(I)]	R1 = 0.0520, wR2 = 0.1207	
R indices (all data)	R1 = 0.0743, wR2 = 0.1248	
Largest diff. peak and hole	3.151 and -0.910 e.A^-3	

Table B-0-3:: Crystal data and structure refinement for [(UO_2)(salen)(py)], **4**

Empirical formula	C21 H19 N3 O4 U	
Formula weight	615.42	
Temperature	150(2) K	
Wavelength	0.71073 A	
Crystal system	Orthorhombic	
Space group	P c 21 b	
Unit cell dimensions	a = 18.3976(5) A	alpha = 90 deg.
	b = 9.0482(2) A	beta = 90 deg.
	c = 11.7985(3) A	gamma = 90 deg.
Volume, Z	1964.04(9) A^3, 4	
Density (calculated)	2.081 Mg/m^3	
Absorption coefficient	8.298 mm^-1	
F(000)	1160	
Crystal size	0.40 x 0.35 x 0.15 mm	
Theta range for data collection	3.16 to 28.89 deg.	
Limiting indices	-13<=h<=23, -9<=k<=11, -15<=l<=15	
Reflections collected	5906	
Independent reflections	3336 [R(int) = 0.0237]	
Absorption correction	Semi-empirical from equivalents	
Max. and min. transmission	0.3691 and 0.1360	
Refinement method	Full-matrix least-squares on F^2	
Data / restraints / parameters	3336 / 1 / 262	
Goodness-of-fit on F^2	0.899	
Final R indices [I>2sigma(I)]	R1 = 0.0236, wR2 = 0.0533	
R indices (all data)	R1 = 0.0409, wR2 = 0.0556	
Absolute structure parameter	0.015(11)	
Largest diff. peak and hole	1.133 and -1.003 e.A^-3	

Table B-0-4:: Crystal data and structure refinement for {[UO_2(salen)μ-K(18C6)][UO_2(salen)]$_3$[μ_8-K]$_2$},**5**

Empirical formula	C87 H91 K3 N10 O22 U4	
Formula weight	2698.12	
Temperature	150(2) K	
Wavelength	0.71073 A	
Crystal system	Monoclinic	
Space group	C2/c	
Unit cell dimensions	a = 35.851(3) A b = 20.8911(10) A c = 30.623(4) A	alpha = 90 deg. beta = 125.332(5) deg. gamma = 90 deg.
Volume, Z	18711(3) A^3, 8	
Density (calculated)	1.916 Mg/m^3	
Absorption coefficient	7.111 mm^-1	
F(000)	10272	
Crystal size	0.15 x 0.15 x 0.04 mm	
Theta range for data collection	3.06 to 24.71 deg.	
Limiting indices	-42<=h<=40, -22<=k<=24, -35<=l<=32	
Reflections collected	27317	
Independent reflections	14268 [R(int) = 0.0452]	
Absorption correction	Semi-empirical from equivalents	
Max. and min. transmission	0.7640 and 0.4151	
Refinement method	Full-matrix least-squares on F^2	
Data / restraints / parameters	14268 / 42 / 1150	
Goodness-of-fit on F^2	0.800	
Final R indices [I>2sigma(I)]	R1 = 0.0630, wR2 = 0.1448	
R indices (all data)	R1 = 0.1273, wR2 = 0.1601	
Largest diff. peak and hole	2.343 and -1.045 e.A^-3	

Table B-0-5: Crystal data and structure refinement for {[UO_2(acacen)]$_4$(μ_8-K)$_2$][K(18C6)]$_2$} 2py, **6**

Empirical formula	C77 H125 K4 N9 O28 U4	
Formula weight	2733.38	
Temperature	150(2) K	
Wavelength	0.71073 A	
Crystal system	Triclinic	
Space group	P -1	
Unit cell dimensions	a = 12.4344(6) A b = 14.8771(10) A c = 15.0363(10) A	alpha = 90.871(5) deg. beta = 110.338(5) deg. gamma = 102.879(5) deg.
Volume, Z	2529.4(3) A^3, 1	
Density (calculated)	1.794 Mg/m^3	
Absorption coefficient	6.620 mm^-1	
F(000)	1318	
Crystal size	0.19 x 0.12 x 0.06 mm	
Theta range for data collection	3.30 to 24.71 deg.	
Limiting indices	-14<=h<=14, -17<=k<=17, -17<=l<=17	
Reflections collected	24310	
Independent reflections	8448 [R(int) = 0.0777]	
Absorption correction	Semi-empirical from equivalents	
Max. and min. transmission	0.6767 and 0.3707	
Refinement method	Full-matrix least-squares on F^2	
Data / restraints / parameters	8448 / 18 / 577	
Goodness-of-fit on F^2	0.876	
Final R indices [I>2sigma(I)]	R1 = 0.0717, wR2 = 0.1739	
R indices (all data)	R1 = 0.1190, wR2 = 0.1874	
Largest diff. peak and hole	4.567 and -1.215 e.A^-3	

Table B-0-6:: Crystal data and structure refinement for {[UO_2(acacen)]$_4$[μ_8-K]} 2[K(222)py], **7**

Empirical formula	C47 H77 K2 N7 O14 U2	
Formula weight	1518.42	
Temperature	150(2) K	
Wavelength	0.71073 A	
Crystal system	Triclinic	
Space group	P-1	
Unit cell dimensions	a = 11.4327(4) A b = 15.8095(6) A c = 17.1320(6) A	alpha = 72.969(3) deg. beta = 83.061(3) deg. gamma = 87.080(3) deg.
Volume, Z	2938.66(19) A^3, 2	
Density (calculated)	1.716 Mg/m^3	
Absorption coefficient	5.709 mm^-1	
F(000)	1484	
Crystal size	0.07 x 0.04 x 0.04 mm	
Theta range for data collection	3.07 to 24.71 deg.	
Limiting indices	-13<=h<=13, -18<=k<=18, -20<=l<=15	
Reflections collected	22978	
Independent reflections	9995 [R(int) = 0.0714]	
Absorption correction	Semi-empirical from equivalents	
Max. and min. transmission	0.8038 and 0.6907	
Refinement method	Full-matrix least-squares on F^2	
Data / restraints / parameters	9995 / 0 / 657	
Goodness-of-fit on F^2	0.735	
Final R indices [I>2sigma(I)]	R1 = 0.0592, wR2 = 0.1000	
R indices (all data)	R1 = 0.1290, wR2 = 0.1101	
Largest diff. peak and hole	1.946 and -0.852 e.A^-3	

Table B-0-7: Crystal data and structure refinement for {[UO_2(salophen)]$_4$[μ_8-K]$_2$[μ_5-KI]$_2$[(K(18C6)]}·2[K(18C6)(thf)$_2$]·2I, **8**

Empirical formula	C148 H192 I4 K8 N8 O45 U4	
Formula weight	4575.62	
Temperature	150(2) K	
Wavelength	0.71073 A	
Crystal system	Monoclinic	
Space group	P 21/n	
Unit cell dimensions	a = 20.5597(4) A b = 18.7475(4) A c = 22.2997(5) A	alpha = 90 deg. beta = 96.718(2) deg. gamma = 90 deg.
Volume, Z	8536.3(3) A^3, 2	
Density (calculated)	1.780 Mg/m^3	
Absorption coefficient	4.779 mm^-1	
F(000)	4456	
Crystal size	0.25 x 0.10 x 0.05 mm	
Theta range for data collection	2.85 to 33.14 deg.	
Limiting indices	-31<=h<=31, -28<=k<=28, -32<=l<=34	
Reflections collected	103664	
Independent reflections	32220 [R(int) = 0.0463]	
Absorption correction	Semi-empirical from equivalents	
Max. and min. transmission	0.7961 and 0.3813	
Refinement method	Full-matrix least-squares on F^2	
Data / restraints / parameters	32220 / 0 / 986	
Goodness-of-fit on F^2	0.747	
Final R indices [I>2sigma(I)]	R1 = 0.0466, wR2 = 0.0992	
R indices (all data)	R1 = 0.0947, wR2 = 0.1058	
Largest diff. peak and hole	3.522 and -0.810 e.A^-3	

Table B-0-8:: Crystal data and structure refinement for $\{[UO_2(dophen)]_4[\mu_8\text{-}K(py)]_2[\mu_4\text{-}K(py)_2]_4[\mu_2\text{-}I]_2\}$, **10**

Empirical formula	C153.50 H118.50 I2 K6 N21.50 O16 U4	
Formula weight	3960.72	
Temperature	150(2) K	
Wavelength	0.71073 A	
Crystal system	Triclinic	
Space group	P -1	
Unit cell dimensions	a = 16.3117(16) A b = 19.0354(13) A c = 27.669(2) A	alpha = 90.254(6) deg. beta = 99.575(8) deg. gamma = 103.257(7) deg.
Volume, Z	8237.6(12) A^3, 2	
Density (calculated)	1.597 g/cm^3	
Absorption coefficient	4.510 mm^-1	
F(000)	3812	
Crystal size	0.09 x 0.09 x 0.05 mm	
Theta range for data collection	3.23 to 23.26 deg.	
Limiting indices	-18<=h<=18, -21<=k<=18, -30<=l<=30	
Reflections collected	43332	
Independent reflections	23544 [R(int) = 0.1002]	
Absorption correction	Semi-empirical from equivalents	
Max. and min. transmission	0.8126 and 0.6817	
Refinement method	Full-matrix-block least-squares on F^2	
Data / restraints / parameters	23544 / 411 / 1644	
Goodness-of-fit on F^2	1.033	
Final R indices [I>2sigma(I)]	R1 = 0.1089, wR2 = 0.2646	
R indices (all data)	R1 = 0.2039, wR2 = 0.3336	
Largest diff. peak and hole	6.089 and -1.099 e.A^-3	

Table B-0-9:: Crystal data and structure refinement for $[UO_2(salen)(py)]_2[Cp^*_2Co]$, **12**

Empirical formula	C57 H63 Co N5 O8 U2	
Formula weight	1481.11	
Temperature	150(2) K	
Wavelength	0.71073 A	
Crystal system	Triclinic	
Space group	P -1	
Unit cell dimensions	a = 11.9294(6) A b = 14.3569(8) A c = 17.4038(10) A	alpha = 67.132(5) deg. beta = 76.897(4) deg. gamma = 78.995(4) deg.
Volume, Z	2657.4(2) A^3, 2	
Density (calculated)	1.851 Mg/m^3	
Absorption coefficient	6.447 mm^-1	
F(000)	1430	
Crystal size	0.40 x 0.22 x 0.04 mm	
Theta range for data collection	3.39 to 26.37 deg.	
Limiting indices	-14<=h<=12, -17<=k<=17, -21<=l<=21	
Reflections collected	31133	
Independent reflections	10468 [R(int) = 0.0693]	
Max. and min. transmission	0.7735 and 0.1819	
Refinement method	Full-matrix least-squares on F^2	
Data / restraints / parameters	10468 / 48 / 690	
Goodness-of-fit on F^2	1.050	
Final R indices [I>2sigma(I)]	R1 = 0.0992, wR2 = 0.2483	
R indices (all data)	R1 = 0.1279, wR2 = 0.2622	
Largest diff. peak and hole	10.592 and -1.674 e.A^-3	

Table B-0-10:: Crystal data and structure refinement for $[UO_2(salen)(py)]_2[Me_4N]$, **13**

Empirical formula	C50 H58 N7 O9 U2	
Formula weight	1377.09	
Temperature	150(2) K	
Wavelength	0.71073 A	
Crystal system	Orthorhombic	
Space group	P b c a	
Unit cell dimensions	a = 10.7829(6) A b = 24.5110(10) A c = 38.443(2) A	alpha = 90 deg. beta = 90 deg. gamma = 90 deg.
Volume, Z	10160.5(9) A^3, 8	
Density (calculated)	1.800 g/cm^3	
Absorption coefficient	6.428 mm^-1	
F(000)	5304	
Crystal size	0.37 x 0.16 x 0.14 mm	
Theta range for data collection	3.65 to 28.28 deg.	
Limiting indices	-14<=h<=10, -32<=k<=15, -35<=l<=51	
Reflections collected	29015	
Independent reflections	12506 [R(int) = 0.0661]	
Absorption correction	Semi-empirical from equivalents	
Max. and min. transmission	0.4708 and 0.2013	
Refinement method	Full-matrix least-squares on F^2	
Data / restraints / parameters	12506 / 50 / 617	
Goodness-of-fit on F^2	0.907	
Final R indices [I>2sigma(I)]	R1 = 0.0602, wR2 = 0.1028	
R indices (all data)	R1 = 0.1199, wR2 = 0.1107	
Largest diff. peak and hole	2.353 and -1.187 e.A^-3	

Table B-0-11:: Crystal data and structure refinement for $[UO_2(salen)]_4[\mu_8\text{-}Na]_2[Na(18C6)(py)_2]_2$, **14**

Empirical formula	C124 H148 N14 Na4 O28 U4	
Formula weight	3326.64	
Temperature	150(2) K	
Wavelength	0.71073 A	
Crystal system	Triclinic	
Space group	P -1	
Unit cell dimensions	a = 12.9942(15) A b = 14.9534(17) A c = 17.888(2) A	alpha = 104.522(10) deg. beta = 103.428(10) deg. gamma = 97.680(10) deg.
Volume, Z	3204.0(6) A^3, 1	
Density (calculated)	1.724 g/cm^3	
Absorption coefficient	5.130 mm^-1	
F(000)	1626	
Crystal size	0.18 x 0.13 x 0.02 mm	
Theta range for data collection	3.31 to 24.71 deg.	
Limiting indices	-15<=h<=13, -17<=k<=17, -21<=l<=16	
Reflections collected	18233	
Independent reflections	10881 [R(int) = 0.0863]	
Absorption correction	Semi-empirical from equivalents	
Max. and min. transmission	0.9044 and 0.4654	
Refinement method	Full-matrix least-squares on F^2	
Data / restraints / parameters	10881 / 30 / 788	
Goodness-of-fit on F^2	1.039	
Final R indices [I>2sigma(I)]	R1 = 0.0972, wR2 = 0.2402	
R indices (all data)	R1 = 0.1440, wR2 = 0.2855	
Largest diff. peak and hole	6.213 and -3.300 e.A^-3	

Table B-0-12:: Crystal data and structure refinement for {[UO_2(salen)]$_4$[μ_8-Rb]$_2$[Rb(18C6)]$_2$}, **15**

Empirical formula	C127.88 H144.10 N16.11 O28 Rb4 U4	
Formula weight	3648.77	
Temperature	150(2) K	
Wavelength	0.71073 A	
Crystal system	Triclinic	
Space group	P -1	
Unit cell dimensions	a = 14.6577(7) A b = 14.9748(6) A c = 18.4509(7) A	alpha = 102.435(3) deg. beta = 95.307(3) deg. gamma = 119.302(4) deg.
Volume, Z	3354.5(2) A^3, 1	
Density (calculated)	1.806 Mg/m^3	
Absorption coefficient	6.331 mm^-1	
F(000)	1764	
Crystal size	0.29 x 0.10 x 0.08 mm	
Theta range for data collection	3.32 to 24.71 deg.	
Limiting indices	-17<=h<=17, -17<=k<=17, -21<=l<=21	
Reflections collected	41616	
Independent reflections	11391 [R(int) = 0.0641]	
Max. and min. transmission	0.6248 and 0.2611	
Refinement method	Full-matrix least-squares on F^2	
Data / restraints / parameters	11391 / 33 / 707	
Goodness-of-fit on F^2	1.042	
Final R indices [I>2sigma(I)]	R1 = 0.1010, wR2 = 0.2985	
R indices (all data)	R1 = 0.1228, wR2 = 0.3058	
Largest diff. peak and hole	7.862 and -2.395 e.A^-3	

Table B-0-13:: Crystal data and structure refinement for {[UO_2(salen)]$_4$[μ_4-O]$_2$[μ_4-Li]$_4$}, **16**

Empirical formula	C64 H56 Li4 N8 O18 U4	
Formula weight	2205.05	
Temperature	150(2) K	
Wavelength	0.71073 A	
Crystal system	Orthorhombic	
Space group	F d d d	
Unit cell dimensions	a = 13.6929(17) A b = 34.252(2) A c = 35.101(2) A	alpha = 90 deg. beta = 90 deg. gamma = 90 deg.
Volume, Z	16463(2) A^3, 8	
Density (calculated)	1.779 g/cm^3	
Absorption coefficient	7.907 mm^-1	
F(000)	8160	
Crystal size	0.11 x 0.08 x 0.05 mm	
Theta range for data collection	3.31 to 23.25 deg.	
Limiting indices	-12<=h<=12, -31<=k<=38, -36<=l<=39	
Reflections collected	9893	
Independent reflections	2549 [R(int) = 0.0466]	
Absorption correction	Semi-empirical from equivalents	
Max. and min. transmission	0.6702 and 0.4906	
Refinement method	Full-matrix least-squares on F^2	
Data / restraints / parameters	2549 / 0 / 209	
Goodness-of-fit on F^2	0.971	
Final R indices [I>2sigma(I)]	R1 = 0.0814, wR2 = 0.2145	
R indices (all data)	R1 = 0.1199, wR2 = 0.2306	
Largest diff. peak and hole	2.103 and -0.713 e.A^-3	

Table B-0-14:: Crystal data and structure refinement for {[UO_2(salen)]$_4$$Ca_2$}, **17**

Empirical formula	C65 H58 Ca2 Cl2 N8 O16 U4	
Formula weight	2310.37	
Temperature	396(2) K	
Wavelength	0.71073 A	
Crystal system	Triclinic	
Space group	P -1	
Unit cell dimensions	a = 11.9759(11) A b = 12.0404(11) A c = 14.1735(16) A	alpha = 113.509(10) deg. beta = 108.910(9) deg. gamma = 96.266(7) deg.
Volume, Z	1704.7(3) A^3, 1	
Density (calculated)	2.251 g/cm^3	
Absorption coefficient	9.773 mm^-1	
F(000)	1074	
Crystal size	0.08 x 0.04 x 0.01 mm	
Theta range for data collection	3.40 to 26.37 deg.	
Limiting indices	-14<=h<=14, -15<=k<=10, -17<=l<=16	
Reflections collected	10224	
Independent reflections	6906 [R(int) = 0.0488]	
Absorption correction	Semi-empirical from equivalents	
Max. and min. transmission	0.9086 and 0.5161	
Refinement method	Full-matrix least-squares on F^2	
Data / restraints / parameters	6906 / 48 / 470	
Goodness-of-fit on F^2	1.013	
Final R indices [I>2sigma(I)]	R1 = 0.0685, wR2 = 0.1214	
R indices (all data)	R1 = 0.1257, wR2 = 0.1440	
Largest diff. peak and hole	1.835 and -1.040 e.A^-3	

Table B-0-15:: Crystal data and structure refinement for [{[UO_2(salen)]$_2$Mn(py)$_3$}$_6$], **18**

Empirical formula	C287 H263 Mn6 N43 O48 U12	
Formula weight	8268.40	
Temperature	150(2) K	
Wavelength	0.71073 A	
Crystal system	Tetragonal	
Space group	I 41/a (Origin at -1)	
Unit cell dimensions	a = 59.4785(8) A b = 59.4785(8) A c = 43.5227(16) A	alpha = 90 deg. beta = 90 deg. gamma = 90 deg.
Volume, Z	153970(6) A^3, 8	
Density (calculated)	0.713 g/cm^3	
Absorption coefficient	2.637 mm^-1	
F(000)	31392	
Crystal size	0.31 x 0.25 x 0.07 mm	
Theta range for data collection	3.43 to 20.82 deg.	
Limiting indices	-50<=h<=51, -36<=k<=59, -43<=l<=43	
Reflections collected	100058	
Independent reflections	40129 [R(int) = 0.1008]	
Absorption correction	Semi-empirical from equivalents	
Max. and min. transmission	0.8328 and 0.4991	
Refinement method	Full-matrix-block least-squares on F^2	
Data / restraints / parameters	40129 / 86 / 1719	
Goodness-of-fit on F^2	0.771	
Final R indices [I>2sigma(I)]	R1 = 0.0620, wR2 = 0.1270	
R indices (all data)	R1 = 0.1262, wR2 = 0.1468	
Largest diff. peak and hole	0.822 and -0.558 e.A^-3	

Table B-0-16:: Crystal data and structure refinement for $[UO_2L]_3$, **19**

Empirical formula	C90 H77 N12 O7 U3	
Formula weight	2152.73	
Temperature	150(2) K	
Wavelength	0.71073 A	
Crystal system	Monoclinic	
Space group	P 1 21/n 1	
Unit cell dimensions	a = 16.7294(13) A b = 16.6323(7) A c = 29.5917(11) A	alpha = 90 deg. beta = 90.954(5) deg. gamma = 90 deg.
Volume, Z	8232.7(8) A^3, 4	
Density (calculated)	1.737 g/cm^3	
Absorption coefficient	5.949 mm^-1	
F(000)	4132	
Crystal size	0.15 x 0.05 x 0.02 mm	
Theta range for data collection	3.23 to 26.37 deg.	
Limiting indices	-20<=h<=12, -20<=k<=20, -36<=l<=34	
Reflections collected	53639	
Independent reflections	15282 [R(int) = 0.1477]	
Absorption correction	Semi-empirical from equivalents	
Max. and min. transmission	0.9056 and 0.4771	
Refinement method	Full-matrix least-squares on F^2	
Data / restraints / parameters	15282 / 54 / 1016	
Goodness-of-fit on F^2	1.096	
Final R indices [I>2sigma(I)]	R1 = 0.0768, wR2 = 0.1393	
R indices (all data)	R1 = 0.1377, wR2 = 0.1614	
Largest diff. peak and hole	3.454 and -1.579 e.A^-3	

Table B-0-17:: Crystal data and structure refinement for $[UO_2(L)Cl]$, **20**

Empirical formula	C29 H23 Cl3 N4 O2 U	
Formula weight	803.89	
Temperature	150(2) K	
Wavelength	0.71073 A	
Crystal system	Triclinic	
Space group	P -1	
Unit cell dimensions	a = 7.2599(4) A	alpha = 99.775(5) deg.
	b = 12.1368(9) A	beta = 90.893(4) deg.
	c = 16.1046(8) A	gamma = 95.133(5) deg.
Volume, Z	1392.11(14) A^3, 2	
Density (calculated)	1.918 g/cm^3	
Absorption coefficient	6.153 mm^-1	
F(000)	768	
Crystal size	0.20 x 0.05 x 0.03 mm	
Theta range for data collection	3.32 to 28.28 deg.	
Limiting indices	-9<=h<=8, -16<=k<=16, -21<=l<=21	
Reflections collected	12801	
Independent reflections	6907 [R(int) = 0.0575]	
Absorption correction	Semi-empirical from equivalents	
Max. and min. transmission	0.8369 and 0.3755	
Refinement method	Full-matrix least-squares on F^2	
Data / restraints / parameters	6907 / 0 / 354	
Goodness-of-fit on F^2	1.070	
Final R indices [I>2sigma(I)]	R1 = 0.0759, wR2 = 0.1862	
R indices (all data)	R1 = 0.0957, wR2 = 0.2005	
Largest diff. peak and hole	13.239 and -2.787 e.A^-3	

Table B-0-18:: Crystal data and structure refinement for {[UO_2(L)]$_2$[μ_2-O]}, **21**

Empirical formula	C57.50 H44.25 N8.75 O5 U2	
Formula weight	1413.83	
Temperature	150(2) K	
Wavelength	0.71073 A	
Crystal system	Monoclinic	
Space group	C 1 2/c 1	
Unit cell dimensions	a = 27.1234(13) A b = 27.3660(13) A c = 28.2322(16) A	alpha = 90 deg. beta = 90.531(4) deg. gamma = 90 deg.
Volume, Z	20954.7(19) A^3, 16	
Density (calculated)	1.793 g/cm^3	
Absorption coefficient	6.232 mm^-1	
F(000)	10792	
Crystal size	0.28 x 0.16 x 0.02 mm	
Theta range for data collection	3.31 to 24.71 deg.	
Limiting indices	-31<=h<=19, -32<=k<=30, -31<=l<=33	
Reflections collected	42381	
Independent reflections	17778 [R(int) = 0.0764]	
Absorption correction	Semi-empirical from equivalents	
Max. and min. transmission	0.8908 and 0.2743	
Refinement method	Full-matrix least-squares on F^2	
Data / restraints / parameters	17778 / 42 / 1321	
Goodness-of-fit on F^2	1.082	
Final R indices [I>2sigma(I)]	R1 = 0.0757, wR2 = 0.1494	
R indices (all data)	R1 = 0.1201, wR2 = 0.1722	
Largest diff. peak and hole	3.369 and -1.593 e.A^-3	

Table B-0-19:: Crystal data and structure refinement for $\{[UO_2(Mesaldien)]K\}_n$, **22**

Empirical formula	C21.50 H23.50 K N3.50 O4 U	
Formula weight	672.07	
Temperature	150(2) K	
Wavelength	0.71073 A	
Crystal system	Monoclinic	
Space group	P 21/c	
Unit cell dimensions	a = 22.925(4) A b = 14.316(3) A c = 14.0547(19) A	alpha = 90 deg. beta = 101.946(15) deg. gamma = 90 deg.
Volume, Z	4512.5(14) A^3, 8	
Density (calculated)	1.978 g/cm^3	
Absorption coefficient	7.412 mm^-1	
F(000)	2560	
Crystal size	0.45 x 0.04 x 0.01 mm	
Theta range for data collection	3.38 to 23.26 deg.	
Limiting indices	-25<=h<=25, -7<=k<=15, -15<=l<=15	
Reflections collected	12681	
Independent reflections	6438 [R(int) = 0.1018]	
Absorption correction	Semi-empirical from equivalents	
Max. and min. transmission	0.9499 and 0.1349	
Refinement method	Full-matrix least-squares on F^2	
Data / restraints / parameters	6438 / 97 / 546	
Goodness-of-fit on F^2	0.987	
Final R indices [I>2sigma(I)]	R1 = 0.0932, wR2 = 0.1986	
R indices (all data)	R1 = 0.1720, wR2 = 0.2419	
Largest diff. peak and hole	1.894 and -1.329 e.A^-3	

Table B-0-20:: Crystal data and structure refinement for {[UO_2(salen)][U(salophen-^{t}Bu$_2$)]$_2$[(U(salen)]$_2$(μO)$_3$(μ_3O), **23**

Empirical formula	C96 H104 N16 O13 U4
Formula weight	2642.07
Temperature	150(2) K
Wavelength	0.71073 A
Crystal system	Orthorhombic
Space group	P b c a
Unit cell dimensions	a = 27.5621(19) A alpha = 90 deg. b = 10.9547(8) A beta = 90 deg. c = 30.626(3) A gamma = 90 deg.
Volume, Z	9246.9(13) A^3, 4
Density (calculated)	1.898 g/cm^3
Absorption coefficient	7.056 mm^-1
F(000)	5056
Crystal size	0.21 x 0.04 x 0.01 mm
Theta range for data collection	3.33 to 26.37 deg.
Limiting indices	-32<=h<=21, -11<=k<=13, -18<=l<=38
Reflections collected	14335
Independent reflections	8400 [R(int) = 0.1045]
Absorption correction	Semi-empirical from equivalents
Max. and min. transmission	0.9264 and 0.3175
Refinement method	Full-matrix least-squares on F^2
Data / restraints / parameters	8400 / 72 / 585
Goodness-of-fit on F^2	1.007
Final R indices [I>2sigma(I)]	R1 = 0.0919, wR2 = 0.1396
R indices (all data)	R1 = 0.1989, wR2 = 0.1823
Largest diff. peak and hole	2.427 and -1.438 e.A^-3

Table B-0-21:: Crystal data and structure refinement for $[UO_2(Mesaldien)]$, **24**

Empirical formula	C38 H42 N6 O8 U2	
Formula weight	1186.84	
Temperature	150(2) K	
Wavelength	0.71073 A	
Crystal system	Monoclinic	
Space group	P 21/c	
Unit cell dimensions	a = 16.3093(7) A b = 10.8301(2) A c = 22.1561(6) A	alpha = 90 deg. beta = 105.356(3) deg. gamma = 90 deg.
Volume, Z	3773.7(2) A^3, 4	
Density (calculated)	2.089 g/cm^3	
Absorption coefficient	8.632 mm^-1	
F(000)	2240	
Crystal size	0.22 x 0.12 x 0.07 mm	
Theta range for data collection	3.36 to 30.51 deg.	
Limiting indices	-18<=h<=23, -7<=k<=15, -31<=l<=17	
Reflections collected	18306	
Independent reflections	11399 [R(int) = 0.0322]	
Absorption correction	Semi-empirical from equivalents	
Max. and min. transmission	0.5873 and 0.2571	
Refinement method	Full-matrix least-squares on F^2	
Data / restraints / parameters	11399 / 0 / 518	
Goodness-of-fit on F^2	0.997	
Final R indices [I>2sigma(I)]	R1 = 0.0377, wR2 = 0.0625	
R indices (all data)	R1 = 0.0594, wR2 = 0.0684	
Largest diff. peak and hole	1.747 and -1.197 e.A^-3	

Table B-0-22:: Crystal data and structure refinement for $[U(Mesaldien)I_2]$·MeCN, **25**

Empirical formula	C20.68 H23.52 I2 N3.84 O2 U	
Formula weight	849.80	
Temperature	150(2) K	
Wavelength	0.71073 A	
Crystal system	Monoclinic	
Space group	P 21/c	
Unit cell dimensions	a = 9.0413(2) A b = 16.1250(4) A c = 17.1733(4) A	alpha = 90 deg. beta = 98.569(2) deg. gamma = 90 deg.
Volume, Z	2475.76(10) A^3, 4	
Density (calculated)	2.280 Mg/m^3	
Absorption coefficient	9.072 mm^-1	
F(000)	1554	
Crystal size	0.59 x 0.27 x 0.13 mm	
Theta range for data collection	3.40 to 28.28 deg.	
Limiting indices	-12<=h<=8, -21<=k<=18, -16<=l<=22	
Reflections collected	13518	
Independent reflections	6132 [R(int) = 0.0308]	
Absorption correction	Semi-empirical from equivalents	
Max. and min. transmission	0.3968 and 0.0747	
Refinement method	Full-matrix least-squares on F^2	
Data / restraints / parameters	6132 / 6 / 274	
Goodness-of-fit on F^2	1.214	
Final R indices [I>2sigma(I)]	R1 = 0.0526, wR2 = 0.1041	
R indices (all data)	R1 = 0.0783, wR2 = 0.1078	
Largest diff. peak and hole	1.656 and -1.485 e.A^-3	

Table B-0-23: Crystal data and structure refinement for {[UO_2(salen)][U(salophen-^{t}Bu$_2$)]$_2$[(U(salen)]$_2$(μ-O)$_3$(μ_3-O)}, **26**

Empirical formula	C128 H147 N14 O16 U5	
Formula weight	3327.75	
Temperature	150(2) K	
Wavelength	0.71073 A	
Crystal system	Monoclinic	
Space group	P 21/n	
Unit cell dimensions	a = 16.8481(5) A b = 31.3059(14) A c = 24.9946(10) A	alpha = 90 deg. beta = 104.442(3) deg. gamma = 90 deg.
Volume, Z	12766.7(8) A^3, 4	
Density (calculated)	1.731 g/cm^3	
Absorption coefficient	6.387 mm^-1	
F(000)	6404	
Crystal size	0.34 x 0.16 x 0.13 mm	
Theta range for data collection	3.34 to 24.71 deg.	
Limiting indices	-12<=h<=19, -36<=k<=35, -29<=l<=20	
Reflections collected	44348	
Independent reflections	21558 [R(int) = 0.0561]	
Absorption correction	Semi-empirical from equivalents	
Max. and min. transmission	0.4953 and 0.2228	
Refinement method	Full-matrix least-squares on F^2	
Data / restraints / parameters	21558 / 154 / 1433	
Goodness-of-fit on F^2	1.106	
Final R indices [I>2sigma(I)]	R1 = 0.1040, wR2 = 0.2542	
R indices (all data)	R1 = 0.1426, wR2 = 0.2769	
Largest diff. peak and hole	3.111 and -3.147 e.A^-3	

Table B-0-24:: Crystal data and structure refinement for $[U_6O_4(OH)_4(C_6H_5COO)_{12}(py)_3]$, **27**

Empirical formula	C113 H95 N7 O32 U6	
Formula weight	3491.14	
Temperature	150(2) K	
Wavelength	0.71073 A	
Crystal system	Orthorhombic	
Space group	C m c m	
Unit cell dimensions	a = 27.4352(4) A b = 16.3250(2) A c = 28.7642(4) A	alpha = 90 deg. beta = 90 deg. gamma = 90 deg.
Volume, Z	12882.9(3) A^3, 4	
Density (calculated)	1.800 g/cm^3	
Absorption coefficient	7.586 mm^-1	
F(000)	6520	
Crystal size	0.31 x 0.14 x 0.11 mm	
Theta range for data collection	3.32 to 28.28 deg.	
Limiting indices	-36<=h<=33, -21<=k<=21, -38<=l<=38	
Reflections collected	66545	
Independent reflections	8304 [R(int) = 0.0332]	
Absorption correction	Semi-empirical from equivalents	
Max. and min. transmission	0.4810 and 0.1992	
Refinement method	Full-matrix least-squares on F^2	
Data / restraints / parameters	8304 / 30 / 465	
Goodness-of-fit on F^2	1.143	
Final R indices [I>2sigma(I)]	R1 = 0.0865, wR2 = 0.2655	
R indices (all data)	R1 = 0.1036, wR2 = 0.2725	
Largest diff. peak and hole	5.447 and -5.634 e.A^-3	

Table B-0-25:: Crystal data and structure refinement for $[UO_2(C_6H_5COO)_2(py)_2]$, **28**

Empirical formula	C24 H20 N2 O6 U	
Formula weight	670.45	
Temperature	150(2) K	
Wavelength	0.71073 A	
Crystal system	Monoclinic	
Space group	P 21/c	
Unit cell dimensions	a = 11.3216(9) A b = 10.0554(8) A c = 10.1130(8) A	alpha = 90 deg. beta = 95.493(8) deg. gamma = 90 deg.
Volume, Z	1146.00(16) A^3, 2	
Density (calculated)	1.943 Mg/m^3	
Absorption coefficient	7.124 mm^-1	
F(000)	636	
Crystal size	1.06 x 0.57 x 0.39 mm	
Theta range for data collection	3.49 to 32.52 deg.	
Limiting indices	-16<=h<=17, -11<=k<=14, -14<=l<=5	
Reflections collected	6840	
Independent reflections	3712 [R(int) = 0.0248]	
Absorption correction	Semi-empirical from equivalents	
Max. and min. transmission	0.1662 and 0.0494	
Refinement method	Full-matrix least-squares on F^2	
Data / restraints / parameters	3712 / 0 / 151	
Goodness-of-fit on F^2	0.978	
Final R indices [I>2sigma(I)]	R1 = 0.0582, wR2 = 0.1428	
R indices (all data)	R1 = 0.0815, wR2 = 0.1499	
Largest diff. peak and hole	5.148 and -1.111 e.A^-3	

Table B-0-26:: Crystal data and structure refinement for $[U_{10}O_8(OH)_6(C_6H_5COO)_{14}I_4(H_2O)_2(MeCN)_2]$, **29**

Empirical formula	C106 H82 I4 N4 O42 U10	
Formula weight	4971.66	
Temperature	150(2) K	
Wavelength	0.71073 A	
Crystal system	Monoclinic	
Space group	C 1 2/c 1	
Unit cell dimensions	a = 30.2312(18) A b = 17.1382(8) A c = 28.1962(18) A	alpha = 90 deg. beta = 120.214(8) deg. gamma = 90 deg.
Volume, Z	12624.1(12) A^3, 4	
Density (calculated)	2.616 g/cm^3	
Absorption coefficient	13.835 mm^-1	
F(000)	8856	
Crystal size	0.21 x 0.12 x 0.02 mm	
Theta range for data collection	3.46 to 26.37 deg.	
Limiting indices	-37<=h<=33, -21<=k<=14, -30<=l<=35	
Reflections collected	42145	
Independent reflections	12869 [R(int) = 0.0668]	
Absorption correction	Semi-empirical from equivalents	
Max. and min. transmission	0.7694 and 0.1601	
Refinement method	Full-matrix least-squares on F^2	
Data / restraints / parameters	12869 / 48 / 776	
Goodness-of-fit on F^2	1.036	
Final R indices [I>2sigma(I)]	R1 = 0.0848, wR2 = 0.1973	
R indices (all data)	R1 = 0.1251, wR2 = 0.2320	
Largest diff. peak and hole	4.426 and -2.018 e.A^-3	

Table B-0-27: Crystal data and structure refinement for $[U_{10}O_8(OH)_6(C_6H_5COO)_{12.82}I_{3.18}(H_2O)_4(MeCN)_3]I_2 \cdot 5MeCN$, **30**

Empirical formula	C105.52 H101.95 I5.21 N8 O43.58 U10	
Formula weight	5220.99	
Temperature	150(2) K	
Wavelength	0.71073 A	
Crystal system	Monoclinic	
Space group	21/n	
Unit cell dimensions	a = 15.0974(6) A b = 16.7923(7) A c = 28.5081(10) A	alpha = 90 deg. beta = 93.609(3) deg. gamma = 90 deg.
Volume, Z	7213.1(5) A^3, 2	
Density (calculated)	2.404 g/cm^3	
Absorption coefficient	12.370 mm^-1	
F(000)	4672	
Crystal size	0.34 x 0.18 x 0.02 mm	
Theta range for data collection	3.32 to 23.26 deg.	
Limiting indices	-16<=h<=16, -17<=k<=18, -31<=l<=15	
Reflections collected	24762	
Independent reflections	10337 [R(int) = 0.0814]	
Absorption correction	Semi-empirical from equivalents	
Max. and min. transmission	0.8080 and 0.1033	
Refinement method	Full-matrix least-squares on F^2	
Data / restraints / parameters	10337 / 124 / 823	
Goodness-of-fit on F^2	0.872	
Final R indices [I>2sigma(I)]	R1 = 0.0788, wR2 = 0.1925	
R indices (all data)	R1 = 0.1310, wR2 = 0.2122	
Largest diff. peak and hole	2.745 and -1.584 e.A^-3	

Table B-0-28:: Crystal data and structure refinement for $\{[K(MeCN)]_2[U_{16}O_{22}(OH)_2(C_6H_5COO)_{24}]\}.4MeCN$, **31**

Empirical formula	C90 H70 K N3 O36 U8	
Formula weight	3712.83	
Temperature	150(2) K	
Wavelength	0.71073 A	
Crystal system	Monoclinic	
Space group	P 21/c	
Unit cell dimensions	a = 19.8428(8) A b = 30.9332(7) A c = 20.7370(7) A	alpha = 90 deg. beta = 116.134(5) deg. gamma = 90 deg.
Volume, Z	11427.1(7) A^3, 4	
Density (calculated)	2.158 g/cm^3	
Absorption coefficient	11.403 mm^-1	
F(000)	6696	
Crystal size	0.26 x 0.21 x 0.13 mm	
Theta range for data collection	3.35 to 28.28 deg.	
Limiting indices	-26<=h<=26, -41<=k<=27, -16<=l<=27	
Reflections collected	52202	
Independent reflections	28161 [R(int) = 0.0457]	
Absorption correction	Semi-empirical from equivalents	
Max. and min. transmission	0.3166 and 0.1576	
Refinement method	Full-matrix least-squares on F^2	
Data / restraints / parameters	28161 / 72 / 1264	
Goodness-of-fit on F^2	0.845	
Final R indices [I>2sigma(I)]	R1 = 0.0845, wR2 = 0.2083	
R indices (all data)	R1 = 0.1486, wR2 = 0.2281	
Largest diff. peak and hole	4.733 and -1.949 e.A^-3	

C-List of compounds

$[(UO_2py_5)(KI_2py_2)]_n$ **1**

$[(UO_2)(salen)K(py)]\cdot 1.4KI$ **2**

$[UO_2(salen)]_4[\mu_8\text{-}K]_2[K(18C6)py]_2$ **3**

$[(UO_2)(salen)(py)]$ **4**

$\{[UO_2(salen)\mu\text{-}K(18C6)][UO_2(salen)]_3[\mu_8\text{-}K]_2\}$ **5**

$\{[UO_2(acacen)]_4(\mu_8\text{-}K)_2][K(18C6)]_2\}$ 2py **6**

$\{[UO_2(acacen)]_4[\mu_8\text{-}K]\}$ 2[K(222)py] **7**

$\{[UO_2(salophen)]_4[\mu_8\text{-}K]_2[\mu_5\text{-}KI]_2[(K(18C6)]\}\cdot 2[K(18C6)(thf)_2]\cdot 2I$ **8**

$[UO_2(salophen)(py)][Cp^*_2Co]$ **9**

$\{[UO_2(dophen)]_4[\mu_8\text{-}K(py)]_2[\mu_4\text{-}K(py)_2]_4[\mu_2\text{-}I]_2\}$ **10**

$[UO_2(salen)(py)][Cp^*_2Co]$ **11**

$[UO_2(salen)(py)]_2[Cp^*_2Co]$ **12**

$[UO_2(salen)(py)]_2[Me_4N]$ **13**

$[UO_2(salen)]_4[\mu_8\text{-}Na]_2[Na(18C6)(py)_2]_2$ **14**

$\{[UO_2(salen)]_4[\mu_8\text{-}Rb]_2[Rb(18C6)]_2\}$ **15**

$\{[UO_2(salen)]_4[\mu_4\text{-}O]_2[\mu_4\text{-}Li]_4\}$ **16**

$\{[UO_2(salen)]_4Ca_2\}$, **17**

$[\{[UO_2(salen)]_2Mn(py)_3\}_6]$, **18**

$[UO_2L]_3$, **19**

$[UO_2(L)Cl]$, **20**

$\{[UO_2(L)]_2[\mu_2\text{-}O]\}$, **21**

$\{[UO_2(Mesaldien)]K\}_n$, **22**

$\{[UO_2(Mesaldien)\text{-}(U(Mesaldien)]_2(\mu\text{-}O)\}$, **23**

$[UO_2(Mesaldien)]$, **24**

$[U(Mesaldien)I_2]\cdot MeCN$, **25**

$\{[UO_2(salen)][U(salophen\text{-}^tBu_2)]_2[(U(salen)]_2(\mu\text{-}O)_3(\mu_3\text{-}O)\}$, **26**

$[U_6O_4(OH)_4(C_6H_5COO)_{12}(py)_3]$, **27**

$[UO_2(C_6H_5COO)_2(py)_2]$, **28**

$[U_{10}O_8(OH)_6(C_6H_5COO)_{14}I_4(H_2O)_2(MeCN)_2]$, **29**

$[U_{10}O_8(OH)_6(C_6H_5COO)_{12.82}I_{3.18}(H_2O)_4(MeCN)_3]I_2\cdot 5MeCN$, **30**

$\{[K(MeCN)]_2[U_{16}O_{22}(OH)_2(C_6H_5COO)_{24}]\}.4MeCN$, **31**

D-List of Abbreviations:

$(^{Ad}ArOH)_3N$ = tris(2-hydroxy-3-adamantyl-5-methylbenzyl)amine

$(^{t\text{-}Bu}ArOH)_3$mes = 1,3,5-trimethyl-2,4,6-tris(2,4-di-tert-butyl-hydroxybenzyl)-Methylbenzene

$(^{tBu}ArOH)_3$tacn) = (1,4,7- tris(3,5-di-tert-butyl-2-hydroxybenzyl)-1,4,7-triazacyclononane

$(teaH_3)$ = triethanolamine

acacenH_2 = N,N'-ethylene-bis(acetylacetoneimine),

BIPMH = $HC(PPh_2NSiMe_3)_2$

bipy = bipyridine

Bz = CH_2Ph

Cp = C_5H_5

Cp* = C_5Me_5

Cp' = MeC_5H_4

Cp'' = 1,3-$(MeSi)_2C_5H_3$

Cp''' = 1,2,4-$^tBu_3C_5H_2$

Cp'''' = C_5Me_4Et

Fc = Ferrocene

H_2BPz_2 = dihydrobispyrazolylborate

hfac = 1,1,1,5,5,5-Hexafluoro-2,4-pentanedione

HMDS = $(N(SiMe_3)_2)^-$

L' = N,N'-bis(3-hydroxysalicylidene)-2-methyl-1,2-propanediamine

L'' = N,N'-bis(3-hydroxysalicylidene)-2,2-dimethyl-1,3-propanediamine

L'''' = 5,6-dicyano-1-methyl-3-(N-methylamino)isoindolyl ligand

MesaldienH_2=N,N'-(2-aminomethyl)diethylenebis(salicylideneimine)

OTbp = 2,4,6-tritert-butylphenoxide

Pcm = "Pac-man" polypyrrolic ligand

salenH_2 = N,N'-ethylene-bis(salicylideneimine),

salophenH_2 = N,N'-phenylene-bis(salicylideneimine))

salophen-$^tBu_2H_2$ = N,N'-phenylene-bis-(3,5-di-tert-butylsalicylideneimine;

saoH_2 = hydroxybenzaldehyde oxime

TEMPO = 2,2,6,6-tetramethylpiperidine-1-oxyl

$TpMe_2$ = (3,5-dimethylpyrazolyl)borate ligand

tpy = terpyridine

Publications

Publications

1. V. Mougel, P. Horeglad, G. Nocton, J. Pécaut, M. Mazzanti., ***Angew. Chem.*****,** 2009, *48,* 8477**,** + *inside cover*.
2. V. Mougel, B. Biswas, J. Pécaut, M. Mazzanti, ***Chem. Comm.*****,** 2010, *46*, 8648
3. V. Mougel, P. Horeglad, G. Nocton, J. Pécaut, M. Mazzanti, ***Chem. Eur. J.*****,** 2010, *16***,** 14365.
4. C. Camp, V. Mougel, P. Horeglad, J. Pécaut, M. Mazzanti, ***Jacs*****,** 2010, *132*, 17374**.**
5. B. Biswas, V. Mougel, J. Pécaut, M. Mazzanti ***, Angew. Chem.***, 2011, *50*, 5745, +*back cover*.
6. R. Copping, V. Mougel, S. Petit, C. Den Auwer, P. Moisi, M. Mazzanti, ***Chem. Comm.***, 2011, *47*, 5497.
7. V. Mougel, J. Pécaut, M. Mazzanti, ***Chem. Comm.***, 2012, *48*, 868.
8. L.Chatelain, V. Mougel, J. Pécaut, M. Mazzanti, ***Chem. Sci.,*** 2012, *3*, 1075
9. R. Copping, V. Mougel, C. Den Auwer, C. Berthon, P. Moisy, M. Mazzanti, ***Dalton Trans.***, 2012, DOI: 10.1039/C2DT31072D + *front cover*.